THE UNIVERSITY OF CHICAGO

DESIGN OF FUNCTIONAL METAL-ORGANIC FRAMEWORKS FOR SENSING AND

CATALYTIC APPLICATIONS

A DISSERTATION SUBMITTED TO

THE FACULTY OF THE DIVISION OF THE PHYSICAL SCIENCES

IN CANDIDACY FOR THE DEGREE OF

DOCTOR OF PHILOSOPHY

DEPARTMENT OF CHEMISTRY

BY

ZEKAI LIN

CHICAGO, ILLINOIS

AUGUST 2017

TABLE OF CONTENTS

LIST OF TABLES

LIST OF FIGURES

LIST OF SCHEMES

LIST OF ABBREVIATIONS

2D	2-dimensional
3D	3-dimensional
°C	degrees Celsius
Å	angstrom
ΔR	change in scattering half-path length
σ^2	mean standard relative deviation of a scatter
AFM	atomic force microscopy
Al-Co(TBP)-MOF	a MOF constructed from aluminum SBUs and Co(TBP) ligand
ANL	Argonne National Laboratory
APS	Advanced Photon Source
B3LYP	Becke 3-parameter, Lee-Yang-Parr (hybrid DFT functional)
bcu	body-center cubic unit
BET	Brunauer-Emmett-Teller
Boc	tert-butyloxycarbonyl protecting group
Boc_2O	di-tert-butyl dicarbonate
bpy	2,2'-bipyridine
BTB	1,3,5-Tris(4-carboxyphenyl)benzene
BTB-MOL	MOL constructed from hafnium SBU and BTB ligand

Co(TBP)	TBP ligand metallated with Co
Co•TPY-MOL	TPY-MOL metallated with Co
CV	cyclic voltammetry; cyclic voltammogram
D_2O	deuterium oxide
DFT	density functional theory
DMA	dimethylammonium
DME	N,N-diethylformamide
DMF	N,N-dimethylformamide
DMSO	dimethyl sulfoxide
DPV	differential pulse voltammetry
DS-PEC	dye-sensitized photoelectrochemical cell
E_0	energy shift of the photoelectron
EDX	energy-dispersive X-ray spectroscopy
EPR	electron paramagnetic resonance
ESI	electrospray ionization
ESI-MS	electrospray ionization mass spectroscopy
EtOH	ethanol
EXAFS	extended X-ray absorption fine structure

fcu	face-center cubic unit
Fe-Co(TBP)-MOF	a MOF constructed from iron SBUs and Co(TBP) ligand
FEFF 6	software for simulating EXAFS spectra
Fe-mTPY-MOL	mTPY-MOL metallated with Fe
Fe•TPY-MOL	TPY-MOL metallated with Fe
GC	gas chromatography
GC-MS	gas chromatography-mass spectrometry
GS	ground state
H_2L-Ir	$[Ir(ppy)_2(bpy)]^+$-derived dicarboxylic acid
H_2L-MA	TPDC ligand functionalized with maleic acid
H_2L-Ru	$[Ru(bpy)_3]^{2+}$-derived dicarboxylic acid
H_2L-SA	TPDC ligand functionalized with succinic acid
HADDF	high angle annular dark field
HER	hydrogen evolution reaction
HRTEM	high resoluation transmission electro microscopy
I_0	incident beam intensity
I_t	transmitted beam intensity
I_r	reference beam intensity

ICP-MS	inductively coupled plasma mass spectroscopy
IFEFFIT	software used for fitting EXAFS spectra
In-TBP-MOF	a MOFconstructed from indium SBUs and TBP ligand
In-Co(TBP)-MOF	In-TBP-MOF with TBP metallated by Co
In-Co(TBP)-MOF	In-TBP-MOF with TBP metallated by In
IR	infrared spectroscopy
K_3PO_4	potassium phosphate tribasic
Kgd	kagome-dual
KIE	kinetic isotope effect
K_{sv}	Stern-Völmer constant
Me_2L-Ir	esterified form of ligand H_2L-Ir
Me_2L-MA	esterified form of ligand H_2L-MA
Me_2L-Ru	esterified form of ligand H_2L-Ru
Me_2L-SA	esterified form of ligand H_2L-SA
MeOH	methanol
MLCT	metal to ligand charge transfer
MOF	metal-organic framework
MOF-Ir	UiO-69 MOF based on H_2L-Ir

MOF-MA UiO-68 MOF functionalized with maleic acid

MOF-Ru UiO-69 MOF based on H_2L-Ru

MOF-SA UiO-68 MOF functionalized with succinic acid

MOL metal-organic layer

mTPY-MOL BTB-MOL doped with TPY ligands

NBO natural bond orbital

NHE normal hydrogen electrode

Ni_4P_2 Ni-containing POM $[Ni_4(H_2O)_2(PW_9O_{34})_2]^{10-}$

Ni_4P_2@MOF-Ir Ni_4P_2 encapsulated in MOF-Ir

Ni_4P_2@MOF-Ru Ni_4P_2 encapsulated in MOF-Ru

NMR nuclear magnetic resonance

NP nanoparticle

PDI pyridinediimine

PEG polyethylene glycol

PFBHA o-(2,3,4,5,6-pentafluorobenzyl) hydroxylamine

PLATON crystallography software package

POM polyoxometalate

POM@MOF POMs encapsulated in MOF channels or pores.

ppb	part-per-billion, $\mu g \, kg^{-1}$
ppy	2-phenylpyridine
PSM	post-synthetic modification
PXRD	powder X-ray diffraction
QE	quantum efficiency
R^2	goodness-of-fit metric
RED	rotation electron diffraction
Reff	scattering half-path length
rGO	reduced graphene oxide
rt, r.t.	room temperature
S_0^2	passive electron reduction factor
SAED	selected area electron diffraction
SBU	secondary building unit
STEM	scanning transmission electron microscopy
TBP	tetrakis(4-benzoic acid)porphyrin
TEM	transmission electron microscopy
TFA	trifluoroacetic acid
TGA	thermogravimetric analysis

THF	tetrahydrofuran
TON	turnover number
tpy	2,2':6',2''-terpyridine
TPY	4'-(4-carboxyphenyl)-[2,2':6',2''-terpyridine]-5,5''-dicarboxylic acid
TPY-MOL	MOL constructed from hafnium SBU and TPY ligand
TPDC	p,p'-terphenyldicarboxylic acid
UiO	University of Oslo
UV-Vis	ultra violet and visible
UV-Vis-NIR	ultra violet and visible and near infrared
XAFS	X-ray absorption fine structure
XANES	X-ray absorption near-edge structure
XAS	X-ray absorption spectroscopy
XPS	X-ray photoelectron spectroscopy
Zr-Co(TBP)-MOF	MOF-545 or PCN-222 with TBP metallated with Co

ABSTRACT

Zekai Lin: Design of Functional Metal-Organic Frameworks for Sensing and Catalytic
Applications

Under the Direction of Professor Wenbin Lin

The first part (Chapter 1) of this dissertation focuses on designing functional metal-organic frameworks (MOFs) by decorating the bridging ligand with orthogonal moieties terminated with succinic acid (MOF-**SA**) and maleic acid (MOF-**MA**). Structural analysis of MOF-**SA** provides the first direct evidence for 8-connected secondary building units (SBUs) in UiO-type MOFs. In contrast, MOF-**MA** contains 12-connected SBUs as seen in the traditional UiO MOF topology. The reduced connectivity results in MOF-**SA** with a larger pore aperture and more accessible metal-binding sites located at the termini of the orthogonal functionalities. The highly porous MOF-**SA** is an excellent fluorescence sensor for metal ions with a detection limit of <0.5 ppb for Mn^{2+} and three to four orders of magnitude greater sensitivity for metal ions than previously reported luminescent MOFs.

The second part (Chapters 2 and 3) of this dissertation focuses on designing MOFs with multiple precisely-spaced catalytic sites for cooperative catalysis. In Chapter 2, we synthesized porous and interpenetrating In-MOFs with strategically placed Co^{III}(porphyrin) active sites for efficient cooperative hydration of terminal alkynes via dual substrate activation. In Chapter 3, we encapsulated a Ni-containing polyoxometalate (POM) into two highly stable and porous phosphorescent MOFs. The proximity of POM to multiple photosensitizers in POM@MOFs allows for facile multi-electron transfer to enable efficient visible-light driven hydrogen

evolution reaction (HER) with turnover numbers (TONs) as high as 1476. Photophysical and electrochemical studies established the oxidative quenching of the photosensitizer excited state by **POM** as the initiating step of HER, explaining the drastic catalytic activity difference between the two POM@MOF systems.

The third part (Chapters 4 and 5) of this dissertation focuses on the development and use of two-dimensional (2D) metal-organic layers (MOLs) as single-site solid catalysts for various organic transformations. Although many research efforts have been devoted to designing MOF catalysts with interesting catalytic activities and selectivities by taking advantage of the site-isolation effect, the diffusion of substrates and products through the framework remains a significant issue for MOF catalysts. This diffusion constraint can be relieved by reducing one dimension of the MOF crystals to afford a new category of 2D materials, MOLs, that are only a few nanometers thick, minimizing diffusion distance. In Chapter 4, we developed a highly scalable bottom-up strategy to assemble MOLs directly from molecular building blocks in one-pot solvothermal reactions. The MOLs were functionalized with Fe-terpyridine catalytic centers to give diffusion-free single-site solid catalysts for the hydrosilylation of terminal olefins. In Chapter 5, we synthesized a terpyridine-based TPY-MOL and metalated TPY-MOL with $CoCl_2$ and $FeBr_2$ to generate M•TPY-MOL (M = Co or Fe) catalysts for benzylic C-H borylation and C_{sp3}-H amination reactions. Interestingly, M•TPY-MOL catalysts showed significantly higher activity and different chemo-selectivity than homogeneous MOF controls. Spectroscopic studies and DFT calculations indicated the formation of unprecedented MOL-stabilized M^{II}-$(TPY^{\bullet\bullet})^{2-}$ species featuring divalent metals and TPY diradical dianions. We believe that the formation of novel M^{II}-$TPY^{\bullet\bullet}$ species endows them with unique and enhanced catalytic activities in C_{sp3}-H borylation and intramolecular C_{sp3}-H amination reactions.

computational chemistry. I would also like to thank Prof. Cheng Wang, Prof. Junliang Sun, Lingyun Cao, and Fei Peng on the MOL projects.

I have always been grateful to all former and present group members who help me survive graduate school. I would like to thank Prof. Cheng Wang and Dr. Teng Zhang for mentoring me at the beginning of graduate school. I would like to thank Dr. Demin Liu, Dr. Joseph Falkowski, Dr. Stephanie Ashford, Dr. Rachael Huxford Phillips, Dr. Marcela Wanderley, Dr. Christopher Poon, and Dr. Seth Barrett for helping me adapt to life in United States. I would like to thank Dr. Carter Abney for teaching me XAFS, an important part of my research work. I would like to thank Dr. Nathan Thacker, Dr. Takahiro Sawano, Dr. Zhi-Ming Zhang, Dr. Xiang-Jian Kong, Dr. Michaël Carboni, Dr. Kuangda Lu, Dr. Kuntal Manna, Dr. Tasha Drake, and Pengfei Ji for the collaborations and helpful advice on my research projects. I would like to thank Daniel Micheroni, Marek Piechowicz, Yang Song, Ruoyu Xu, Wenbo Han, Guangxu Lan, Kaiyuan Ni, Joseph Solomon, Dr. Chunbai He, Dr. Xiaopin Duan, and Christina Chan simply for their supports, encouragements, and helpful discussions.

It is a great honor to be in this prestigious university and department with so many excellent professors, staffs, postdocs, and students. I would like to thank Prof. John Anderson and his group members for their help and advice on EPR experiments. I would like to thank Dr. Qiti Guo and Dr. Justin Jureller from MRSEC for their support and guidance on using many of their facilities. I would like to thank Dr. Alex Filatov for the help on XRD and XPS. I would like to thank Dr. Antoni Jurkiewicz for the help on NMR. I would like to thank Dr. C. Jin Qin for the help on MS. I would also like to thank John Phillips for the help on assembly of new instruments.

I would like to thank the Windt Memorial Fund Graduate Fellowship for funding.

And finally, I would like to thank my parents and sister for their constant and unconditional love, support, and encouragement, without which I could have never made it to this point of my life. And to my wife, Dong Dong, thank you for being considerate, supportive and giving me love, warmth, and happiness. This work is dedicated to them.

CHAPTER 1 A Metal-Organic Framework Containing Unusual Eight-Connected Zr-Oxo Secondary Building Units and Orthogonal Carboxylic Acids for Ultra-sensitive Metal Detection

1.1. Introduction

Metal-organic frameworks (MOFs), also known as porous coordination polymers or porous coordination networks, date back to as early as late 1950s and early 1960s.[1-5] However, due to the difficulty of growing large single crystals that are suitable for X-ray diffraction studies and the lack of computational capability to study/visualize complicated solid-state structures, this field remained relatively unexplored. The field of coordination polymers was revitalized after a series of seminal papers from Robson and coworkers on the synthesis and structural analysis of coordination networks constructed from Cu(I), Zn(II) and Cd(II) metal nodes and cyano- or nitrile-bridging ligands in 1989 and the early 1990s,[6-9] followed by a large number of coordination polymers/MOFs constructed from various metal nodes and bridging ligands from many other research groups, including Fujita, Yaghi, Zaworotko, Kitagawa, Moore/Lee and Férey, Lin, and others.[10-21]

MOFs now refer to hybrid porous materials composed of inorganic secondary building units (SBU, metal ions or clusters) that connect organic bridging ligands via moderate coordination bonds to form 1-, 2-, or 3-dimensional crystalline infinite networks.[22-24] MOFs possess three fundamental features: crystallinity, reticular synthesis, and ease of installing functionalities. First, the highly ordered and crystalline structures of MOFs can be determined by X-ray crystallography, providing a convenient way to elucidate the structure-property relationships. Second, reticular synthesis can be described as the design and engineering of MOFs by assembling judiciously chosen molecular building blocks (SBUs and bridging ligands)

with different shapes or connectivity, into predetermined ordered structures, allowing for the design of a large library of MOF structures and therefore properties and functions.[25] Third, functionalities can be easily installed by either using pre-functionalized building blocks before MOF synthesis or via a process now known as post-synthetic modification (PSM) after MOF synthesis.[26-31] By taking advantage of these features, MOFs have been designed and explored for potential applications in many fields, including gas storage/separation,[32-35] nonlinear optics,[36] chemical sensing,[37] catalysis,[38,39] solar energy harvesting,[40] and biomedical applications.[41,42]

A large amount of MOFs have been found to be photoluminescent, resulting from their organic bridging linkers containing aromatic units. In addition, some SBUs can also contribute to photoluminescence. Consequently, photoluminescent MOFs can be potentially used as chemical sensors since the intensities of photoluminescence of MOFs can be altered in response to interactions between the guest species and the frameworks.[37,43] MOF-based sensors have three interesting features: 1) MOFs with high surface areas can take up guest species into their internal volumes with higher internal concentrations than in the external medium due to preferential interactions between the guest species and pore surfaces, known as pre-concentration effect, to enhance sensitivity; 2) finely-tuned sizes, shapes, and chemical compositions of frameworks can achieve specific host-guest interactions, thus leading to improved selectivity; and 3) porosity and framework flexibility enable reversible uptake and release of guest species to facilitate regeneration and reuse of MOF sensors. [44]

Decorating the bridging ligand with an orthogonal functionality, such as amine, carboxylic acid, and other functional groups, represents an effective strategy to functionalize MOF channels, which have resulted in promising MOF materials for chemical sensing[45-48] and other applications.[49-59] Direct synthesis of MOFs using pre-functionalized ligands is challenging,

as the orthogonal moieties may coordinate to metals during MOF preparation or decompose during MOF synthesis. While post-synthetic modification [29,30] and protection/deprotection[60] are effective strategies for introducing these functionalities, quantitative functionalization is rarely achieved. As a result, few examples of MOFs containing non-coordinated orthogonal functionalities have been reported, either through the use of pre-functionalized ligands[61] or via PSM processes,[62] severely limiting the applications of these MOFs.

First reported by Lillerud and co-workers, the UiO family of MOFs possess robust $Zr_6O_4(OH)_4(RCO_2)_{12}$ SBUs and linear dicarboxylate bridging ligands and are stable under a wide range of conditions.[63,64] Using a p,p'-terphenyldicarboxylic (TPDC) ligand pre-functionalized with a phosphorylurea moiety, Lin and coworkers previously demonstrated that the UiO platform was sufficiently stable for extracting U(VI) from aqueous solutions.[65] While the high connectivity of the $Zr_6O_4(OH)_4(RCO_2)_{12}$ SBU helps to stabilize the MOF structure, partial removal of ligands would result in a larger pore aperture, enhancing the rate of diffusion into the MOF interior and permitting larger molecules to be internalized. Recent publications reveal that the addition of acid modulators during synthesis results in UiO materials with increased surface area and larger pore sizes.[66] It has been proposed that these effects are due to the formation of site defects at the MOF SBUs, resulting in fewer than six dicarboxylate bridging ligands connecting the Zr-oxo clusters. This postulation was supported through various indirect analyses, such as TGA, ^{19}F NMR, and IR,[67,68] as well as more advanced techniques such as PXRD/EXAFS[69] and high-resolution power neutron diffraction,[70] but has thus far evaded single-crystal X-ray diffraction analysis owing to the randomly distributed and stochastically oriented site defects in the previous UiO MOF materials.

In this chapter, I will discuss the preparation of two MOFs based on Zr-oxo SBUs and TPDC ligands pre-functionalized with orthogonal moieties terminated with succinic acid (MOF-**SA**) and maleic acid (MOF-**MA**). Single crystal X-ray structure analyses revealed 8-connected $Zr_6O_8(OH_2)_8(RCO_2)_8$ SBUs in MOF-**SA** and 12-connected $Zr_6O_8(OH)_4(RCO_2)_{12}$ SBUs in MOF-**MA**, which was confirmed by fitting EXAFS data. MOF-**SA** provides the first direct evidence for a UiO-type MOF possessing a SBU with fewer than six bridging ligands. MOF-**SA** exhibits larger pore apertures than MOF-**MA** and is highly sensitive for detecting metal ions via fluorescence quenching.

1.2. Results and Discussion

1.2.1. Synthesis and Characterization of MOFs
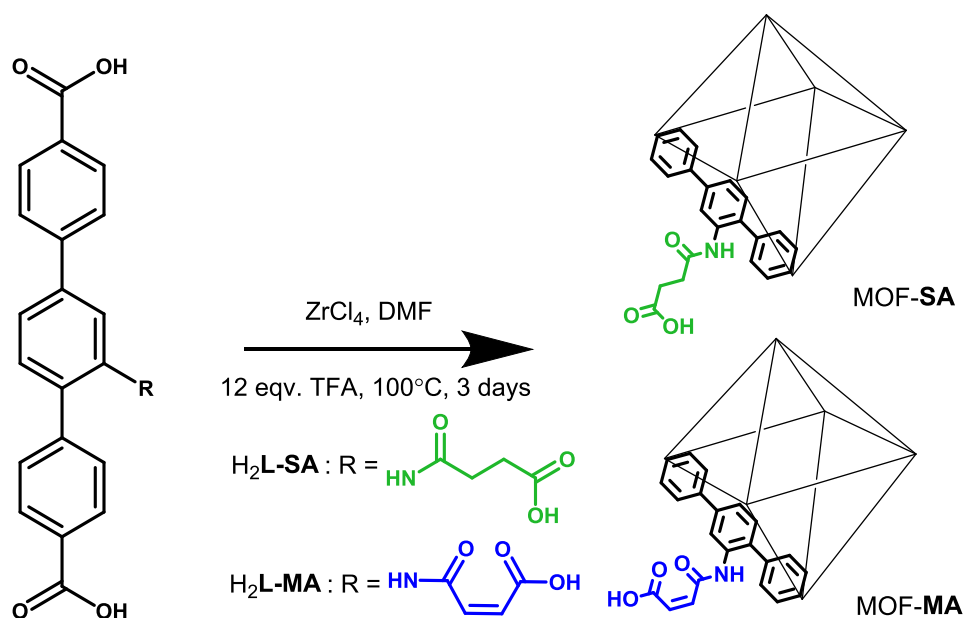
Scheme 1-1. Direct synthesis of MOFs **SA** and **MA** with pre-functionalized ligands possessing orthogonal carboxylic acid moieties. Copyright 2014 John Wiley and Sons.

The TPDC ligands with orthogonal succinic acid and maleic acid functionalities, H$_2$**L-SA** and H$_2$**L-MA**, were prepared by treating 2,5-bis(4-carboxyphenyl)aniline (TPDC-NH$_2$) with

succinic or maleic anhydride in dry DMSO at room temperature for 12 h. Following solvent removal, the solid was washed with water and ethanol, then dried under vacuum to afford pure H$_2$**L-SA** and H$_2$**L-MA** ligands. Crystals of MOF-**SA** and MOF-**MA** were obtained by heating a solution of ZrCl$_4$, H$_2$**L-SA** or H$_2$**L-MA**, and trifluoroacetic acid (TFA) in DMF at 100 °C for 3 days (**Scheme 1-1**).

A single crystal X-ray diffraction study showed that MOF-**SA** crystallizes in the tetragonal *I*4/*mmm* space group (**Figure 1-1**). The asymmetric unit consists of 1/16 of the Zr$_6$O$_8$(OH$_2$)$_8$(CO$_2$)$_8$ cluster and 1/4 of the bridging ligands. Unlike commonly observed UiO MOFs, the Zr SBU in MOF-**SA** is only 8-connected, with the formula of Zr$_6$O$_8$(OH$_2$)$_8$(**L-SA**)$_4$. Compared to a typical Zr$_6$O$_4$(OH)$_4$(**L**)$_6$ cluster, the four bridging carboxylate groups on the equatorial plane of the Zr$_6$ octahedra are missing, and substituted by aqua coordination. The resulting MOF possesses the *bcu* network topology with $\{4^{24} \cdot 6^4\}$ connectivity. Although a similar SBU was later reported in Zr MOFs constructed from tetracarboxylate ligands,[71,72] this is the first direct crystallographic evidence for an 8-connected Zr SBU with a linear bridging ligand, confirming the earlier proposal put forward by Lillerud, Zhou, De Vos, and Hupp. [67-70,73]
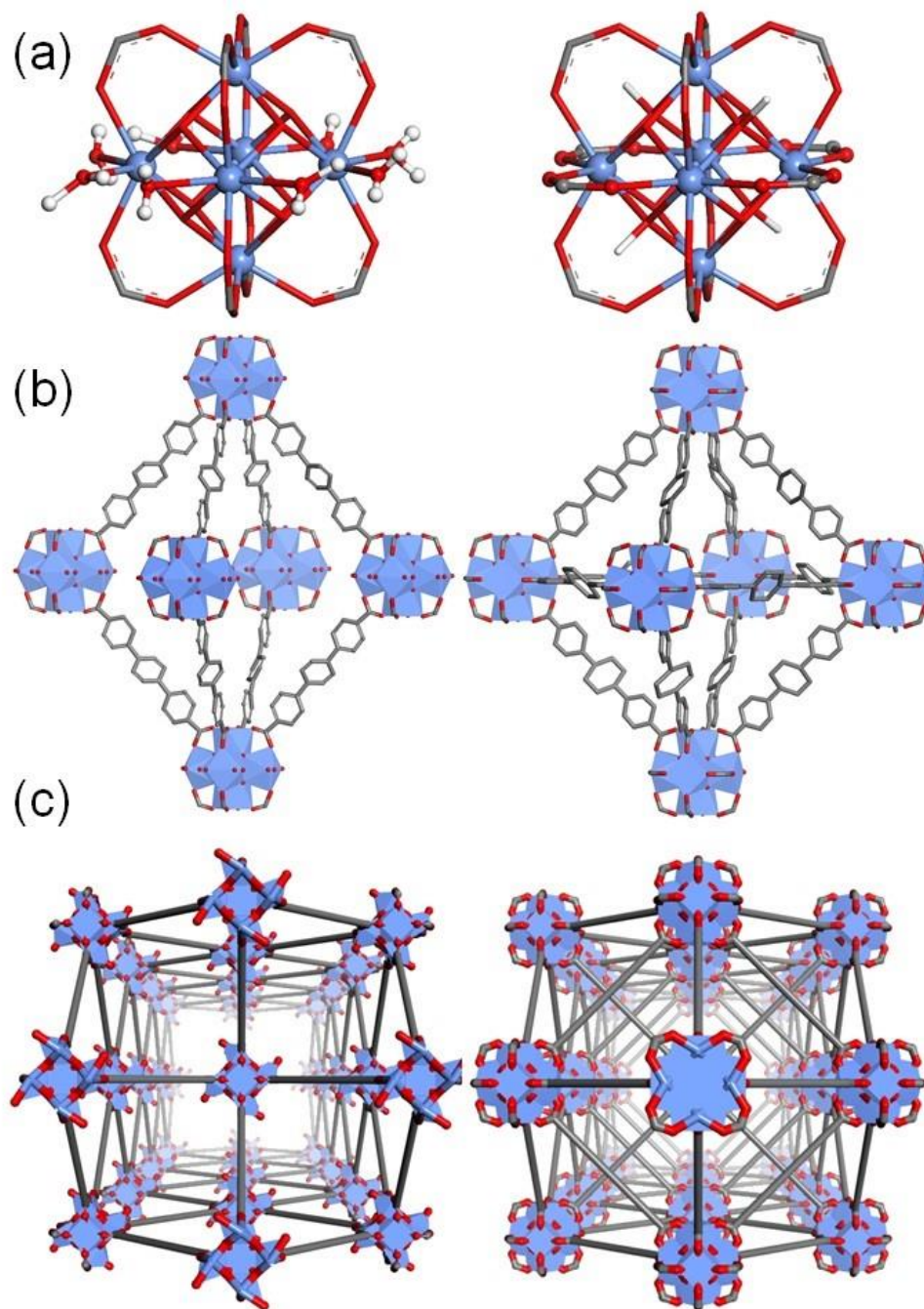
Figure 1-1. Comparison of 8- and 12-connected MOF topologies from the UiO family. The figures for 8-connected MOF-**SA** are displayed on the left, and the figures for 12-connected MOF-**MA** are shown on the right. (a) SBUs, (b) octahedral cavities, and (c) perspective views along the z axis. Channels of both MOFs show distinct differences as a result of different SBU

Figure 1-1, continued connectivity. Purple polyhedra and spheres are Zr atoms, with red and grey representing oxygen and carbon, respectively. Hydrogen atoms are omitted for clarity, with the exception of those on equatorial water molecules and bridging μ_3-OH groups on the SBUs. Copyright 2014 John Wiley and Sons.

MOF-**MA** crystallizes in the cubic $Fm\bar{3}m$ space group. The asymmetric unit consists of 1/48 of the $Zr_6O_4(OH)_4(CO_2)_{12}$ cluster and 1/8 of the bridging ligands. The SBU is comprised of six Zr cations, with each Zr bridged by μ_3-O, μ_3-OH, and carboxylate groups. Each SBU is connected to twelve neigbhoring SBUs by six dicarboxylate linkers. Like other well-established UiO MOFs, MOF-**MA** possesses the *fcu* network topology.

Table 1-1. Crystallographic data obtained for the single crystal structures of MOF-**SA** and MOF-**MA.**

Name	MOF-**SA**	MOF-**MA**
Framework Formula	$Zr_6(O)_8(OH_2)_8\mathbf{L}_4$	$Zr_6(O)_4(OH)_4\mathbf{L}_6$
Fw	2068.5	2404.8
Temperature	296 (2)	296 (2)
Wavelength (Å)	0.41328	0.41328
Crystal system	Tetragonal	Cubic
Space group	$I4$/mmm	$Fm\bar{3}m$
a, Å	21.638 (5)	32.5090(16)
b, Å	21.638 (5)	32.5090(16)
c, Å	34.103 (8)	32.5090(16)
α °	90	90
β °	90	90
γ °	90	90
V, Å^3	15968 (6)	34357(3)

Table 1-1, continued

Z	2	4
Density (calcd. g/cm^3)	0.430	0.465
Absorption coeff. (mm^{-1})	0.279	0.259
F(000)	2048.0	4768
θ range data collection	0.69 – 11.29	0.73 – 9.25
Limiting indices	-20<=h<=20,	-25<=h<=25,
	-20<=k<=20,	-25<=k<=25,
	-32<=l<=32	-25<=l<=25
Reflection collected	68589	37917
Independent reflections	2052	480
R(int)	0.223	0.125
Data/restraints/parameters	2052/0/99	480/53/50
Goodness-of-fit on F^2	1.333	1.882
Final R indices [I>2σ(I)]	R1 = 0.0834,	R1 = 0.1272,
	wR2 = 0.2015	wR2 = 0.3527
R indices (all data)	R1 = 0.1075,	R1 = 0.1715,
	wR2 = 0.2098	wR2 = 0.3855
CCDC	1012331	1012332

Owing to the crystallographically imposed disorder for the bridging ligands in UiO-type MOFs, the identities of the bridging ligands in MOFs-**SA** and -**MA** cannot be established by single crystal X-ray structure analyses. Instead, the identities of bridging ligands in MOFs-**SA** and -**MA** were determined by integration of proton peaks in the ^{1}H NMR spectra of digested samples of MOFs-**SA** and -**MA** in K$_3$PO$_4$/D$_2$O/DMSO-d$_6$. ^{1}H NMR spectroscopy unambiguously revealed that the H$_2$**L-SA** ligand did not decompose during the MOF synthesis; the ^{1}H NMR spectrum obtained for digested MOF-**SA** (**Figure 1-2**) matches perfectly with that of pure ligand

H$_2$**L-SA** in a solution of K$_3$PO$_4$/D$_2$O/DMSO-d$_6$ (**Figure 1-2**). ESI-MS analysis (**Figure 1-3**) supports the purity of the digested MOF-**1** with a unique peak at m/z = 432.1 corresponding to [H$_2$**L-SA**-H]$^-$. Unlike MOF-**SA**, significant decomposition of the ligand is observed in the ^{1}H NMR spectrum of digested MOF-**MA** (**Figure 1-4**). Integration of the ethylene peaks (δ 5.75 and 6.25) indicate that ~25 % of the original **L-MA** ligand remained intact after MOF synthesis. This was further supported by ESI-MS analysis (**Figure 1-5**) exhibiting signals at m/z = 432.1 ([H$_2$**L-MA**+H]$^+$), m/z = 470.1 ([H$_2$**L-MA**+K]$^+$), and m/z = 334.1 ([H$_2$**L-NH$_2$**+H]$^+$). The decomposition of H$_2$**L-MA** can be reduced to 50% by decreasing the duration of MOF-**MA** synthesis to 1 day, while prolonging heating (7 days) resulted in a 91% degradation of **L-MA** ligands (**Figure 1-6**). It is expected the difference in topology can be attributed to the hydrolysis of the orthogonal functionality in MOF-**MA,** alleviating steric effects and accommodating formation of a 12-connected SBU.
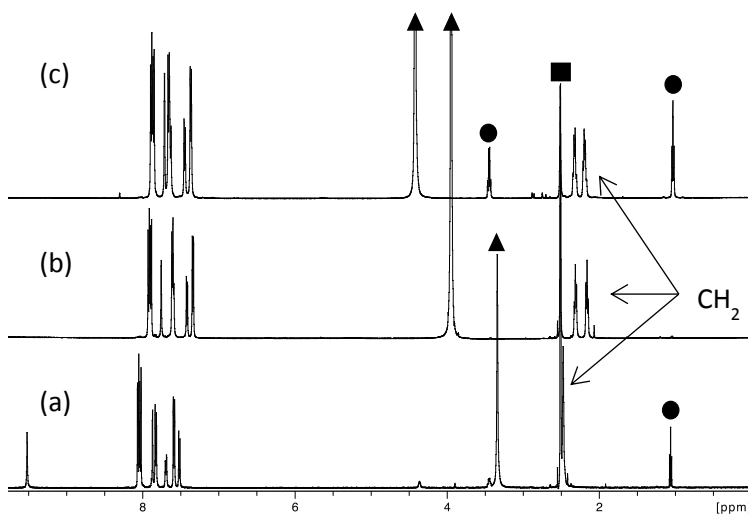
Figure 1-2. ^{1}H NMR spectra of MOF-**SA** samples digested in K$_3$PO$_4$/D$_2$O/DMSO-d$_6$. (a) NMR spectrum of the H$_2$**L-SA** in DMSO-d$_6$. (b) NMR spectrum of H$_2$**L-SA** in K$_3$PO$_4$/D$_2$O/DMSO-d$_6$.

Figure 1-2, continued (c) NMR of the digested MOF-**SA** in K_3PO_4/D_2O/DMSO-d_6. Circles, squares and triangles denote peaks due to residual solvents, EtOH, DMSO, and H_2O, respectively. Copyright 2014 John Wiley and Sons.
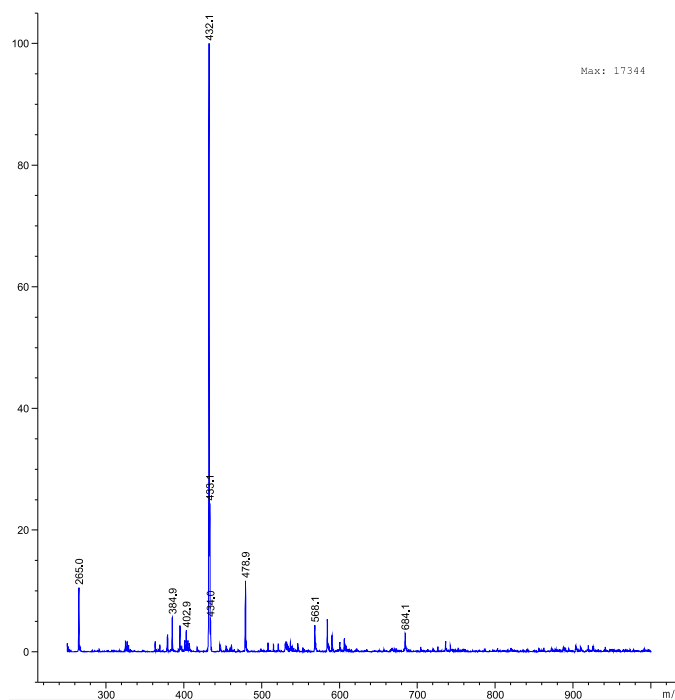
Figure 1-3. ESI-MS analysis of digested MOF-**SA**. Copyright 2014 John Wiley and Sons.
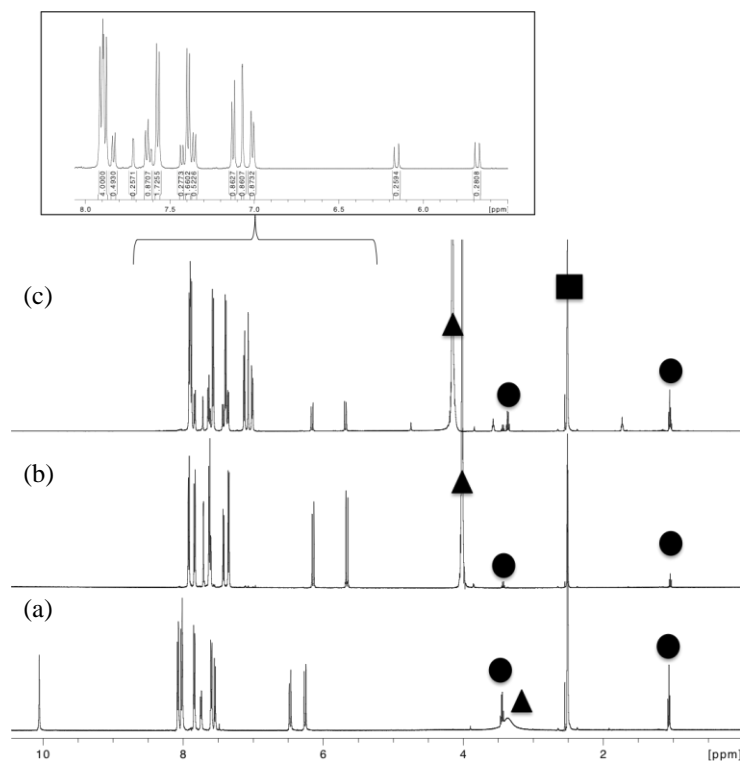
Figure 1-4. ^{1}H NMR spectra of MOF-**MA** samples digested in $K_3PO_4/D_2O/DMSO$-d_6. (a) NMR spectrum of the H_2**L-MA** in DMSO-d_6. (b) NMR spectrum of H_2**L-MA** in $K_3PO_4/D_2O/DMSO$-d_6. (c) NMR of the digested MOF-**MA** in $K_3PO_4/D_2O/DMSO$-d_6. Circles, squares, and triangles denote peaks due to residual solvents, EtOH, DMSO, and H_2O, respectively. Copyright 2014 John Wiley and Sons.
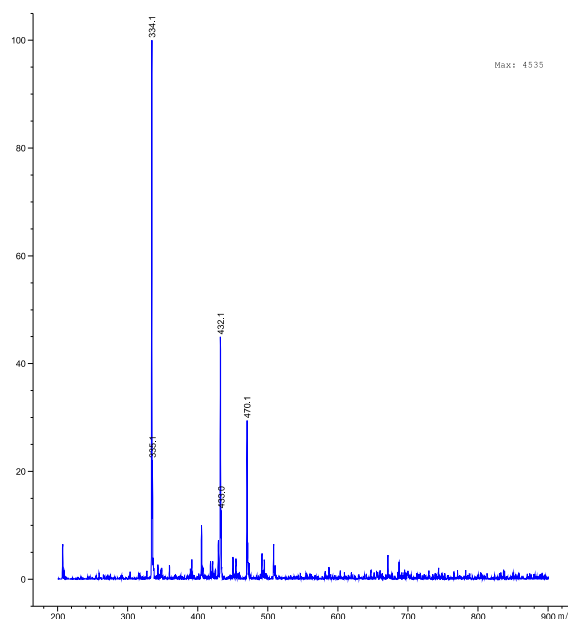
Figure 1-5. ESI-MS analysis of digested MOF-**MA**. Copyright 2014 John Wiley and Sons.
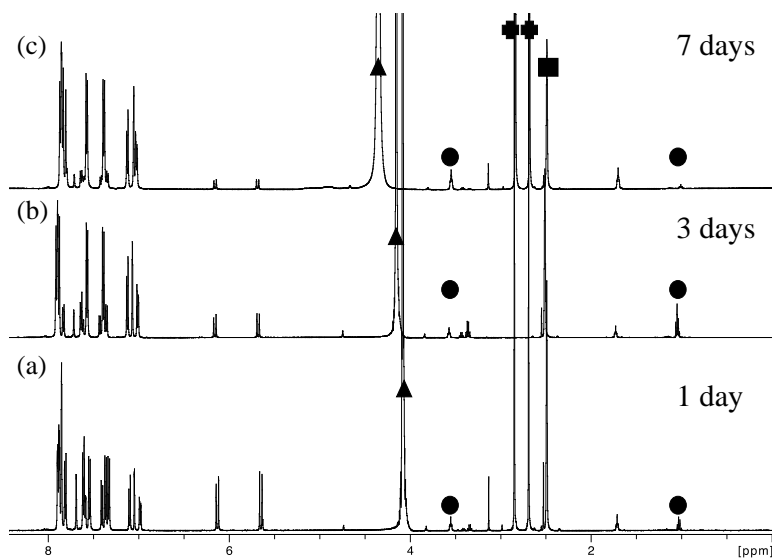
Figure 1-6. ^{1}H NMR spectra of MOF-**MA** formed after different times of reaction at 100 °C and digested in K_3PO_4/D_2O/DMSO-d_6. (a) After one day. (b) After 3 days. (c) After 7 days. Circles, squares, triangles and plus sign are associated to residual solvent peaks, EtOH, DMSO, H_2O, and DMF, respectively. Copyright 2014 John Wiley and Sons.

12

Thermogravimetric analysis (TGA) results were consistent with the formulations of MOFs-**SA** and -**MA** as established by X-ray crystallography and NMR analyses (**Figure 1-7**, **Table 1-2**). While the TGA profile obtained for MOF-**SA** is in agreement with the presence of pure **L-SA** ligands, the TGA data for MOF-**MA** is consistent with the partial decomposition of **L-MA** ligands during MOF synthesis.
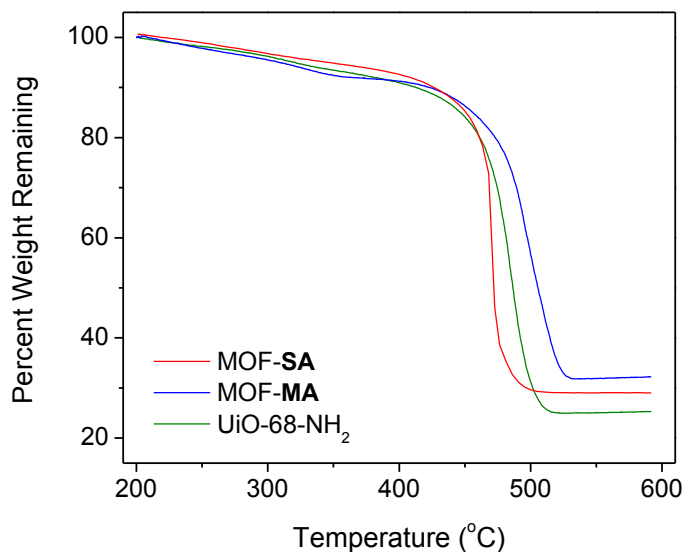
Figure 1-7. TGA curves for UiO-68-NH$_2$ (green), MOF-**SA** (red), and MOF-**MA** (blue). Copyright 2014 John Wiley and Sons.

Table 1-2. Theoretical compositions compared to the experimental values obtained by TGA for MOF-**SA**, MOF-**MA** and UiO-68-NH$_2$

		% L	% Residual mass
MOF-**SA**	Calculated	70.9	29.1
	Experimental	71	29
MOF-**MA**	Calculated	73.7	26.3
	(*25% **L-MA** / 75 % **L-NH$_2$***)		
	Experimental	68	32

Table 1-2, continued

UiO-68-NH$_2$	Calculated	73	27
	Experimental	75	25

[*] The percentages of ligand remaining in MOF-**MA** have been determined by NMR analysis of MOF-**MA** digested with K$_3$PO$_4$ in DMSO (**Figure 1-4**).
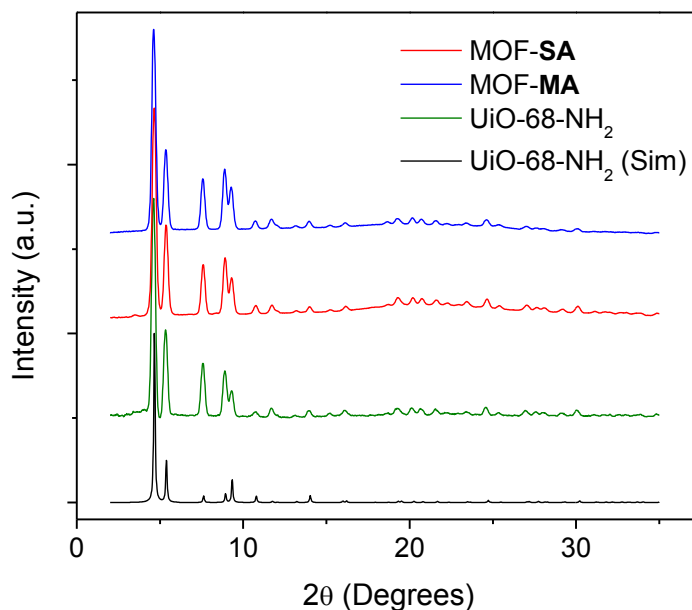
Figure 1-8. Experimental powder X-Ray patterns for UiO-68-NH$_2$ (green), MOF-**SA** (red), and MOF-**MA** (blue) compared to the simulated powder X-Ray pattern for UiO-68-NH$_2$ (black). Copyright 2014 John Wiley and Sons.

In spite of the significant structural difference between MOF-**SA** and MOF-**MA**, their PXRD patterns appear remarkably similar (**Figure 1-8**), thus offering no insight into the number of bridging ligands linking the SBUs in the bulk materials of MOFs-**SA** and -**MA**. We have utilized X-ray absorption spectroscopy (XAS) to lend additional support for the structural assignments of MOFs-**SA** and -**MA** and to prove the phase purity of these functionalized UiO materials.

MOF-**SA**, MOF-**MA**, and UiO-68-NH$_2$ were investigated by XAS at the Zr K-edge. Data were processed using the Athena and Artemis programs of the IFEFFIT package based on FEFF 6.[74,75] Prior to merging, spectra were aligned to the first and largest peak in the smoothed first derivative of the absorption spectrum, their background was removed, and then spectra were processed to obtain a normalized unit edge step. Data were processed with k^3-weighting and an Rbkg value of 1.0.

Merged data sets were aligned to the first and largest peak in the smoothed first derivative of the absorption spectrum. Normalized μ(E) data were compared directly using the Athena program of the IFEFFIT package.[74]

A comparison of the X-ray absorption near-edge (XANES) region reveals slight differences between the three MOFs (**Figures 1-9** to **1-10**). MOF-**1** has slightly lower intensity in the XANES region when compared to MOF-**MA** and UiO-68-NH$_2$. As XAS measures the average spectrum for all absorbing elements, this difference in pre-edge intensity can be attributed to the presence of two crystallographically inequivalent Zr centers in the SBUs: the axial Zr centers are coordinated by four μ$_3$-oxo groups and four carboxylic oxygens, whereas the equatorial Zr centers are coordinated by four μ$_3$-oxo groups, two carboxylic oxygens, and two coordinating water molecules. For MOF-**MA** and UiO-68-NH$_2$, all Zr are crystallographically equivalent, and their XANES spectra are identical in intensity.
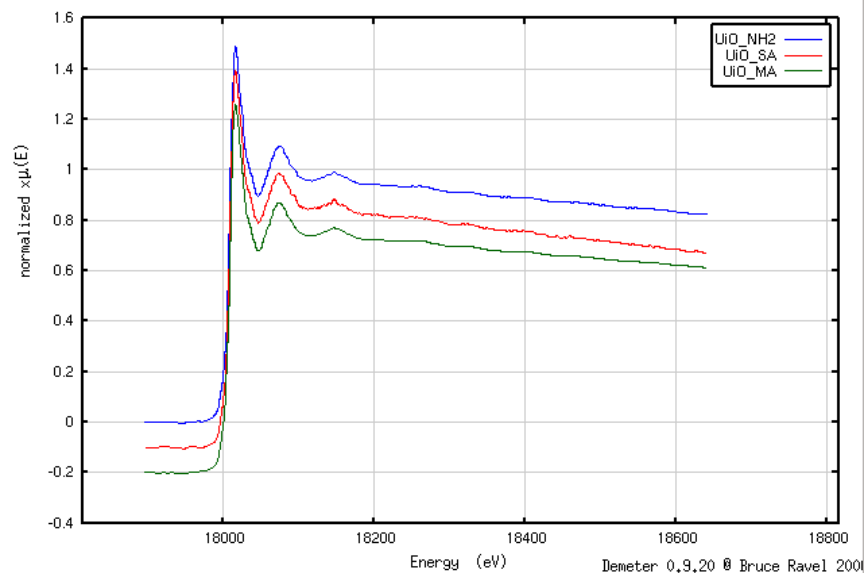
Figure 1-9. Normalized μ(E) data for UiO-68-NH$_2$ (Blue), MOF-**SA** (Red), and MOF-**MA** (Green). For clarity, the data has been manually offset by 0.1 arbitrary units. Copyright 2014 John Wiley and Sons.
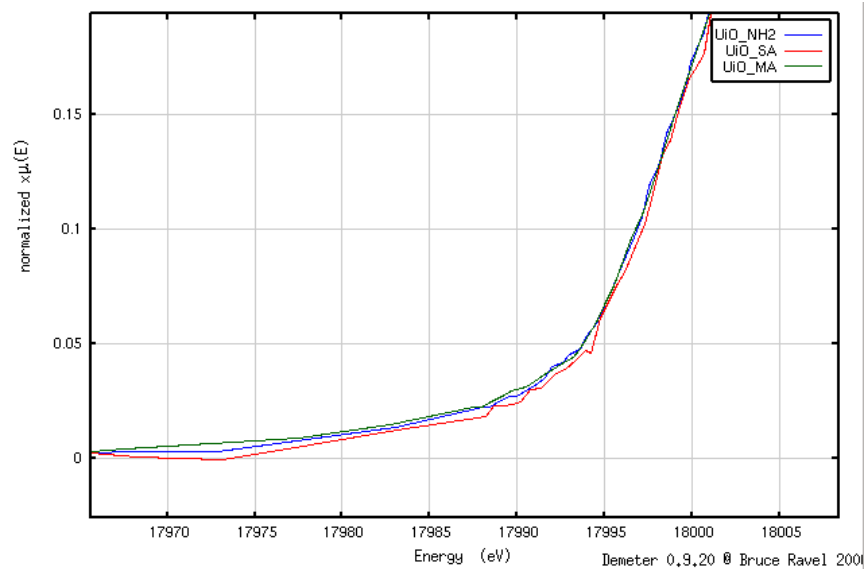
Figure 1-10. Pre-edge region of XANES spectra for UiO-68-NH$_2$ (Blue), MOF-**SA** (Red), and MOF-**MA** (Green). The data have not been offset in this figure. Copyright 2014 John Wiley and Sons.

16

Fits of the EXAFS region were obtained for UiO-68-NH$_2$, MOF-**SA**, and MOF-**MA** using the crystal structures of UiO-68-NH$_2$ and MOF-**SA** as theoretical models. Fits were performed using the Artemis program of the IFEFFIT package,[74] with a refinement process similar to work previously published.[69] Namely, all single-scattering and multiple-scattering paths with relative intensity greater than 9% of the first Zr-O single-scattering path and half path length (Reff) less than 4.5Å were used for fitting. All fits were performed with a k-weight of 2 in R-space, with ΔR = 1.2 - 4.5 Å, and Δk = 2.0 − 10.87, affording 18 independent points. Refinement was performed by optimizing an amplitude factor S_0^2 and energy shift ΔE_0, which are common to all paths, in addition to parameters for bond length (ΔR) and Debye-Waller factor (σ^2). For MOF-**SA** and MOF-**MA**, the S_0^2 parameter was fixed at 1.048, which is the value obtained from the UiO-68-NH$_2$ fitting. Unique parameters for ΔR and σ^2 were provided for the two (12-connected) or three (8-connected) differentiable first shell Zr-O single scattering paths, as well as the Zr-C and Zr-Zr single scattering paths. Due to possessing a cubic space group, isotropic expansion was assumed and all remaining single-scattering and multiple-scattering paths had ΔR and σ^2 values parameterized as a function of their individual Reff values. A global σ^2 was scaled by the square root of Reff for each σ^2, and the variable α parameterized the path length variation, so that ΔR = α·Reff. For all fits, the number of parameters used was less than 2/3 the total number of independent points, as determined by the Nyquist Equation. For 8-connected models, two crystallographically inequivalent Zr atoms are present in the SBU at a ratio of 2:1 (equatorial Zr : axial Zr). The degeneracy was adjusted in the fit by scaling the S_0^2 parameter by 0.666 and 0.333, respectively, as degeneracy and S_0^2 are directly correlated in the EXAFS equation. Due to similarity in bond length, Zr-O scattering paths were grouped as follows: Zr$_a$-O and Zr$_e$-O$_{\mu3}$ as R$_O$ and σ^2 (O), and Zr$_a$- O$_{\mu3}$ and Zr$_e$-O as R$_{\mu3O}$ and σ^2 (μ_3-O). The Zr$_e$-OH$_2$

pathways were uniquely parameterized as R_{H2O} and σ^2 (H_2O). A summary of EXAFS refinement for all structures is provided below, as are plots of experimental and best fit data in both R- and k-space.
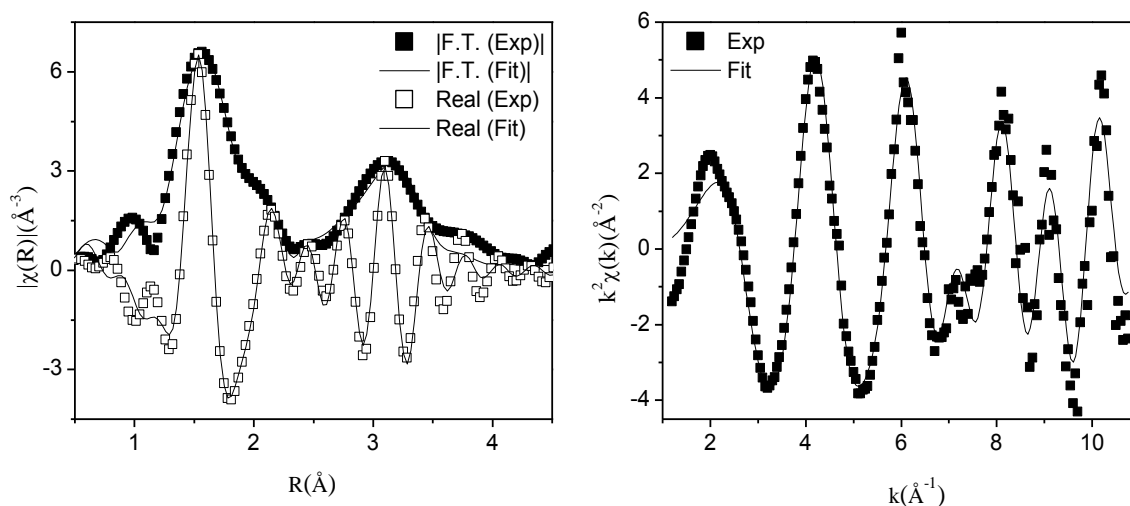
Figure 1-11. Comparison between experimental EXAFS data (squares) and best fit (line) for UiO-68-NH$_2$. Data are displayed in *R*-space (left) and as k^2-weighted χ(k) data (right). *R*-space plot shows magnitude of Fourier Transform and real component for both data and fit. A final *R*-factor of 0.01 was obtained for the UiO-68-NH$_2$ fit. Copyright 2014 John Wiley and Sons.
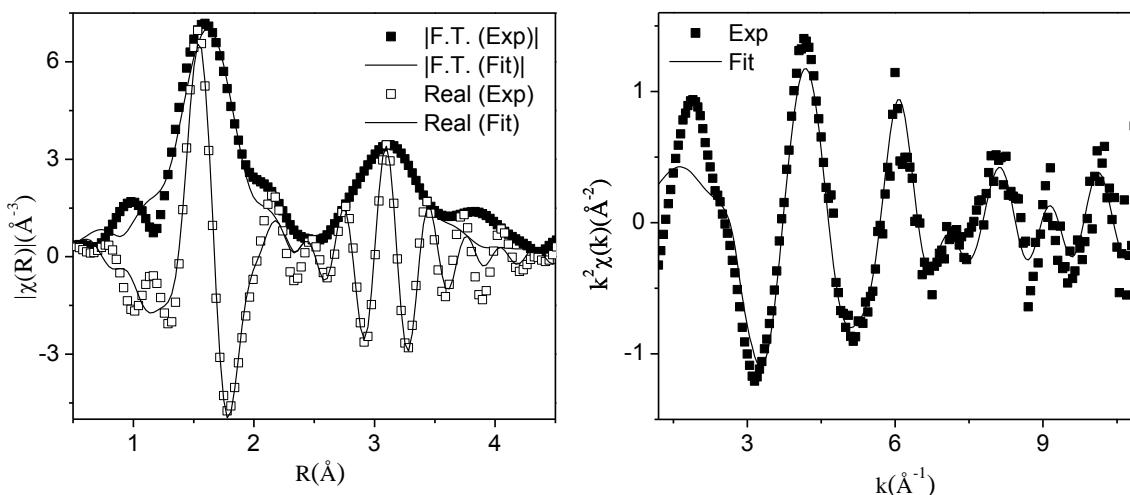
Figure 1-12. Comparison between experimental EXAFS data (squares) and best fit (line) for MOF-**SA**. Data are displayed in R-space (left) and as k^2-weighted χ(k) data (right). R-space plot

Figure 1-12, continued shows magnitude of Fourier Transform and real component for both data and fit. A final R-factor of 0.02 was obtained for the MOF-**SA** fit. Copyright 2014 John Wiley and Sons.
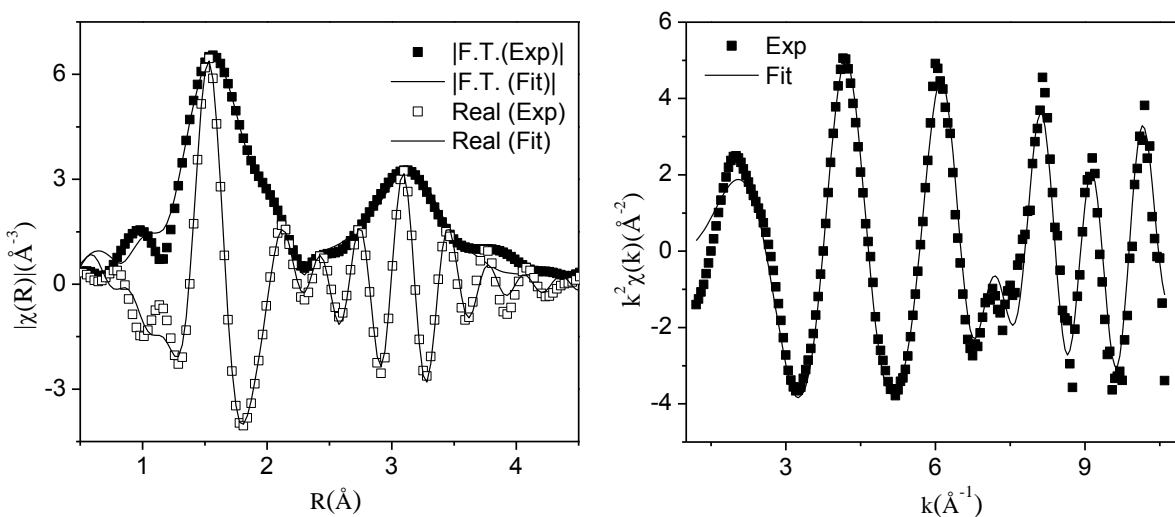
Figure 1-13. Comparison between experimental EXAFS data (squares) and best fit (line) for MOF-**MA**. Data are displayed in R-space (left) and as k^2-weighted $\chi(k)$ data (right). R-space plot shows magnitude of Fourier Transform and real component for both data and fit. A final R-factor of <0.01 was obtained for the MOF-**MA** fit. Copyright 2014 John Wiley and Sons.

Table 1-3. Summary of EXAFS Refinements

	UiO-68-NH$_2$	MOF-**SA**	MOF-**MA**
R-factor	0.01	0.02	< 0.01
Independent points	19	18	18
Variables	12	13	11
ΔE_0 (eV)	2.7 ± 1.5	3.8 ± 1.9	2.3 ± 1.3
S_0^2	1.048 ± 0.14	1.048	1.048
$R_{\mu3\text{-}O}$ (Å)	2.31 ± 0.02	2.28 ± 0.09	2.30 ± 0.01
σ^2 (μ_3-O) (Å^2)	0.002 ± 0.001	0.003 ± 0.001	0.003 ± 0.001
R_O (Å)	2.15 ± 0.01	2.14 ± 0.06	2.14 ± 0.01
σ^2 (O) (Å^2)	0.002 ± 0.001	0.007 ± 0.003	0.003 ± 0.001
R_{H2O} (Å)	---	2.3 ± 0.2	---
σ^2 (H$_2$O) (Å^2)	---	0.003 ± 0.001	---
R_C (Å)	3.04 ± 0.04	3.05 ± 0.02	3.12 ± 0.09
σ^2 (C) (Å^2)	0.04 ± 0.06	0.020 ± 0.002	0.02 ± 0.02
R_{Zr} (Å)	3.56 ± 0.01	3.56 ± 0.02	3.55 ± 0.01
σ^2 (Zr) (Å^2)	0.008 ± 0.001	0.007 ± 0.002	0.007 ± 0.001
α	0.001 ± 0.04	0.06 ± 0.02	-0.02 ± 0.02
σ^2 (global) (Å^2)	0.02 ± 0.03	0.01 ± 0.01	0.015 ± 0.007

Analysis of the EXAFS fits reveals some differences between the Zr coordination environments in MOF-**SA**, MOF-**MA**, and UiO-68-NH$_2$, as is expected from the different SBUs obtained by single crystal diffraction (**Figure 1-1**). The spectral component attributable to single scattering off the bridging μ_3-oxo group indicates a shorter path length for MOF-**SA** than the other two MOFs. This is expected, as the 12-connected UiO is known to have alternating μ_3-

oxo/μ_3-hydroxo species to accomodate charge balance in the SBU, while the 8-connected SBU would only possess μ_3-oxo moieties. The single scattering path off of the carboxylic carbon is longer for MOF-**MA** than MOF-**SA** or UiO-68. Minimal signal is observed in this region due to destructive interference from multiple scattering paths,[69] making definitive analysis challenging. Importantly, the inclusion of a Zr-OH$_2$ scattering path was essential to obtain a good fit for MOF-**SA**, as the Zr-O bond lengths for the μ_3-oxo and carboxylic oxygen are 0.25 and 0.1 Å shorter, respectively. The high quality of these EXAFS fits confirm the phase purity and structure of the MOFs as determined by single crystal analysis.

Permanent porosity of MOFs-**SA** and -**MA** were determined after removal of solvent molecules by a previously published freeze-drying process.[76] Nitrogen sorption at 77 K showed type I isotherms for both MOFs-**SA** and -**MA**, as well as UiO-68-NH$_2$, indicating their microporous structures. The BET surface areas for MOFs-**SA** and -**MA** were slightly lower than that of UiO-68-NH$_2$ due to functionalization of the bridging ligand (2101, 3025, and 3750 m^{2}g^{-1} for MOF-**SA**, MOF-**MA**, and UiO-68-NH$_2$, respectively). The much lower surface area of MOF-**SA** suggests significant framework distortion in the solvent-free MOF; such framework breathing phenomena have been observed for many MOFs with large open channels.[54,77] The reduced surface area of MOF-**SA** is thus consistent with the structural differences between the three MOFs, as the 8-fold connectivity at the SBU of MOF-**SA** is more susceptible to framework breathing even following solvent removal under mild conditions. The pore size distribution of MOF-**SA** and -**MA** was broader than that of UiO-68-NH$_2$, with pore apertures spanning 7 − 12 Å.
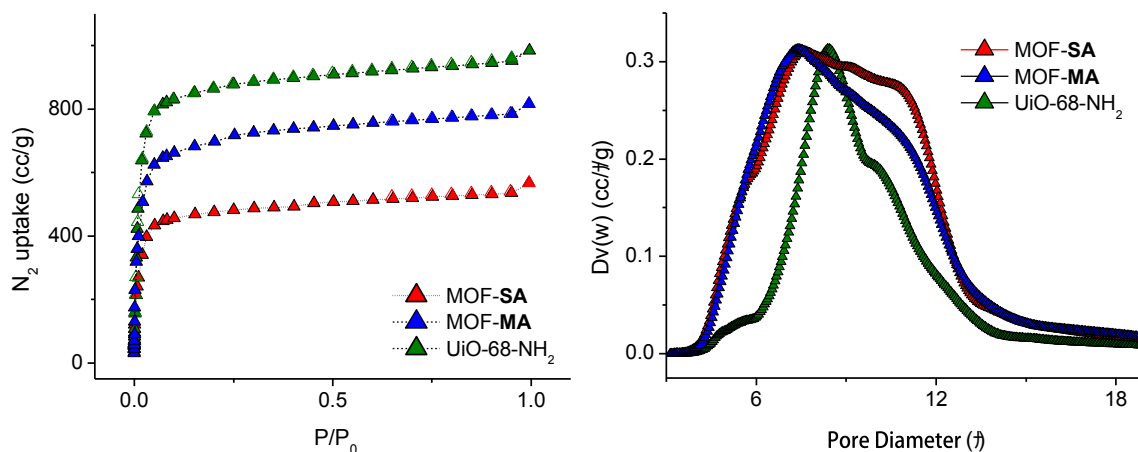
Figure 1-14. N_2 uptake isotherms (left) and pore size distributions (right) for UiO-68-NH$_2$ (green), MOF-**SA** (red), and MOF-**MA** (blue). Copyright 2014 John Wiley and Sons.

1.2.2. Metal Sensing Studies

The orthogonal amide and carboxylic acid groups within the MOF channel are expected to have high affinity for transition metal cations. As MOF-**SA** displays a broad emission band at 390 nm upon excitation at 330 nm, chelating of transition metal cations will likely lead to changes of the fluorescence intensity. MOFs have been investigated for various sensing applications, often taking advantage of the intrinsic fluoresence of the aromatic bridging ligands or the luminescence of the metals in the SBU.[47,78-80] MOFs have also been applied to metal sensing, specifically with an emphasis on the detection of Cu^{2+}, Fe^{3+}, Ag^+, Tb^{3+} and Eu^{3+}.[45,81-90] Despite extensive research, the best metal-sensing MOFs in the literature only possess detection limits of 20 ppb[85] and K_{sv} values of 250 mM^{-1}.[83] We performed fluorescence quenching studies of MOF-**SA** with different metal cations (M^{2+} = Fe^{2+}, Mn^{2+}, Co^{2+}, Cd^{2+}, Cu^{2+}, Ni^{2+}, Zn^{2+}, and Mg^{2+}) in MeOH solutions. The fluorescence signals of MOF-**SA** were measured in the presence of various metal ions in different concentrations (**Figure 1-15**), and the Stern-Völmer constants are summarized in **Table 1-4**.

As shown in **Table 1-4**, transition metal ions with unpaired d electrons, such as Mn^{2+}, Cu^{2+}, Fe^{2+}, Co^{2+}, and Ni^{2+}, exhibited significant quenching effects, while diamagnetic cations Mg^{2+}, Zn^{2+}, and Cd^{2+} had negligible effects upon fluorescence. The proposed quenching mechanism is enhanced non-radiative deactivation in the presence of nearby unpaired spins. The fluorescence quenching follows the Stern-Völmer (SV) equation: $I_0/I = 1 + K_{SV}[M]$, where I_0 and I correspond to the luminescence intensity for MOF-**SA** in the absence and presence of metal cations, respectively, [M] is the metal concentration, and K_{SV} is the Stern-Völmer constant. MOF-**SA** shows dramatic fluorescence quenching at very low metal concentrations, with remarkable sensitivity to Mn^{2+} and Cu^{2+} over other metal ions. An exceptionally high K_{SV} value of $(0.91\pm0.04)\times10^6$ M^{-1} was obtained for Mn^{2+}, while K_{SV} for Cu^{2+} was $(0.47\pm0.02)\times10^6$ M^{-1} (**Table 1-4**). The sensitivity of MOF-**SA** is 3 to 4 orders of magnitude higher than previous reported MOFs with K_{sv} values in the range of tens to hundreds M^{-1} [45,82].
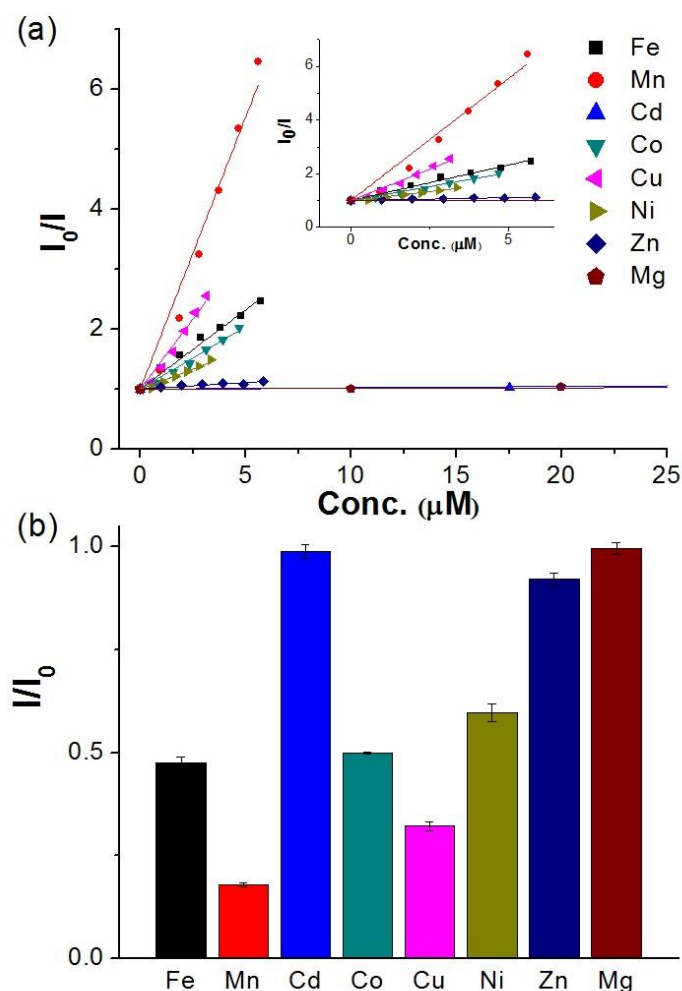
Figure 1-15. (a) Stern-Völmer (SV) plots of the fluorescence emissions of MOF-**SA** quenched by different metal in MeOH with 330 nm excitation (Emission decays were monitored at 390 nm). Inset: Magnification of SV plots in the low concentration range. (b) Fluorescence intensity of MOF-**SA** in 4.5 µM MeOH solutions of different metals. Copyright 2014 John Wiley and Sons.

Quenching studies were also conducted on the homogeneous compound Me_2**L-SA** under identical experimental conditions. However, no fluorescence quenching was observed for any of the metal cations except Ni^{2+}, which exhibits modest quenching of the Me_2**L-SA** fluorescence

(**Figures 1-16** to **1-23**). Furthermore, investigation of MOF-**SA** by PXRD after soaking in 45 mM Mn^{2+} solution overnight reveals no loss of crystallinity (**Figure 1-24**).

Table 1-4. Stern-Völmer constants of MOF-**SA** and homogeneous controls with different metal quenchers.

Metal ions	K_{SV} [mM^{-1}] (MOF-SA)	R^2(MOF-SA)	K_{SV} [mM^{-1}] (Me$_2$L-SA)	R^2(Me$_2$L-SA)
Fe^{2+}	264.2 ± 7.6	0.9817	4.7 ± 0.7	0.7406
Mn^{2+}	906.5 ± 41.2	0.9658	-11.3 ± 3.12	-0.926
Co^{2+}	207.8 ± 6.2	0.9853	10.5 ± 2.7	0.5861
Cd^{2+}	2.2 ± 0.1	0.9568	-1.2 ± 0.1	0.7659
Cu^{2+}	468.0 ± 19.9	0.9718	-1.3 ± 6	-0.111
Ni^{2+}	134.0 ± 6.2	0.9678	38.8 ± 1.9	0.9644
Zn^{2+}	21.7 ± 1.4	0.9098	-29.4 ± 2.1	0.8826
Mg^{2+}	1.0 ± 0.1	0.8645	-1.9 ± 0.2	0.5108
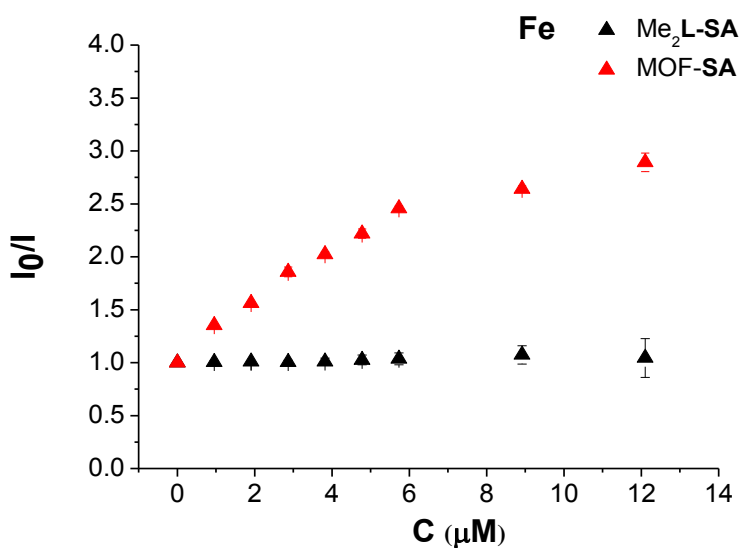
Figure 1-16. Comparison of Fe metal sensing between Me$_2$**L-SA** and MOF-**SA**. Copyright 2014 John Wiley and Sons.
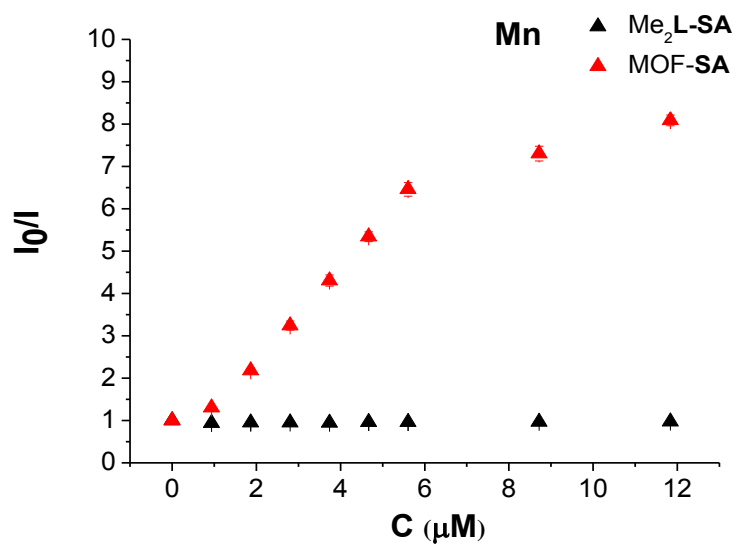
Figure 1-17. Comparison of Mn metal sensing between Me$_2$**L-SA** and MOF-**SA**. Copyright 2014 John Wiley and Sons.
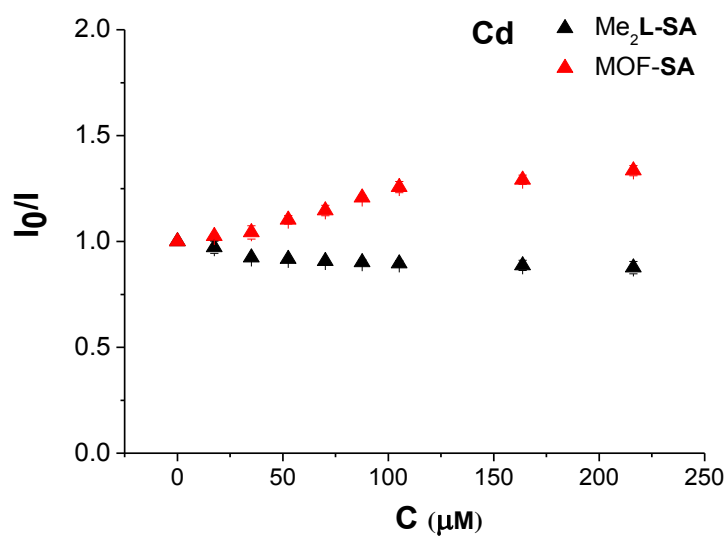
Figure 1-18. Comparison of Cd metal sensing between Me$_2$**L-SA** and MOF-**SA**. Copyright 2014 John Wiley and Sons.
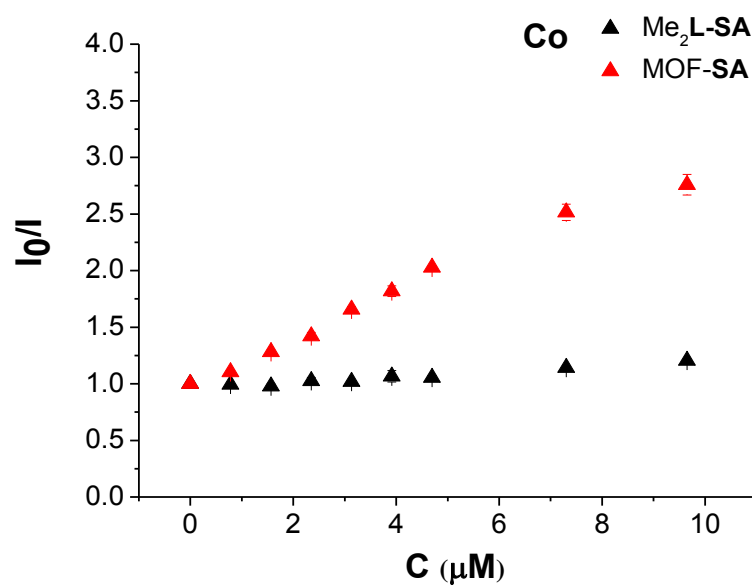
Figure 1-19. Comparison of Co metal sensing between Me$_2$**L-SA** and MOF-**SA**. Copyright 2014
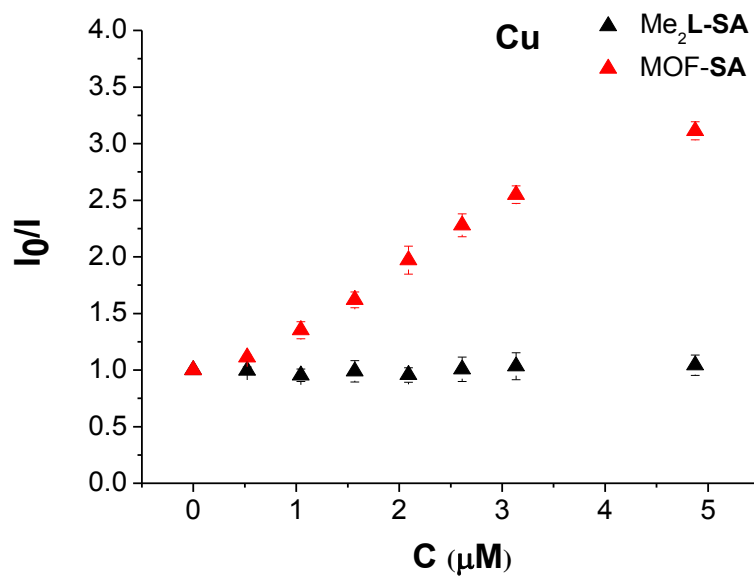
John Wiley and Sons.

Figure 1-20. Comparison of Cu metal sensing between Me$_2$**L-SA** and MOF-**SA**. Copyright 2014
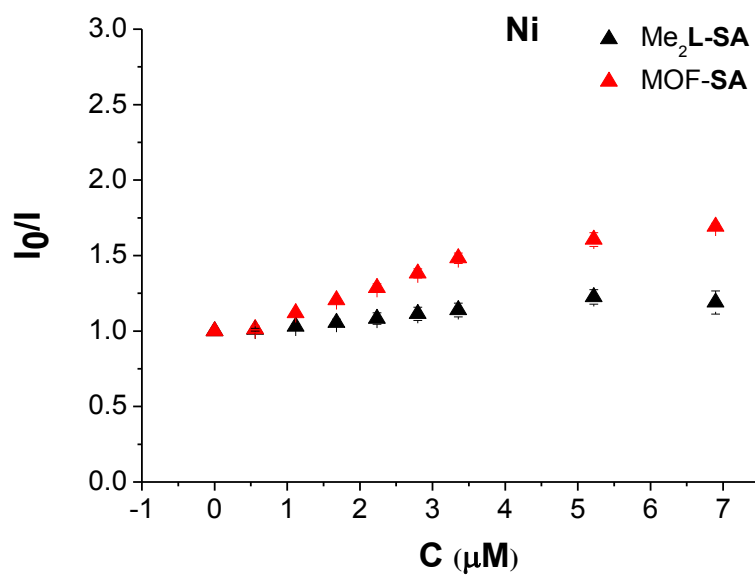
John Wiley and Sons.

Figure 1-21. Comparison of Ni metal sensing between Me$_2$**L-SA** and MOF-**SA**. Copyright 2014 John Wiley and Sons.
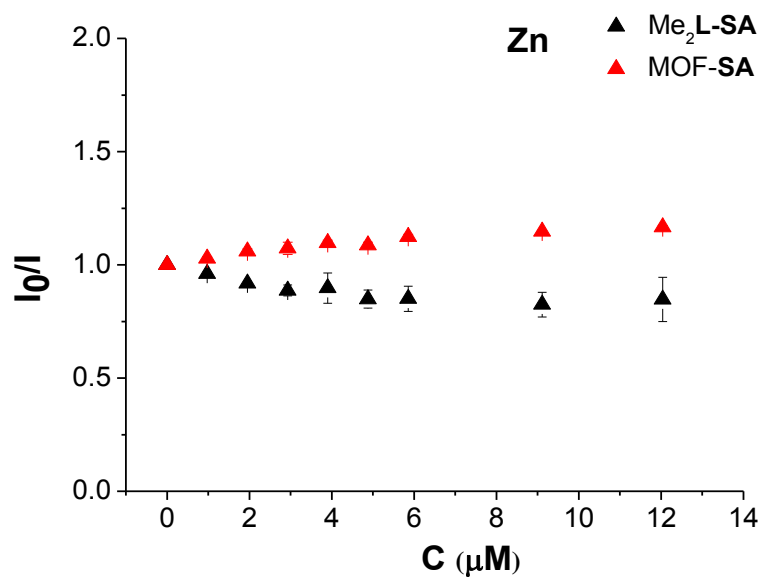
Figure 1-22. Comparison of Zn metal sensing between Me$_2$**L-SA** and MOF-**SA**. Copyright 2014 John Wiley and Sons.
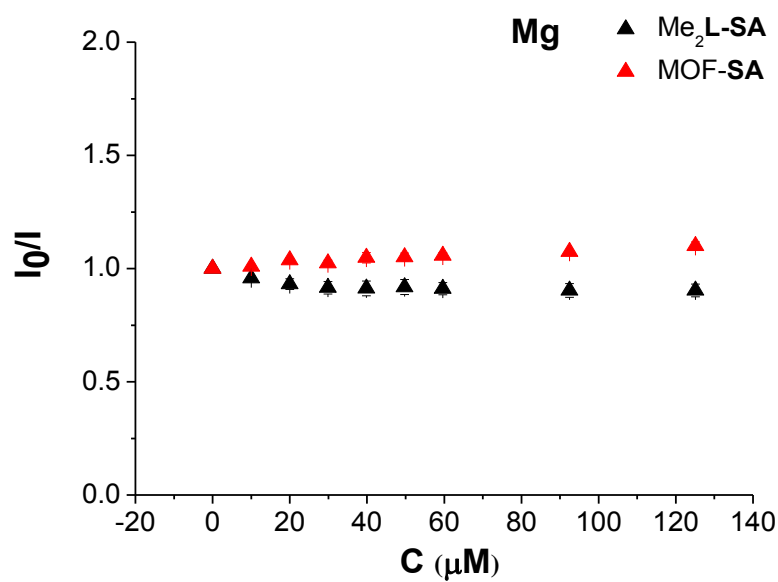
Figure 1-23. Comparison of Mg metal sensing between Me$_2$**L-SA** and MOF-**SA**. Copyright 2014 John Wiley and Sons.
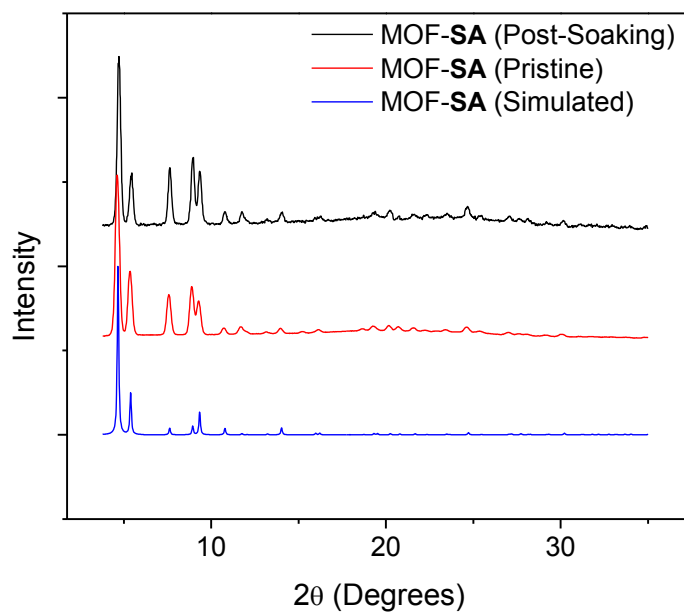
Figure 1-24. PXRD patterns for MOF-**SA** as simulated (blue), as synthesized (red), and soaking in Mn^{2+} solutions. Copyright 2014 John Wiley and Sons.

The enhancement of fluorescent quenching at low concentrations can be partly attributed to pre-concentration of metal ions within the MOF channels. To verify this, we soaked MOF-**1** in solutions of different metal cations (50 µM), and determined the distribution of metal cations in the supernatants and MOF channels by inductively coupled plasma-mass spectrometry (ICP-MS). ICP-MS analysis indicated that the concentrations of 12.2 mM of Mn^{2+} and 7.6 mM of Cu^{2+} within the channels of MOF-**1** were 300 and 501 times respectively more concentrated than that in the supernatant (**Table 1-5**).

Table 1-5. Metals and corresponding preconcentration factors.

Metals	c_{MOF} [µM]	c_{sln} [µM]	Preconcentration factors
Fe	5810.8	28.7	202
Mn	12162.2	40.6	300
Co	2094.6	27.7	76
Cu	7567.6	15.1	501
Ni	2905.4	16.8	173
Zn	4459.5	37.3	120
Mg	2094.6	41.6	50
Cd	-	-	-

To further corroborate the high sensitivity of MOF-**SA** compared to other reported systems, we determined the detection limit for Mn^{2+} first by the Taylor method,[91] then confirmed it experimentally. The absolute standard deviations of the calibrators were plotted against their respective concentrations to give the background level S_0 as the y-intercept of the plot. The detection limit was estimated to be $3S_o$, which equals 0.6 ppb. Experimentally, the fluorescence intensity of the MOF solutions was determined to be 347.10 ± 3.94, decreasing to 321.71 ± 4.32

with the addition of 0.5 ppb Mn^{2+}. The experiment indicated that the detection limit for Mn^{2+} was below 0.5 ppb, consistent with the estimation by the Taylor method.

Table 1-6. MOF fluorescence intensities in the absence and presence of 0.5 ppb of Mn^{2+}

Measurement	I_0	I	I_0/I
1	348.590	317.047	--
2	351.712	326.929	--
3	342.387	320.879	--
4	349.692	318.311	--
5	343.637	325.790	--
average	347.104±3.939	321.709±4.321	1.079±0.019

1.3. Conclusion

We have successfully prepared two Zr MOFs by pre-functionalization of the TPDC-NH$_2$ ligand with succinic acid and maleic anhydride. Single crystal analysis and EXAFS fits of MOF-**SA** provide the first direct evidence of a UiO type SBU possessing reduced connectivity, while MOF-**MA** possesses the traditional 12-connected motif. Due to the highly accessible metal-binding sites located at the terminus of the orthogonal functionalities, MOF-**SA** serves as a highly sensitive fluorescent sensor for metal ions, capable of detecting Mn^{2+} at concentrations less than 0.5 ppb. MOF-**SA** was >1000 times more sensitive for metal cations than previously reported MOFs, demonstrating the utility of orthogonal functionalities for developing highly sensitive MOF-based sensors.

1.4. Materials and Experimental Details

1.4.1. General Experimental

All solvents were purchased from commercial sources and used without further purification. Thermogravimetric analysis (TGA) was performed in air using a Shimadzu TGA-50 equipped with a platinum pan and heated at a rate of 5 °C per minute under air. ^{1}H and ^{13}C NMR spectra were recorded on Bruker Advance II+ 11.7 Tesla NMR. The ^{1}H spectra were referenced to the proton resonance resulting from incomplete deuteration of deuterated DMSO-d_6 (δ 2.49). The ^{13}C spectra were referenced to deuterated DMSO-d_6 (δ 39.52). Surface area and pore size distribution were measured on an Autosorb-1 Quantachrome porosimeter. Mass spectrometric analyses were conducted using positive or negative-ion electrospray ionization on an Agilent 1100 LC-MSD Mass Spectrometer. Powder X-ray diffraction (PXRD) patterns were collected on a Bruker D8 Venture dual microsource (Cu and Mo) diffractometer with a CMOS detector. Cu Kα radiation was used. The PXRD patterns were processed with the APEX 2 package using PILOT plug-in. Fluorescence experiments were performed with a Shimadzu RF-5301 PC spectrofluorophotometer in methanol solutions (for the ligand) and suspensions (for the MOF). ICP-MS data were obtained with an Agilent 7700x ICP-MS and analyzed using ICP-MS MassHunter version B01.03. Samples were diluted in a 2% HNO_3 matrix and analyzed with a ^{159}Tb internal standard against a six-point calibration curve over the range from 0.1 ppb to 1000 ppb. The correlation coefficient was >0.9997 for all analytes of interest, and counts per second relative standard deviations were less than 5% for all samples and calibrators. Internal standard recovery was less than +/- 10% for all samples and calibrators. Data collection was performed in Spectrum Mode with five replicates per sample and 100 sweeps per replicate.

1.4.2. Synthesis of Ligands
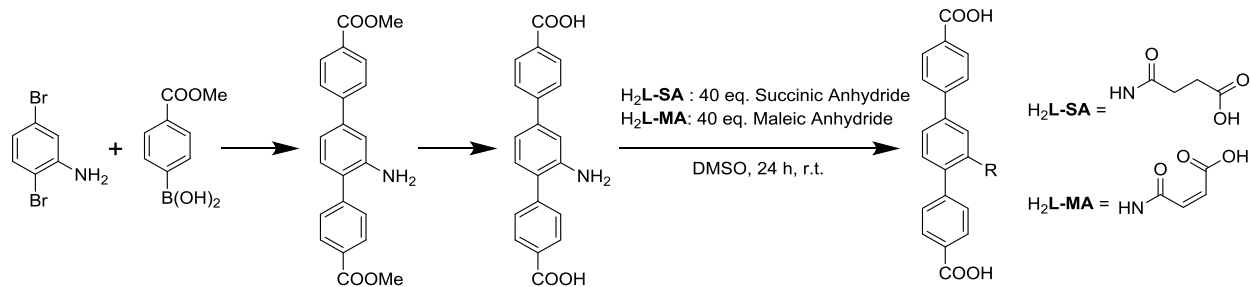
Scheme 1-2. Synthesis of ligands. Copyright 2014 John Wiley and Sons.

1.4.2.1. Synthesis of Me₂L-NH₂

Ligand Me₂**L-NH₂** was prepared by a report protocol.[65] Under air- and moisture-sensitive conditions, 2,5-dibromoaniline (0.50 g, 2.00 mmol), 4-(methoxycarbonyl)phenylboronic acid (1.10 g, 6.10 mmol), and CsF (2.00 g, 1.30 mmol) were dissolved in THF (15 mL). To this solution, 0.15 g (0.70 mmol) of Pd(OAc)$_2$, and 0.40 g (2 mmol) of PPh$_3$ were added, and the reaction mixture was stirred at 60°C for 48 h. After cooling to room temperature, the reaction mixture was poured into deionized water (25 mL) and the aqueous phase was extracted with CH$_2$Cl$_2$. The combined organic phases were concentrated *in vacuo*. The brown solid residue was dissolved in CH$_2$Cl$_2$ and purified by silica gel column chromatography. Elution with CH$_2$Cl$_2$/Et$_2$O (50 :1 by volume; Rf = 0.35) gave a slightly yellow solid (0.33 g, 1 mmol, yield: 25 %). ^{1}H NMR (400 MHz, (CD$_3$)$_2$SO): 8.05 (4H), 7.79 (2H), 7.66 (2H), 7.17 (2H), 7.04 (1H), 5.13 (2H, NH$_2$), 3.89 (6H, OMe). ^{13}C NMR: (100 MHz, (CD$_3$)$_2$SO): 167.17, 166.95, 145.59, 143.73, 141.08, 131.96, 130.27, 130.14, 129.1, 129.05, 129.00, 127.05, 126.56, 117.86, 114.57, 52.27, 52.15. ESI-MS: m/z [M+H]$^+$ = 362.21 (expected: 362.13).

1.4.2.2. Synthesis of H$_2$L-NH$_2$

A suspension of Me$_2$**L-NH$_2$** (0.33 g, 1 mmol) in THF (65 mL) was heated to 40°C. A solution of KOH in methanol (5.50 mol.L^{-1}; 32 mL, 0.18 mol) was added and the reaction mixture was stirred at 40°C for 16 h. The suspension was cooled to room temperature and precipitate was collected by centrifugation. The isolated colorless solid was suspended in THF (25 mL) and 3.30 mL trifluoroacetic acid was added. After the suspension had been stirred for 1.5 h at room temperature, 65 mL of water were added, and the yellow solid was isolated, washed with Et$_2$O, and dried *in vacuo* to obtain 0.30 g (0.90 mmol, yield : 90 %) of slight yellow powder. ^{1}H NMR: (400 MHz, (CD$_3$)$_2$SO):12.94 (brs, 2H, OH), 8.02 (4H), 7.72 (2H), 7.61 (2H), 7.15 (2H), 7.03 (1H), 5.11 (brs, 2H, NH$_2$). ^{13}C NMR: (100 MHz, (CD$_3$)$_2$SO): 167.63, 146.20, 144.99, 144.24, 139.96, 131.31, 130.40, 130.28; 129.99, 129.56; 129.19, 126.96; 125.07; 115.99; 114.29. ESI-MS: m/z = 331.21.

1.4.2.3. Synthesis of H$_2$L-SA

Under air- and moisture-sensitive conditions, 100 mg (0.3 mmol) of H$_2$**L-NH$_2$** were dissolved in 5 mL of dry DMSO, to which 40 eq. of succinic anhydride (12 mmol) was added. The solution was stirred 24 h. The solvent was removed under vacuum. The resulting powder was washed 5 times with water and finally with EtOH to give 75 mg of a slight yellow powder. (Yield : 60 %). ^{1}H NMR: (500 MHz, (CD$_3$)$_2$SO): 9.52 (s, 1H), 8.04 (m, 4 H), 7.87 (s, 1H), 7.83 (d, 2H), 7.68 (d, 1H), 7.58 (d, 2H), 7.51 (d, 1H), 2.47 (s, 4H). ^{13}C NMR: (100 MHz, (CD$_3$)$_2$SO): 174.32, 174.07, 167.68, 167.56, 143.76, 143.26, 139.36, 135.97, 135.37, 131.43, 130.56, 130.38, 130.03, 129.95, 129.48, 127.20 ,125.91, 42.25, 29.95. ESI-MS: m/z [M-H]$^-$ = 432.1 (expected: 432.12).

1.4.2.4. Synthesis of H₂L-MA

Under air- and moisture-sensitive conditions, 100 mg (0.30 mmol) of H₂**L-NH₂** were dissolved in 5 mL of dry DMSO, to which 40 eq. of maleic anhydride (12 mmol) was added. The solution was stirred 24 h. The solvent was removed under vaccuum. The resulting powder was washed 5 times with water and finally with EtOH to give 80 mg of a slight yellow powder. (Yield : 62 %) ^{1}H NMR: (500 MHz, (CD₃)₂SO) : 12.87 (brs, 2H), 9.52 (s, 1H), 8.04 (m, 4H), 7.87 (s, 1H), 7.83 (d, 2H), 7.69 (d, 1H), 7.59 (d, 2H), 7.52 (d, 1H), 2.42 (s, 4H). ^{13}C NMR: (100 MHz, (CD₃)₂SO): 174.32, 174.06, 167.68, 143.76, 143.26, 139.36, 135.97, 135.37, 131.43, 130.56, 130.38, 130.03, 129.95, 129.48, 127.20 ,125.91, 42.25, 29.95. ESI-MS: m/z [M-H]⁻ = 430.2 (expected: 430.10).

1.4.2.5. Synthesis of Me₂L-SA

Under air- and moisture-sensitive conditions, 100 mg (0.30 mmol) of Me₂**L-NH₂** were dissolved in 5 mL of CHCl₃, to which 40 eq. of succinic anhydride (12 mmol) was added. The solution was refluxed for 2 h. The solvent was removed under vacuum. The resulting powder was washed 5 times with water and finally with Et₂O to give 75 mg of a slight yellow powder. (Yield : 60 %) ^{1}H NMR: (500 MHz, (CD₃)₂SO): 8.08 (d, 2H), 8.05 (d, 2 H), 7.87 (s, 2H), 7.85 (s, 1H), 7.71 (d, 1H), 7.62 (d, 2H), 7.53 (d, 1H), 3.89 (s, 6H), 2.45 (s, 4H). ESI-MS: m/z [M+H]⁺ = 462.1 (expected: 462.15).

1.4.3. Synthesis of Metal-Organic Frameworks

1.4.3.1. Synthesis of MOF-SA

MOF-**SA** was prepared by dissolving 67 mg (0.15 mmol) of H₂**L-SA** in 10 ml of DMF with 0.145 mL of trifluoroacetic acid (12 eq.). A solution of 66 mg of ZrCl₄ in 14 mL of DMF

was added, and the mixture was heated at 100 °C for 3 days, yielding crystalline material that was collected by centrifugation and washed 5 times with DMF. Yield = 65 %.

1.4.3.2. Synthesis of MOF-MA

MOF-**MA** was prepared by dissolving 67 mg (0.15 mmol) of H$_2$**L-MA** in 10 ml of DMF with 0.098 mL of trifluoroacetic acid (8 eq.). A solution of 66 mg of ZrCl$_4$ in 14 ml of DMF was added, and the mixture was heated at 90 °C for 3 days, yielding crystalline material that was collected by centrifugation and washed 5 times with DMF. Yield =60 %

1.4.3.3. Synthesis of UiO-68-NH$_2$

60 mg of ZrCl$_4$ (0.25 mmol), 970 mg of benzoic acid (8.00 mmol) were dissolved in 12 mL of DMF, aided by 5 minutes of sonication. To this clear solution, 102 mg (0.30 mmol) of H$_2$**L-NH$_2$** were dissolved and 0.02 mL of water were added. The solution was heated to 70°C for 3 days, yielding a white crystalline powder. The solid was collected by centrifugation, followed by washing 5 times with DMF and 3 times with EtOH, followed by drying under vacuum. Yield = 70 %

1.4.4. Characterization of MOFs

1.4.4.1. X-ray Structure Determination

Single crystal X-ray diffraction of MOF **SA** and **MA** were collected with a Bruker APEX II CCD-based detector at ChemMatCARS (Sector 15), Advanced Photon Source (APS), Argonne National Laboratory. The frames were integrated with the Bruker SAINT© build in APEX II software package using a narrow-frame integration algorithm, which also corrects for the Lorentz and polarization effects. Absorption corrections were applied using SADABS. Structures were solved by direct methods and refined to convergence by least squares method on F^2 using the SHELXTL software suite. Due to the disorder caused by the random orientation, the

succinamic acid and maleamic acid side chains could not be located in the electron density map, and thus are not presented in the single crystal structures.

1.4.4.2. Characterization of Bridging Ligands via MOF Digestion

10 mg of MOF was added to 0.5 ml of DMSO-d_6. To this solution was added 0.5 ml of saturated solution of K_3PO_4 in D_2O. After shaking for 2 minutes, the MOF was fully dissolved, and the organic phase was analyzed by ^{1}H NMR and ESI-MS.

1.4.4.3. X-ray Absorption Fine Structure Spectroscopy

X-ray absorption data were collected at Beamline 13-BM-D at the Advanced Photon Source (APS) at Argonne National Laboratory. Spectra were collected at the zirconium K-edge (17998 eV) in transmission mode. The X-ray beam was monochromatized by a Si(111) monochromator and detuned by 20% to minimize harmonics. A ZrO_2 standard prepared as powder-on-tape was used as the reference for energy calibration and was measured prior to collecting data for any experimental samples. The incident beam intensity (I_0) was measured by an ionization chamber with 100% N_2 gas composition. The transmitted beam intensity (I_t) was measured by an ionization chamber with 100% Ar gas composition. Data was collected in three regions: a pre-edge region –100 to –10 eV (5 eV step size, dwell time 2.0 s), XANES region – 10 to 25 eV (0.5 eV step size, dwell time 2.0 s), and EXAFS region 2.56 Å^{-1} to 13 Å^{-1} (0.04 Å^{-1} step size, dwell time increased linearly from 2.0 to 4.0 seconds over the region to facilitate higher k-weighted data processing). All energies are listed relative to the elemental Zr K-edge (17998 eV). Multiple x-ray absorption spectra were collected at room temperature for each sample (UiO-68-NH$_2$: 7, MOF-**SA**: 6, MOF-**MA**: 6). Samples were prepared as powders on tape, which were stacked to achieve approximately one absorption length.

1.4.5. Metal Sensing Experiments

1.4.5.1. Procedures for Quenching Measurements

Crystals of MOF-**SA** were washed and soaked in MeOH to remove any other solvent remaining in the channels. 5 mg of crystals of MOF-**SA** in 1 ml of MeOH were mechanically crushed by vigorous stirring with a stir bar overnight. The resulting white suspension was diluted with MeOH to 25 mL, and 0.1 mL of this solution was then diluted to 15 mL.

To obtain the Stern-Volmer plot, 3 mL of this MOF stock solution was added to a quartz cuvette. Fluorimeter instrumental parameters were set with excitation $\lambda = 330$ nm and emission $\lambda = 390$ nm. Each scan collected intensity data for a duration of three seconds, while stirring, to minimize light exposure and prevent photodecomposition. Samples were allowed to stir for ten minutes after addition of each quencher to give sufficient time for the diffusion of quencher through the MOF-**SA** channels. An average intensity was then taken from the 150 data points collected within the three seconds, and used as the intensity for that given quencher concentration. Three parallel measurements were done to prove the reproducibility. Concentrations of metal ion solutions were determined by ICP-MS.

As a control experiment, a quenching measurement with the homogenous ligand Me$_2$**L**-**SA** was performed in the same conditions of ligands and metal concentration.

1.4.5.2. Procedures for Preconcentration Measurements

In a typical experiment, 1 mg of MOF-**SA** crystals was soaked in 1 mL of 50 μM (c_0) metal solution in MeOH. The supernatant was then separated from the MOF crystals via centrifugation, and the concentration of metal in supernatant was determined by ICP-MS as c_{sln}.

Analysis: The formula of the MOF-**SA** is $Zr_6(O)_8(OH_2)_8L_4$ (MW = 2553.14). The solvent accessible void space inside the MOF calculated by PLATON[92] is 78.9% (φ). The unit cell volume of the MOF is 15968 Å3 (Vcell), and the crystallograghic Z number is 2, leading to a total guest accessible free space inside MOF of :

$$V_{free} = \frac{m}{MW \times Z} \times V_{cell} \times \varphi \times N_A$$

For MOF-**SA**, we found V_{free} = 0.00148 mL

The concentration of metals in MOF channels can be calculated based on this formula :

$$c_{MOF} = (c_0 - c_{sln}) \cdot \frac{V_{sln}}{V_{free}}$$

The preconcentration factor is defined as :

$$f = \frac{c_{MOF}}{c_{sln}}$$

1.5. References

(1)   Knobloch, F. W.; Rauscher, W. H. *J. Polym. Sci.* **1959**, *38*, 261.
(2)   Berlin, A. A.; Matveeva, N. G. *Russ. Chem. Rev.* **1960**, *29*, 119.
(3)   Kubo, M.; Kishita, M.; Kuroda, Y. *J. Polym. Sci.* **1960**, *48*, 467.
(4)   Block, B. P.; Roth, E. S.; Schaumann, C. W.; Simkin, J.; Rose, S. H. *J. Am. Chem. Soc.* **1962**, *84*, 3200.
(5)   Tomic, E. A. *J. Appl. Polym. Sci.* **1965**, *9*, 3745.
(6)   Abrahams, B. F.; Hoskins, B. F.; Robson, R. *J. Chem. Soc., Chem. Commun.* **1990**, 60.
(7)   Gable, R. W.; Hoskins, B. F.; Robson, R. *J. Chem. Soc., Chem. Commun.* **1990**, 762.
(8)   Hoskins, B. F.; Robson, R. *J. Am. Chem. Soc.* **1989**, *111*, 5962.
(9)   Hoskins, B. F.; Robson, R. *J. Am. Chem. Soc.* **1990**, *112*, 1546.
(10)   Gardner, G. B.; Venkataraman, D.; Moore, J. S.; Lee, S. *Nature* **1995**, *374*, 792.
(11)   Kitagawa, S.; Matsuyama, S.; Munakata, M.; Emori, T. *J. Chem. Soc. Dalton* **1991**, 2869.
(12)   Fujita, M.; Kwon, Y. J.; Washizu, S.; Ogura, K. *J. Am. Chem. Soc.* **1994**, *116*, 1151.

(13)   Yoshizawa, M.; Takeyama, Y.; Kusukawa, T.; Fujita, M. *Angew. Chem. Int. Ed.* **2002**, *41*, 1347.
(14)   Yaghi, O. M.; Li, G. M.; Li, H. L. *Nature* **1995**, *378*, 703.
(15)   Li, H.; Eddaoudi, M.; O'Keeffe, M.; Yaghi, O. M. *Nature* **1999**, *402*, 276.
(16)   Eddaoudi, M.; Kim, J.; Rosi, N.; Vodak, D.; Wachter, J.; O'Keeffe, M.; Yaghi, O. M. *Science* **2002**, *295*, 469.
(17)   Subramanian, S.; Zaworotko, M. J. *J. Chem. Soc., Chem. Commun.* **1993**, 952.
(18)   Zaworotko, M. J. *Chem. Soc. Rev.* **1994**, *23*, 283.
(19)   Riou, D.; Roubeau, O.; Ferey, G. *Micropor. Mesopor. Mat.* **1998**, *23*, 23.
(20)   Evans, O. R.; Xiong, R. G.; Wang, Z. Y.; Wong, G. K.; Lin, W. B. *Angew. Chem. Int Ed.* **1999**, *38*, 536.
(21)   Lin, W. B.; Evans, O. R.; Xiong, R. G.; Wang, Z. Y. *J. Am. Chem. Soc.* **1998**, *120*, 13272.
(22)   Wang, C.; Liu, D. M.; Lin, W. B. *J. Am. Chem. Soc.* **2013**, *135*, 13222.
(23)   Zhou, H. C.; Long, J. R.; Yaghi, O. M. *Chem. Rev.* **2012**, *112*, 673.
(24)   Furukawa, H.; Cordova, K. E.; O'Keeffe, M.; Yaghi, O. M. *Science* **2013**, *341*, 1230444.
(25)   Yaghi, O. M.; O'Keeffe, M.; Ockwig, N. W.; Chae, H. K.; Eddaoudi, M.; Kim, J. *Nature* **2003**, *423*, 705.
(26)   Kiang, Y. H.; Gardner, G. B.; Lee, S.; Xu, Z. T.; Lobkovsky, E. B. *J. Am. Chem. Soc.* **1999**, *121*, 8204.
(27)   Seo, J. S.; Whang, D.; Lee, H.; Jun, S. I.; Oh, J.; Jeon, Y. J.; Kim, K. *Nature* **2000**, *404*, 982.
(28)   Cui, Y. J.; Li, B.; He, H. J.; Zhou, W.; Chen, B. L.; Qian, G. D. *Acc. Chem. Res.* **2016**, *49*, 483.
(29)   Tanabe, K. K.; Cohen, S. M. *Chem. Soc. Rev.* **2011**, *40*, 498.
(30)   Wang, Z. Q.; Cohen, S. M. *Chem. Soc. Rev.* **2009**, *38*, 1315.
(31)   Wu, C. D.; Hu, A.; Zhang, L.; Lin, W. *J. Am. Chem. Soc.* **2005**, *127*, 8940.
(32)   Suh, M. P.; Park, H. J.; Prasad, T. K.; Lim, D. W. *Chem. Rev.* **2012**, *112*, 782.
(33)   He, Y. B.; Zhou, W.; Qian, G. D.; Chen, B. L. *Chem. Soc. Rev.* **2014**, *43*, 5657.
(34)   Li, J. R.; Kuppler, R. J.; Zhou, H. C. *Chem. Soc. Rev.* **2009**, *38*, 1477.
(35)   Van de Voorde, B.; Bueken, B.; Denayer, J.; De Vos, D. *Chem. Soc. Rev.* **2014**, *43*, 5766.
(36)   Wang, C.; Zhang, T.; Lin, W. B. *Chem. Rev.* **2012**, *112*, 1084.
(37)   Hu, Z. C.; Deibert, B. J.; Li, J. *Chem. Soc. Rev.* **2014**, *43*, 5815.
(38)   Ma, L.; Abney, C.; Lin, W. *Chem. Soc. Rev.* **2009**, *38*, 1248.
(39)   Rogge, S. M. J.; Bavykina, A.; Hajek, J.; Garcia, H.; Olivos-Suarez, A. I.; Sepulveda-Escribano, A.; Vimont, A.; Clet, G.; Bazin, P.; Kapteijn, F.; Daturi, M.; Ramos-Fernandez, E. V.; Llabres, I. X. F. X.; Van Speybroeck, V.; Gascon, J. *Chem. Soc. Rev.* **2017**.
(40)   Zhang, T.; Lin, W. *Chem. Soc. Rev.* **2014**, *43*, 5982.
(41)   Horcajada, P.; Gref, R.; Baati, T.; Allan, P. K.; Maurin, G.; Couvreur, P.; Ferey, G.; Morris, R. E.; Serre, C. *Chem. Rev.* **2012**, *112*, 1232.
(42)   Della Rocca, J.; Liu, D. M.; Lin, W. B. *Acc. Chem. Res.* **2011**, *44*, 957.
(43)   Kreno, L. E.; Leong, K.; Farha, O. K.; Allendorf, M.; Van Duyne, R. P.; Hupp, J. T. *Chem.Rev.* **2012**, *112*, 1105.
(44)   Yi, F. Y.; Chen, D. X.; Wu, M. K.; Han, L.; Jiang, H. L. *Chempluschem* **2016**, *81*, 675.
(45)   Chen, B. L.; Wang, L. B.; Xiao, Y. Q.; Fronczek, F. R.; Xue, M.; Cui, Y. J.; Qian, G. D. *Angew. Chem. Int. Ed.* **2009**, *48*, 500.

(46) Wanderley, M. M.; Wang, C.; Wu, C. D.; Lin, W. *J. Am. Chem. Soc.* **2012**, *134*, 9050.

(47) Xie, Z.; Ma, L.; deKrafft, K. E.; Jin, A.; Lin, W. *J. Am. Chem. Soc.* **2009**, *132*, 922.

(48) Lin, R.-B.; Li, F.; Liu, S.-Y.; Qi, X.-L.; Zhang, J.-P.; Chen, X.-M. *Angew. Chem. Int. Ed.* **2013**, *52*, 13429.

(49) Luo, F.; Wang, M. S.; Luo, M. B.; Sun, G. M.; Song, Y. M.; Li, P. X.; Guo, G. C. *Chem. Commun.* **2012**, *48*, 5989.

(50) Reimer, N.; Gil, B.; Marszalek, B.; Stock, N. *Crystengcomm.* **2012**, *14*, 4119.

(51) Torrisi, A.; Bell, R. G.; Mellot-Draznieks, C. *Cryst. Growth Des.* **2010**, *10*, 2839.

(52) Fracaroli, A. M.; Furukawa, H.; Suzuki, M.; Dodd, M.; Okajima, S.; Gándara, F.; Reimer, J. A.; Yaghi, O. M. *J. Am. Chem. Soc.* **2014**, *136*, 8863.

(53) McDonald, T. M.; Lee, W. R.; Mason, J. A.; Wiers, B. M.; Hong, C. S.; Long, J. R. *J. Am. Chem. Soc.* **2012**, *134*, 7056.

(54) Horcajada, P.; Chalati, T.; Serre, C.; Gillet, B.; Sebrie, C.; Baati, T.; Eubank, J. F.; Heurtaux, D.; Clayette, P.; Kreuz, C.; Chang, J.-S.; Hwang, Y. K.; Marsaud, V.; Bories, P.-N.; Cynober, L.; Gil, S.; Ferey, G.; Couvreur, P.; Gref, R. *Nat. Mater.* **2010**, *9*, 172.

(55) Manna, K.; Zhang, T.; Lin, W. *J. Am. Chem. Soc.* **2014**, *136*, 6566.

(56) Falkowski, J. M.; Sawano, T.; Zhang, T.; Tsun, G.; Chen, Y.; Lockard, J. V.; Lin, W. *J. Am. Chem. Soc.* **2014**, *136*, 5213.

(57) Lalonde, M. B.; Farha, O. K.; Scheidt, K. A.; Hupp, J. T. *ACS Catal.* **2012**, *2*, 1550.

(58) Mo, K.; Yang, Y.; Cui, Y. *J Am Chem Soc* **2014**, *136*, 1746.

(59) Yang, X.-L.; Xie, M.-H.; Zou, C.; He, Y.; Chen, B.; O'Keeffe, M.; Wu, C.-D. *J. Am. Chem.Soc.* **2012**, *134*, 10638.

(60) Yamada, T.; Kitagawa, H. *J. Am. Chem. Soc.* **2009**, *131*, 6312.

(61) Custelcean, R.; Gorbunova, M. G. *J. Am. Chem. Soc.* **2005**, *127*, 16362.

(62) Gadzikwa, T.; Farha, O. K.; Mulfort, K. L.; Hupp, J. T.; Nguyen, S. T. *Chem. Commun.* **2009**, 3720.

(63) Cavka, J. H.; Jakobsen, S.; Olsbye, U.; Guillou, N.; Lamberti, C.; Bordiga, S.; Lillerud, K. P. *J. Am. Chem. Soc.* **2008**, *130*, 13850.

(64) Kandiah, M.; Nilsen, M. H.; Usseglio, S.; Jakobsen, S.; Olsbye, U.; Tilset, M.; Larabi, C.; Quadrelli, E. A.; Bonino, F.; Lillerud, K. P. *Chem. Mater.* **2010**, *22*, 6632.

(65) Carboni, M.; Abney, C. W.; Liu, S. B.; Lin, W. B. *Chem. Sci.* **2013**, *4*, 2396.

(66) Schaate, A.; Roy, P.; Godt, A.; Lippke, J.; Waltz, F.; Wiebcke, M.; Behrens, P. *Chem. Eur. J.* **2011**, *17*, 6643.

(67) Vermoortele, F.; Bueken, B.; Le Bars, G.; Van de Voorde, B.; Vandichel, M.; Houthoofd, K.; Vimont, A.; Daturi, M.; Waroquier, M.; Van Speybroeck, V.; Kirschhock, C.; De Vos, D. E. *J. Am. Chem. Soc.* **2013**, *135*, 11465.

(68) Katz, M. J.; Brown, Z. J.; Colon, Y. J.; Siu, P. W.; Scheidt, K. A.; Snurr, R. Q.; Hupp, J. T.; Farha, O. K. *Chem. Commun.* **2013**, *49*, 9449.

(69) Valenzano, L.; Civalleri, B.; Chavan, S.; Bordiga, S.; Nilsen, M. H.; Jakobsen, S.; Lillerud, K. P.; Lamberti, C. *Chem. Mater.* **2011**, *23*, 1700.

(70) Wu, H.; Chua, Y. S.; Krungleviciute, V.; Tyagi, M.; Chen, P.; Yildirim, T.; Zhou, W. *J. Am. Chem. Soc.* **2013**, *135*, 10525.

(71) Feng, D. W.; Gu, Z. Y.; Li, J. R.; Jiang, H. L.; Wei, Z. W.; Zhou, H. C. *Angew. Chem. Int. Ed.* **2012**, *51*, 10307.

(72) Morris, W.; Volosskiy, B.; Demir, S.; Gandara, F.; McGrier, P. L.; Furukawa, H.; Cascio, D.; Stoddart, J. F.; Yaghi, O. M. *Inorg. Chem.* **2012**, *51*, 6443.

(73) Schaate, A.; Roy, P.; Godt, A.; Lippke, J.; Waltz, F.; Wiebcke, M.; Behrens, P. *Chem.-Eur. J.* **2011**, *17*, 6643.

(74) Ravel, B.; Newville, M. *J. Synchrotron Radiat.* **2005**, *12*, 537.

(75) Rehr, J. J.; Albers, R. C. *Rev. Mod. Phys.* **2000**, *72*, 621.

(76) Ma, L.; Jin, A.; Xie, Z.; Lin, W. *Angew. Chem. Int. Ed.* **2009**, *48*, 9905.

(77) Llewellyn, P. L.; Maurin, G.; Devic, T.; Loera-Serna, S.; Rosenbach, N.; Serre, C.; Bourrelly, S.; Horcajada, P.; Filinchuk, Y.; Férey, G. *J. Am. Chem. Soc.* **2008**, *130*, 12808.

(78) Lan, A.; Li, K.; Wu, H.; Olson, D. H.; Emge, T. J.; Ki, W.; Hong, M.; Li, J. *Angew. Chem. Int. Ed.* **2009**, *48*, 2334.

(79) Barrett, S. M.; Wang, C.; Lin, W. *J. Mater. Chem.* **2012**, *22*, 10329.

(80) Chen, B.; Wang, L.; Zapata, F.; Qian, G.; Lobkovsky, E. B. *J. Am. Chem. Soc.* **2008**, *130*, 6718.

(81) Liu, S.; Li, J.; Luo, F. *Inorg. Chem. Commun.* **2010**, *13*, 870.

(82) Xiao, Y.; Cui, Y.; Zheng, Q.; Xiang, S.; Qian, G.; Chen, B. *Chem. Commun.* **2010**, *46*, 5503.

(83) Xiang, Z.; Fang, C.; Leng, S.; Cao, D. *J. Mater. Chem. A* **2014**, *2*, 7662.

(84) Hao, Z.; Song, X.; Zhu, M.; Meng, X.; Zhao, S.; Su, S.; Yang, W.; Song, S.; Zhang, H. *J.Mater. Chem. A* **2013**, *1*, 11043.

(85) Zhou, X.-H.; Li, L.; Li, H.-H.; Li, A.; Yang, T.; Huang, W. *Dalton Trans.* **2013**, *42*, 12403.

(86) Cao, J.; Gao, Y.; Wang, Y.; Du, C.; Liu, Z. *Chem. Commun.* **2013**, *49*, 6897.

(87) Song, B.-Q.; Wang, X.-L.; Yang, G.-S.; Wang, H.-N.; Liang, J.; Shao, K.-Z.; Su, Z.-M. *Crystengcomm.* **2014**, *16*, 6882.

(88) Cai, D.; Guo, H.; Wen, L.; Liu, C. *Crystengcomm* **2013**, *15*, 6702.

(89) Zhang, L.; Jian, Y.; Wang, J.; He, C.; Li, X.; Liu, T.; Duan, C. *Dalton Trans.* **2012**, *41*, 10153.

(90) Dang, S.; Ma, E.; Sun, Z.-M.; Zhang, H. *Journal of Materials Chemistry* **2012**, *22*, 16920.

(91) Taylor, J. K. *Quality Assurance of Chemical Measurements*; Lewis Publishers: Boca Raton, FL, 1984.

(92) Spek, A. *Acta Crystallogr. Sec. D* **2009**, *65*, 148.

CHAPTER 2 Highly Efficient Cooperative Catalysis by Co^{III}(Porphyrin) Pairs in Interpenetrating Metal-Organic Frameworks

2.1. Introduction

Over the past 20 years, MOFs have been explored for many potential applications. [1-11] In particular, MOFs have provided an ideal platform for designing solid catalysts for various organic reactions as a result of several key advantages: (1) easily tunable framework structures of MOFs provide many possibilities for uniform incorporation of catalytically active sites; (2) high surface area and porosity allow the facile access of substrates to the catalytically active sites; (3) high thermal and chemical stability relative to catalytically active species; (4) the solid nature of MOF catalysts allows the easy separation, recovery, and reuse of MOF catalysts, as well as straightforward product purification via simple filtration.[7,12-15]

The single-site nature of many MOF catalysts is of particular interest.[8,12,16-43] The molecular catalysts immobilized in MOFs are site isolated from each other, preventing intermolecular deactivation pathways. As a result, many single-site MOF catalysts have shown catalytic activity orders of magnitude higher than their homogeneous analogs. [24,44,45]

While single-site MOF catalysts have been well studied, MOFs catalysts with multiple active sites are far less explored.[46] The active sites incorporated in MOFs can be classified into three categories: (1) coordinatively unsaturated SBUs and functional linkers; (2) functional groups attached to SBUs and/or linkers; (3) catalytic active guest species encapsulated in the pores or channels. We surmised that MOFs with active sites in close proximity can be used for cooperative catalysis via synergistic substrate activations or for tandem/cascade catalysis.[47,48]

Cooperative catalysis, in which multiple catalytic sites work synergistically to effect an organic transformation, is prevalent in nature,[49-52] and has emerged as a powerful strategy in synthetic chemistry.[51,53-62] By simultaneously activating the substrates using different active sites, cooperative catalysts can lower the energy of the transition states of the rate-limiting steps to a much greater degree than catalysts working independently. Cooperative catalysis can afford improved efficiency and specificity over monocatalytic systems, but is not operative at the low catalyst loading typical of traditional homogeneous catalysts. Because MOFs can be designed with multiple, precisely spaced catalytic sites at very high local concentrations, they are an ideal platform to engineer recyclable and reusable solid catalysts for cooperative catalysis.

In this chapter, I will discuss the design of porous and interpenetrating In-MOFs with strategically placed Co^{III}(porphyrin) active sites for efficient cooperative hydration of terminal alkynes via dual substrate activation. The two-fold interpenetrating MOF structure brings adjacent Co^{III}(porphyrins) in the two networks parallel to each other with a distance of *ca.* 8.8 Å, an ideal distance for the simultaneous activation of both substrates in alkyne hydration reactions. As a result, the In−[Co^{III}(porphyrin)] MOFs exhibit much higher (up to 38 times) catalytic activity than either homogeneous catalysts or MOF controls with isolated Co^{III}(porphyrin) centers.

2.2. Results and Discussion

2.2.1. Synthesis and Characterization of MOFs

The new In-TBP MOF with the framework formula In(TBP)$_x$[In(TBP)(H$_2$O)]$_{(1-x)}$[DMA]$_x$, (DMA = dimethylammonium; x > 0.9) was synthesized by heating indium nitrate and tetrakis(4-benzoic acid)porphyrine (H$_4$TBP) in a mixture of DEF, DMF, and H$_2$O, resulting in purple crystals in 40% yield. The TBP ligand was partially metalated with In during the reaction. The

porphyrin in the In-TBP MOF could be metalated with Co^{III} ions *in situ* by adding Co^{2+} salts to the reaction mixtures to afford In-Co(TBP) in a similar yield. The extent of TBP metalation can be tuned by varying the amounts of metal salts. The resulting Co metalated In-TBP MOF has the framework formula, $In(TBP)_x[M^{III}(TBP)]_{(1-x)}[DMA]_x$, (M = Co or In, x=0.006 to 0.906). The overal charge of the MOF is determined by the metallation level of the TBP ligand. The counter ion DMA is formed from the decomposition of DMF during MOF synthesis and the amount of DMA corresponds to that of the non-metalated TBP ligand (**Figure 2-1**).

Table 2-1. Tuning the extent of TBP metalation by varying the amounts of $Co(NO_3)_2 \cdot 6H_2O$.[a]

$Co(NO_3)_2 \cdot 6H_2O$ (μmol)	H_2SO_4 (μL)	In/Co molar ratio in the MOF[b]	Space groups[c]
137.4	35	1.03	*Cccm*
68.7	30	1.29	*Cccm*
55.0	30	1.35	*Cccm*
27.5	22	1.45	*Cccm*
13.7	15	1.55	*Cccm*
4.12	15	1.61	*Cccm*
2.75	15	2.76	C_2/c
1.37	15	5.00	C_2/c
0.69	15	14.3	C_2/c
0.34	15	20.00	C_2/c
0.17	15	35.00	C_2/c
0	15	N/A	C_2/c

[a] $In(NO_3)_3 \cdot xH_2O$ (22.17 mg, 73.70 µmol), H_4TBP (2.80 mg, 3.54 µmol); [b] the In : Co ratio was determined by ICP-MS; [c] at a low level of metalation, the MOFs crystallized in the monoclinic C2/c space group. When the ratio of Co/TBP in the reaction was greater than 1, they crystallized in orthorhombic space group Cccm.
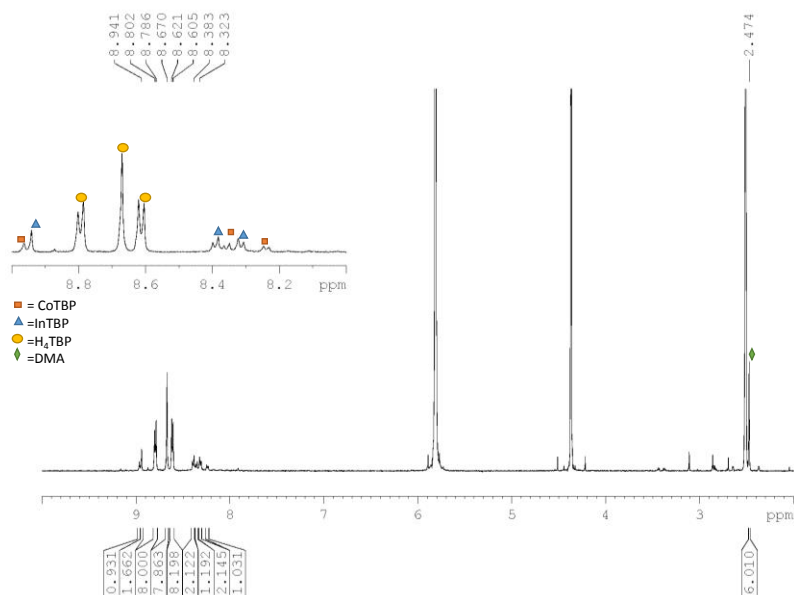
Figure 2-1. ^{1}H NMR of digested Co-metalated In-TBP MOF. Copyright 2016 John Wiley and Sons.

As the metalation on TBP is quite complicated due to the pressence of excess indium salt and the equilibrium between metalation and demetalation under the MOF synthesis condition, there are three possible porphyrin species in the MOF: TBP, Co-TBP, and In-TBP. ICP-MS alone cannot accurately quantify their contents, but UV-Vis spectra serve as a powerful quantification method due to their distinct electronic spectra.

Standard complexes: H$_4$TBP, Co^{III}-TBP ([Tetrakis(4-benzoic acid)porphyrinato]-Co(III) chloride), and In-TBP ([Tetrakis(4-benzoic acid)porphyrinato]-In(III)) chloride were dissolved in DMSO/HCl (10:1) to obtain standard solutions with concentrations of 0.5 µM, 1.0 µM, 1.5 µM, and 2.0 µM.
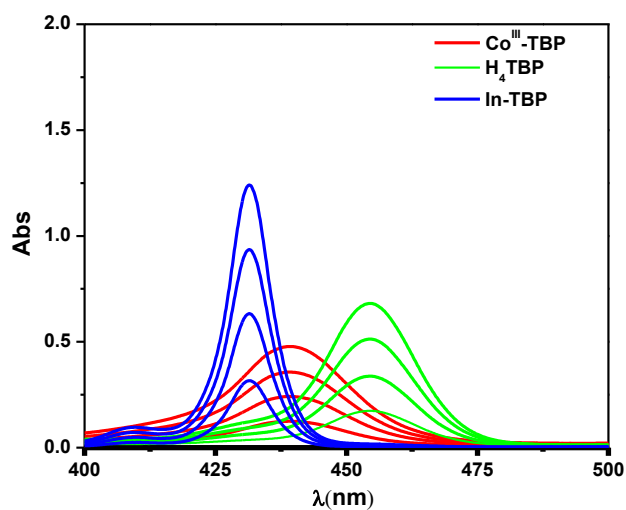
Figure 2-2. UV-Vis spectra of TBP standard solutions. Copyright 2016 John Wiley and Sons.

Table 2-2. ε values for TBPs at different λ's.

	$\varepsilon(\lambda_1)/mM^{-1}cm^{-1}$	$\varepsilon(\lambda_2)/mM^{-1}cm^{-1}$	$\varepsilon(\lambda_3)/mM^{-1}cm^{-1}$
TBP	62.65	97.02	340.84
Co^{III}-TBP	178.99	239.41	99.29
In-TBP	623.32	143.67	8.61

$\lambda_1 = 431.5$ nm, $\lambda_2 = 439.2$ nm, $\lambda_3 = 454.5$ nm.

The concentrations of Co^{III}-TBP, TBP, and In-TBP within In-Co(TBP)-MOFs were calculated by linear combination fitting of UV-Vis spectra of the digested MOFs to the standards. $A_1(\lambda_i)$, $A_2(\lambda_i)$, and $A_3(\lambda_i)$ are the absorptions of Co^{III}-TBP, TBP, and In-TBP standards (0.5 µM) at different wavelengths (λ_i).

$$A_{\text{fit}}(\lambda_i) = k_1 A_1(\lambda_i) + k_2 A_2(\lambda_i) + k_3 A_3(\lambda_i)$$

$$\Delta A(\lambda_i) = A_{\text{fit}}(\lambda_i) - A_{\text{exp}}(\lambda_i)$$

The least squares method was applied to obtain the best fit, minimizing the value of $S_\Delta = \sum_i [\Delta A(\lambda_i)]^2$.

Thus,

$$\frac{\partial S_\Delta}{\partial k_1} = \frac{\partial S_\Delta}{\partial k_2} = \frac{\partial S_\Delta}{\partial k_3} = 0$$

$$\frac{\partial S_\Delta}{\partial k_1} = \sum_i 2\Delta A(\lambda_i)A_1(\lambda_i) = 2\sum[(A_1{}^2 k_1) + (A_1 A_2 k_2) + (A_1 A_3 k_3) - (A_1 A_{exp})] = 0 \quad (1)$$

$$\frac{\partial S_\Delta}{\partial k_2} = \sum_i 2\Delta A(\lambda_i)A_2(\lambda_i) = 2\sum[(A_1 A_2 k_1) + (A_2{}^2 k_2) + (A_2 A_3 k_3) - (A_2 A_{exp})] = 0 \quad (2)$$

$$\frac{\partial S_\Delta}{\partial k_3} = \sum_i 2\Delta A(\lambda_i)A_3(\lambda_i) = 2\sum[(A_1 A_3 k_3) + (A_2 A_3 k_3) + (A_3{}^2 k_3) - (A_3 A_{exp})] = 0 \quad (3)$$

$k_1, k_2,$ and k_3 can be obtained by solving Eqn. 1 to 3.
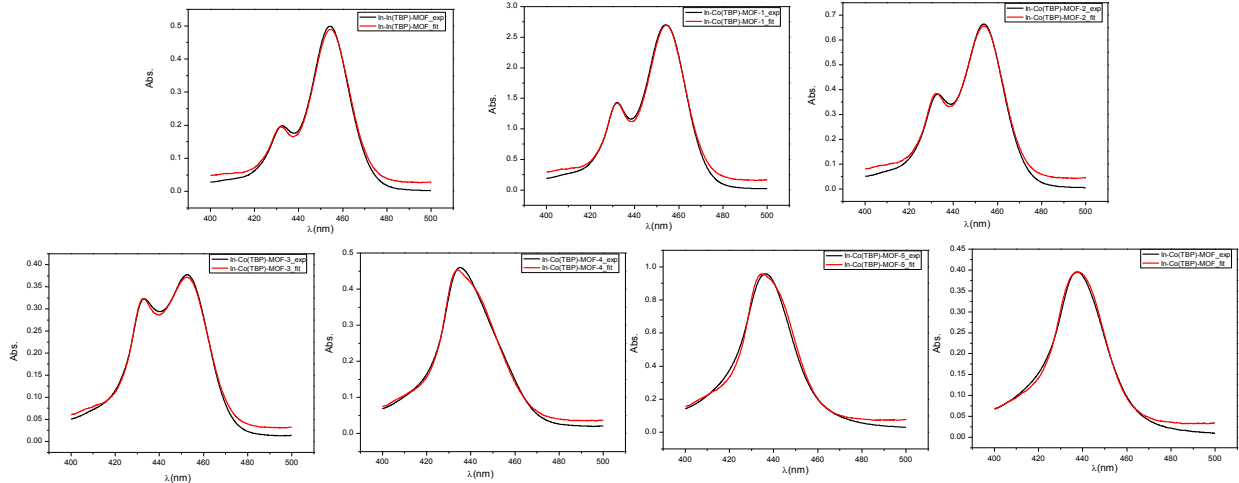
Figure 2-3. Linear combination fitting of UV-Vis spectra of digested MOFs. Copyright 2016 John Wiley and Sons.

Table 2-3. Percentage of TBPs within the MOFs.

	Co^{III}-TBP/%	TBP/%	In-TBP/%	In/Co from UV-Vis[a]	In/Co from ICP-MS
In-In(TBP)-MOF	-	90.6	9.4	-	-
In-Co(TBP)-MOF-1	6.3	81.0	12.7	17.8	20.0
In-Co(TBP)-MOF-2	17.6	71.5	10.9	6.30	5.00
In-Co(TBP)-MOF-3	38.8	49.6	11.6	2.87	2.76
In-Co(TBP)-MOF-4	78.7	10.5	10.8	1.41	1.45
In-Co(TBP)-MOF-5	90.1	0.6	9.3	1.21	1.29
In-Co(TBP)-MOF	93.8	1.8	4.3	1.11	1.03

[a] In/Co = [2×n(In-TBP) + n(Co^{III}-TBP) + n(TBP)]/ n(Co^{III}-TBP)

The presence of 0 to 38.8 equiv of Co^{2+} ions w.r.t. H_4TBP led to the formation of 0 to 93.8% Co(TBP) in the resulting MOF, as quantified by ICP-MS (**Table 2-1**) and UV-Vis spectra analysis (**Table 2-3**). The addition of $HfOCl_2 \cdot 8H_2O$ improved the crystallinity of the MOFs, although no Hf was detected in the MOFs by ICP-MS. In-Co(TBP)-MOF could also be synthesized by using premetalated ligand Co^{III}-TBP.
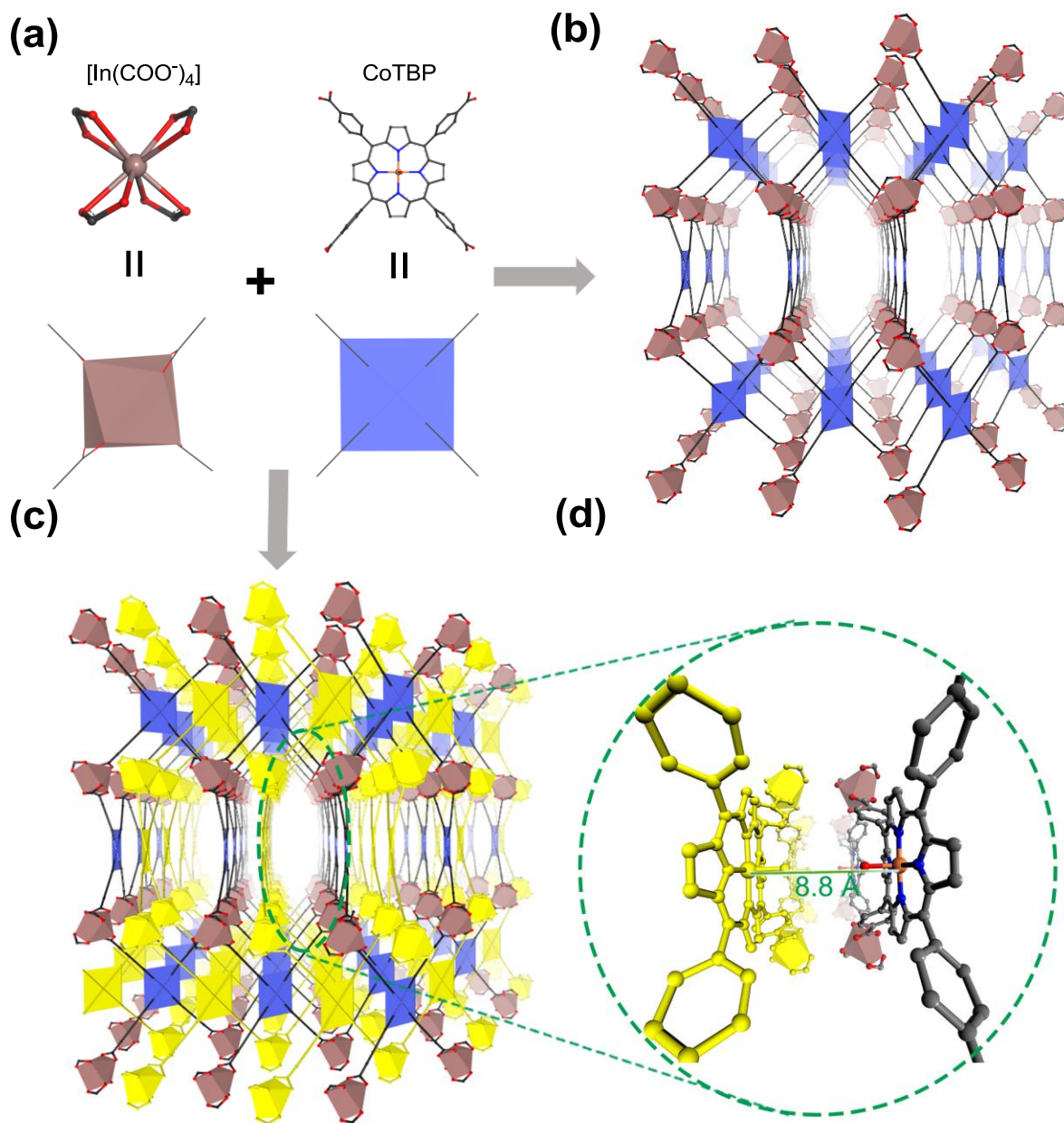
Figure 2-4. (a) Chemical structures of [In(COO⁻)₄] SBUs and Co(TBP) linkers; a graphic representation of the structure and connectivity of (b) one 3D unit of the MOF and (c) two-fold interpenetrated In-Co(TBP)-MOF; (d) close-up view of two Co^{III}(TBP) units brought into proximity to each other by two-fold interpenetration. Yellow color indicates the interpenetrated 3D framework. Copyright 2016 John Wiley and Sons.
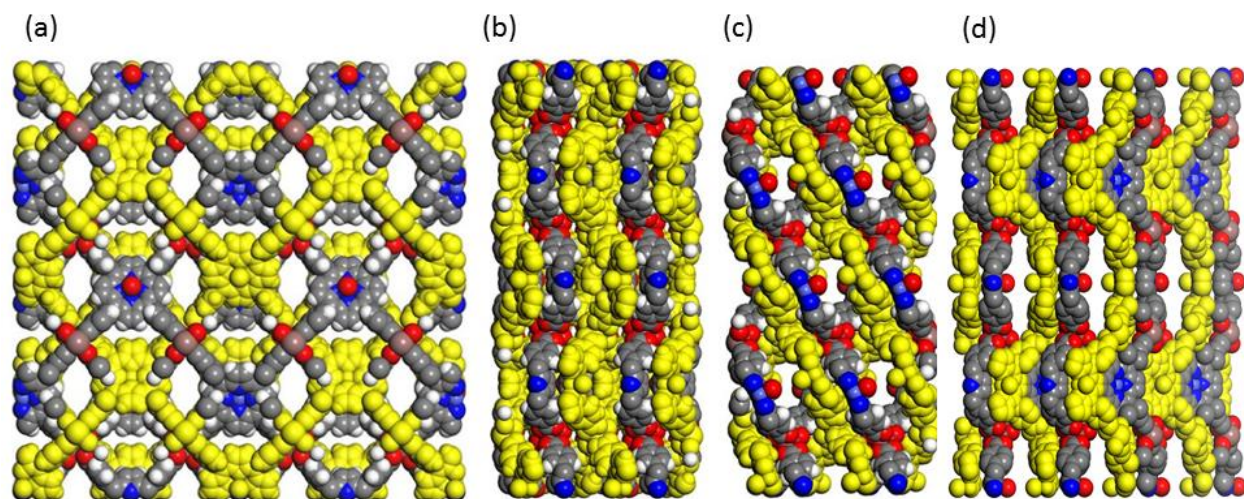
Figure 2-5. Space-filling model of In-Co(TBP)-MOF in (a) the (100) direction, (b) the (010) direction, (c) the (001) direction, and (d) the (110) direction. Copyright 2016 John Wiley and Sons.
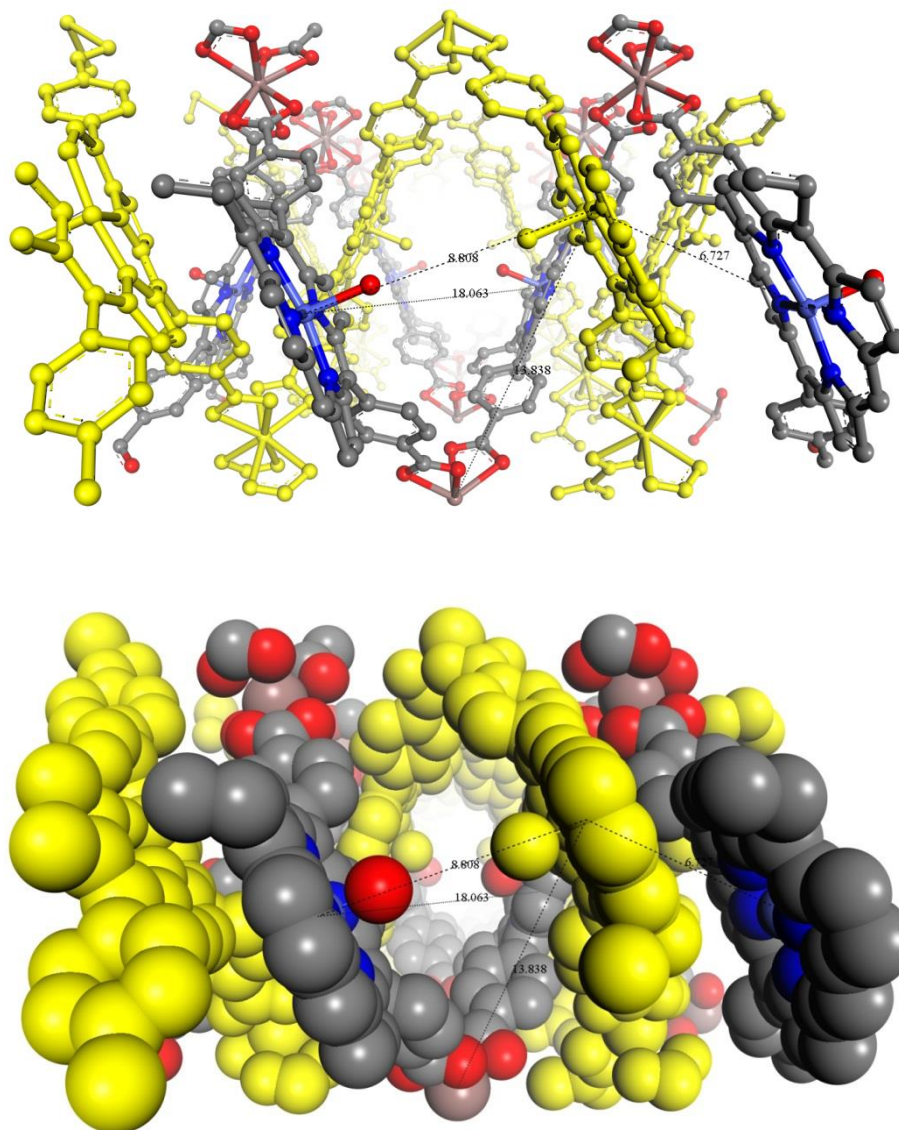
Figure 2-6. Close-up view of the open channel along the (001) direction. Copyright 2016 John Wiley and Sons.

Single crystal X-ray crystallographic studies of the In-Co(TBP)-MOF revealed that each 4-connected Co(TBP) ligand links four 4-connected $[In(COO^-)_4]$ SBUs, forming a two-fold interpenetrated 3D framework of pts topology (the $[In(COO^-)_4]$ tetrahedral node has a vertex symbol of $4 \cdot 4 \cdot 8_2 \cdot 8_2 \cdot 8_8 \cdot 8_8$ and the CoTBP square planar node has a vertex symbol of $4 \cdot 4 \cdot 8_7 \cdot 8_7 \cdot 8_7 \cdot 8_7$). The void space was 54.8%, as calculated by PLATON. However, a low surface

area of 186.0 ± 10.2 m²/g was obtained by nitrogen sorption studies, likely due to the severe distortion of the MOF framework during the drying process (**Figure 2-7**). This drying process was not needed for the MOF catalysts used in liquid phase catalytic reactions. Within each Co(TBP) unit, the cobalt cation has a penta-coordinated environment completed by the four N atoms of the TBP and an axial aqua group, which form a [Co(TBP)(OH$_2$)] unit. The Co-N bond lengths ranged from 1.94 to 1.97 Å, and the Co-O bond length was 2.05 Å. In one 3D unit of the two-fold interpenetrated framework, the Co(TBP) functional units were parallel to each other, with distances of 1.72 nm and 1.44 nm, respectively, and each 3D porous framework possessed different pores 1.52 nm × 1.52 nm and 2.23 nm × 1.25 nm in size, which were large enough to accommodate a second 3D framework, resulting in a two-fold interpenetrated structure. Interpenetration of the 3D frameworks brings a pair of CoTBP units into close proximity with each other, with a Co-Co distance of *ca.* 8.8 Å (**Figure 2-4**), affording an excellent platform for cooperative catalysis.
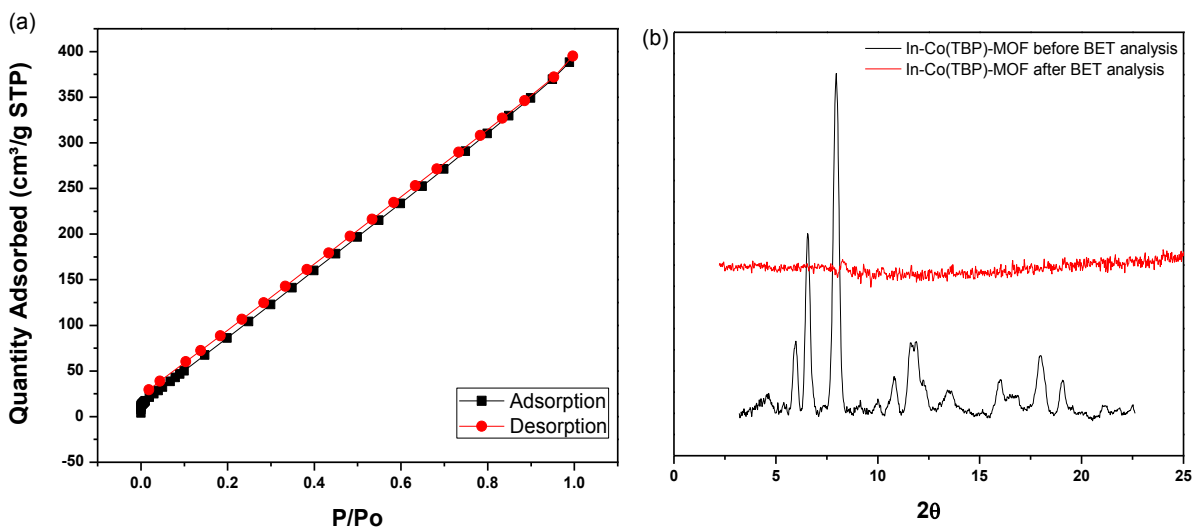
Figure 2-7. Nitrogen sorption isotherms (a) of In-Co(TBP)-MOF (77K). In-Co(TBP)-MOF has BET surface areas of 186.02 ± 10.08 m²/g. The low surface area is due to the distortion of the

53

frameworks upon removal of the solvents, as shown by the PXRD patterns (b) of In-Co(TBP)-MOF after BET analysis. Copyright 2016 John Wiley and Sons.

The structure of In-In(TBP)-MOF was also analyzed by single crystal X-ray diffraction (SXRD). Despite crystallizing in a different space group (C2/*c*), In-In(TBP)-MOF adopts similar connectivity and topology to In-Co(TBP)-MOF and is thus isostructural to In-Co(TBP)-MOF. 25% TBP ligands were metalated by indium by refining the occupancy of indium at TBP. The percentage of TBP metalation was also determined experimentally by digesting bulk crystals of In-In(TBP)-MOF and analyzed by UV-Vis and ^{1}H NMR spectroscopy (**Figure 2-8**), which indicated 10% of TBP was metalated by indium. The difference between individual single crystals and the bulk sample was not unexpected, due to the different behaviors of individual crystals.
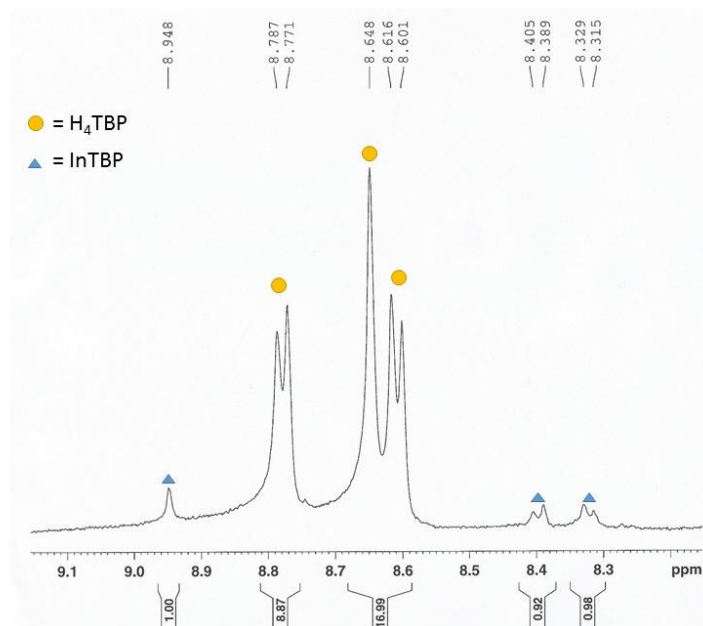
Figure 2-8. ^{1}H NMR spectrum of digested bulk crystals of In-In(TBP)-MOF. Copyright 2016 John Wiley and Sons.

Table 2-4. Crystal Data and Structure Refinement.

	In-In(TBP)-MOF	In-Co(TBP)-MOF
Empirical formula	$C_{49.5}H_{32}In_{1.25}N_{4.75}O_{8.25}$	$C_{48}H_{26}CoInN_4O_9$
M	968.82	976.48
λ/Å	0.41328	0.41328
T/K	100(2)	100(2)
Crystal system	Monoclinic	Orthorhombic
Space group	$C2$/c	$Cccm$
a/Å	29.820(6)	14.3986(8)
b/Å	15.037(3)	31.365(2)
c/Å	33.124(6)	32.0647(16)
β/°	91.598(2)	90
V/Å^3	14847(5)	14480.8(14)
Z	8	8
D_c/Mg m^{-3}	0.867	0.896
μ/mm^{-1}	0.062	0.462
$F(000)$	3916	3920
θ Range/°	0.79–14.498	0.75–14.50
Data/restraints/parameters	13182 / 6 / 576	6683 / 18 / 289
$R_1(I>2\sigma(I))$ [a]	0.0845	0.1029
wR_2 (all data) [a]	0.2573	0.2773
Goodness	0.907	1.095
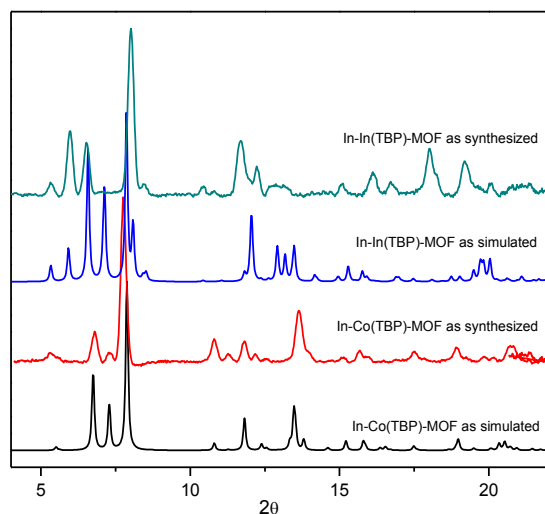
Figure 2-9. Powder X-ray Diffraction patterns of various In-MOF samples. Copyright 2016 John Wiley and Sons.

Thermogravimetric analysis (TGA) indicates high thermal stability of the In-MOFs. The weight loss from 20 to 200 °C corresponds to the loss of solvent molecules within the MOF channels and pores. The weight loss from 300 to 500 °C corresponds to the decomposition of the ligand (**Figure 2-10**).
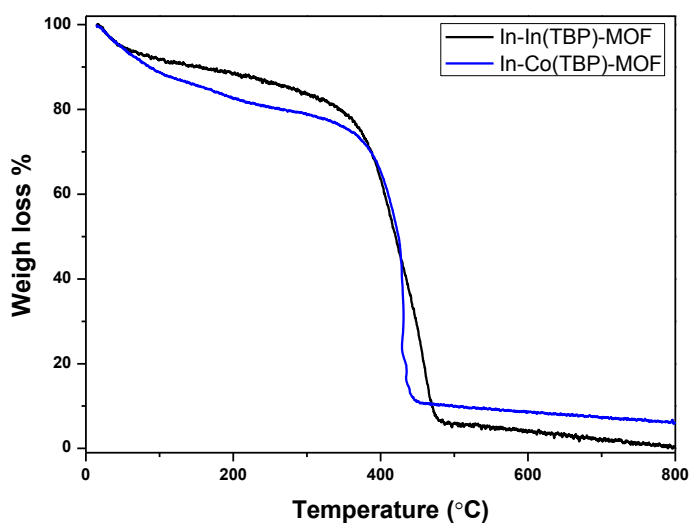
Figure 2-10. TGA of In-MOFs. Copyright 2016 John Wiley and Sons.

X-ray absorption fine structure (XAFS) spectroscopy at the Co K-edge was used to investigate the oxidation states and local coordination environment of Co within the In-Co(TBP)-MOF. These data were processed and analyzed using the Athena and Artemis programs of the IFEFFIT package based on FEFF 6.[63,64] X-ray absorption near edge structure (XANES) analysis indicated the 3+ oxidation state of Co center of In-Co(TBP)-MOFs, since their energy of pre-edge peaks (7709.8 eV) are identical to those of Co(III) reference compounds (**Figure 2-11**). In-Co(TBP)-MOF was fitted to its corresponding crystal structure, with a Co-N bond length of 1.96 Å and a Co-O bond length of 1.96 Å (**Figure 2-12** and **2-13**).
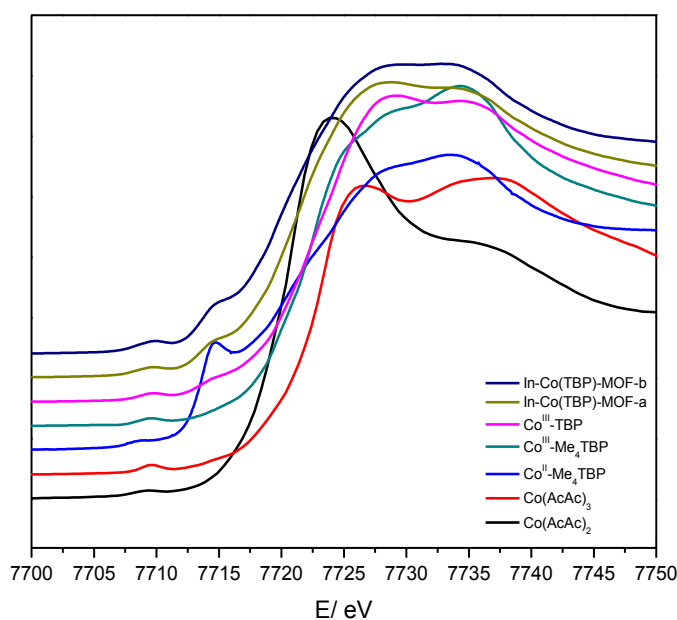
Figure 2-11. XANES spectra of $Co(AcAc)_2$, $Co(AcAc)_3$, Co^{II}-Me$_4$TBP, Co^{III}-Me$_4$TBP, Co^{III}-TBP, and In-Co(TBP)-MOFs ([a] synthesized by in-situ metalation with $Co(NO_3)_2 \cdot 6H_2O$; [b] synthesized using Co^{III}-TBP). Copyright 2016 John Wiley and Sons.
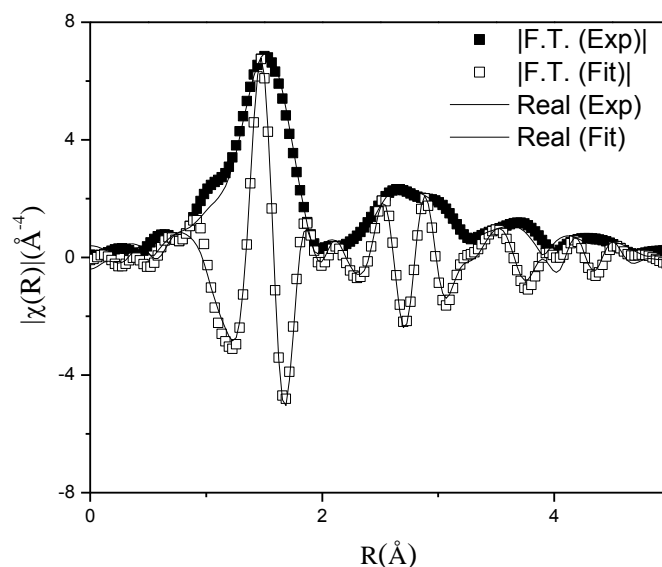
Figure 2-12. EXAFS data (squares) and best fits (lines) for In-Co(TBP)-MOF-a in *R*-space. Data are displayed in *R*-space containing both magnitude of Fourier Transform and real components. A final *R*-factor of 0.01 was obtained for In-Co(TBP)-MOF-a with a reduced χ^2 of 59.60. Copyright 2016 John Wiley and Sons.

Table 2-5. EXAFS fitting parameters for In-Co(TBP)-MOF-a.

Sample	In-Co(TBP)-MOF-a
Fitting range	k 3.00 – 12.20 Å^{-1}
	R 1.0 – 4.80 Å
Independent points	22.0
Variables	12
S_0^2	0.897±0.108
ΔE_0(eV)	0.07±1.21
R (Co-N) (Å)	1.958±0.011
σ^2 (Co-N) (Å^2)	0.0057±0.0021
R (Co-O) (Å)	1.960±0.023
σ^2 (Co-O) (Å^2)	0.0076±0.0118

Table 2-5, continued

R (Co-C9) (Å)	2.988±0.010
σ^2 (Co-C9) (Å^2)	0.0058±0.0013
R (Co-C16) (Å)	3.376±0.018
σ^2 (Co-C16) (Å^2)	0.0056±0.0020
R (Co-C10) (Å)	4.111±0.040
σ^2 (Co-C10) (Å^2)	0.0025±0.0037
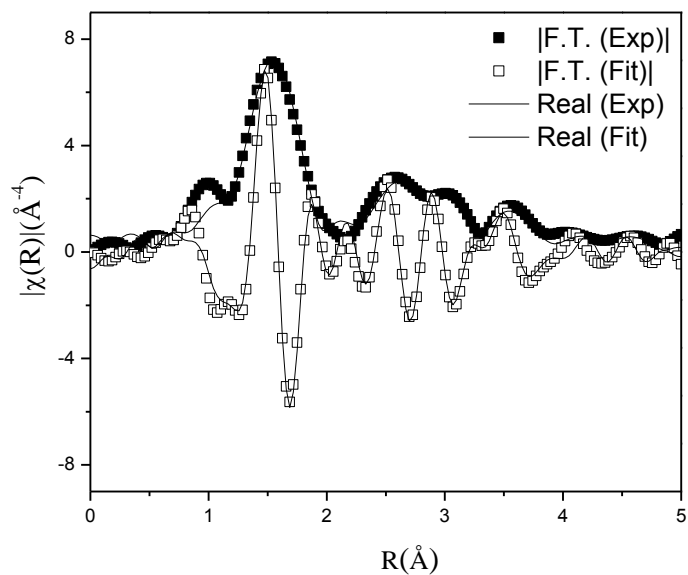
Figure 2-13. EXAFS data (squares) and best fits (lines) for In-Co(TBP)-MOF-b in R-space. Data are displayed in R-space containing both the magnitude of Fourier Transform and real components. A final R-factor of 0.02 was obtained for In-Co(TBP)-MOF-b with a reduced χ^2 of 40.97. Copyright 2016 John Wiley and Sons.

Table 2-6. EXAFS fitting parameters for In-Co(TBP)-MOF-b.

Sample	In-Co(TBP)-MOF-b
Fitting range	k 2.90 – 11.50 Å^{-1}
	R 1.0 – 4.80 Å
Independent points	20.0
Variables	12
S_0^2	0.782±0.122
ΔE_0(eV)	4.05±1.71
R (Co-N) (Å)	1.990±0.023
σ^2 (Co-N) (Å^2)	0.0058±0.0024
R (Co-O) (Å)	1.954±0.029
σ^2 (Co-O) (Å^2)	0.0010±0.0003
R (Co-C18) (Å)	2.999±0.011
σ^2 (Co-C18) (Å^2)	0.0024±0.0014
R (Co-C19) (Å)	3.403±0.030
σ^2 (Co-C19) (Å^2)	0.0056±0.0033
R (Co-C6) (Å)	4.136±0.081
σ^2 (Co-C6) (Å^2)	0.0151±0.0093

2.2.2. Catalytic Hydration of Terminal Alkynes

Catalytic hydration of alkynes forms carbonyl derivatives, which are key intermediates for both bulk and fine chemical industries. Terminal alkynes are often used as substrates for the hydration reaction because they exclusively produce methyl ketones.[65-68] Previous studies have indicated that mercury(II) salts, such as HgO, are efficient catalysts for the hydration of alkynes with the assistance of acid. Because of the toxicity of mercury compounds, much effort has been devoted to exploring alternative catalysts based on transition metals, such as Pt,[69-71] Fe,[72,73]

Pd,[74,75] Ir,[76] Ag,[77,78] Co,[79-81] and Au.[82-92] However, most of them exhibit lower reactivity and selectivity than mercury salts. Because of their distinctive catalytic activities, cobalt(III) porphyrin complexes were found to be an efficient homogeneous catalyst for the hydration of terminal alkynes.[79]

In 2014, Naka and coworkers reported that a Co(III) porphyrin complex, Na_3[Co(TPPS)], could catalyze the hydration of terminal alkynes.[79] We decided to test this reaction using In-Co(TBP)-MOF, in which the TBP ligands were metalated by cobalt cations. To our delight, at 0.1 mol% loading, In-Co(TBP)-MOF was extremely active for hydration of phenylacetylene, with 100% conversion, while homogeneous controls, Na_3[Co(TPPS)] and Co^{III}-TBP, only resulted in 24% and 18.6% conversion, respectively. Furthermore, In-Co(TBP)-MOF remained active at a very low catalyst loading (0.01 mol%), whereas the homogeneous analog was totally inactive (**Table 2-7**, entries 3 and 6; **Figure 2-14a**). These results indicated that the reaction may involve two Co(TBP) complexes to allow cooperative activation. For In-Co(TBP)-MOF, two Co(TBP) units adjacent to each other were relatively fixed; thus, a linear relation was observed for conversions at different catalyst loadings. For the homogeneous control, the possibility of two Co(TBP) complexes meeting each other decreased at a lower catalyst concentration, resulting in a nonlinear relation between conversion and catalyst loading (**Figure 2-14b**).

Table 2-7. Hydration of phenylacetylene.

Entry	Catalysts (mol%)	Time	Conv. (%)[a]
1	In-Co(TBP)-MOF (0.1)	12 h	95.2
2	In-Co(TBP)-MOF (0.1)	20 h	100
3	In-Co(TBP)-MOF (0.01)	7 d	92
4[b]	Na$_3$[Co(TPPS)] (0.1)	12 h	24
5	Co^{III}-(TBP) (0.1)	20 h	18.6
6	Co^{III}-(TBP) (0.01)	7 d	0
7	In-In(TBP)-MOF (0.2)	20 h	0
8	Zr-Co(TBP)-MOF (0.1)	20 h	2.0

[a]Conversions were determined by GC with undecane as an internal standard. [b]ref. 79.
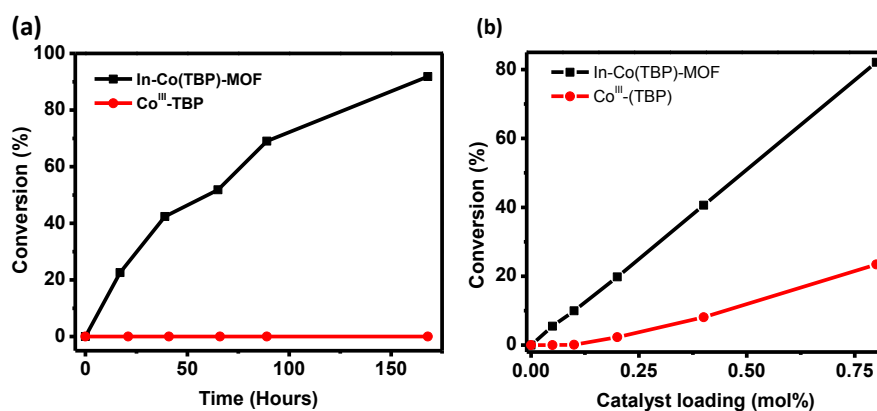
Figure 2-14. (a) Plot of conversion vs time using 0.01 mol% In-Co(TBP)-MOF and Co^{III}-(TBP) (b) plot of conversion vs catalyst loading using In-Co(TBP)-MOF and Co^{III}-(TBP). Reaction time: 2 hours. Copyright 2016 John Wiley and Sons.

When isostructural In-In(TBP)-MOF was used, no conversion was observed, ruling out the contribution from [In(COO)$_4$]$^-$ SBUs (**Table 2-7**, entry 7). More importantly, Zr-Co(TBP)-

MOF, which has a similar topology to MOF-545 or PCN-222,[33,93] served as a good control to demonstrate our proposed cooperative mechanism, since its Co-to-Co distance is 11.0 Å within its trigonal channel or 36.6 Å within its hexagonal channel, greater than that of In-Co(TBP)-MOFs (**Figure 2-15**). All Co(TBP) units of Zr-Co(TBP)-MOF were oxidized to Co^{III}(TBP) prior to catalysis (**Figure 2-16**). Due to its larger channel/pore size, which enables faster diffusion of substrates and products, Zr-Co(TBP)-MOF was expected to have a higher catalytic activity if a monometallic activation pathway was dominant. However, only 2% conversion was achieved when Zr-Co(TBP)-MOF was used for the hydration of phenylacetylene at the same catalyst loading as In-Co(TBP)-MOF or homogeneous Co^{III}-TBP (**Table 2-7**, entry 8), further supporting the bimetallic activation mechanism for In-Co(TBP)-MOF.
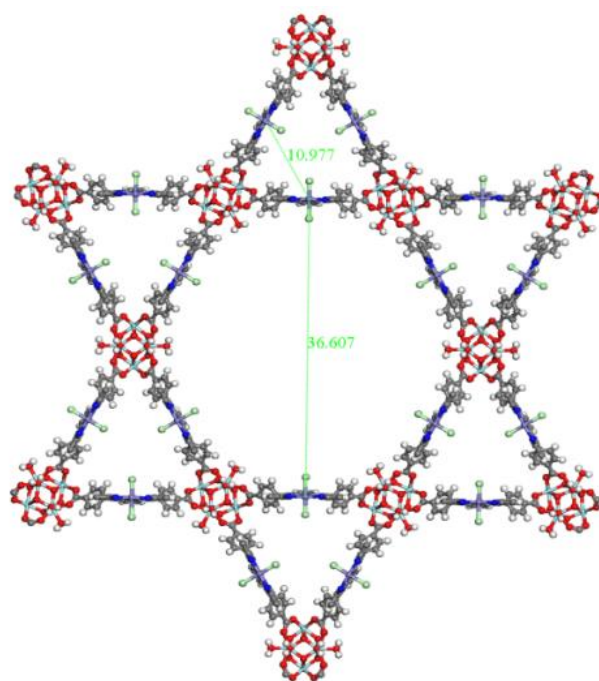
Figure 2-15. Co-Co distances in Zr-Co(TBP)-MOF.
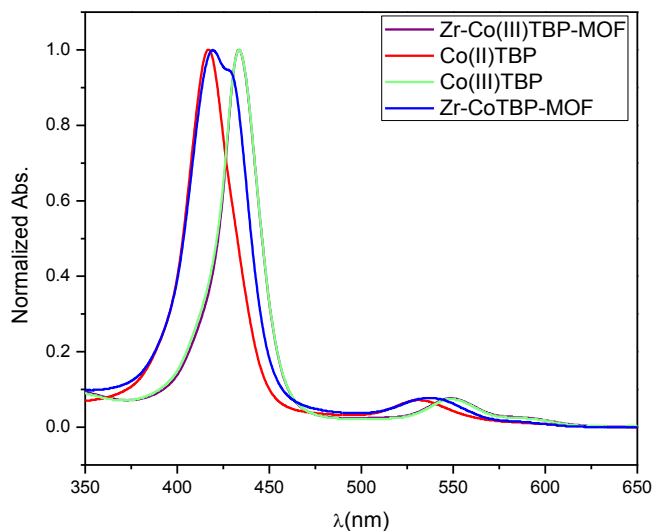
Figure 2-16. UV-Vis spectra of as-synthesized Zr-Co(TBP)-MOF indicate Co^{III}-TBP was partially reduced to Co^{II}-TBP (blue) during MOF synthesis. The partially reduced Zr-Co(TBP)-MOF was post-synthetically oxidized by treatment with 1M HCl. The UV-Vis spectrum of the HCl-treated Zr-CoTBP-MOF (brown) overlaps completely with that of Co(III)TBP (green), indicating oxidation of all Co centers to the +3 oxidation state. Copyright 2016 John Wiley and Sons.

There are two reported MOFs with close proximity of porphyrin pairs.[94,95] Al-Co(TBP)-MOF and Fe-Co(TBP)-MOF were synthesized according to the reported methods with pre-metalated Co^{III}-TBP ligand. At 0.1 mol% loading, neither MOF gave any conversion. For Al-Co(TBP)-MOF, the CoTBP is right on top of the other one, with the Co to Co distance of 6.58 Å. However, the channel is only 3.2 Å×5.2 Å. The space filling model of this MOF indicates that the substrate cannot penetrate through the channel. It is even more difficult for bimetallic activation to happen within such a small space (**Figure 2-17**). For Fe-Co(TBP)-MOF, the Co-Co distance is 7.38 Å but the distance between two porphyrin plane is only 4.28 Å. The MOF is

three-fold interpenetrated and all frameworks are packed very closely, resulting in no space for the substrates to diffuse in and react with Co^{III}(TBP) centers (**Figure 2-18**). Therefore, this MOF is also inactive.
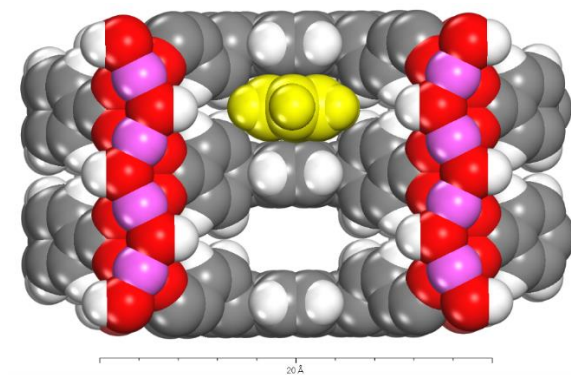
Figure 2-17. Space filling model of Al-Co(TBP)-MOF with phenylacetylene (yellow).
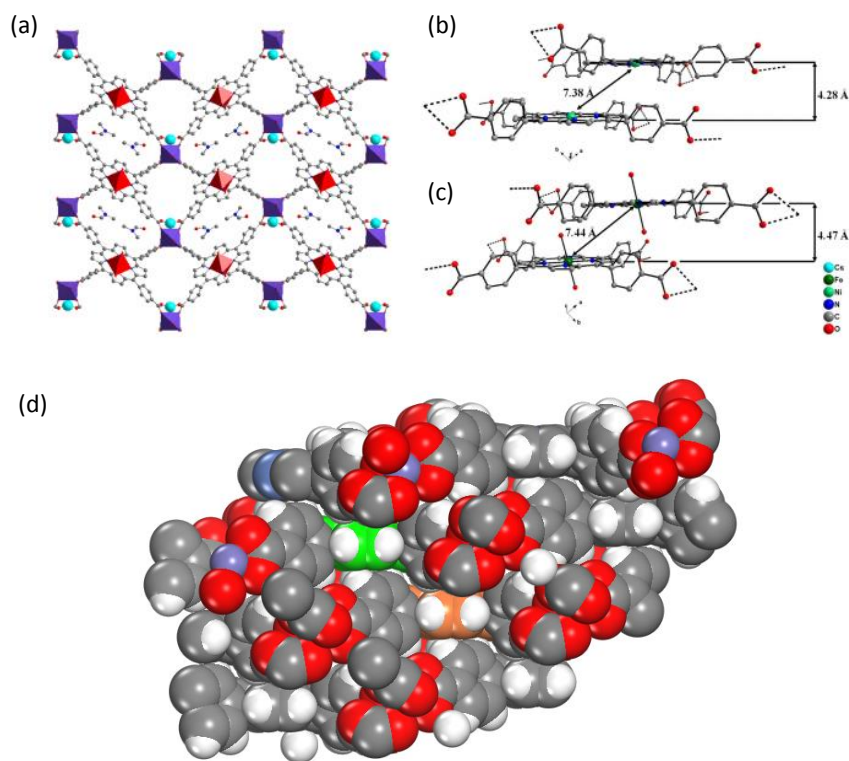
Figure 2-18. Crystal structure of Fe-Co(TBP)-MOF showing the distance between adjacent porphyrin centers and planes (a, b, c: copied from ref 95). Space-filling model of Fe-Co(TBP)-MOF, green and orange represents two adjacent porphyrins (d).

We also investigated whether the exposed cationic $[Co(TBP)(OH_2)]^+$ within the In-Co(TBP)-MOF was responsible for higher catalytic activity than homogeneous Co^{III}-TBP, as indicated by a recent work where [Mn-porphyrin]$^+$ has higher reactivity than Mn-porphyrin-Cl for cycloisomerization of enynes.[29] The reported cycloisomerization of enynes does not apply in our case because $Co^{III}Cl(TPP)$ can easily undergo ionic dissociation in polar ethanol, forming $[Co^{III}(TPP)(C_2H_5OH)_2]^{+}.$[96] We synthesized $Co^{III}(BF_4)(Me_4TBP)$ from $Co^{III}Cl(Me_4TBP)$ by adding $AgBF_4$.[29] In the absence of a strongly bound chloride ligand, the Q band of the $Co^{III}(BF_4)(TBPMe_4)$ blue-shifted in nonpolar toluene. However, in polar MeOH, there is no difference for UV-Vis spectra of $Co^{III}(BF_4)(Me_4TBP)$ and $Co^{III}Cl(Me_4TBP)$, indicating ready displacement of chloride by MeOH, which was previously reported (**Figure 2-19**).[97] As a result, homogeneous Co^{III}-TBP should undergo ionic dissociation and form $[Co^{III}(TBP)(CH_3OH)_2]^+$ under our reaction conditions.
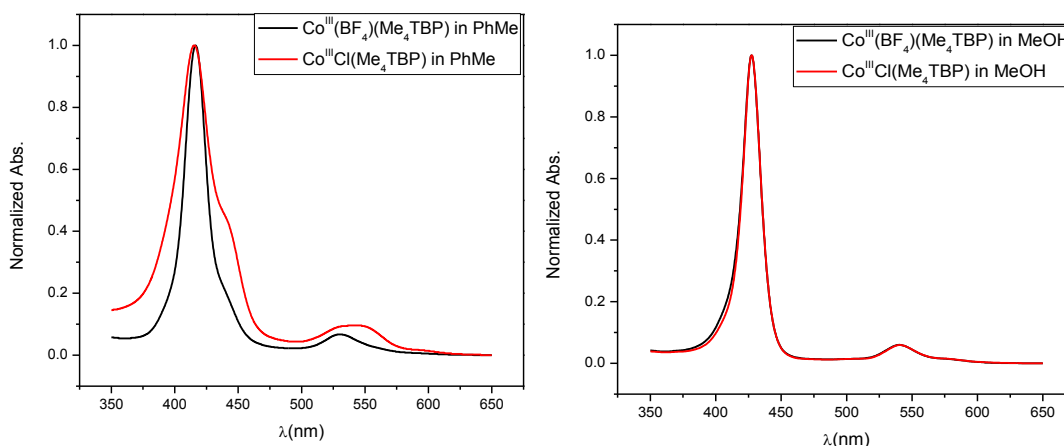
Figure 2-19. UV-Vis spectra of $Co^{III}(BF_4)(Me_4TBP)$ and $Co^{III}Cl(Me_4TBP)$ in nonpolar toluene (left) and polar MeOH (right). Copyright 2016 John Wiley and Sons.

Based on the above results, we propose that our reaction involves a cooperative mechanism: Co(TBP) serves as a Lewis acid to activate the terminal alkyne *via* π-coordination,

while the adjacent Co(TBP) coordinates to MeOH to make it more nucleophilic. In the meantime, the adjacent CoTBP-coordinates to MeOH bring it in a close distance to attack the activated alkyne to afford methyl vinyl ether, which is hydrolyzed by water to give a ketone as the final product and to regenerate MeOH (**Scheme 2-1**).
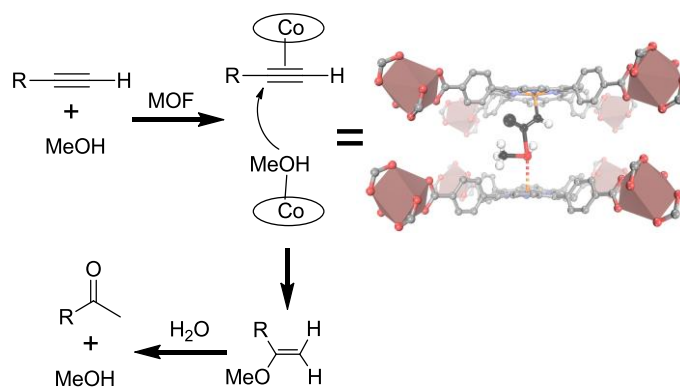
Scheme 2-1. Proposed mechanism for cooperative activation in Co(TBP)-catalyzed hydration of alkynes. Copyright 2016 John Wiley and Sons.

We further investigated the substrate scope of alkyne hydration. In-Co(TBP)-MOF displayed excellent hydration activity for a wide range of aliphatic and aromatic terminal alkynes (**Table 2-8**). Aromatic alkyne derivatives with either electron-donating or electron-withdrawing substituents at the *para* position reacted smoothly to afford the desired methyl ketone products (**Table 2-8**, entries 3 to 8). For the substrate **S10**, no hydration took place using either MOF or homogeneous catalysts (**Table 2-8**, entries 10 and 11). The steric clash between the methyl group of 3-methylphenylacetylene and the phenyl group of Co(TBP) upon coordination led to diminished catalytic activity (**Figure 2-20a**). Similarly, little conversion was observed for **S11** (**Table 2-8**, entry 12). These results further demonstrate that the alkyne was activated by Co(TBP) via pi-coordination.

We found that In-Co(TBP)-MOF could be recycled via simple centrifugation and reused at least six times without obvious diminishing of catalytic activity (**Figure 2-20b**). PXRD of the recovered In-Co(TBP)-MOF was identical to that of the pristine catalyst, indicating the stability of the MOF catalyst during catalytic reactions (**Figure 2-20c**).

Table 2-8. Hydration of terminal alkynes.
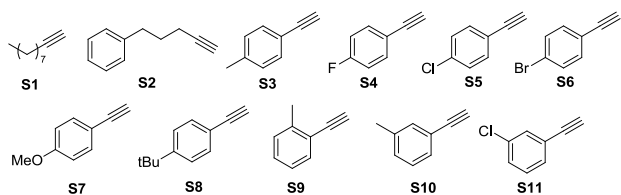
Entry	Substrate	Catalyst (mol%)	Time	Yield. (%)[a]
1	**S1**	In-Co(TBP)-MOF (0.2)	2 d	98
2	**S2**	In-Co(TBP)-MOF (0.2)	2 d	93
3	**S3**	In-Co(TBP)-MOF (0.1)	1 d	92
4	**S4**	In-Co(TBP)-MOF (0.1)	1 d	95
5	**S5**	In-Co(TBP)-MOF (0.1)	1 d	100
6	**S6**	In-Co(TBP)-MOF (0.1)	1 d	90 (86[b])
7	**S7**	In-Co(TBP)-MOF (0.1)	1 d	95
8	**S8**	In-Co(TBP)-MOF (0.1)	1 d	94
9	**S9**	In-Co(TBP)-MOF (0.1)	3 d	97
10	**S10**	In-Co(TBP)-MOF (0.1)	3 d	0
11	**S10**	Co^{III}-TBP (0.1)	3 d	0
12	**S11**	In-Co(TBP)-MOF (0.1)	1 d	2.5

[a]Yield were determined by ^{1}H NMR with nitromethane as internal standard; [b]isolated yield.
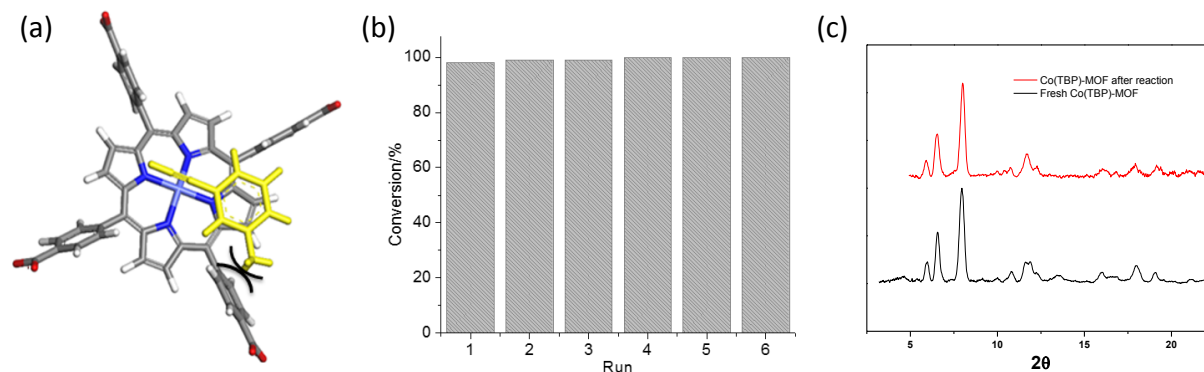
Figure 2-20. (a) Proposed steric clash between the methyl group of 3-methylphenylacetylene and the phenyl group of Co(TBP); (b) Plot of conversions (%) at various runs in the hydration of phenylacetylene; (c) PXRD patterns of In-Co(TBP)-MOF before and after hydration of phenylacetylene. Copyright 2016 John Wiley and Sons.

2.3. Conclusion

We have synthesized a series of porous two-fold interpenetrated metal-metalloporphyrin frameworks and used them in the hydration of terminal alkynes. Controlled loading of transition metal cations into the MOFs supplied the opportunity to study the catalytic mechanism for the hydration of terminal alkynes. The two-fold interpenetration brings catalytically active metalloporphyrin centers adjacent to each other, allowing cooperative activation, which results in excellent efficiency compared to their homogeneous analogs. Zr-Co(TBP)-MOF, isostructural In-In(TBP)-MOF, and the homogeneous reaction were examined to confirm the proposed cooperative catalytic mechanism. This work highlights how MOFs can afford cooperative catalysis in organic synthesis and provide a new strategy for constructing efficient heterogeneous catalysts.

2.4. Materials and Experimental Details

2.4.1. General Experimental

All the reagents were commercially purchased and used without further purification. UV/Vis spectroscopy was performed with a Varian Cary 50 spectrophotometer in the range of 200–800 nm. ^{1}H NMR spectra were recorded on a Bruker NMR 500 DRX spectrometer at 500 MHz and referenced to the proton resonance resulting from incomplete deuteration of DMSO-d_6 (δ 2.50). Thermogravimetric analysis (TGA) was performed in air using a Shimadzu TGA-50 equipped with a platinum pan and heated at a rate of 5 °C per minute. Single-crystal X-ray diffraction was performed on a Bruker APEX II CCD-based detector at ChemMatCARS (Sector 15), Advanced Photon Source (APS), Argonne National Laboratory. Powder X-ray diffraction (PXRD) patterns were collected on a Bruker D8 Venture, dual microsource (Cu and Mo) diffractometer with a CMOS detector. Cu Kα radiation was used for single crystal diffractions. The PXRD patterns were processed with the APEX 2 package using the PILOT plugin. ICP-MS data was obtained with an Agilent 7700x ICP-MS and analyzed using ICP-MS MassHunter version B01.03. Samples were diluted in a 2% HNO_3 matrix and analyzed with a 159Tb internal standard against a ten-point standard curve over the range from 1 ppb to 500 ppb. The correlation coefficient was > 0.9997 for all analyses of interest. Data collection was performed in Spectrum Mode with five replicates per sample and 100 sweeps per replicate.

2.4.2. Synthesis of Ligands

2.4.2.1. [Tetrakis(4-benzoic acid)porphyrinato]-Co(III) chloride [Co[III]-TBP)]

Co[III]-TBP was synthesized according to the literature.[98] $CoCl_2 \cdot 6H_2O$ (434 mg, 1.82 mmol), and H4TBP (261 mg, 0.33 mmol) were dissolved in 25 mL of DMSO and refluxed for two days. After cooling to room temperature, the purple solid was filtered and washed with water

several times and dried *in vacuo*. The crude product was then dissolved in 0.2 M NaOH (ca. 100 mL), to which 2 M HCl was added to cause the precipitation of the product. The resulting purple solid was collected via filtration and dried *in vacuo*. Yield: 240 mg (80%). UV-Vis (MeOH): λ_{max} = 428.0 nm.

2.4.2.2. [Tetrakis(4-methy benzoato)porphyrinato]-Co(II) (Co^{II}-Me$_4$TBP)

Tetra(methyl ester) of tetrakis(4-methy benzoato)porphine (Me$_4$TBP) (85 mg, 0.1 mmol) and CoCl$_2$·6H$_2$O (310 mg, 1.3 mmol) were dissolved in 10 mL of DMF and refluxed under nitrogen overnight. After the mixture was cooled to room temperature, 20 mL of H$_2$O was added. The red solid was filtered and washed with 10 mL of H$_2$O twice. The obtained solid was dissolved in CHCl$_3$ and washed with water three times. The organic layer was dried over anhydrous magnesium sulfate, and the solvent was removed to afford the product as a red solid. Yield: 86 mg (95%). UV-Vis (CHCl$_3$): λ_{max} = 412.5 nm.

2.4.2.3. [Tetrakis(4-methy benzoato)porphyrinato]-Co(III) chloride (Co^{III}-Me$_4$TBP)

Co^{II}-Me$_4$TBP (18 mg, 0.02 mmol) was suspended in methanol (4 mL), followed by the addition of conc. HCl (20 uL). The mixture was stirred at room temperature in an open flask for several hours. After the oxidation was completed (monitored by UV-Vis), removal of the solvent resulted in a violet solid. The solid was further washed with water several times and dried *in vacuo* to afford the violet solid in a quantitative yield. UV-Vis (MeOH): λ_{max} = 428.0 nm.

2.4.2.4. [Tetrakis(4-benzoic acid)porphyrinato]-In(III) chloride (In-TBP)

In-TBP was synthesized according to the literature.[99] In$_2$O$_3$ (168 mg, 0.6 mmol), tetrakis(4-benzoic acid)porphine (H$_4$TBP) (158 mg, 0.2 mmol), and NaOAc (205 mg, 2.5 mmol) were dissolved in 15 mL of acetic acid and refluxed for two days. After cooling to room temperature, the purple solid was collected via filtration, washed with water several times, and

dried in vacuo. The crude product was then dissolved in 0.2M NaOH (ca. 100 mL), to which 2 M HCl was added to precipitate the product. The resulting purple solid was collected via filtration and dried in vacuo. Yield: 134 mg (70%).

2.4.3. Synthesis of MOFs

2.4.3.1. In-In(TBP)-MOF

In(NO$_3$)$_3$·xH$_2$O (22.17 mg, 73.70 μmol), H$_4$TBP (2.80 mg, 3.54 μmol), and HfOCl$_2$·8H$_2$O (3.83 mg, 9.35 μmol) were added to 0.75 mL of a DMF/DEF (v:v = 2:1) mixture, followed by sonication for 20 min to obtain a clear violet solution. Then, 15 µL of concentrated sulfuric acid and 50 µL of water were added to the mixed solution before heating it at 120 °C for 72 h. After cooling to room temperature, the resulting purple block crystals were isolated by decanting the supernatant and washing repeatedly with DMF, methanol, and water. Yield: 1.3 mg (40%)

2.4.3.2. In-Co(TBP)-MOF

In-Co(TBP)-MOF could be synthesized using premetalated Co^{III}-TBP ligands or H$_4$TBP with excess of Co(NO$_3$)$_2$·6H$_2$O.

2.4.3.2.1. In-Co(TBP)-MOF-a: Synthesized by *in situ* Metalation using Co(NO$_3$)$_2$·6H$_2$O

In(NO$_3$)$_3$·xH$_2$O (22.17 mg, 73.70 µmol), H$_4$TBP (2.80 mg, 3.54 µmol), and HfOCl$_2$·8H$_2$O (3.83 mg, 9.35 µmol) were added to 0.75 mL of a solution of DMF/DEF (v:v = 2:1), followed by sonication for 20 min to obtain a clear violet solution. Then, 35 μL of concentrated sulfuric acid and 50 μL of 800 mg/mL Co(NO$_3$)$_2$·6H$_2$O were added to the solution before heating it at 120 °C for 72 h. After cooling to room temperature, the resulting purple block crystals were isolated by decanting the supernatant solution and washing repeatedly with DMF, methanol, and water. Yield : 1.4 mg (42%)

2.4.3.2.2. In-Co(TBP)-MOF-b: Synthesized by using Premetalated Co^{III}-TBP ligand.

In(NO$_3$)$_3$·xH$_2$O (22.17 mg, 73.70 μmol), Co^{III}-TBP (3.21 mg, 3.54 μmol), and HfOCl$_2$·8H$_2$O (3.83 mg, 9.35 μmol) were added to 0.75 mL of a solution of DMF/DEF (v:v = 2:1), followed by sonication for 20 min to obtain a clear violet solution. Then, 50 µL of water and 15 µL of concentrated sulfuric acid were added to the solution before heating it at 120 °C for 24 h. After cooling to room temperature, the resulting purple block crystals were isolated by decanting the supernatant solution and washing repeatedly with DMF, methanol, and water.

The In : Co molar ratio was determined to be 1.16 by ICP-MS, indicating that ~14% of Co^{III}-TBP had been demetalated during MOF synthesis.

2.4.3.3. Zr-Co(TBP)-MOF

ZrCl$_4$ (7 mg, µmol), Co^{III}-TBP (5 mg, µmol), and benzoic acid (270 mg, µmol) were added to 0.8 mL DMF and heated at 120 °C for 72 h. After cooling to room temperature, the resulting purple needle crystals were isolated by decanting the supernatant solution and washing repeatedly with DMF and methanol. Zr/Co molar ratio was determined to be 3.38 by ICP-MS, indicating that ~11% of Co-TBP has been demetalated during MOF synthesis. UV-Vis spectrum of the as-synthesized Zr-Co(TBP)-MOF indicates Co^{III}-TBP was partially reduced to Co^{II}-TBP. By post-synthetically adding 1 M HCl into Zr-Co(TBP)-MOF suspended in MeOH for a few hours, all Co-TBP species were oxidized to Co(III) as indicated by UV-Vis spectra (**Figure 2-15**). The resulting Zr-Co(TBP)-MOF was isolated by centrifugation and washed repeatedly with water and methanol.

2.4.4. Characterization of MOFs

2.4.4.1. X-ray Structure Determination

Single crystal X-ray diffraction of compounds: In-In(TBP)-MOF and In-Co(TBP)-MOF, were collected with a Bruker APEX II CCD-based detector at ChemMatCARS (Sector 15), Advanced Photon Source (APS), Argonne National Laboratory. The frames were integrated with the Bruker SAINT build in APEX II software package using a narrow-frame integration algorithm, which also corrected for the Lorentz and polarization effects. Absorption corrections were applied using SADABS. Structures were solved by direct methods and refined to convergence by least squares method on F^2 using the SHELXTL software suite. During the refinement, the command 'isor' was used to restrain the non-H atoms with ADP and NPD problems, which leads to the restraint values 18 and 6 for In-In-MOF and In-Co-MOF, respectively. The command 'omit-3 29' is used to omit the weak reflection above 29 degrees for these two compounds. Carbon-bound hydrogen atoms were placed in geometrically calculated positions. Squeeze analysis was performed on these two-crystal data, revealing that there are still accessible solvent voids in these two-crystal structures. CCDC reference number 1485691 for In-In(TBP)-MOF and 1485692 for In-Co(TBP)-MOF contain the supplementary crystallographic data for this paper.

Table 2-9. Channel Size of In-Co(TBP)-MOF viewed along different directions.

Direction	Channel Size
(100)	9.0 Å × 4.8 Å
(010)	n.a.
(001)	5.0 Å × 8.5 Å
(110)	6.0 Å × 9.0 Å

2.4.4.2. X-Ray Absorption Spectroscopic Analysis

2.4.4.2.1. Data Collection.

X-ray absorption data were collected at Beamline 9-BM-C at the Advanced Photon Source (APS) at Argonne National Laboratory. Spectra were collected at the cobalt K-edge in transmission mode. The X-ray beam was monochromatized by a Si(111) monochromater and detuned by 25% to minimize harmonics. A metallic cobalt foil standard was used as the reference for energy calibration and was measured simultaneously with experimental samples. The incident beam intensity (I_0) was measured by an ionization chamber with 30% N_2 and 70% He gas composition. Data was collected in three regions: a pre-edge region -150 to -20 eV (5 eV step size, dwell time 1.0 s), XANES region $-$ 20 to 50 eV (0.5 eV step size, dwell time 1.0 s), and EXAFS region 3.62 Å $^{-1}$ to 13.93 Å $^{-1}$ (0.05 Å $^{-1}$ step size, dwell time increased linearly from 1.0 to 3.9 seconds over the region to facilitate higher k-weighted data processing). All energies are listed relative to the elemental Co K-edge (7709 eV). Multiple X-ray absorption spectra were collected at room temperature for each sample. Samples were ground and mixed with polyethyleneglycol (PEG) and packed in a 6-shooter sample holder to achieve adequate absorption lengths.

2.4.4.2.2. Data Processing.

Data were processed using the Athena and Artemis programs of the IFEFFIT package based on FEFF 6. Prior to merging, spectra were calibrated against the reference spectra (metallic Co) and aligned to the first peak in the smoothed first derivative of the absorption spectrum, the backgrounds were removed, and the spectra were processed to obtain a normalized unit edge step.

2.4.4.2.3. EXAFS Fitting.

Fits of the EXAFS region were performed using the Artemis program of the IFEFFIT package. For all fits, the number of parameters used was less than 2/3 the total number of independent points, as determined by the Nyquist Equation. Fits were performed with a k-weight of 3 in R-space. Refinement was performed by optimizing amplitude factor S_0^2 and energy shift ΔE_0, which are common to all paths, as well as parameters for bond length (ΔR) and Debye-Waller factor (σ^2). In-Co(TBP)-MOFs were fitted with their corresponding crystal structures. Co^{II}-Me$_4$TBP and Co^{III}-TBP were fitted with the reported crystal structures HUPZEY and CTPOCO, respectively, obtained from the Cambridge Crystallographic Database.

2.4.5. Procedures for Catalytic Hydration of Terminal Alkynes.

A mixture of phenylacetylene (0.76 mmol, 84 µL), H_2O (3.3 mmol, 60 µL), In-Co(TBP)-MOF (7.6 µmol), and CH_3OH (1.0 mL) was heated at 80 °C for 20 h under air in a closed vial. The conversion of the reaction was determined using GC. Methanol was necessary since the hydration essentially involved hydroalkoxylation of the alkyne with methanol, followed by hydrolysis to form a ketone.

Table 2-10. Condition optimization of In-Co(TBP)-MOF catalyzed hydration of phenylacetylene
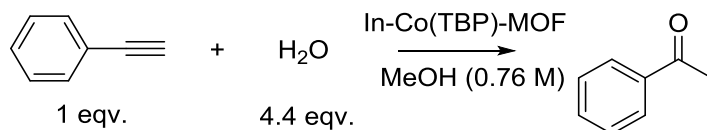
Entry	Cat. loading	Solvent	Time	Conversion (%)[a]	TON
1[b]	0.3	MeOH	20 h	76	253
2	0.15	MeOH	20 h	100	714
3	0.15	1,4 Dioxane	20 h	0	0
4	0.15	1,4 Dioxane + MeOH	20 h	0	0
5	0.15	Toluene	20 h	0	0
6	0.15	Toluene + MeOH	20 h	36.3	259
7	0.01	MeOH	7 d	92	9200

[a] All conversions were determined by GC. [b] The MOFs were damaged by stirring.

2.4.6. Reuse and Recycle of Co(TBP)-MOF for Hydration of Terminal Alkyne.

A mixture of phenylacetylene (0.76 mmol, 84 µL), H_2O (3.3 mmol, 60 µL), In-Co(TBP)-MOF (7.6 µmol), and CH_3OH (1.0 mL) was heated at 80 °C under air in a closed vial. After 20 hours, the reaction mixture was cooled and the conversion detected by GC with undecane as an internal standard. MOFs were separated via centrifugation and washed with MeOH several times before use in the subsequent cycle. The recovered In-Co(TBP)-MOF was transferred into a vial followed by the addition of phenylacetylene (0.76 mmol, 84 µL), H_2O (3.3 mmol, 60 µL), and CH_3OH (1.0 mL) to complete the next cycle of reaction.

2.5. References

(1)   Suh, M. P.; Park, H. J.; Prasad, T. K.; Lim, D. W. *Chem. Rev.* **2012**, *112*, 782.
(2)   He, Y. B.; Zhou, W.; Qian, G. D.; Chen, B. L. *Chem. Soc. Rev.* **2014**, *43*, 5657.

(3)   Li, J. R.; Kuppler, R. J.; Zhou, H. C. *Chem. Soc. Rev.* **2009**, *38*, 1477.

(4)   Van de Voorde, B.; Bueken, B.; Denayer, J.; De Vos, D. *Chem. Soc. Rev.* **2014**, *43*, 5766.

(5)   Wang, C.; Zhang, T.; Lin, W. B. *Chem. Rev.* **2012**, *112*, 1084.

(6)   Hu, Z. C.; Deibert, B. J.; Li, J. *Chem. Soc. Rev.* **2014**, *43*, 5815.

(7)   Ma, L.; Abney, C.; Lin, W. *Chem. Soc. Rev.* **2009**, *38*, 1248.

(8)   Rogge, S. M. J.; Bavykina, A.; Hajek, J.; Garcia, H.; Olivos-Suarez, A. I.; Sepulveda-Escribano, A.; Vimont, A.; Clet, G.; Bazin, P.; Kapteijn, F.; Daturi, M.; Ramos-Fernandez, E. V.; Llabres, I. X. F. X.; Van Speybroeck, V.; Gascon, J. *Chem. Soc. Rev.* **2017**.

(9)   Zhang, T.; Lin, W. *Chem. Soc. Rev.* **2014**, *43*, 5982.

(10)   Horcajada, P.; Gref, R.; Baati, T.; Allan, P. K.; Maurin, G.; Couvreur, P.; Ferey, G.; Morris,   R. E.; Serre, C. *Chem. Rev.* **2012**, *112*, 1232.

(11)   Della Rocca, J.; Liu, D. M.; Lin, W. B. *Acc. Chem. Res.* **2011**, *44*, 957.

(12)   Yoon, M.; Srirambalaji, R.; Kim, K. *Chem. Rev.* **2012**, *112*, 1196.

(13)   Liu, J. W.; Chen, L. F.; Cui, H.; Zhang, J. Y.; Zhang, L.; Su, C. Y. *Chem. Soc.Rev.***2014**, *43*, 6011.

(14)   Chughtai, A. H.; Ahmad, N.; Younus, H. A.; Laypkov, A.; Verpoort, F. *Chem. Soc. Rev.* **2015**, *44*, 6804.

(15)   Lee, J.; Farha, O. K.; Roberts, J.; Scheidt, K. A.; Nguyen, S. T.; Hupp, J. T. *Chem. Soc. Rev.* **2009**, *38*, 1450.

(16)   Falkowski, J. M.; Sawano, T.; Zhang, T.; Tsun, G.; Chen, Y.; Lockard, J. V.; Lin, W. *J. Am. Chem. Soc.* **2014**, *136*, 5213.

(17)   Fei, H.; Shin, J.; Meng, Y. S.; Adelhardt, M.; Sutter, J.; Meyer, K.; Cohen, S. M. *J. Amer. Chem. Soc.* **2014**, *136*, 4965.

(18)   Ma, L.; Falkowski, J. M.; Abney, C.; Lin, W. *Nat. Chem.* **2010**, *2*, 838.

(19)   Manna, K.; Zhang, T.; Greene, F. X.; Lin, W. *J. Amer. Chem. Soc.* **2015**, *137*, 2665.

(20)   Manna, K.; Zhang, T.; Carboni, M.; Abney, C. W.; Lin, W. *J. Amer. Chem. Soc.* **2014**, *136*, 13182.

(21)   Manna, K.; Zhang, T.; Lin, W. *J. Amer. Chem. Soc.* **2014**, *136*, 6566.

(22)   Zhang, X.; Xamena, F.; Corma, A. *J. Catal.***2009**, *265*, 155.

(23)   Zhao, M.; Ou, S.; Wu, C.-D. *Acc. Chem. Res.* **2014**, *47*, 1199.

(24)   Sawano, T.; Lin, Z.; Boures, D.; An, B.; Wang, C.; Lin, W. *J. Amer. Chem. Soc.* **2016**, *138*, 9783.

(25)   Manna, K.; Ji, P.; Lin, Z.; Greene, F. X.; Urban, A.; Thacker, N. C.; Lin, W. *Nat. Commun.*   **2016**, *7*, 12610.

(26)   Klet, R. C.; Tussupbayev, S.; Borycz, J.; Gallagher, J. R.; Stalzer, M. M.; Miller, J. T.; Gagliardi, L.; Hupp, J. T.; Marks, T. J.; Cramer, C. J.; Delferro, M.; Farha, O. K. *J. Amer. Chem. Soc.* **2015**, *137*, 15680.

(27)   Comito, R. J.; Fritzsching, K. J.; Sundell, B. J.; Schmidt-Rohr, K.; Dincă, M. *J. Amer. Chem. Soc.* **2016**, *138*, 10232.

(28)   Li, B. Y.; Leng, K. Y.; Zhang, Y. M.; Dynes, J. J.; Wang, J.; Hu, Y. F.; Ma, D. X.; Shi, Z.; Zhu, L. K.; Zhang, D. L.; Sun, Y. Y.; Chrzanowski, M.; Ma, S. Q. *J. Amer. Chem. Soc.* **2015**, *137*, 4243.

(29)   Johnson, J. A.; Petersen, B. M.; Kormos, A.; Echeverria, E.; Chen, Y. S.; Zhang, J. *J. Amer. Chem. Soc.* **2016**, *138*, 10293.

(30)   Genna, D. T.; Wong-Foy, A. G.; Matzger, A. J.; Sanford, M. S. *J. Amer. Chem. Soc.* **2013**, *135*, 10586.

(31)   Xiao, D. J.; Bloch, E. D.; Mason, J. A.; Queen, W. L.; Hudson, M. R.; Planas, N.; Borycz, J.; Dzubak, A. L.; Verma, P.; Lee, K.; Bonino, F.; Crocella, V.; Yano, J.; Bordiga, S.; Truhlar, D. G.; Gagliardi, L.; Brown, C. M.; Long, J. R. *Nat. Chem.* **2014**, *6*, 590.

(32)   Horike, S.; Dinca, M.; Tamaki, K.; Long, J. R. *J. Amer. Chem. Soc.* **2008**, *130*, 5854.

(33)   Feng, D. W.; Gu, Z. Y.; Li, J. R.; Jiang, H. L.; Wei, Z. W.; Zhou, H. C. *Angew. Chem. Int. Ed.* **2012**, *51*, 10307.

(34)   Rimoldi, M.; Nakamura, A.; Vermeulen, N. A.; Henkelis, J. J.; Blackburn, A. K.; Hupp, J. T.; Stoddart, J. F.; Farha, O. K. *Chem. Sci.* **2016**, *7*, 4980.

(35)   Metzger, E. D.; Brozek, C. K.; Comito, R. J.; Dinca, M. *Acs Cent. Sci.* **2016**, *2*, 148.

(36)   Li, Z.; Schweitzer, N. M.; League, A. B.; Bernales, V.; Peters, A. W.; Getsoian, A.; Wang, T. C.; Miller, J. T.; Vjunov, A.; Fulton, J. L.; Lercher, J. A.; Cramer, C. J.; Gagliardi, L.; Hupp, J. T.; Farha, O. K. *J. Amer. Chem. Soc.* **2016**, *138*, 1977.

(37)   Ji, P. F.; Manna, K.; Lin, Z. K.; Urban, A.; Greene, F. X.; Lan, G. X.; Lin, W. B. *J. Amer. Chem. Soc.* **2016**, *138*, 12234.

(38)   Manna, K.; Ji, P. F.; Greene, F. X.; Lin, W. B. *J. Amer. Chem. Soc.* **2016**, *138*, 7488.

(39)   Phan, A.; Czaja, A. U.; Gandara, F.; Knobler, C. B.; Yaghi, O. M. *Inorg. Chem.* **2011**, *50*, 7388.

(40)   Jiang, J. C.; Gandara, F.; Zhang, Y. B.; Na, K.; Yaghi, O. M.; Klemperer, W. G. *J. Amer. Chem. Soc.* **2014**, *136*, 12844.

(41)   Liu, L. J.; Harris, T. D. *Acs Cent. Sci.* **2016**, *2*, 125.

(42)   Li, X. L.; Van Zeeland, R.; Maligal-Ganesh, R. V.; Pei, Y. C.; Power, G.; Stanley, L.; Huang, W. Y. *Acs Catal.* **2016**, *6*, 6324.

(43)   McGuirk, C. M.; Katz, M. J.; Stern, C. L.; Sarjeant, A. A.; Hupp, J. T.; Farha, O. K.; Mirkin, C. A. *J. Amer. Chem. Soc.* **2015**, *137*, 919.

(44)   Zhang, T.; Manna, K.; Lin, W. *J. Amer. Chem. Soc.* **2016**, *138*, 3241.

(45)   Thacker, N. C.; Lin, Z.; Zhang, T.; Gilhula, J. C.; Abney, C. W.; Lin, W. *J. Ame. Chem. Soc.* **2016**, *138*, 3501.

(46)   Huang, Y. B.; Liang, J.; Wang, X. S.; Cao, R. *Chem. Soc. rev.* **2017**, *46*, 126.

(47)   Zhu, C. F.; Yuan, G. Z.; Chen, X.; Yang, Z. W.; Cui, Y. *J. Amer. Chem. Soc.* **2012**, *134*, 8058.

(48)   Zhang, T.; Song, F. J.; Lin, W. B. *Chem. Commun.* **2012**, *48*, 8766.

(49)   Sträter, N.; Lipscomb, W. N.; Klabunde, T.; Krebs, B. *Angew. Chem. Int. Ed.* **1996**, *35*, 2024.

(50)   van den Beuken, E. K.; Feringa, B. L. *Tetrahedron* **1998**, *54*, 12985.

(51)   Gianneschi, N. C.; Bertin, P. A.; Nguyen, S. T.; Mirkin, C. A.; Zakharov, L. N.; Rheingold, A. L. *J. Amer. Chem. Soc.* **2003**, *125*, 10508.

(52)   Wiester, M. J.; Ulmann, P. A.; Mirkin, C. A. *Angew. Chem. Int. Ed.* **2011**, *50*, 114.

(53)   Park, J.; Hong, S. *Chem. Soc. rev.* **2012**, *41*, 6931.

(54)   Allen, A. E.; MacMillan, D. W. C. *Chem. Sci.* **2012**, *3*, 633.

(55)   In *Cooperative Catalysis*; Wiley-VCH Verlag GmbH & Co. KGaA: 2015, p I.

(56)   Konsler, R. G.; Karl, J.; Jacobsen, E. N. *J. Amer. Chem. Soc.* **1998**, *120*, 10780.

(57)   Mazet, C.; Jacobsen, E. N. *Angew. Chem. Int. Ed.* **2008**, *47*, 1762.

(58)   Breinbauer, R.; Jacobsen, E. N. *Angew. Chem. Int. Ed.* **2000**, *39*, 3604.

(59) Thomas, R. M.; Widger, P. C. B.; Ahmed, S. M.; Jeske, R. C.; Hirahata, W.; Lobkovsky, E. B.; Coates, G. W. *J. Amer. Chem. Soc.* **2010**, *132*, 16520.

(60) Ready, J. M.; Jacobsen, E. N. *Angew. Chem. Int. Ed.* **2002**, *41*, 1374.

(61) Park, J.; Lang, K.; Abboud, K. A.; Hong, S. *J. Amer. Chem. Soc.* **2008**, *130*, 16484.

(62) Venkatasubbaiah, K.; Zhu, X.; Kays, E.; Hardcastle, K. I.; Jones, C. W. *ACS Catal.* **2011**, *1*, 489.

(63) Ravel, B.; Newville, M. *J. Synchrotron Radiat.* **2005**, *12*, 537.

(64) Rehr, J. J.; Albers, R. C. *Rev. Mod. Phys.* **2000**, *72*, 621.

(65) Alonso, F.; Beletskaya, I. P.; Yus, M. *Chem. Rev.* **2004**, *104*, 3079.

(66) Beller, M.; Seayad, J.; Tillack, A.; Jiao, H. *Angew. Chem. Int. Ed.* **2004**, *43*, 3368.

(67) Hintermann, L.; Labonne, A. *Synthesis* **2007**, *2007*, 1121.

(68) Brenzovich, W. E. *Angew. Chem. Int. Ed.* **2012**, *51*, 8933.

(69) Hiscox, W.; Jennings, P. W. *Organometallics* **1990**, *9*, 1997.

(70) Jennings, P. W.; Hartman, J. W.; Hiscox, W. C. *Inorg. Chim. Acta* **1994**, *222*, 317.

(71) Francisco, L. W.; Moreno, D. A.; Atwood, J. D. *Organometallics* **2001**, *20*, 4237.

(72) Damiano, J. P.; Postel, M. *J. Organomet. Chem.* **1996**, *522*, 303.

(73) Wu, X. F.; Bezier, D.; Darcel, C. *Adv. Synth. Catal.* **2009**, *351*, 367.

(74) Fukuda, Y.; Shiragami, H.; Utimoto, K.; Nozaki, H. *J. Org. Chem.* **1991**, *56*, 5816.

(75) Xu, C.; Du, W.; Zeng, Y.; Dai, B.; Guo, H. *Org. Lett.* **2014**, *16*, 948.

(76) Hirabayashi, T.; Okimoto, Y.; Saito, A.; Morita, M.; Sakaguchi, S.; Ishii, Y. *Tetrahedron* **2006**, *62*, 2231.

(77) Venkateswara, K. T.; Prasad, P. S. S.; Lingaiah, N. *Green Chem.* **2012**, *14*, 1507.

(78) Thuong, M. B. T.; Mann, A.; Wagner, A. *Chem. Commun.* **2012**, *48*, 434.

(79) Tachinami, T.; Nishimura, T.; Ushimaru, R.; Noyori, R.; Naka, H. *J. Amer. Chem. Soc.* **2013**, *135*, 50.

(80) Wang, S.; Miao, C.; Wang, W.; Lei, Z.; Sun, W. *ChemCatChem* **2014**, *6*, 1612.

(81) Lu, J.; Dimroth, J.; Weck, M. *J. Amer. Chem. Soc.* **2015**, *137*, 12984.

(82) Fukuda, Y.; Utimoto, K. *J. Org. Chem.* **1991**, *56*, 3729.

(83) Teles, J. H.; Brode, S.; Chabanas, M. *Angew. Chem., Int. Ed.* **1998**, *37*, 1415.

(84) Mizushima, E.; Sato, K.; Hayashi, T.; Tanaka, M. *Angew. Chem., Int. Ed.* **2002**, *41*, 4563.

(85) Casado, R.; Contel, M.; Laguna, M.; Romero, P.; Sanz, S. *J. Am. Chem. Soc.* **2003**, *125*, 11925.

(86) Zhou, C. Y.; Chan, P. W. H.; Che, C. M. *Org. Lett.* **2006**, *8*, 325.

(87) Marion, N.; Ramon, R. S.; Nolan, S. P. *J. Am. Chem. Soc.* **2009**, *131*, 448.

(88) Almassy, A.; Nagy, C. E.; Benyei, A. C.; Joo, F. *Organometallics* **2010**, *29*, 2484.

(89) Cavarzan, A.; Scarso, A.; Sgarbossa, P.; Strukul, G.; Reek, J. N. H. *J. Am. Chem. Soc.* **2011**, *133*, 2848.

(90) Li, L.; Herzon, S. B. *J. Am. Chem. Soc.* **2012**, *134*, 17376.

(91) Wang, D.; Cai, R.; Sharma, S.; Jirak, J.; Thummanapelli, S. K.; Akhmedov, N. G.; Zhang, H.; Liu, X.; Petersen, J. L.; Shi, X. *J. Am. Chem. Soc.* **2012**, *134*, 9012.

(92) Xu, Y.; Hu, X.; Shao, J.; Yang, G.; Wu, Y.; Zhang, Z. *Green Chem.* **2015**, *17*, 532.

(93) Morris, W.; Volosskiy, B.; Demir, S.; Gandara, F.; McGrier, P. L.; Furukawa, H.; Cascio, D.; Stoddart, J. F.; Yaghi, O. M. *Inorg. Chem.* **2012**, *51*, 6443.

(94) Fateeva, A.; Chater, P. A.; Ireland, C. P.; Tahir, A. A.; Khimyak, Y. Z.; Wiper, P. V.; Darwent, J. R.; Rosseinsky, M. J. *Angew. Chem. Int. Ed.* **2012**, *51*, 7440.

(95)   Fateeva, A.; Clarisse, J.; Pilet, G.; Greneche, J. M.; Nouar, F.; Abeykoon, B. K.; Guegan, F.; Goutaudier, C.; Luneau, D.; Warren, J. E.; Rosseinsky, M. J.; Devic, T. *Cryst Growth Des* **2015**, *15*, 1819.

(96)   Hoshino, M.; Katayama, S.; Yamamoto, K. *B Chem Soc Jpn* **1985**, *58*, 3360.

(97)   Sugimoto, H.; Ueda, N.; Mori, M. *B Chem Soc Jpn* **1981**, *54*, 3425.

(98)   Fu, S.; Liu, Y. D.; Ding, Y.; Du, X. Q.; Song, F. Y.; Xiang, R.; Ma, B. C. *Chem. Commun.* **2014**, *50*, 2167.

(99)   Hong, T. N.; Sheu, Y. H.; Jang, K. W.; Chen, J. H.; Wang, S. S.; Wang, J. C.; Wang, S. L. *Polyhedron* **1996**, *15*, 2647.

CHAPTER 3 Hierarchical Integration of Photosensitizing Metal−Organic Frameworks and Nickel-Containing Polyoxometalates for Efficient Visible-Light-Driven Hydrogen Evolution

3.1. Introduction

The development and prosperity of humanity depends greatly on sustainable production of energy. The increase of global populations and living standards is expected to double the current annual global energy consumption by 2050.[1,2] More than 80% of current power generation is provided by burning non-renewable fossil fuels.[3] The greenhouse gases emitted by the combustion of fossil fuels are a significant threat to our living conditions, causing severe environmental issues such as climate change. The development of a large-scale, sustainable, and eco-friendly energy supply is one of the most important goals of current scientific research.

Solar energy is a promising alternative energy source since it is abundant, green, and widely distributed geographically. The sun delivers energy to the earth's surface at an average rate of about 120000 TW, which is about 4 orders of magnitude larger than the current rate of worldwide energy usage.[4] Solar energy can be converted into heat, electricity, or fuels; among them, solar fuels are the most desirable because of the ease of their storage and transportation. However, there are no practical technologies for large-scale solar fuel production currently.

The process of converting solar energy to chemical energy, known as artificial photosynthesis, requires three key steps:[4,5] first, light-harvesting units (antenna) absorb sunlight to create charge-separated excited states; second, electrochemical energy (redox equivalents) created by charge-separated excited states migrates to reactive centers; finally, the generated electrons and holes are used to drive uphill reactions, and thus store chemical energy in the resulting products. Although all of the three steps can be studied individually, a device including

all the components is needed to perform solar energy conversion. The efficiency of the overall system not only depends on the individual parts, but also on how these parts are integrated.[6]

The first artificial photo-driven water splitting was achieved by Honda and Fujishima in solid-state semiconductor systems.[7] Since then, there has been strong interest in using molecular systems for artificial photosynthesis. Molecular systems are not only capable of performing these individual steps, but also can be fine-tuned to optimize efficiency of each step. For example, tetrapyrroles, $[Ru(bpy)_3]^{2+}$ (bpy = 2,2'-bipyridine), and $[Ir(ppy)_2(bpy)]^+$ (ppy = 2-phenylpyridine) derivatives have been used to construct antenna systems.[4] More molecular catalysts have been used for energy-storing reactions such as hydrogen evolution[8-10], water oxidation,[5] and carbon dioxide reduction.[9,11] In addition, photocatalytic molecular systems capable of organic transformations have also been developed.[12,13] Most importantly, molecular components in this approach can be easily investigated using a variety of spectroscopic techniques, to provide deeper insights into the fundamental steps and to optimize their performances.

Small molecule functional components freely moving in the solution cannot work cooperatively to generate a solar fuel device. There is a strong need in developing methods to integrate these molecular components into hierarchically organized structures. Dye-sensitized photoelectrochemical cells (DS-PECs) show the potential of such a design.[5,14,15] In DS-PEC, the excited states generated from chromophore excitation can simultaneously inject electrons into the conduction band of a semiconductor (such as TiO_2) to drive proton or CO_2 reduction by molecular catalysts and holes to metal oxide or molecular catalysts to drive the water oxidation reaction. As mentioned in the previous chapter, multi-functional MOFs can be obtained through incorporation of different components. We surmised that different types of molecular and

nanoparticle (NP) components can be incorporated into MOF frameworks in a hierarchical order to carry out three fundamental steps for solar fuel production.

Photocatalytic hydrogen evolution reaction (HER) is an essential half reaction of water splitting,[16-22] in which effective generation of charge-separated excited states (electron-hole pairs) is followed by facile transfer of the electrons to HER centers to reduce proton to hydrogen.[23,24] Recent studies have demonstrated the feasibility of integrating the two essential components -- the photosensitizer and the HER catalyst -- into MOFs to enable light-driven proton reduction.[25-29] For example, by loading noble metal Pt nanoparticles into the cavities of a photosensitizing MOF, our group showed that the Pt@MOF system facilitated electron injection from the MOF framework to the encapsulated Pt nanoparticles to enable photocatalytic proton reduction with a high turnover number of ~7000.[29]

As a large family of nano-sized inorganic clusters with oxygen-rich surfaces, polyoxometalates (POMs) can readily undergo multi-electron reduction and oxidation processes, thus representing excellent candidates as HER and water oxidation catalysts.[30-33] In order to transition to HER catalysts based on earth-abundant elements, our group recently used the noble-metal free Wells-Dawson POM $[P_2W_{18}O_{62}]^{6-}$ as the electron acceptor to construct the POM@MOF molecular catalytic system for photocatalytic HER.[33] The $[P_2W_{18}O_{62}]$@MOF system enabled visible light-driven HER as a result of fast six-electron injection from multiple $[Ru(bpy)_3]^{2+}$ ligands to each encapsulated $[P_2W_{18}O_{62}]^{6-}$ cluster, but at a modest TON of 79. Notably, the fact that methanol functions as a sacrificial donor is quite unique, and there are few examples of such light driven dehydrogenation reactions.[34-36] Transition-metal-substituted POMs have recently been shown to possess higher visible-light photocatalytic activity, because of their extensive tunability, rich redox chemistry, and synergism between the heterometallic ions.[37-41]

In this chapter, I will discuss the design of a highly effective photocatalytic HER system by encapsulating Ni-containing POM $[Ni_4(H_2O)_2(PW_9O_{34})_2]^{10-}$ (**Ni$_4$P$_2$**) into $[Ir(ppy)_2(bpy)]^+$-derived UiO-MOF (ppy is 2-phenylpyridine and bpy is 2,2'-bipyridine). We also carried out detailed photophysical and electrochemical studies to establish the HER mechanism and to account for the catalytic activity difference between two different **Ni$_4$P$_2$**@MOFs.

3.2. Results and Discussion

3.2.1. Synthesis and Characterizations of MOFs

The $[Ir(ppy)_2(bpy)]^+$-derived dicarboxylic acid (H$_2$**L-Ir**) and $[Ru(bpy)_3]^{2+}$-derived dicarboxylic acid (H$_2$**L-Ru**) were synthesized as reported previously.[33,42] Na$_6$K$_4$[Ni$_4$(H$_2$O)$_2$(PW$_9$O$_{34}$)$_2$]·32H$_2$O and $[(n-C_4H_9)_4N]_{10}[Ni_4(H_2O)_2(PW_9O_{34})_2]$ were synthesized according to the literature.[43,44] $[(n-C_4H_9)_4N]_{10}[Ni_4(H_2O)_2(PW_9O_{34})_2]$ was characterized by IR, as shown in **Figure 3-1**.
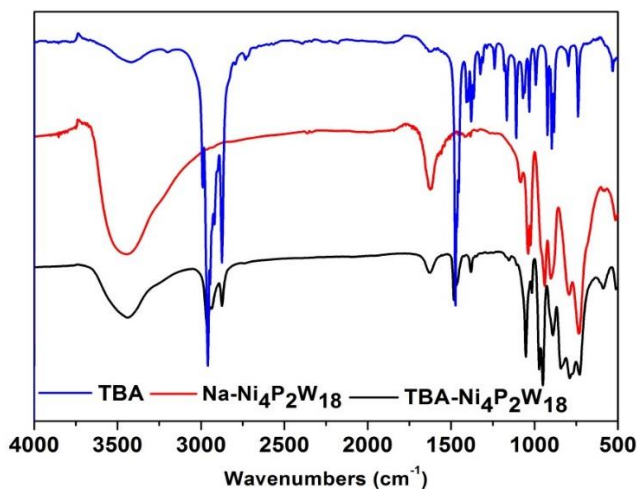
Figure 3-1. IR spectra of Na$_6$K$_4$[Ni$_4$(H$_2$O)$_2$(PW$_9$O$_{34}$)$_2$]·32H$_2$O (Na-Ni$_4$P$_2$W$_{18}$), $(n-C_4H_9)_4$NBr (TBABr), and $[(n-C_4H_9)_4N]_{10}[Ni_4(H_2O)_2(PW_9O_{34})_2]$ (TBA-Ni$_4$P$_2$W$_{18}$). Copyright 2016 John Wiley and Sons.

MOF-**Ir**, formulated as $[Zr_6(\mu_3\text{-}O)_4(\mu_3\text{-}OH)_4(\textbf{L-Ir})_6]\cdot(CF_3CO_2)_6$, and MOF-**Ru**, formulated as $[Zr_6(\mu_3\text{-}O)_4(\mu_3\text{-}OH)_4(\textbf{L-Ru})_6]\cdot(CF_3CO_2)_{12}$, were obtained by treating $ZrCl_4$ and H$_2$**L-Ir**/H$_2$**L-Ru** in DMF at 100 °C for 72 h. **Ni$_4$P$_2$**@MOF-**Ir** (**Ir1−Ir6**) and **Ni$_4$P$_2$**@MOF-**Ru** (**Ru1−Ru6**) were prepared *via in situ* assembly by heating a mixture of $ZrCl_4$, H$_2$**L-Ir**/H$_2$**L-Ru**, and **Ni$_4$P$_2$** at different molar ratios. Powder X−ray diffraction (PXRD) studies show that both MOF-**Ir** and MOF-**Ru** adopt UiO structures with large tetrahedral and octahedral cavities (**Figure 3-2**).[45] Based on charge balance, six and twelve $CF_3CO_2^-$ anions per molecular formula are present in the cavities of MOF-**Ir** and MOF-**Ru**, respectively. The large cationic polyhedral cavities in the UiO structures are ideally suited for the encapsulation of the anionic **Ni$_4$P$_2$** POM. As the **Ni$_4$P$_2$** loading increased, the strong diffraction peaks at 2θ = 3.96 and 7.92° became weaker while the weak diffraction peaks at 2θ = 4.56, 6.56, and 7.56° became stronger in **Ir1-Ir6** (**Figure 3-2**). A similar trend was also observed for **Ru1-Ru6**. Since the tetrahedral cage of 1.4 nm is smaller than the large dimension of the **Ni$_4$P$_2$** POM (1.6 nm), only octahedral cages (2.2 nm) can encapsulate **Ni$_4$P$_2$** POMs (**Figure 3-3**). The selective encapsulation in octahedral cages is supported by the similarity between the observed and simulated PXRDs of the POM@MOF (**Figure 3-2**).
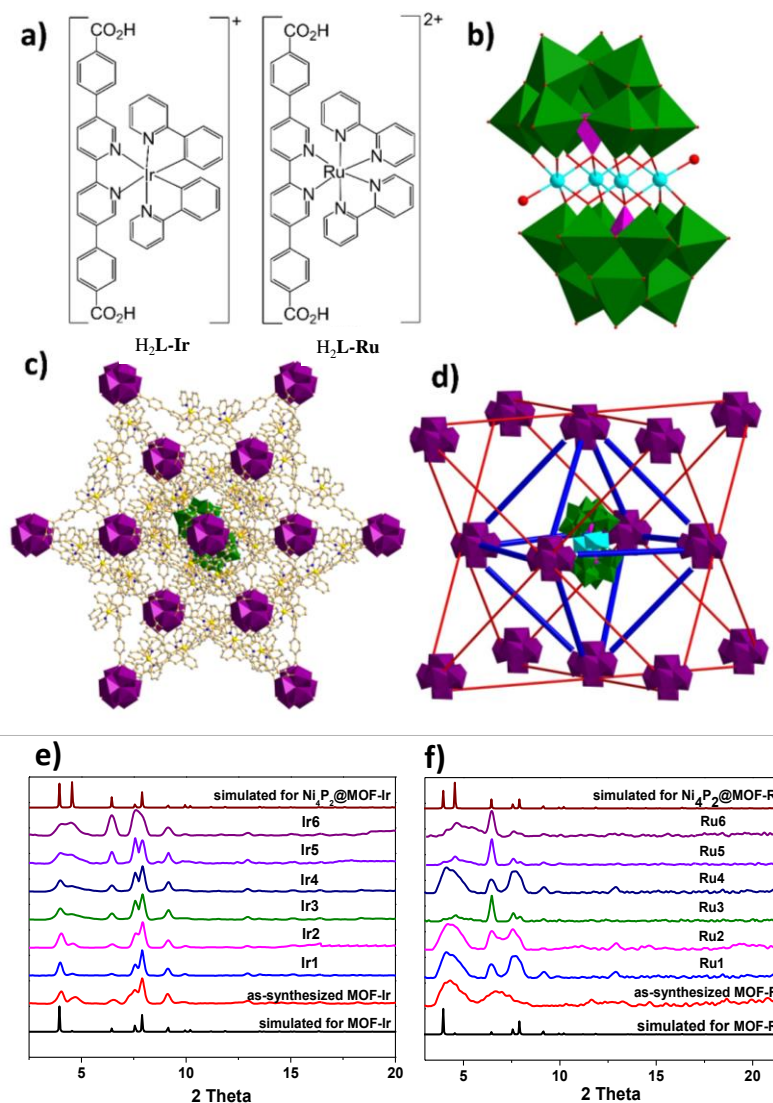
Figure 3-2. a) Chemical structures of H_2**L-Ir** and H_2**L-Ru**; b) Polyhedral view of the structure of $[Ni_4(H_2O)_2(PW_9O_{34})_2]^{10-}$ (**Ni₄P₂**); c) Structural model of **Ni₄P₂**@MOF as viewed along the [111] direction; d) Structural model showing unoccupied tetrahedral cavities and the central **Ni₄P₂**-loaded octahedral cavity; e) Predicted and experimental PXRD patterns of MOF-**Ir** and **Ni₄P₂**@MOF-**Ir** (**Ir1−Ir6**); f) Predicted and experimental PXRD patterns of MOF-**Ru** and **Ni₄P₂**@MOF-**Ru** (**Ru1-Ru6**). Copyright 2016 John Wiley and Sons.
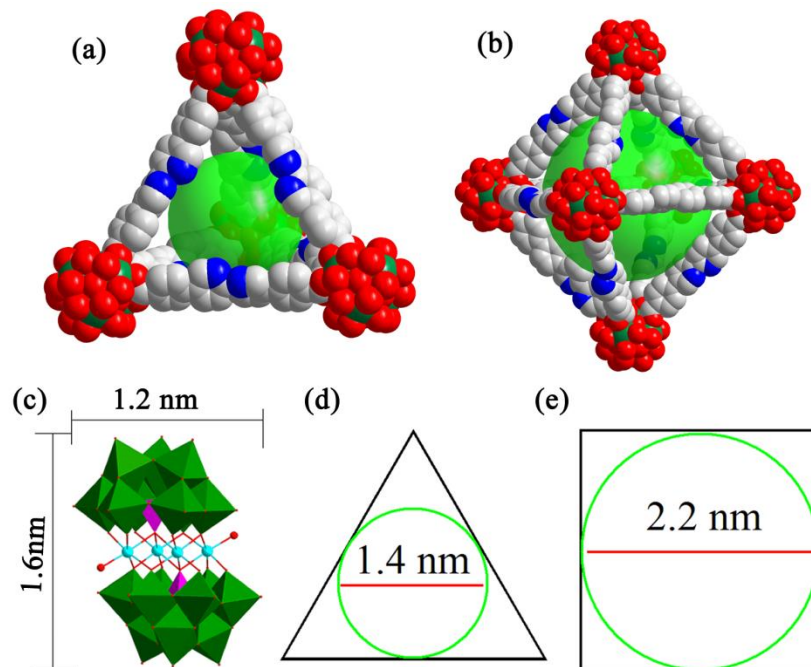
Figure 3-3 a) Structure of tetrahedral cage of MOF-**Ir**; b) structure of an octahedral cage of MOF-**Ir**; c) the size of **Ni₄P₂**; d) the diameter of the circle in the tetrahedral cage; e) the diameter of the circle in the octahedral cage.Copyright 2016 John Wiley and Sons.

The loadings of **Ni₄P₂** in **Ni₄P₂**@MOF-**Ir** and **Ni₄P₂**@MOF-**Ru** were quantified by ICP−MS. The **Ni₄P₂** loadings were in the range of 0.005−0.34 for **Ir1−Ir6** and 0.008−0.53 for **Ru1−Ru6** per molecular formula (calculated based on the ratio of W_{18}/Zr_6, **Table 3-1**). TGA results for **Ir1−Ir6** and **Ru1−Ru6** (**Figures 3-4** and **3-5**) are consistent with these loadings. The weight loss of solvent-free MOF-**Ir** between 200 ℃ and 250 ℃ (8.7 % with respect to the dry MOF-**Ir**) is consistent with the decomposition of six trifluoroacetate groups (expected: 8.6 % for MOF-Ir). For POM@MOF **Ir1−Ir6**, weight loss decreases between 200 ℃ and 250 ℃, suggesting that POM replaces some of trifluoroacetate anions in the channel. TGA analysis shows that the weight losses between 200 ℃ and 500 ℃ are 68.9% for MOF-**Ir**, 63.7 % for **Ir1**, 59.6% for **Ir2**, 51.9% for **Ir3**, 45.2% for **Ir4**, 41.3% for **Ir5**, and 36.8% for **Ir6**, respectively. The

weight loss of solvent-free MOF-**Ru** between 200 °C and 300 °C (17.3 % with respect to the dry

MOF-**Ru**) is consistent with the decomposition of twelve trifluoroacetate anions (expected: 17.0 %

for MOF-**Ru**). For POM@MOF **Ru1-Ru6**, weight loss decreases between 200 °C and 300 °C,

suggesting that POM replaces some of trifluoroacetate anions in the channel. TG analysis shows

that the weight losses between 200 °C and 500 °C are 58.2% for MOF-**Ru**, 50.5 % for **Ru1**, 49.8%

for **Ru2**, 47.4% for **Ru3**, 39.6% for **Ru4**, 30.1% for **Ru5**, and 25.8 % for **Ru6**, respectively. The

weight loss decreases indicate the increase of POM in MOF. Notably, as the POM loading

increases, the POM@MOF structures become more and more stable.

Table 3-1. ICP-MS results of the W/Ni, W/Zr and Ni_4P_2/Zr_6 in Ni_4P_2@MOFs.

Compounds	W/Zr (in reactions)	W/Ni (in POM@MOF)	W/Zr (in POM@MOF)	Ni_4P_2/Zr_6 (in POM@MOF)
Ir1	0.015	4.65	0.017	0.005
Ir2	0.029	5.18	0.042	0.014
Ir3	0.088	4.86	0.125	0.042
Ir4	0.176	6.28	0.403	0.135
Ir5	0.351	5.51	0.893	0.270
Ir6	0.878	4.76	1.02	0.34
Ru1	0.015	3.66	0.023	0.008
Ru2	0.029	5.89	0.048	0.016
Ru3	0.088	6.81	0.361	0.120
Ru4	0.219	5.29	0.57	0.19
Ru5	0.439	5.09	0.97	0.321
Ru6	0.878	5.66	1.61	0.537
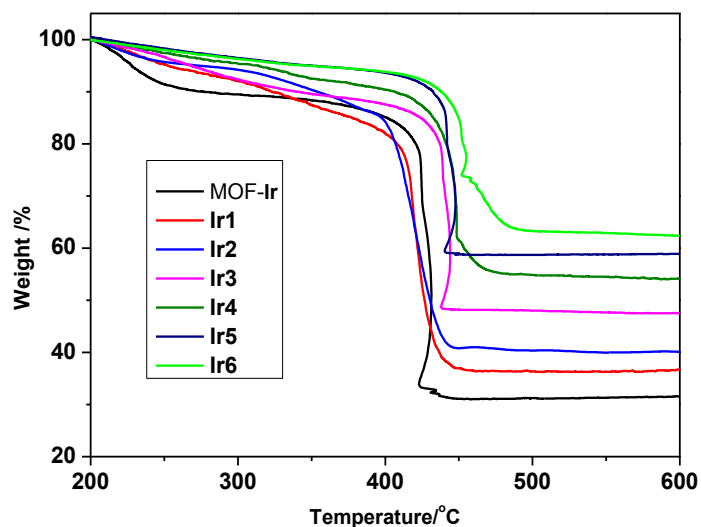
Figure 3-4. TGA results of MOF-**Ir** and **Ir1-Ir6**. For **Ir1-Ir6**, the weight loss decreases with an increasing W/Zr atomic ratio in the feed, indicating the increase of POM loading in the MOFs. All samples were heated at a rate of 5 °C per minute under air. Copyright 2016 John Wiley and Sons.

.
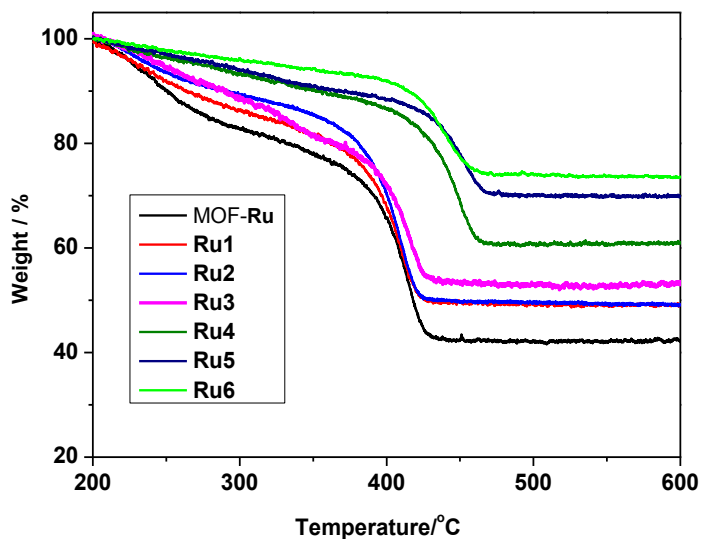
Figure 3-5. TGA results of MOF-**Ru** and **Ru1-Ru6**. For **Ru1-Ru6**, the weight loss decreases with an increasing W/Zr atomic ratio in the feed, indicating the increase of POM loading in the

MOFs. All samples were heated at a rate of 5 °C per minute under air. Copyright 2016 John Wiley and Sons.

The stability of **Ni₄P₂** during the POM@MOF synthesis was supported by electrospray ionization-mass spectrometry (ESI−MS) (**Figure 3-6**). The observed peaks are consistent with the calculated mass for POM-related species (**Table 3-2**), suggesting the chemical stability of **Ni₄P₂** during **Ni₄P₂**@MOF synthesis.
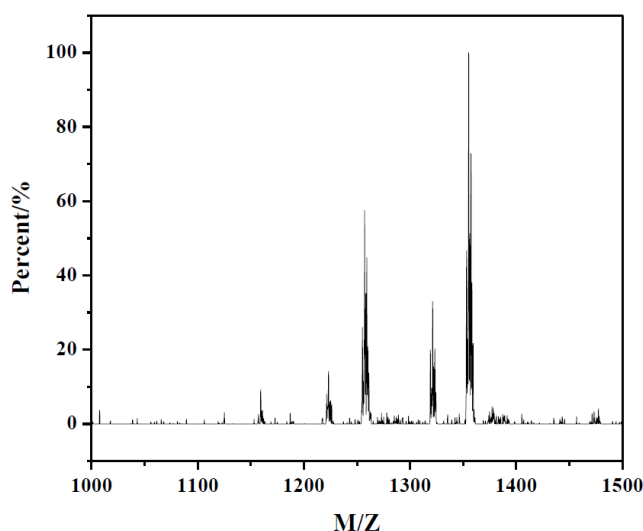
Figure 3-6. ESI-MS spectrum of the **Ir6** after being digested by H_3PO_4 in DMSO, and measured with MeOH injection. Copyright 2016 John Wiley and Sons.

Table 3-2. The list of *m/z* peak assignments in the ESI-MS spectrum of **Ir6**.

Peak assignments	Calculated m/z	Observed m/z
$\{[Ni_4(H_2O)_2(PW_9O_{34})_2][(Ir(ppy)_2]K_5\}^{4-}$	1356.5	1357.3
$\{[Ni_4(H_2O)_2(PW_9O_{34})_2][Ir(ppy)_2(bpydc)]_2KNa_2\}^{5-}$	1321.8	1321.3
$\{[Ni_4(H_2O)_2(PW_9O_{34})_2][Ir(ppy)_2(bpydc)]_2[Ir(ppy)_2]_2(H_2O)\}^{6-}$	1257.2	1257.3
$\{[Ni_4(H_2O)_2(PW_9O_{34})_2]K_3Na_2H\}^{4-}$	1223.4	1223.2
$\{[Ni_4(H_2O)_2(PW_9O_{34})_2][Ir(ppy)_2]_2Na_3\}^{5-}$	1160.0	1159.4

3.2.2. Photocatalytic Hydrogen Evolution Reaction (HER)

The integration of the photosensitizing MOF framework and the POM catalyst allows for facile electron transfer to enable photocatalytic proton reduction. The visible−light−driven ($\lambda >$ 400 nm) HER catalytic activities of **Ni$_4$P$_2$**@MOFs were studied in an acidic aqueous solution (pH 1.2) with methanol as the sacrificial electron donor. The amounts of H$_2$ generated were quantified by gas chromatography analysis of the headspace gas in the reactor. H$_2$ production increased linearly with time at a rate of 4.4 mmol h^{-1} g^{-1} with respect to [Ni$_4$(H$_2$O)$_2$(PW$_9$O$_{34}$)$_2$]$^{10-}$ for **Ir1** (**Figure 3-7**). The turnover number (TON) [defined as n(1/2H$_2$)] reached 1476 in 72 h irradiation. The HER TON of **Ir1**−**Ir4** inversely depended on the **Ni$_4$P$_2$** loading in the POM@MOF, which is consistent with the need to inject multiple electrons in the HER process (**Figure 3-8**).
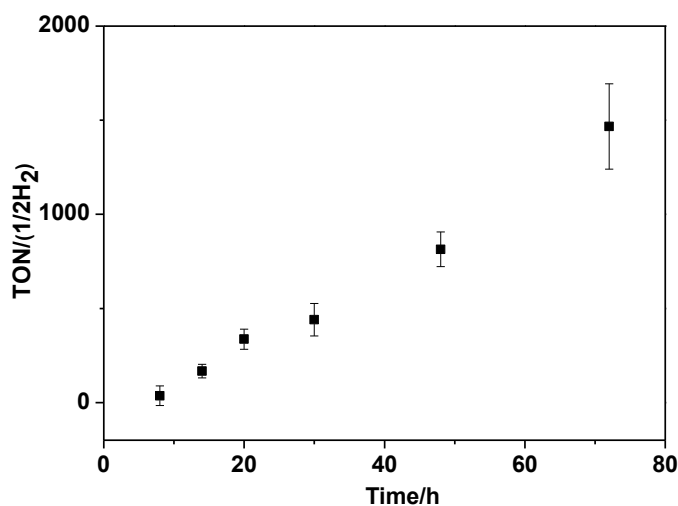
Figure 3-7. Time-dependent TONs of **Ir1** with methanol as the sacrificial electron donor in aqueous solution (pH 1.2) under visible-light ($\lambda >$ 400 nm) irradiation. Copyright 2016 John Wiley and Sons.
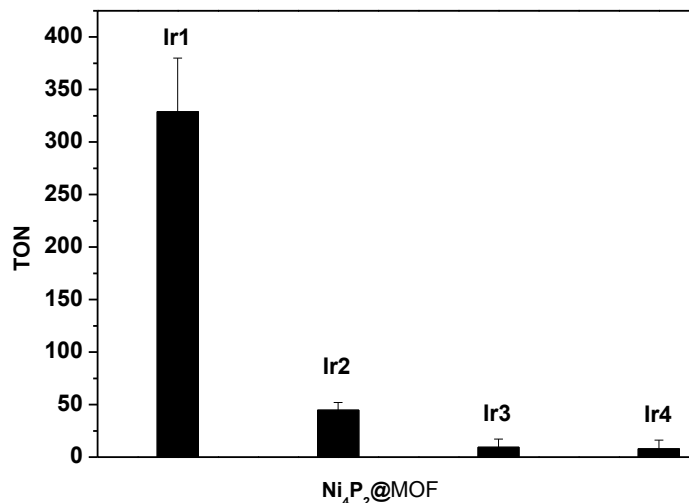
Figure 3-8. TONs of 336 for **Ir1**, 45 for **Ir2**, 10 for **Ir3**, and 8 for **Ir4**. Photocatalytic conditions: methanol as the sacrificial electron donor, in aqueous solution (pH = 1.2) under 20 hours of visible-light ($\lambda > 400$ nm) irradiations. Copyright 2016 John Wiley and Sons.

The **Ni$_4$P$_2$@MOF-Ir** catalyst was recovered and used for photocatalytic HER for three times with only a slight decrease of TON (346 ± 53, 329 ± 77, 297 ± 65; **Figure 3-9**). ICP-MS studies showed that only 0.2 % Ir leached into the solution after 20 h photocatalytic HER. Transmission electron microscope (TEM) images of **Ni$_4$P$_2$@MOF-Ir** remained unchanged before and after photocatalysis (**Figure 3-10**), whereas PXRD patterns of the solid recovered after 20 h reactions were similar to those of the pristine **Ni$_4$P$_2$@MOF-Ir** catalyst (**Figure 3-10**).
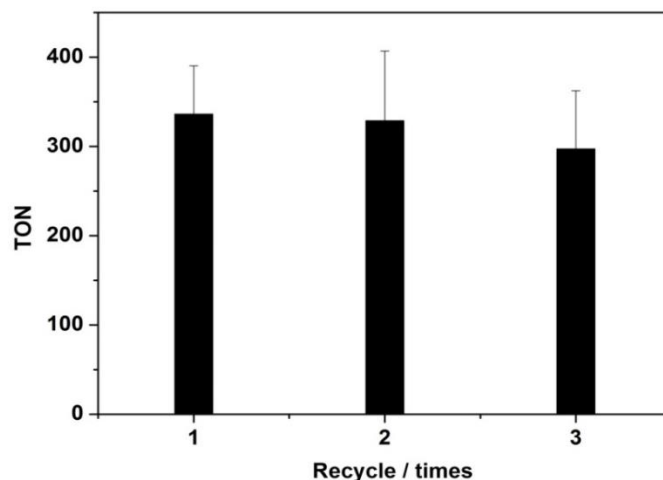
Figure 3-9. TONs of **Ir1** for reusing three times (336±53 for first run, 329±77 for second run, and 297±65 for third run). Photocatalytic conditions: methanol as the sacrificial electron donor in aqueous solution (pH = 1.2) under 20 hours visible-light ($\lambda > 400$ nm) irradiations. Copyright 2016 John Wiley and Sons.
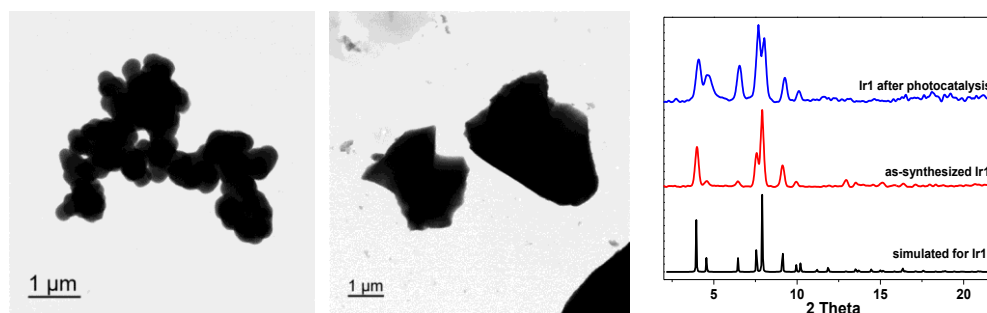
Figure 3-10. TEM micrographs of **Ir1** before (left) and after photocatalytic experiment (middle); PXRD of **Ir1** before and after photocatalytic reaction (right). Copyright 2016 John Wiley and Sons.

The elemental mapping and energy-dispersive X-ray spectroscopy (EDX) of POM elements of **Ni$_4$P$_2$**@MOF before and after photocatalytic experiments were also performed. As shown in **Figure 3-11** to **3-13**, the W, Ni, P elements are uniformly distributed throughout the

94

crystal, suggesting the stability of **Ni₄P₂** during the POM@MOF synthesis and the photocatalytic HER reaction. **Ni₄P₂**@MOFs before and after photocatalytic experiments were digested and analysed with ESI-MS to further prove the stability of **Ni₄P₂** (**Figure 3-14**, **Table 3-3**).
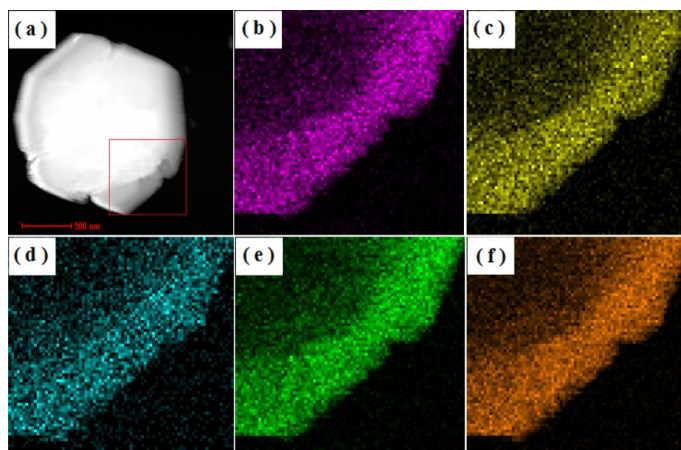
Figure 3-11. TEM image of the **Ir6** (a) and elemental mapping of Zr(b), Ir(c), Ni(d), P(e), and W(f) in **Ir6**. Copyright 2016 John Wiley and Sons.
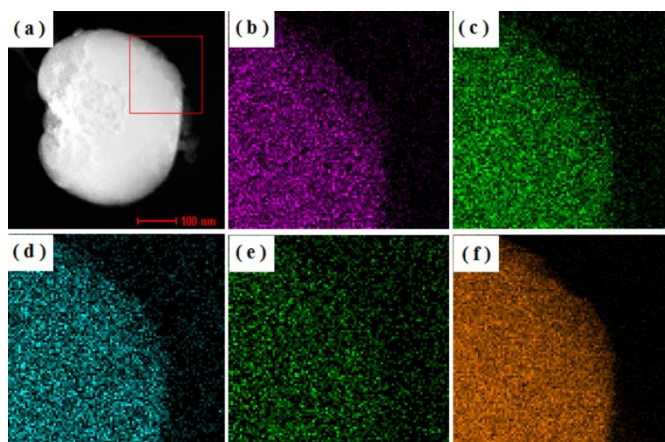
Figure 3-12. TEM image of the **Ir6** after photocatalytic experiment (a) and elemental mapping of Zr(b), Ir(c), Ni(d), P(e) and W(f) in **Ir6** after photocatalytic experiment. Copyright 2016 John Wiley and Sons.
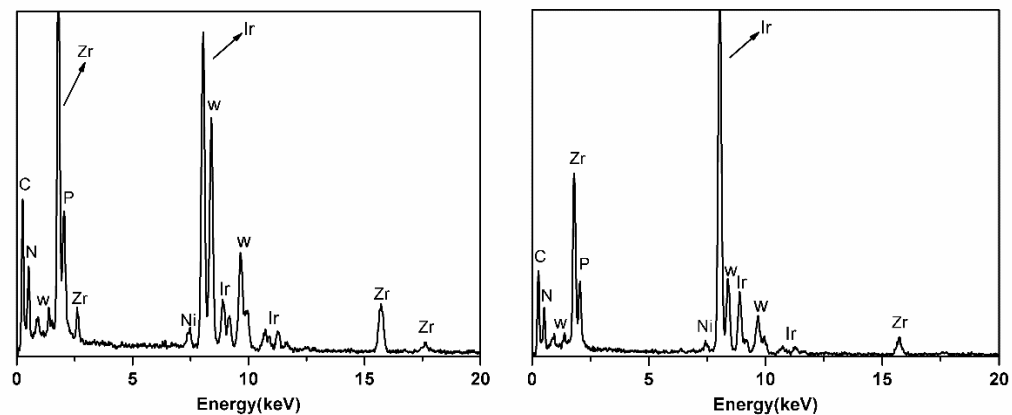
Figure 3-13. EDX of the **Ir6** as synthesized (left) and **Ir6** after photocatalytic experiment (right). Copyright 2016 John Wiley and Sons.
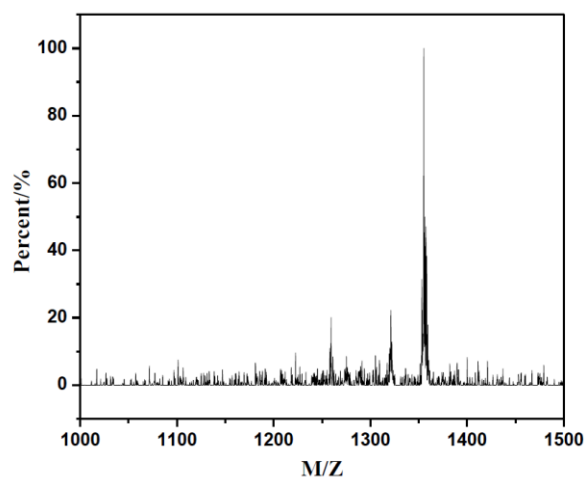
Figure 3-14. ESI-MS spectrum of the **Ir6** after being digested by H_3PO_4 in DMSO, and measured with MeOH injection. Copyright 2016 John Wiley and Sons.

Table 3-3. The list of *m/z* peak assignments in the ESI-MS spectrum of **Ir6** after photocatalytic experiment.

Peak assignments	Calculated m/z	Observed m/z
$\{[Ni_4(H_2O)_2(PW_9O_{34})_2][(Ir(ppy)_2]K_5\}^{4-}$	1356.5	1357.3
$\{[Ni_4(H_2O)_2(PW_9O_{34})_2][Ir(ppy)_2(bpydc)]_2KNa_2\}^{5-}$	1321.8	1321.3
$\{[Ni_4(H_2O)_2(PW_9O_{34})_2][Ir(ppy)_2(bpydc)]_2[Ir(ppy)_2]_2(H_2O)\}^{6-}$	1257.2	1257.3

Control experiments using MOF-**Ir** without encapsulated **Ni₄P₂** and homogeneous mixtures of $[Ni_4(H_2O)_2(PW_9O_{34})_2]^{10-}$ and Me₂**L-Ir** produced only trace amounts of H₂ (with TONs < 13 and 2) after 20 h of visible-light irradiations. These results indicate that the **Ni₄P₂**@MOF-**Ir** catalyst is stable and the hierarchical organization of the photosensitizing framework and the **Ni₄P₂** POM in **Ni₄P₂**@MOF-**Ir** is responsible for the high photocatalytic HER. The actinometric measurement with 460 nm light irradiation showed that **Ir1** has a modest quantum efficiency (QE) of 2×10^{-5}.

The $[Ru(bpy)_3]^{2+}$-derived **Ni₄P₂**@MOF **Ru1−Ru5** were also used in photocatalytic H₂ production experiments. To our surprise, **Ru1−Ru5** only gave trace amounts of H₂ after 20 h visible-light irradiations under the same photocatalytic conditions as **1a**. The HER TONs are ≤3 for **Ru1** and ≤1 for **Ru2-Ru5**. These background-level TON values indicate that the $[Ru(bpy)_3]^{2+}$-derived **Ni₄P₂**@MOF-**Ru** is inactive for photocatalytic HER.

To investigate the HER mechanism, we studied electron transfer processes by luminescence quenching and lifetime measurements. The photosensitizer excited state can be quenched either reductively (by the methanol electron donor) or oxidatively (by the **Ni₄P₂** electron acceptor), which can be ascertained by measuring the luminescence of Me₂**L-Ir** and

Me$_2$**L-Ru** with added methanol or **Ni$_4$P$_2$**. As shown in **Figure 3-15**, the luminescence of Me$_2$**L-Ir** was efficiently quenched by **Ni$_4$P$_2$** but was not affected much by the added methanol, suggesting that the first step of photocatalytic HER mainly occurs via electron transfer from the photosensitizer excited state to **Ni$_4$P$_2$** (i.e., oxidative quenching), but not via electron transfer from methanol to the photo-generated electron-hole pair of the photosensitizer (i.e., reductive quenching). This oxidative quenching mechanism is further supported by time–resolved photoluminescence measurements of MOF-**Ir** and **Ir1−Ir5**. As shown in **Table 3-4**, MOF-**Ir** exhibited a lifetime of 201 ns upon excitation at 405 nm, consistent with the long-lived ^{3}MLCT phosphorescence emission. The lifetimes are 154, 166, 166, 142, 133, and 74.8 ns for **Ir1−Ir5**. Lifetimes of the ligand Me$_2$**L-Ir** and homogeneous solutions of Me$_2$**L-Ir** and **Ni$_4$P$_2$** are 77.9, 77.8, 77.6, 76.9, 75.4, 68.9, and 59.4 ns, respectively. Comparisons of lifetime decreases of **Ni$_4$P$_2$**@MOFs and corresponding homogeneous solutions caused by the quencher indicate that **Ni$_4$P$_2$**@MOF exhibited enhanced quenching, consistent with the comparisons of the decrease of luminescence intensity (**Figure 3-16**). This observation can be attributed to the facile electron transfer from the excited photosensitizer to the POM due to their proximity to each other.
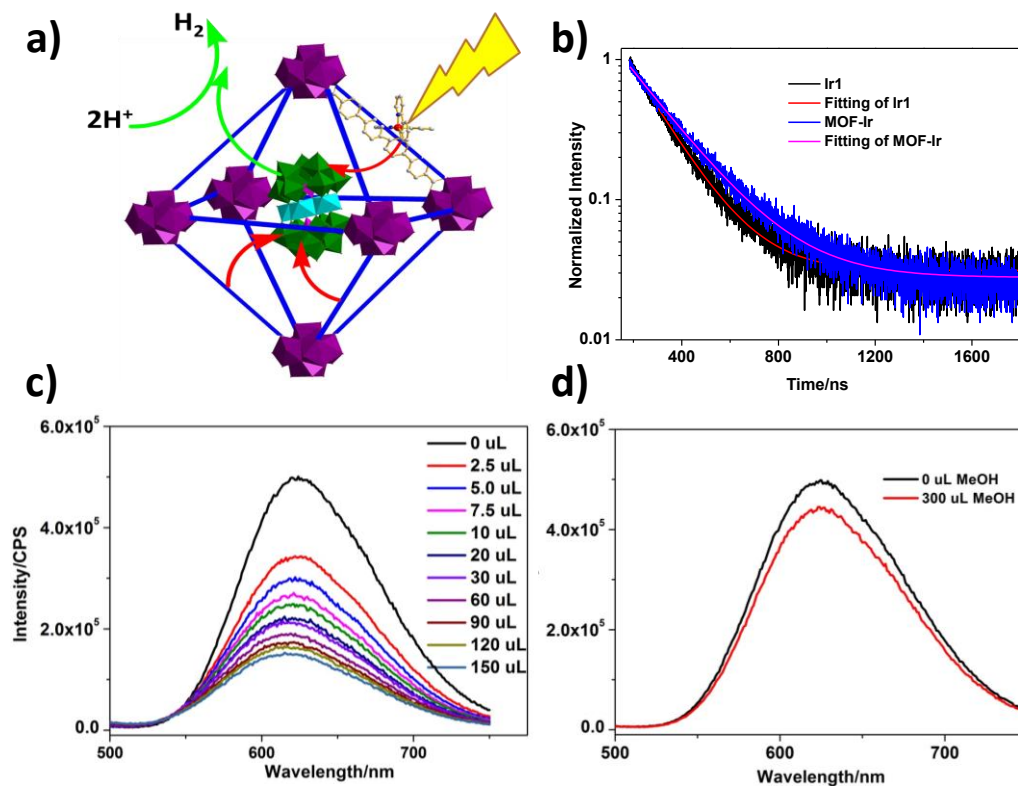
Figure 3-15. (a) Schematic showing the injection of three electrons to the same **Ni₄P₂** upon photoexcitation of the MOF framework to enable proton reduction; (b) normalized luminescence decay trace of **Ir1** and MOF-**Ir** measured at the 625 nm emission wavelength (with 405 nm excitation) in CH₃CN; the emission decays were fit to exponential expression $A = A_0 + A_1 e^{-t/\tau 1}$. The fitted curve is marked in red; emission spectra of Me₂**L-Ir** (0.05 mM) after the addition of different amounts of **Ni₄P₂** (c) and 300 uL MeOH (d) in CH₃CN with 405 nm excitation. Copyright 2016 John Wiley and Sons.

Table 3-4. The lifetimes of MOF-**Ir**, **Ni₄P₂**@MOF-**Ir** (**Ir1 –Ir6)** and their homogeneous controls in CH₃CN.

Compounds	Lifetime (ns)	Homogeneous Control	Lifetime (ns)
MOF-**Ir**	201	Me₂**L-Ir**	77.9
Ir1	154	**Ir1'**	77.8
Ir2	166	**Ir2'**	77.6
Ir3	166	**Ir3'**	76.9
Ir4	142	**Ir4'**	75.4
Ir5	133	**Ir6'**	68.9
Ir6	74.8	**Ir6'**	59.5
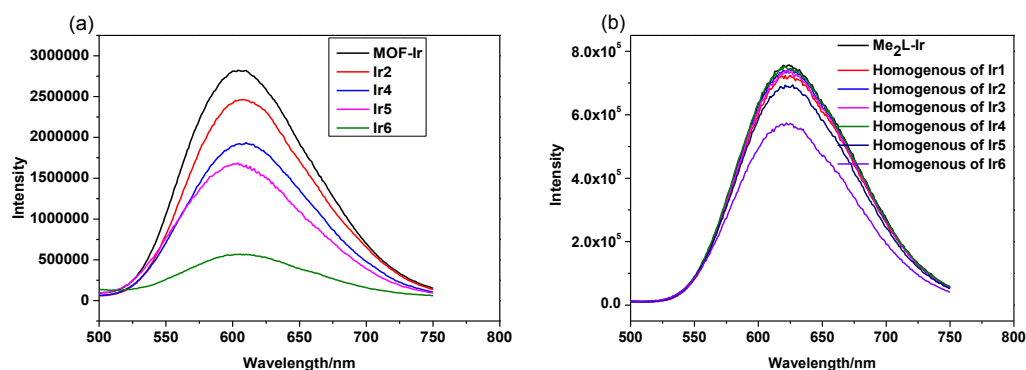
Figure 3-16. Emission spectra of MOF-**Ir** and **Ni₄P₂**@MOF-**Ir** with 0.26 mM [**L-Ir**] (a) and homogenous solutions of Me₂**L-Ir** with 0.26 mM and **Ni₄P₂** POM in 3 mL CH₃CN (b).

Cyclic voltammograms (CVs) of the photosensitizer and **Ni₄P₂** were studied to provide additional insights into the H₂ production mechanism. **Ni₄P₂** shows two reversible reduction peaks at −0.37 and −0.55 V *vs* NHE and an irreversible catalytic peak with an onset potential of −0.65 V (**Figure 3-17**), suggesting that the H₂ production commences upon the injection of three

electrons. This is supported by differential pulse voltammetry which showed a proton reduction peak at −0.66 eV for **Ni₄P₂** (**Figure 3-17**).
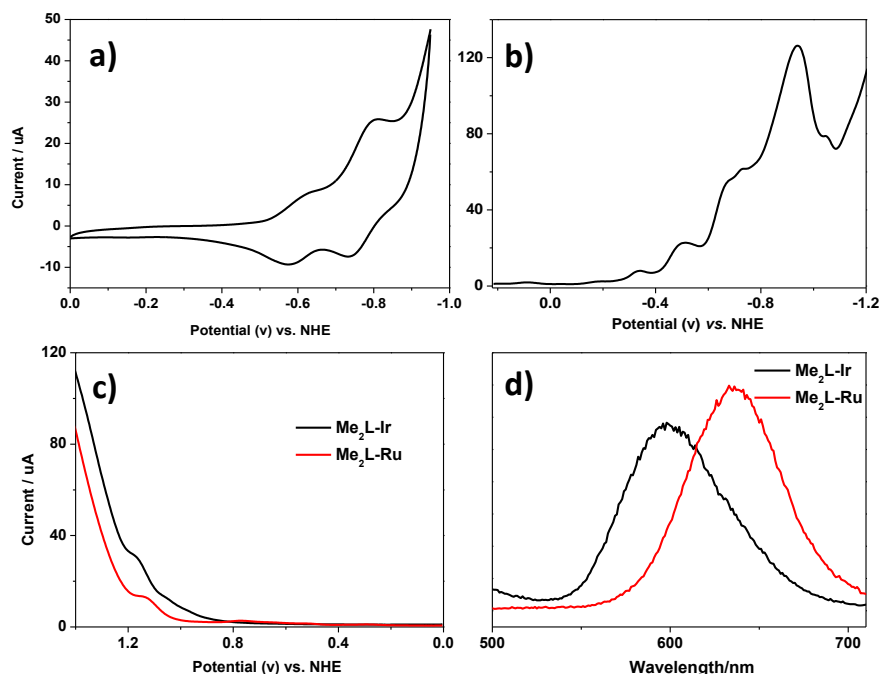
Figure 3-17. (a) Cyclic voltammograms (CVs) of 0.2 mM **Ni₄P₂** in a 2M NaCl aqueous solution (pH = 1.2); Differential pulse voltammetry (DPV) of 0.2 mM **Ni₄P₂** (b), and 0.2 mM **Me₂L-Ir** and **Me₂L-Ru** (c) in a 2M NaCl aqueous solution (pH = 1.2) with a scan rate of 100 mV/s; (d) Emission spectra of **Me₂L-Ir** and **Me₂L-Ru** in aqueous solution (pH = 1.2) with 360 nm excitation for **Me₂L-Ir** and 400 nm excitation for **Me₂L-Ru**. Copyright 2016 John Wiley and Sons.
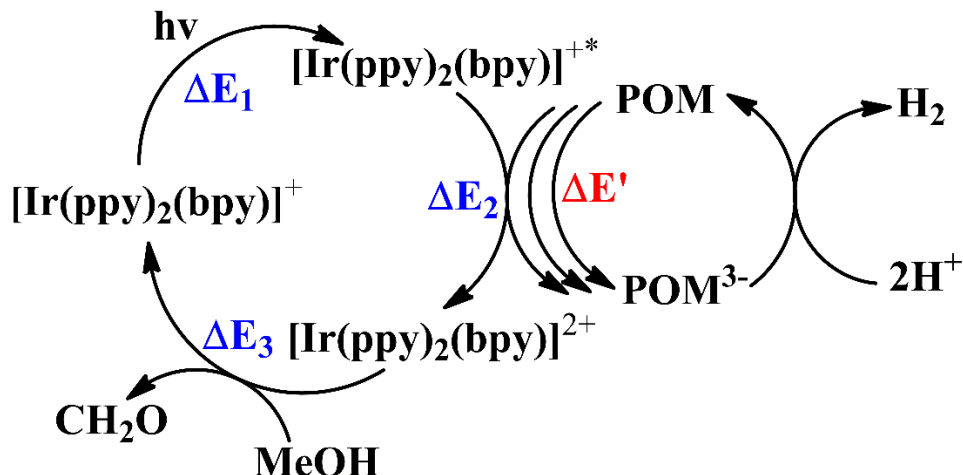
Scheme 3-1. Proposed catalytic cycle for visible-light-driven hydrogen evolution catalyzed by **Ni₄P₂**@MOF-**Ir**. Copyright 2016 John Wiley and Sons.

Based on these experimental data, we propose the photocatalytic HER mechanism in **Scheme 3-1** for **Ni₄P₂**@MOF-**Ir**. Under the visible-light irradiation, the ligand $[Ir(ppy)_2(bpy)]^+$ will be excited to the $[Ir(ppy)_2(bpy)]^{+*}$ excited state, which can transfer one electron to the **Ni₄P₂** POM to generate $[Ir(ppy)_2(bpy)]^{2+}$. After each POM has accepted three electrons, the $[POM]^{3-}$ can drive the proton reduction to generate H_2. The $[Ir(ppy)(bpy)]^{2+}$ can be reduced back to the $[Ir(ppy)(bpy)]^+$ by the MeOH sacrificial donor to complete the catalytic cycle. Formaldehyde formed by the oxidation of the sacrificial methanol was quantified by gas chromatography-mass spectrometry (GC-MS) after derivatization with o-(2,3,4,5,6-pentafluorobenzyl) hydroxylamine PFBHA.[46] After 20 h of visible-light irradiations, the **Ir1** produced 0.271 umol formaldehyde, which is slightly larger than the calculated value of 0.235 umol.

CV scans showed that Me₂**L-Ir** and Me₂**L-Ru** displayed oxidation peaks at 1.38 and 1.34 eV, respectively (**Figure 3-17c**). As shown in **Figure 3-17d**, Me₂**L-Ir** and Me₂**L-Ru** exhibit luminescence emission peaks at 598 nm and 633 nm, respectively. These correspond to energy

gaps between the photosensitizer excited state and ground state of 2.08 and 1.96 eV for Me$_2$**L-Ir** and Me$_2$**L-Ru**, respectively. Based on the energy loop as shown in **Scheme 3-1**, the energy difference ΔE' between [Ir(ppy)$_2$(bpy')]$^{+*}$ and [Ir(ppy)$_2$(bpy)]$^{2+}$ is 1.38−2.08 = −0.70 eV, which is negative enough (compared to −0.65 eV for proton reduction by **Ni$_4$P$_2$**) to drive the H$_2$ production. In contrast, the energy gap ΔE' between [Ru(bpy)$_2$(bpy')]$^{2+*}$ and [Ru(bpy)$_2$(bpy')]$^{3+}$ is 1.34−1.96 = −0.62 eV, which is not negative enough to drive H$_2$ production by **Ni$_4$P$_2$**. This analysis thus explains why **Ru1−Ru5** are inactive for photocatalytic HER with methanol as the sacrificial electron donor.

3.3. Conclusion

We have successfully encapsulated tetra-nickel-containing **Ni$_4$P$_2$** POMs into the pores of phosphorescent MOFs built from [Ir(ppy)$_2$(bpy)]$^+$ and [Ru(bpy)$_3$]$^{2+}$-derived dicarboxylate ligands. Visible-light-driven hydrogen evolution experiments show that the proximity of **Ni$_4$P$_2$** to multiple photosensitizers in **Ni$_4$P$_2$@MOF** is key to facile multi-electron transfer and efficient HER. Photophysical and electrochemical studies established the oxidative quenching of the photosensitizer excited state by **Ni$_4$P$_2$** as the initiating step of HER and explained the drastic catalytic activity difference between the two POM@MOF systems. Hierarchically organized POM@MOF assemblies thus not only provide a tunable platform for achieving synergistic functions from multiple components, but also facilitate mechanistic studies of these processes.

3.4. Materials and Experimental Details

3.4.1. General Experimental

All of the chemicals were purchased from Aldrich and Fisher Scientific, and used as received. Thermogravimetric analysis (TGA) was carried out on a Shimadzu TGA-50 equipped with a Pt pan. Inductively coupled plasma-mass spectrometry (ICP-MS) data was obtained with

an Agilent 7700x ICP-MS and analyzed using ICP-MS MassHunter version B01.03. IR spectra were recorded in the range of 400–4000 cm^{-1} on an Alpha Centaurt FT-IR Spectrophotometer with pressed KBr pellets. Amounts of H_2 generated in the photo-catalytic experiments were determined by gas chromatography (GC) using an Agilent 7890B Gas Chromatograph with the nitrogen carrier gas and a TCD detector. Steady-state and time-resolved emission spectra were recorded on an Edinburgh FLS 920 spectrometer. Powder X-ray diffraction (PXRD) patterns were collected on a Bruker D8 Venture, dual microsource (Cu and Mo) diffractometer with a CMOS detector; Cu Kα radiation was used. The PXRD patterns were processed with the APEX2 package using PILOT plug-in. Time-domain lifetimes were measured on a ChronosBH lifetime fluorimeter (ISS, Inc.) using the photon counting method. TEM, EDX, and element mapping were collected on a TECNAI F30 HRTEM. Gas chromatography-mass spectrometry (GC-MS) analysis was processed with a Shimadzu GCMS-QP2010 SE and a SH-Rxi-Sil MS 30m × 0.2mm × 0.2μm column.

3.4.2. Synthesis of MOFs

3.4.2.1. Synthesis of [Zr$_6$(μ$_3$-O)$_4$(μ$_3$-OH)$_4$(L-Ir)$_6$](CO$_2$CF$_3$)$_6$ (MOF-Ir)

MOF-Ir was synthesized according to the literature.[42] ZrCl$_4$ (1.0 mg, 0.0043 mmol), H$_2$L-Ir (3.9 mg, 0.0043 mmol), and trifluoroacetic acid (5 μL, 0.0875 mmol) were dissolved in DMF (0.25 mL), sealed in a vial, and placed in an oven. The temperature was kept at 100 °C for 72 hours. After cooling to room temperature, the resulting solid was isolated by decanting the supernatant solution. The crystalline solid was then washed with DMF and methanol. Yield: 4.0 mg (32 %).

3.4.2.2. Synthesis of POM@MOF (Ir1)

ZrCl$_4$ (0.5 mg, 0.00215 mmol), H$_2$**L-Ir**(1.95 mg, 0.00215 mmol), [(n-C$_4$H$_9$)$_4$N]$_{10}$[Ni$_4$(H$_2$O)$_2$(PW$_9$O$_{34}$)$_2$] (0.0125mg) and trifluoroacetic acid (5 μL, 0.0875mmol) were dissolved in 0.5 mL DMF, sealed in a 2.5 mL vial, and placed in a 100 °C oven for 72 hours. After cooling to room temperature, the resulting solid was isolated by decanting the supernatant solution. The crystalline solid was then washed with DMF and methanol. Yield: 1.0 mg (35 %).

3.4.2.3. Synthesis of POM@MOF (Ir2-Ir6)

Ir2-Ir6 were synthesized in a similar fashion as **Ir1**, except that different amounts of [(n-C$_4$H$_9$)$_4$N]$_{10}$[Ni$_4$(H$_2$O)$_2$(PW$_9$O$_{34}$)$_2$] and TFA were used. The detailed conditions are listed in **Table 3-5**.

Table 3-5. The detailed synthesis conditions for MOF-**Ir** and **Ir1-Ir6**.

Entry	ZrCl$_4$/mg	H$_2$**L-Ir** /mg	**Ni$_4$P$_2$**/mg	TFA/μL	Yield/%
MOF-**Ir**	1.0	3.9	0	5	32
Ir1	0.5	1.95	0.0125	5	35
Ir2	0.5	1.95	0.025	6	34
Ir3	0.5	1.95	0.075	7	36
Ir4	0.5	1.95	0.15	8	30
Ir5	0.5	1.95	0.30	10	32
Ir6	0.5	1.95	0.75	12	28

3.4.2.4. Synthesis of [Zr$_6$(μ_3-O)$_4$(μ_3-OH)$_4$(L-Ru)$_6$](CO$_2$CF$_3$)$_{12}$ (MOF-Ru)

MOF-**Ru** was synthesized according to the literature.[33] ZrCl$_4$ (0.5 mg, 0.00215 mmol), H$_2$**L-Ru** (1.51 mg, 0.00215 mmol), and trifluoroacetic acid (4 μL, 0.1 mmol) were dissolved in

DMF (0.25 mL), sealed in a vial, and placed in an oven. The temperature was kept at 100 °C for 72 hours. After cooling to room temperature, the resulting solid was isolated by decanting the supernatant solution. The crystalline solid was then washed with DMF and methanol. Yield: 0.76 mg (29 %).

3.4.2.5. Synthesis of POM@MOF (Ru1)

ZrCl$_4$ (0.5 mg, 0.00215 mmol), H$_2$**L-Ru** (1.51 mg, 0.00215 mmol), [(n-C$_4$H$_9$)$_4$N]$_{10}$[Ni$_4$(H$_2$O)$_2$(PW$_9$O$_{34}$)$_2$] (0.0125mg), and trifluoroacetic acid (4 μL, 0.07 mmol) were dissolved in 0.5 mL DMF, sealed in a 2.5 mL vial, and placed in a 100 °C oven for 72 hours. After cooling to room temperature, the resulting solid was isolated by decanting the supernatant solution. The crystalline solid was then washed with DMF and methanol. Yield: 1.0 mg (30 %).

3.4.2.6. Synthesis of POM@MOF (Ru2-Ru6)

Ru2-Ru6 were synthesized in a similar fashion as **Ru1**, except that different amounts of [(n-C$_4$H$_9$)$_4$N]$_{10}$[Ni$_4$(H$_2$O)$_2$(PW$_9$O$_{34}$)$_2$] and TFA were used. The detailed conditions are listed in **Table 3-6**.

Table 3-6. The detailed synthesis conditions for MOF-**Ru** and **Ru1-Ru6**.

Entry	ZrCl$_4$/mg	H$_2$**L-Ru** /mg	**Ni$_4$P$_2$**/mg	TFA/μL	Yield/%
MOF-**Ru**	0.5	1.51	0	4	29
Ru1	0.5	1.51	0.0125	4	30
Ru2	0.5	1.51	0.025	4	32
Ru3	0.5	1.51	0.075	6	26
Ru4	0.5	1.51	0.1875	7	26
Ru5	0.5	1.51	0.375	9	30
Ru6	0.5	1.51	0.75	10	31

3.4.3. Visible Light-driven Hydrogen Production.

Photocatalytic H_2 production was carried out in an external illumination type reaction vessel with a magnetic stirrer. Samples were prepared in 4.58 mL septum-sealed glass vials. Each sample was made up to a volume of 2.00 mL of 10% methanol (v:v) aqueous solution with the pH value of 1.2 (adjusted by using 6 M HCl). Samples typically contained 0.36 µM of the $[Ni_4(H_2O)_2(PW_9O_{34})_2]^{10-}$ catalyst. Sample vials were capped and deoxygenated by bubbling nitrogen through them for 20 min to ensure complete air removal. The solution was irradiated by a 230 W solid state light source with a 400 nm filter. After the hydrogen evolution reaction, the gas in the headspace of the vial was analyzed by GC to determine the amount of hydrogen generated.

Table 3-7. Photocatalytic hydrogen production by MOFs and their homogeneous controls in the aqueous solution with methanol as the sacrificial electron donor.

Entry	Catalyst	Irradiation times/h	H_2 amount(µl)	TON
1	$Na_6K_4[Ni_4(H_2O)_2(PW_9O_{34})_2]$ and Me$_2$**L-Ir** (homogeneous control)	20	0.02	2
2	MOF-**Ir**	20	0.10	-
3	**Ir1**	8	0.28	36
4	**Ir1**	14	1.43	167
5	**Ir1**	20	2.66	336
6	**Ir1**	30	3.50	440
7	**Ir1**	48	6.56	814
8	**Ir1**	72	12.02	1476
9	**Ir2**	20	0.36	45
10	**Ir3**	20	0.12	10
11	**Ir4**	20	0.08	8
12	$Na_6K_4[Ni_4(H_2O)_2(PW_9O_{34})_2]$ and Me$_2$**L-Ru** (homogeneous control)	20	0.02	-
13	MOF-**Ru**	20	0.02	-
14	**Ru1**	20	0.03	3
15	**Ru2**	20	0.02	1
16	**Ru3**	20	0.02	<1
17	**Ru5**	20	0.02	<1

TON is defined as $n_{(1/2H2)}/n_{(POM)}$

Quantum efficiency determination of HER was performed in a 4.58 mL septum-sealed glass vial containing 1.0 uM **Ir1** in 2.00 mL of 10% methanol (v:v) aqueous solution with the pH value of 1.2 (adjusted by using 6 M HCl). After being degassed for 20 min with nitrogen, the

solution was irradiated with 460 nm LED light source for 24 hours, and the gas in the headspace

was analyzed by GC to quantify the production of hydrogen. Photon flow density of the LED

photochemical apparatus was determined by actinometric methods using $K_3Fe(C_2O_4)_3$ as a

standard following a reported procedure.[47]

3.5. References

(1) Hoffert, M. I.; Caldeira, K.; Jain, A. K.; Haites, E. F.; Harvey, L. D. D.; Potter, S. D.; Schlesinger, M. E.; Schneider, S. H.; Watts, R. G.; Wigley, T. M. L.; Wuebbles, D. J. *Nature* **1998**, *395*, 881.
(2) Mohanty, K. K. *AIChE Journal* **2003**, *49*, 2454.
(3) Hammarström, L.; Hammes-Schiffer, S. *Acc. Chem. Res.* **2009**, *42*, 1859.
(4) Gust, D.; Moore, T. A.; Moore, A. L. *Acc. Chem. Res.* **2009**, *42*, 1890.
(5) Concepcion, J. J.; Jurss, J. W.; Brennaman, M. K.; Hoertz, P. G.; Patrocinio, A. O. v. T.; Murakami Iha, N. Y.; Templeton, J. L.; Meyer, T. J. *Acc. Chem. Res.* **2009**, *42*, 1954.
(6) Ward, M. D.; Raithby, P. R. *Chem. Soc. rev.* **2013**.
(7) Fujishima, A.; Honda, K. *Nature* **1972**, *238*, 37.
(8) Esswein, A. J.; Nocera, D. G. *Chem. Rev.* **2007**, *107*, 4022.
(9) Rakowski Dubois, M.; Dubois, D. L. *Acc. Chem. Res.* **2009**, *42*, 1974.
(10) Dempsey, J. L.; Brunschwig, B. S.; Winkler, J. R.; Gray, H. B. *Acc. Chem. Res.* **2009**, *42*, 1995.
(11) Morris, A. J.; Meyer, G. J.; Fujita, E. *Acc. Chem. Res.* **2009**, *42*, 1983.
(12) Narayanam, J. M. R.; Stephenson, C. R. *J. Chem. Soc. Rev.* **2011**, *40*, 102.
(13) Prier, C. K.; Rankic, D. A.; MacMillan, D. W. C. *Chem.Rev.* **2013**, *113*, 5322.
(14) Youngblood, W. J.; Lee, S. H. A.; Kobayashi, Y.; Hernandez-Pagan, E. A.; Hoertz, P. G.; Moore, T. A.; Moore, A. L.; Gust, D.; Mallouk, T. E. *J. Amer. Chem. Soc.* **2009**, *131*, 926.
(15) Wasielewski, M. R. *Acc.Chem. Res.* **2009**, *42*, 1910.
(16) Chen, X. B.; Shen, S. H.; Guo, L. J.; Mao, S. S. *Chem. Rev.* **2010**, *110*, 6503.
(17) Wang, X. C.; Maeda, K.; Thomas, A.; Takanabe, K.; Xin, G.; Carlsson, J. M.; Domen, K.; Antonietti, M. *Nat. Mater.* **2009**, *8*, 76.
(18) Yu, Z.; Li, F.; Sun, L. C. *Energy Environ. Sci.* **2015**, *8*, 760.
(19) Wang, M.; Han, K.; Zhang, S.; Sun, L. C. *Coordin. Chem. Rev.* **2015**, *287*, 1.
(20) Lakadamyali, F.; Kato, M.; Muresan, N. M.; Reisner, E. *Angew. Chem. Int. Ed.* **2012**, *51*, 9381.
(21) Singh, W. M.; Baine, T.; Kudo, S.; Tian, S.; Ma, X. A.; Zhou, H.; DeYonker, N. J.; Pham, T. C.; Bollinger, J. C.; Baker, D. L.; Yan, B.; Webster, C. E.; Zhao, X. *Angew. Chem. Int. Ed.* **2012**, *51*, 5941.
(22) DiSalle, B. F.; Bernhard, S. *J. Amer. Chem. Soc.* **2011**, *133*, 11819.
(23) Kind, H.; Yan, H. Q.; Messer, B.; Law, M.; Yang, P. D. *Adv. Mater.* **2002**, *14*, 158.
(24) Hou, W. B.; Cronin, S. B. *Adv. Funct. Mater.* **2013**, *23*, 1612.

(25) Zhang, T.; Lin, W. B. *Chem. Soc. Rev.* **2014**, *43*, 5982.
(26) Kataoka, Y.; Sato, K.; Miyazaki, Y.; Masuda, K.; Tanaka, H.; Naito, S.; Mori, W. *Energy Environ. Sci.* **2009**, *2*, 397.
(27) Pullen, S.; Fei, H. H.; Orthaber, A.; Cohen, S. M.; Ott, S. *J. Amer. Chem. Soc.* **2013**, *135*, 16997.
(28) Fateeva, A.; Chater, P. A.; Ireland, C. P.; Tahir, A. A.; Khimyak, Y. Z.; Wiper, P. V.; Darwent, J. R.; Rosseinsky, M. J. *Angew. Chem. Int. Ed.* **2012**, *51*, 7440.
(29) Wang, C.; deKrafft, K. E.; Lin, W. *J. Am. Chem. Soc.* **2012**, *134*, 7211.
(30) Rausch, B.; Symes, M. D.; Chisholm, G.; Cronin, L. *Science* **2014**, *345*, 1326.
(31) Qin, J. S.; Du, D. Y.; Guan, W.; Bo, X. J.; Li, Y. F.; Guo, L. P.; Su, Z. M.; Wang, Y. Y.; Lan, Y. Q.; Zhou, H. C. *J. Amer. Chem. Soc.* **2015**, *137*, 7169.
(32) Nohra, B.; El Moll, H.; Albelo, L. M. R.; Mialane, P.; Marrot, J.; Mellot-Draznieks, C.; O'Keeffe, M.; Biboum, R. N.; Lemaire, J.; Keita, B.; Nadjo, L.; Dolbecq, A. *J. Amer. Chem. Soc.* **2011**, *133*, 13363.
(33) Zhang, Z. M.; Zhang, T.; Wang, C.; Lin, Z. K.; Long, L. S.; Lin, W. B. *J. Amer. Chem. Soc.* **2015**, *137*, 3197.
(34) Irie, R.; Li, X. M.; Saito, Y. *J. Mol. Catal.* **1983**, *18*, 263.
(35) Mena, I.; Casado, M. A.; Polo, V.; Garcia-Orduna, P.; Lahoz, F. J.; Oro, L. A. *Angew. Chem. Int. Ed.* **2012**, *51*, 8259.
(36) Kagalwala, H. N.; Maurer, A. B.; Mills, I. N.; Bernhard, S. *Chemcatchem* **2014**, *6*, 3018.
(37) Lv, H.; Guo, W.; Wu, K.; Chen, Z.; Bacsa, J.; Musaev, D. G.; Geletii, Y. V.; Lauinger, S. M.; Lian, T.; Hill, C. L. *J. Am. Chem. Soc.* **2014**, *136*, 14015.
(38) von Allmen, K.; More, R.; Muller, R.; Soriano-Lopez, J.; Linden, A.; Patzke, G. R. *Chempluschem* **2015**, *80*, 1389.
(39) Han, X. B.; Li, Y. G.; Zhang, Z. M.; Tan, H. Q.; Lu, Y.; Wang, E. B. *J. Amer. Chem. Soc.* **2015**, *137*, 5486.
(40) Stracke, J. J.; Finke, R. G. *Acs Catal.* **2014**, *4*, 79.
(41) Lv, H. J.; Geletii, Y. V.; Zhao, C. C.; Vickers, J. W.; Zhu, G. B.; Luo, Z.; Song, J.; Lian, T. Q.; Musaev, D. G.; Hill, C. L. *Chem. Soc. rev.* **2012**, *41*, 7572.
(42) Wang, C.; deKrafft, K. E.; Lin, W. B. *J. Amer. Chem. Soc.* **2012**, *134*, 7211.
(43) Clemente-Juan, J. M.; Coronado, E.; Galan-Mascaros, J. R.; Gomez-Garcia, C. J. *Inorg. Chem.* **1999**, *38*, 55.
(44) Lv, H. J.; Guo, W. W.; Wu, K. F.; Chen, Z. Y.; Bacsa, J.; Musaev, D. G.; Geletii, Y. V.; Lauinger, S. M.; Lian, T.; Hill, C. L. *J. Amer. Chem. Soc.* **2014**, *136*, 14015.
(45) Cavka, J. H.; Jakobsen, S.; Olsbye, U.; Guillou, N.; Lamberti, C.; Bordiga, S.; Lillerud, K. P. *J. Amer. Chem. Soc.* **2008**, *130*, 13850.
(46) Wardencki, W.; Orlita, J.; Namiesnik, J. *Fresen J. Anal. Chem.* **2001**, *369*, 661.
(47) Hatchard, C. G.; Parker, C. A. *Proc. R. Soc. Lon. Ser.-A* **1956**, *235*, 518.

CHAPTER 4 Self-Supporting Metal-Organic Layers as Single-Site Solid Catalysts

4.1. Introduction

As the majority of industrially used catalysts are heterogeneous, it is desirable to immobilize molecular catalysts onto porous solid supports that are compatible with industrial processes. Metal-organic frameworks (MOFs), porous solids assembled from organic ligands and metal coordination nodes, have provided a versatile platform for the immobilization of molecular catalysts.[1-9] However, their activity is often limited by the rates of diffusion of substrates and products within the frameworks.[10,11] Although many strategies have been devised to overcome the diffusion limitation of MOFs, such as elongating functional ligands[12] or diluting them with catalytically inactive spectator ligands to construct MOFs with larger channels and pores,[13] only moderate success has been achieved to date. MOFs constructed from elongated ligands tend to suffer from interpenetration as well as framework distortion, whereas MOFs built from mixed functional and spectator ligands have diminished atom efficiency. We surmised that this diffusional constraint can be relieved by reducing one dimension of the MOF crystals to only a few nanometers to minimize the diffusion distance. This dimensional reduction results in two-dimensional (2D) metal-organic layers (MOLs), a new category of 2D material. MOLs not only provide the benefit of readily accessible active sites in a thin layer but also inherit the heterogeneous nature, ordered structure, and molecular tunability of MOF catalysts.

2D coordination layers have been reported in the literature,[14] along with other prominent 2D materials such as graphenes and metal dichalcogenides.[15,16] 2D coordination layers were previously assembled on flat metal surfaces[17,18] or created at air/liquid or liquid/liquid interfaces by the Langmuir-Blodgett method.[19-21] However, these methods cannot produce sufficient quantities of self-supporting nano-sheets for catalytic applications. Recently, top-down chemical

or physical exfoliation has also been used to prepare nano-sheets from layered 3D MOFs.[22-24] In this chapter, I will discuss a highly scalable bottom-up strategy to assemble MOLs directly from molecular building blocks in one-pot solvothermal reactions. Importantly, the MOLs were functionalized with Fe catalytic centers to give diffusion-free single-site solid catalysts.

4.2. Results and Discussion

4.2.1. Synthesis and Characterizations of MOLs

Nanostructures with high surface energy such as MOLs can, in principle, be prepared in the presence of surfactants, which reduce surface energies through the hydrophobic protecting shell. However, this surfactant coating layer also blocks the catalytic sites.[25,26] Alternatively, high index face nanoparticles (with high surface energies) can be prepared by a supersaturation of crystallization.[27] This strategy can be rationalized by the Thomson-Gibbs equation,

$$\Delta\mu = \mu_l - \mu_c = \sigma S$$

which relates the difference between the chemical potentials ($\Delta\mu$) of the supersaturated solution species (μ_l) and the crystallized ones (μ_c) to additional surface energies of the crystallites (σS) as a result of energy conservation. We combined the two above strategies to create MOLs by (1) introducing small capping molecules that lessen the surface energy penalty without blocking the catalytic sites, and (2) creating a supersaturation of the building blocks in the MOL synthesis to tolerate additional surface energies as compared to bulk 3D-crystals.

The Hf^{4+} cluster $[Hf_6(\mu_3\text{-}O)_4(\mu_3\text{-}OH)_4(\text{carboxlyate})_{12}]$[28-30] was chosen for MOL synthesis because of the tendency of Hf to form stable coordination bonds with carboxylates. The 12-connectivity of the Hf_6 cluster, however, violates the geometric requirement of a 2D layer. We used a capping method to overcome the geometric mismatch. In this method, six of the

connection sites on the cluster were protected by formate groups, leaving the remaining six in the same plane to connect to the 1,3,5-Tris(4-carboxyphenyl)benzene (BTB) moieties. The 6-connected Hf_6 SBUs and the 3-connected BTB ligands link to each other to form an infinite 3,6-connected 2D network, **BTB-MOL**, with a $Hf_6(\mu_3\text{-O})_4(\mu_3\text{-OH})_4(HCO_2)_6(BTB)_2$ formula and kagome-dual (kgd) topology (**Figure 4-1**). The supersaturation of the SBUs was created by adding water to the reaction mixture to take advantage of the partial hydrolysis of Hf^{4+}: $6Hf^{4+} + 8H_2O + 6HCO_2H \rightarrow [Hf_6(\mu_3\text{-O})_4(\mu_3\text{-OH})_4(HCO_2)_6]^{6+} + 18H^+$. In addition, water also accelerates N,N-dimethylformamide (DMF) decomposition to generate dimethylamine that neutralizes the HCl generated from the reaction.
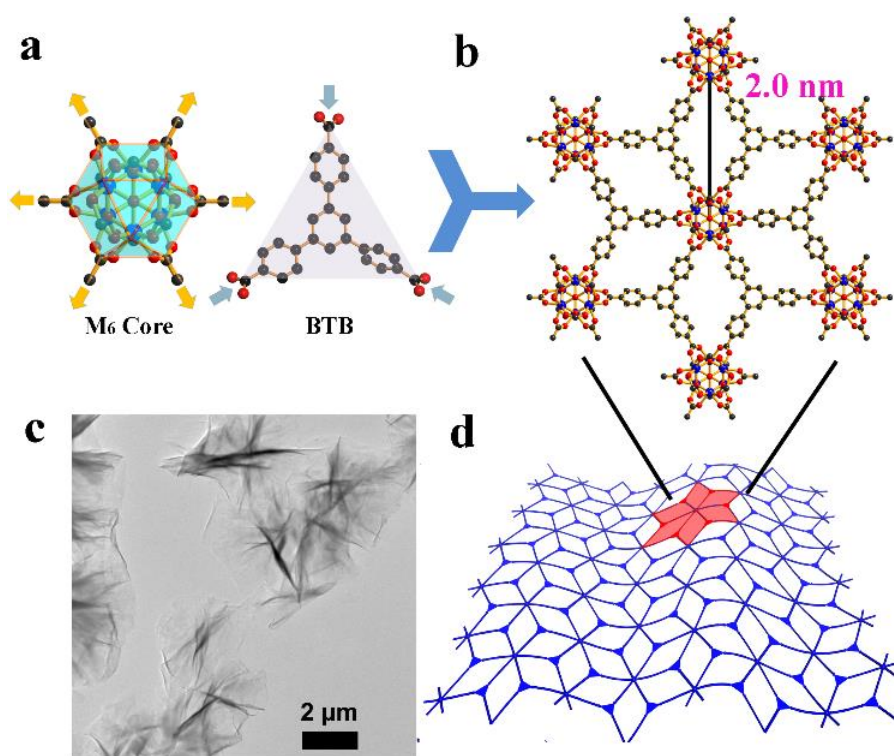
Figure 4-1. (a) The $[Hf_6O_4(OH)_4(HCO_2)_6(\text{carboxylate})_6]$ SBU in **BTB-MOL** with the connectivity indicated by golden arrows; structure of the BTB ligand with the connectivity featured by light blue arrows; (b) Formation of 2D kgd lattice from 6-connected SBUs and 3-

Figure 4-1, continued connected BTB ligands; Blue: Hf; black: C; red: O; (c) TEM image of nano-sheets of $Hf_6O_4(OH)_4(HCO_2)_6(BTB)_3$; (d) Structural representation of the ruffled sheet of kgd topology. Copyright 2016 John Wiley and Sons.

The synthetic conditions for **BTB-MOLs** were optimized by systematically exploring the parameter space. The addition of water is key to obtaining ultra-thin nano-sheets. As shown in **Figure 4-2**, with increasing amount of water added, the structure changed from 3D MOF to MOLs. Increasing the BTB concentration in the reaction also facilitates the formation of the nano-sheets, which highlights the importance of supersaturation. On the other hand, increasing formic acid concentration leads to the formation of bulk crystals, presumably by reducing the concentration of reactive SBUs (**Figure 4-3**). Knowing MOL assembly kinetics, we can fine-tune the thickness of the nano-sheets from bulk crystals to few-layers by adjusting the synthetic parameters. In these experiments, a mixture of $HfCl_4$ (14 mg) and H_3BTB (12.5 mg) was dissolved in a mixture of DMF, HCOOH, and water in pyrex vials, and kept at 120 ^{o}C for 2 days. White precipitates or crystals were obtained. Uniform **BTB-MOL** down to the monolayer thickness can be obtained using a reactant molar ratio of $HfCl_4$:BTB:HCOOH:H_2O:DMF=1.5:1:830:290:2280 by heating the mixture at 120 ^{o}C for 48 hours.
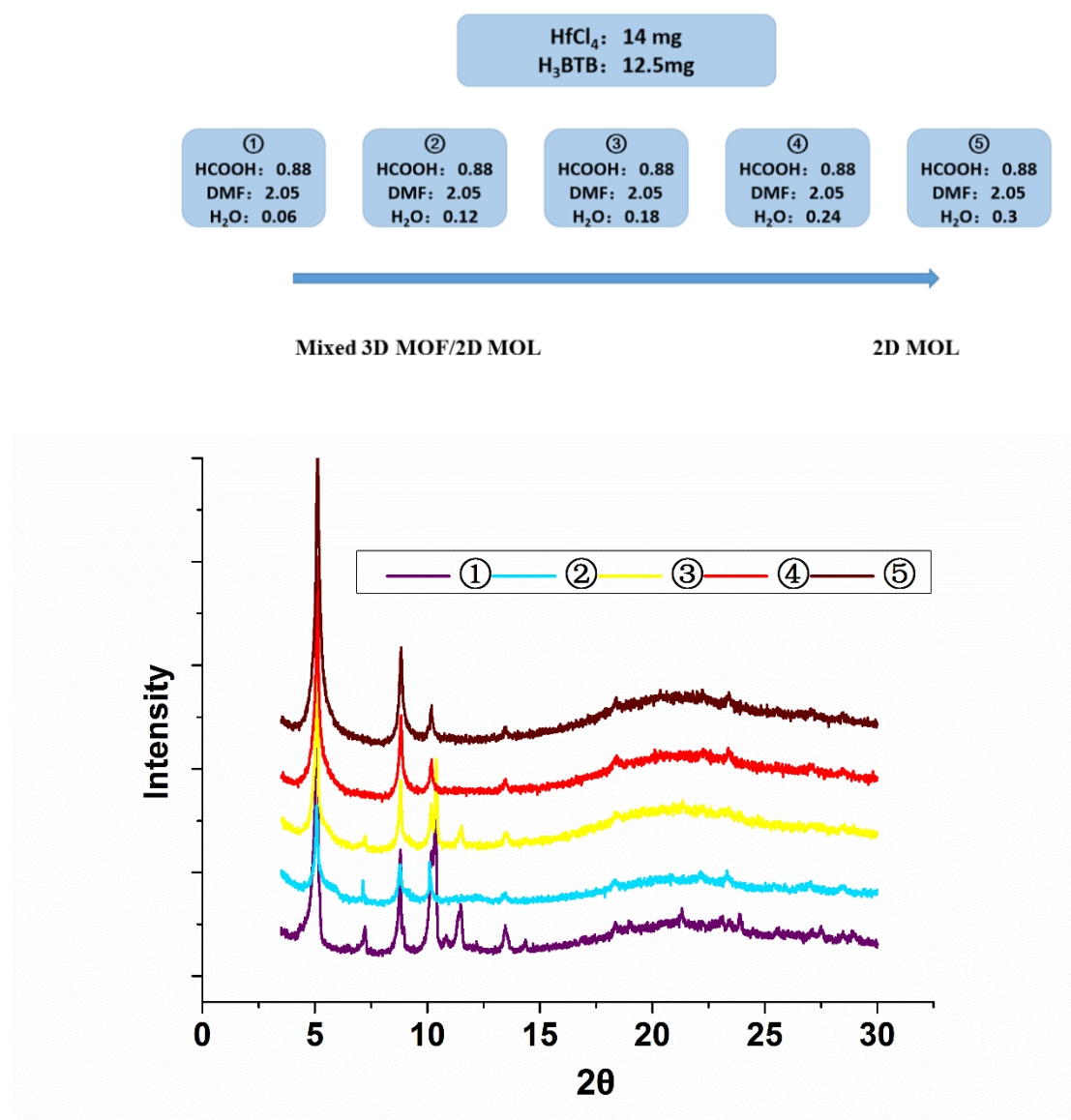
Figure 4-2. Top, formation of 3D MOF vs. 2D MOL as a function of the water amount in the solvothermal synthesis. Bottom, PXRD patterns of samples prepared with different solvent compositions (in mL) at 120 °C for 2 days. By increasing the amount of water, the sample changed from a mixture of 3D MOF and 2D MOL to pure 2D MOL. Copyright 2016 John Wiley and Sons.
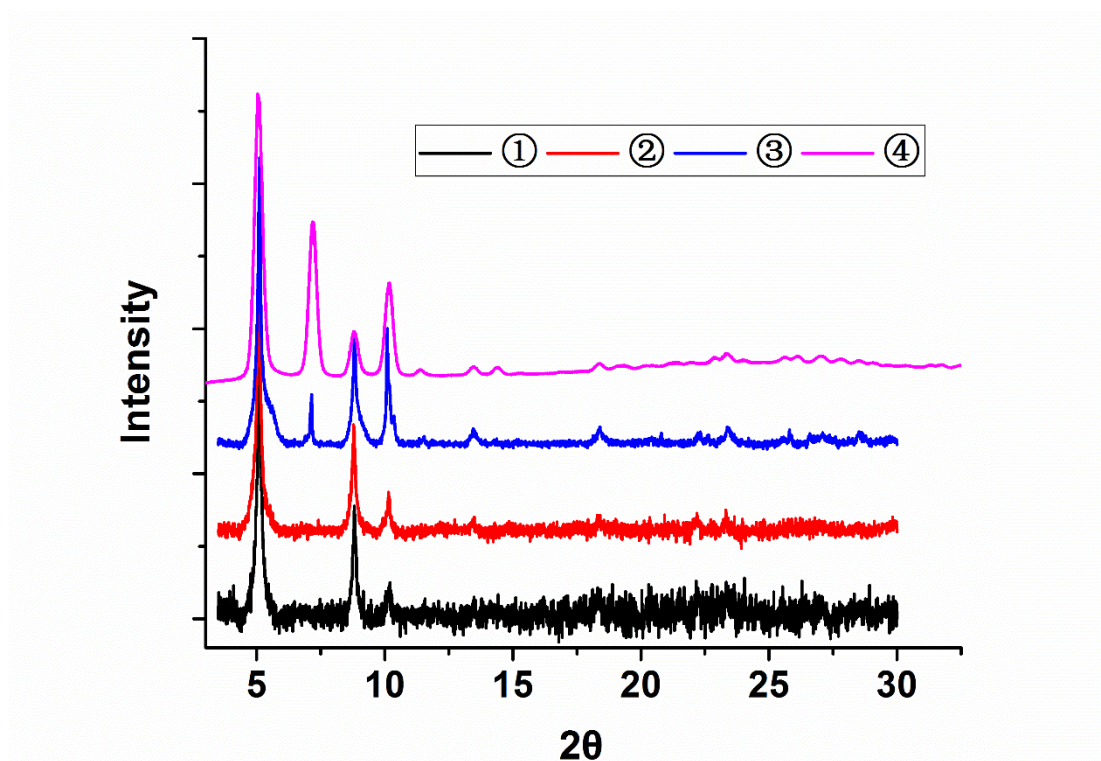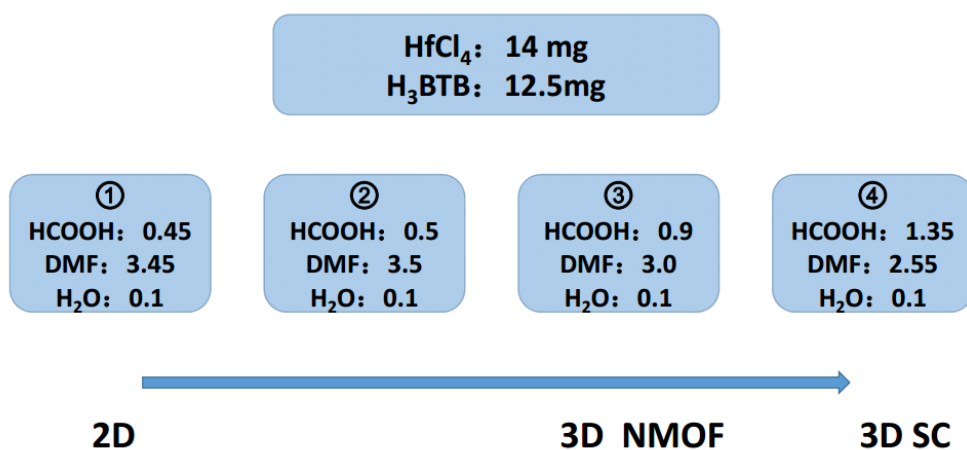
Figure 4-3. Top, formation of 2D MOL vs. 3D NMOF vs. single-crystalline 3D MOF as a function of solvent compositions in the solvothermal synthesis. Bottom, PXRD patterns of samples prepared with different solvent compositions (in mL) at 120 °C for 2 days. By increasing the amount of formic acid, the samples changed from a 2D MOL to 3D MOF. NMOF stands for nano-MOF and SC stands for single crystal. Copyright 2016 John Wiley and Sons.

TEM images showed wrinkled ultra-thin films of MOLs with an average sheet area of ~4 × 4 μm² (**Figure 4-1c**). The as-prepared MOLs were highly creased to minimize surface energy, resembling images of other 2D materials such as reduced graphene oxide (rGO).[31] PXRD patterns of the sample give only three broad intra-layer peaks, consistent with our modelled pattern of the MOLs with one or two layers (**Figure 4-4**). These nano-films also exhibit a high specific surface area of 661.7m²/g from the nitrogen adsorption measurement (**Figure 4-5**). The simulated surface area is 883 m²/g for the MOL monolayer using Materials Studio software. This small discrepancy is possibly due to the presence of a small percentage of bilayers and/or folding of monolayers in the sample.
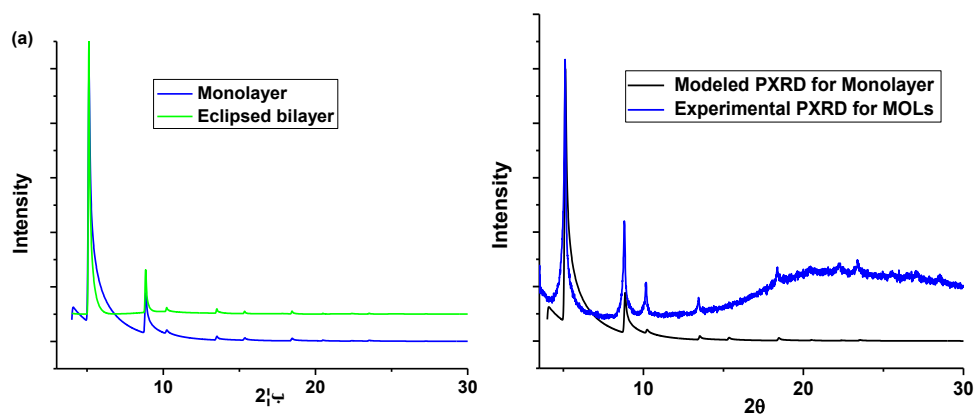
Figure 4-4. (a) Simulated PXRD patterns of monolayer and bilayer samples. (b) Comparison between the modelled monolayer PXRD and the experimental PXRD. Copyright 2016 John Wiley and Sons.
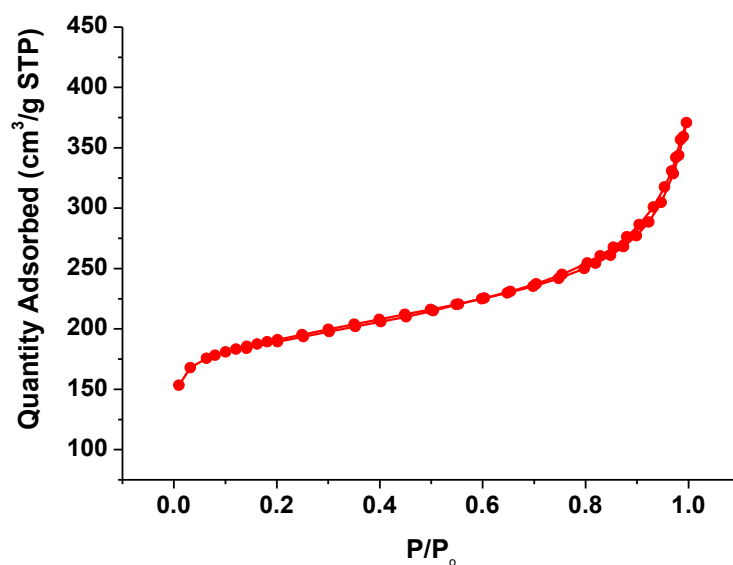
Figure 4-5. Nitrogen sorption measurements of **BTB-MOL**. Copyright 2016 John Wiley and Sons.

Atomic Force Microscopy (AFM) images of **BTB-MOL** gave monolayer thickness for many of the nano-sheets. The measured height of 1.2±0.2 nm (**Figure 4-6a, b**) is very close to the van der Waals size of the Hf_6 cluster. The edges of the measured monolayers were usually slightly higher than the middle part due to the wrinkling. Nano-sheets with thickness of 2.2±0.2 nm and 3.2±0.2 nm were also found (**Figure 4-7**), corresponding to bilayer and trilayer structures.
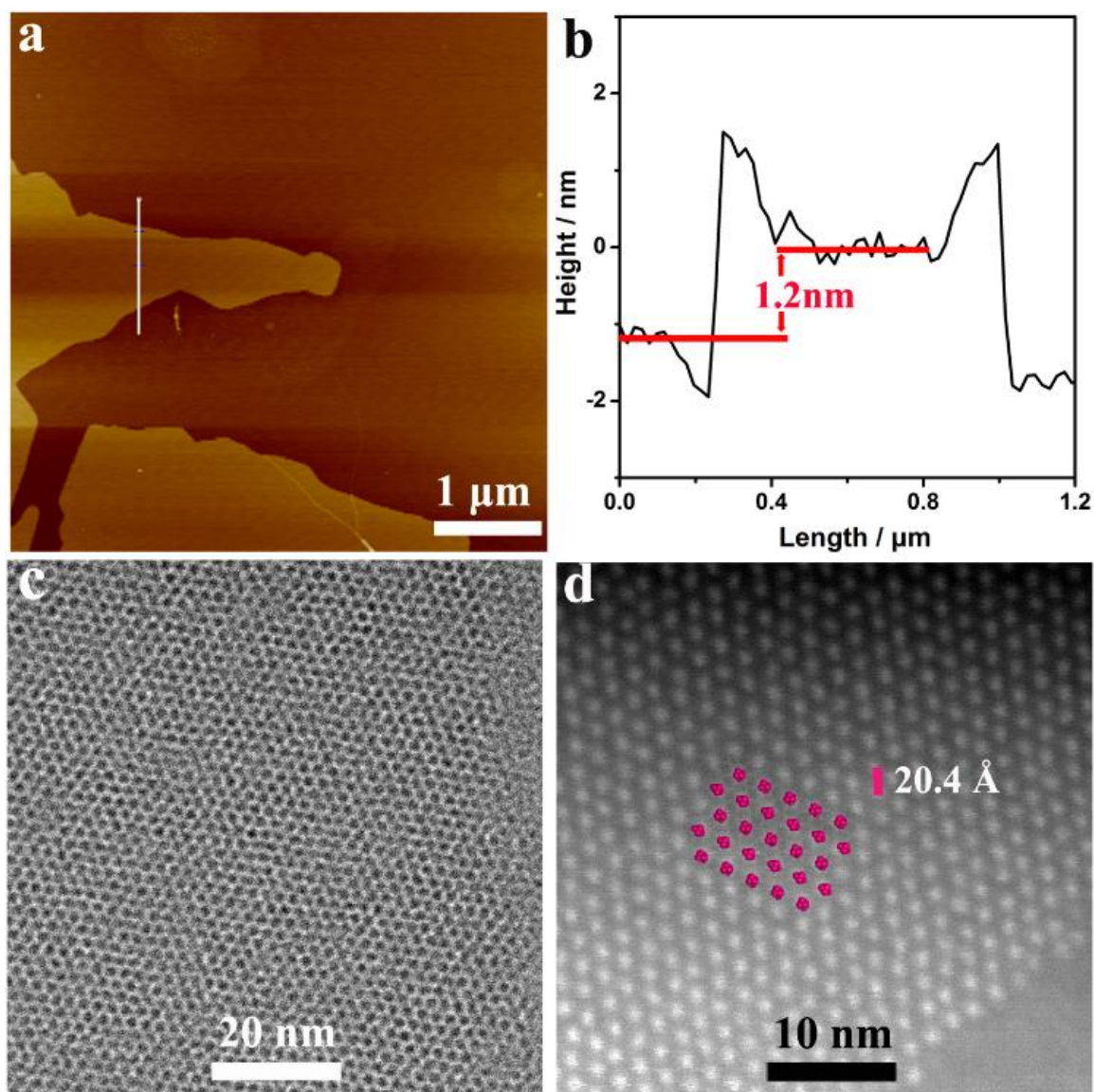
Figure 4-6. AFM images (a) tapping-mode AFM-topography, (b) the height profile along the white line in (a); (c) HRTEM images of MOLs. (d) HAADF images of **BTB-MOL**. Copyright 2016 John Wiley and Sons.
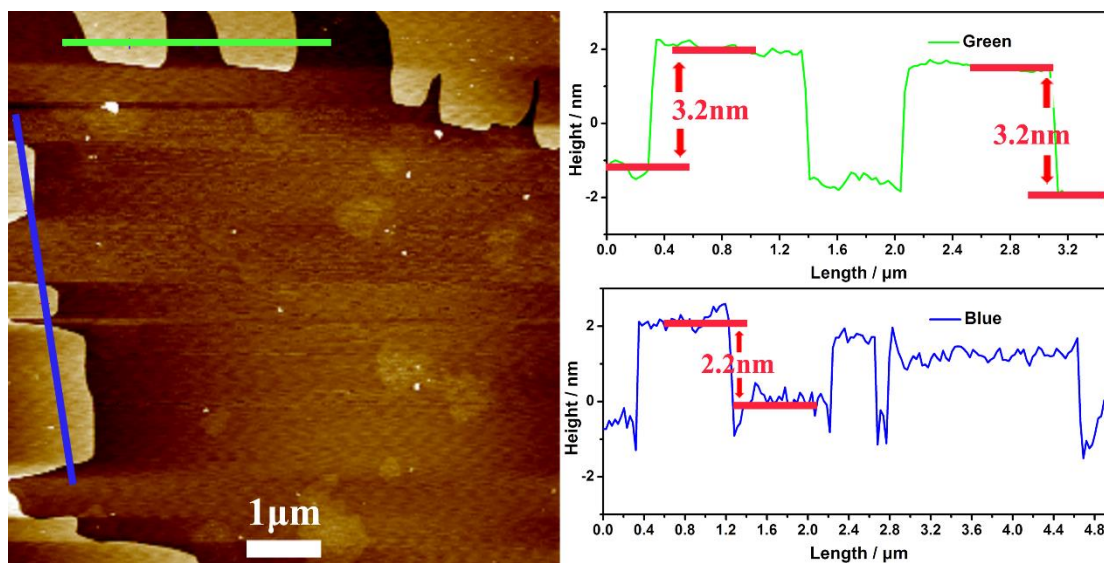
Figure 4-7 Tapping-mode AFM-topographic image (left) with its height profiles (right) showing thickness of trilayers (green line) and bilayers (blue line). Copyright 2016 John Wiley and Sons.

The chemical structures of the monolayer and stacked multilayers were surveyed by High Resolution Transmission Electron Microscopy (HRTEM) and Scanning Transmission Electron Microscopy (STEM). Direct imaging of MOF lattices has only been reported a few times in the literature.[32-34] The HRTEM images of **BTB-MOL** showed clear lattice fringes. The Hf_6 clusters appear as dark spots on the images as compared to the background and non-metallic atoms, consistent with a positive contrast (**Figure 4-6c**). In the High Angle Annular Dark Field (HAADF) images taken under STEM mode, clear 2D kgd nets with white spots representing the Hf_6 clusters were observed (**Figure 4-6d**). The arrangement of the spots matches our proposed atomic model of the kgd monolayer. The distances between adjacent spots on the HRTEM image (20.1 Å) and the STEM-HAADF image (20.4 Å) match that between two adjacent SBUs in the atomic model (20.02 Å). Besides the regular kgd lattice, we also observed a number of distorted lattices or complex lines, and even ripples, in HRTEM/STEM-HAADF images. These features were either due to tilted sample orientations or Moiré pattern of stacked layers (**Figure 4-8**).
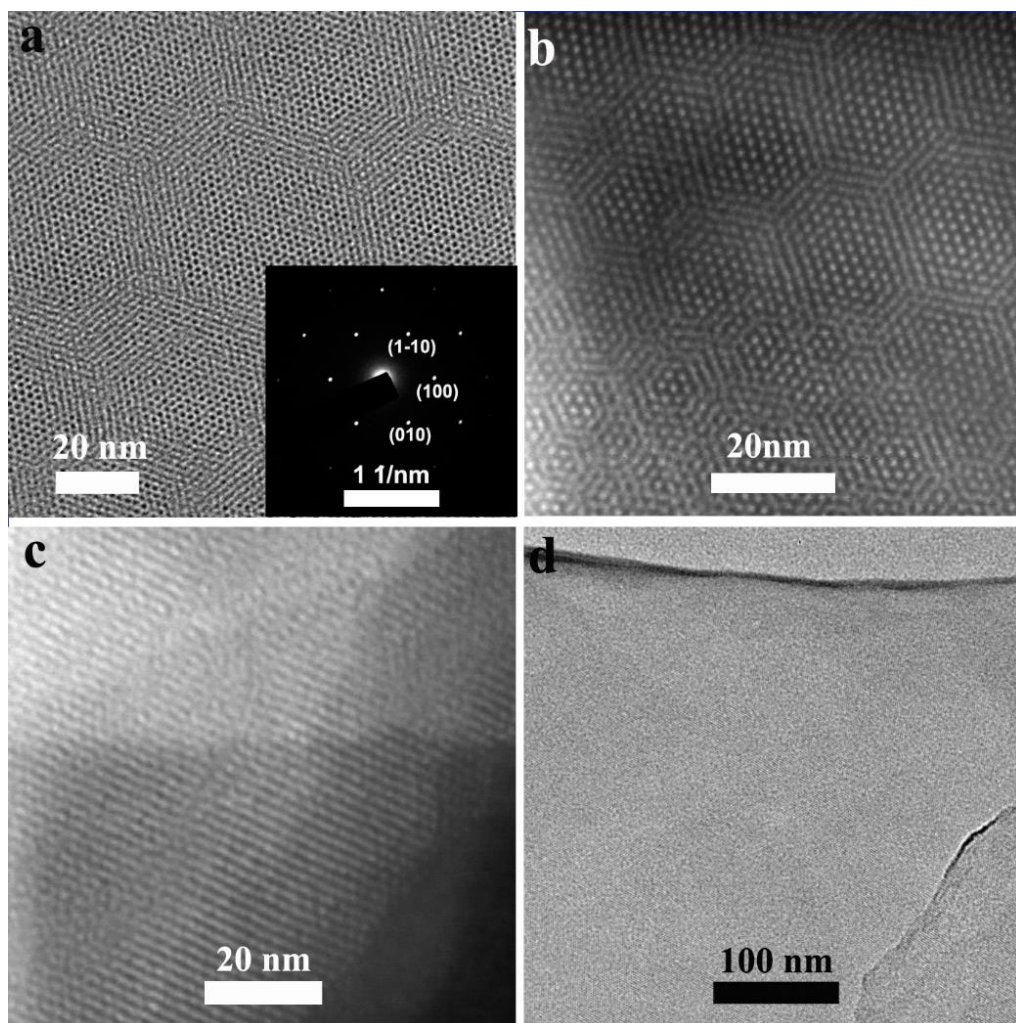
Figure 4-8 (a) HRTEM image of the MOLs and SAED pattern of the MOLs along [001] zone axis (inset); (b) STEM-HADDF image of stacked layers with Moiré pattern (c) STEM-HADDF image of tilted layer (d) TEM images of flat MOLs prepared from samples dispersed in n-hexane. Copyright 2016 John Wiley and Sons.

A 3D reciprocal lattice was reconstructed from the rotation electron diffraction (RED) data of **BTB-MOL** (**Figure 4-9**). The spots in the reciprocal space showed a hexagonal pattern along the c* axis perpendicular to the thin layer, consistent with the 2D kgd net (**Figure 4-9a**). This lattice could be indexed to a hexagonal unit-cell with a=19.4 Å, which corresponds well to our model within the experimental error. In directions parallel to the layers, streaks of diffraction

rods were observed (**Figure 4-9b, c**), which are characteristic of very thin films. These patterns match our simulated results for the monolayer (**Figure 4-10**).
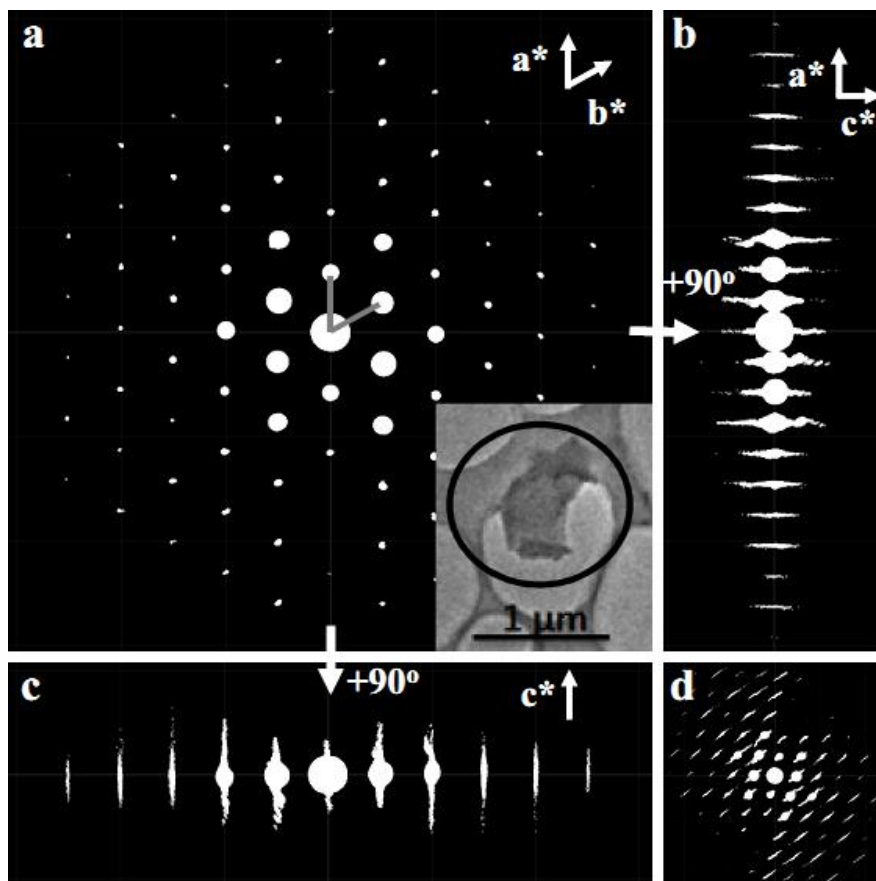
Figure 4-9. Reconstructed 3D reciprocal lattices from the RED data. (a) The reciprocal lattice along c* (perpendicular to the nano-sheet); (b) The reciprocal lattice from rotating (a) by 90 ° with respect to the vertical axis; (c) The reciprocal lattice from rotating (a) by 90 ° with respect to the horizontal axis; (d) Representative image of the 3D RED data. The inserted image in (a) is the TEM image of the selected nano-sheet. Copyright 2016 John Wiley and Sons.
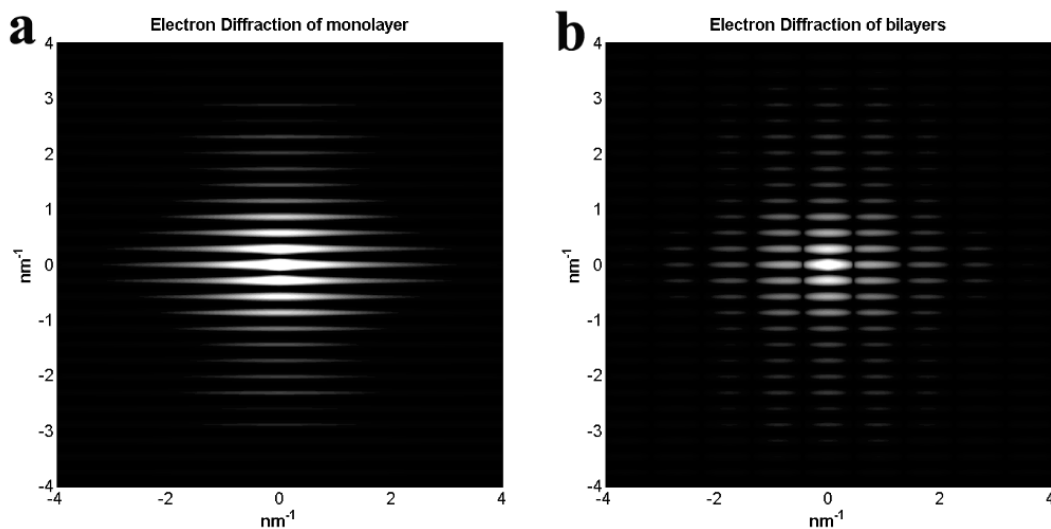
Figure 4-10. Simulated SAEDs parallel to the nano-sheets for monolayer and bilayer MOLs. Copyright 2016 John Wiley and Sons.

Consistent with our proposed structural model, we observed such layers in the X-ray structures of two closely related 3D single crystals (**Figure 4-11**).[35] Single crystals of a MOF with a framework formula of $Zr_6(\mu_3\text{-}O)_4(\mu_3\text{-}OH)_4(HCO_2)_6(BTB)_2$ (**Zr-BTB-MOF-1**) were obtained by us and others[29] using $ZrOCl_2 \cdot 8H_2O$ as the metal source. The same crystalline phase for Hf was also obtained (**BTB-MOF-1**). **Zr-BTB-MOF-1** contains the aforementioned 3,6-connected kgd layers (**Figure 4-11a**), which are interlocked within each other in two orthogonal directions to give the 3D structure (**Figure 4-11c**). Six formates terminate six connections on the Zr_6 SBUs as the capping ligands. In another crystal structure **Zr-BTB-MOF-2**, the same 2D kgd layers stack on each other in a staggered arrangement (**Figure 4-11b**). The same crystalline phase for Hf was also obtained (**BTB-MOF-2**). The observation of such layers as building blocks in the 3D crystal structures confirms the feasibility of our proposed atomic model for **BTB-MOL**.
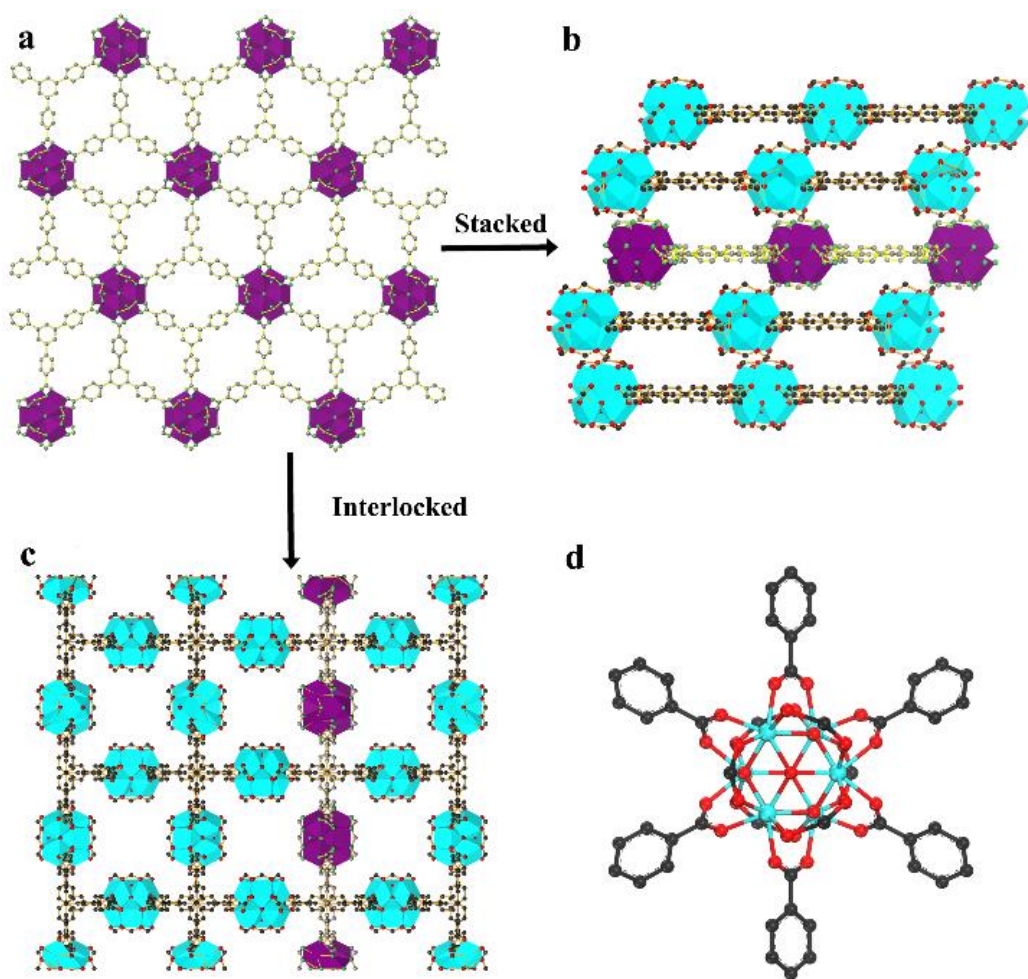
Figure 4-11. (a) Structure of a monolayer of **BTB-MOL**; (b) 3D crystal structure of the stacked layers in **BTB-MOF-2**; (c) 3D interlocked structure in **BTB-MOF-1**; (d) Structure of SBU. Copyright 2016 John Wiley and Sons.

Table 4-1. Crystal data and structure refinements for **Zr-BTB-MOF-1 and 2.**

Identification code	**Zr-BTB-MOF-1**	**Zr-BTB-MOF-2**
Empirical formula	$C_{30}H_{15}O_{18}Zr_3$	$C_{54}H_{32}O_{32}Zr_6$
Formula weight	1874.16	1740.16
Temperature/K	100(2)	100(2)
Crystal system	Tetragonal	Monoclinic
Space group	$I4_1/amd$	$C2/m$

Table 4-1, continued

a/Å	34.539(2)	20.274(7)
b/Å	34.539(2)	34.841(11)
c/Å	20.303(2)	16.008(8)
α/°	90.00	90.00
β/°	90.00	106.170(13)
γ/°	90.00	90.00
Volume/Å^3	24220(4)	10860(7)
Z	8	4
ρ_{calc}g/cm^3	1.028	1.045
μ/mm^{-1}	0.734	0.817
F(000)	7344.0	3280.0
Crystal size/mm^3	0.05× 0.1 × 0.1	0.2× 0.2 × 0.05
Radiation	λ = 0.41328	λ = 0.41328
2Theta range for data collection/°	1.38 to 25.42	1.36 to 26.2
Index ranges	-36 ≤ h ≤ 36	-20 ≤ h ≤ 19
	-36 ≤ k ≤ 36	0≤ k ≤ 38
	-20 ≤ l ≤ 21	0≤ l ≤ 17
Reflections collected	100562	6868
Independent reflections	3991 [R_{int} = 0.1837, R_{sigma} = 0.0648]	6868 [R_{int} = 0.0000, R_{sigma} =0.2709]
Data/restraints/parameters	3991/1/231	6869/51/262
Goodness-of-fit on F^2	1.125	1.067
Final R indexes [I>=2σ (I)]	R_1 = 0.0603, wR_2 = 0.1529	R_1 = 0.1399, wR_2 =0.3487
Final R indexes [all data]	R_1 = 0.0927, wR_2 = 0.1664	R_1 = 0.2060, wR_2 =0.3842
Largest diff. peak/hole / e Å^{-3}	0.89/-0.58	2.21/-2.22

X-ray absorption spectroscopy was used to further characterize the Hf$_6$ SBU in **BTB-MOL**. Fourier-transformed EXAFS profiles of **BTB-MOL** were very similar to that of **BTB-**

MOF-1, confirming a common SBU for the two structures. EXAFS fitting showed that Hf^{4+} adopts octa-coordination with oxygens in the SBU, with Hf-(μ_3-O) distances of 2.26±0.01 Å, Hf-(μ_3-OH) distances of 2.30±0.01 Å, and Hf-O (carboxylate) distances of 2.12±0.01 Å (**Figure 4-12, Table 4-2**). We have ascertained and quantified the formate capping ligands by EXAFS and NMR spectroscopy. First, fitting the EXAFS data to the secondary sphere of Hf^{4+} gives Hf-C(BTB) distances of 3.15±0.03 Å and Hf-C (Formate) distances of 3.22±0.03 Å, which correspond to six formates as the capping groups and six carboxylates from the BTB ligands (**Figure 4-12, Table 4-2**). Second, the ^{1}H-NMR spectrum of the digested MOLs gives a molar ratio of formate:BTB = 3:1 (**Figure 4-13**), which matches the one expected for the formate-capped structure.
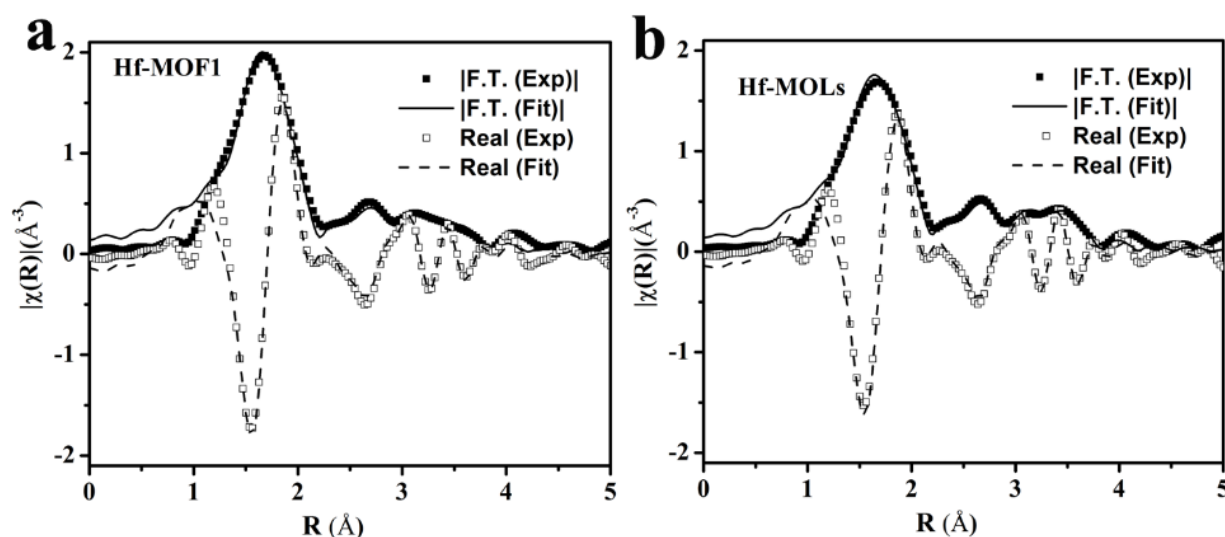
Figure 4-12. Fourier-transformed EXAFS spectra of **BTB-MOF-1** (a) and **BTB-MOL** (b). The absolute magnitudes and their fittings are shown in solid squares and solid lines, respectively, and the real components and their fittings are shown in hollow squares and dash. Copyright 2016 John Wiley and Sons.

Table 4-2. Summary of EXAFS fitting parameters for **BTB-MOF-1** and **BTB-MOL**.

Sample	BTB-MOF-1	BTB-MOL
Fitting range	k 1.50 – 11.30 Å^{-1}	k 1.50 – 11.30 Å^{-1}
	R 1.25 – 4.75 Å	R 1.25 – 4.75 Å
Independent points	21	21
Variables	13	13
Reduced chi-square	336.55.26	2595.5
R-factor	0.017	0.017
S_0^2	1.005± 0.001	1.050± 0.002
ΔE_0(eV)	6.19±0.80	6.56±0.87
R (Hf-O1) (Å)	2.26±0.01	2.26±0.01
σ^2 (Hf-O1) (Å^2)	0.002±0.002	0.001±0.001
R (Hf-O2) (Å)	2.30±0.01	2.30±0.01
σ^2 (Hf-O2) (Å^2)	0.002±0.002	0.001±0.001
R (Hf-O3) (Å)	2.12±0.01	2.13±0.01
σ^2 (Hf-O3) (Å^2)	0.003±0.002	0.001±0.001
R (Hf-C1) (Å)	3.15±0.03	3.16±0.04
σ^2 (Hf-C1) (Å^2)	0.002±0.004	0.003±0.006
R (Hf-C2) (Å)	3.22±0.03	3.23±0.04
σ^2 (Hf-C2) (Å^2)	0.002±0.004	0.003±0.006
R (Hf-Hf1) (Å)	3.52±0.04	3.55±0.08
σ^2 (Hf-Hf1) (Å^2)	0.006±0.002	0.008±0.010
R (Hf-O4) (Å)	3.74±0.13	3.74±0.18
σ^2 (Hf-O4) (Å^2)	0.003±0.002	0.001±0.001
R (Hf-O5) (Å)	3.81±0.13	3.82±0.18
σ^2 (Hf-O5) (Å^2)	0.003±0.002	0.001±0.001

Table 4-2, continued

R (Hf-O6) (Å)	4.04±0.13	4.05±0.18
σ^2 (Hf-O6) (Å^2)	0.003±0.002	0.001±0.001
R (Hf-O7) (Å)	4.15±0.14	4.10±0.40
σ^2 (Hf-O7) (Å^2)	0.018±0.023	0.040±0.064
R (Hf-O8) (Å)	4.22±0.14	4.18±0.40
σ^2 (Hf-O8) (Å^2)	0.018±0.023	0.040±0.064
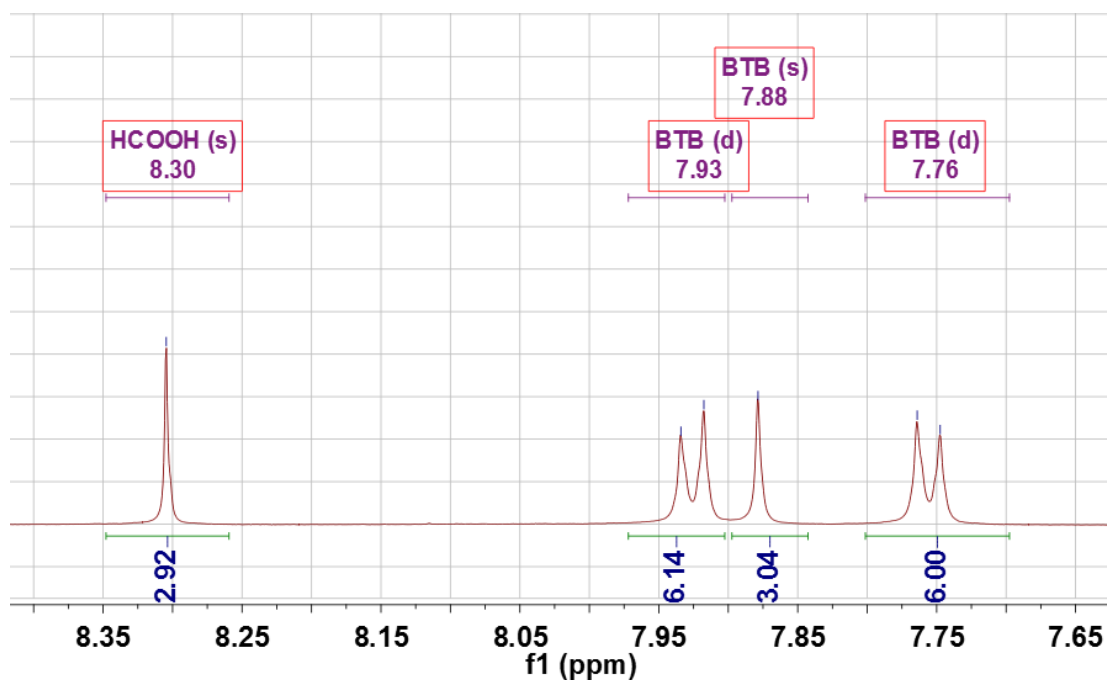
Figure 4-13. ^{1}H NMR spectra of digested **BTB-MOL** in d[6]-DMSO. A ratio of n(HCOOH): n(BTB)=3:1 was obtained from the integrations. Copyright 2016 John Wiley and Sons.

4.2.2. Fe-mTPY-MOL Catalyzed Hydrosilylation of Olefins.

The MOLs were doped with the terpyridine-based TPY ligand by taking advantage of the matching shape and size between TPY and BTB (**Figure 4-14**). The resultant **mTPY-MOL** with 30% TPY (**Figure 4-15**, based on total tridentate ligands) was metalated with FeBr$_2$ (1.05 eq

w.r.t TPY) and activated by NaEt₃BH. The final **Fe-mTPY-MOL** catalyst contains 100% of Fe with respect to TPY as determined by ICP-MS. PXRD (**Figure 4-16**) and TEM (**Figure 4-14**) studies confirmed that the **Fe-mTPY-MOL** catalyst adopts the same nano-sheet structure as the undoped MOL. As control samples, the 3D interlocked **mTPY-MOF-1** and 3D stacked **mTPY-MOF-2** were also doped with the TPY ligand (**Figure 4-17**), metalated with FeBr₂, and treated with NaBHEt₃ to give **Fe-mTPY-MOF-1** and **Fe-mTPY-MOF-2**. The homogeneous control sample **Homo-Fe-tpy** was prepared by mixing equal amounts of 2,2':6',2''-terpyridine and FeBr₂ in THF, followed by reduction with NaEt₃BH.
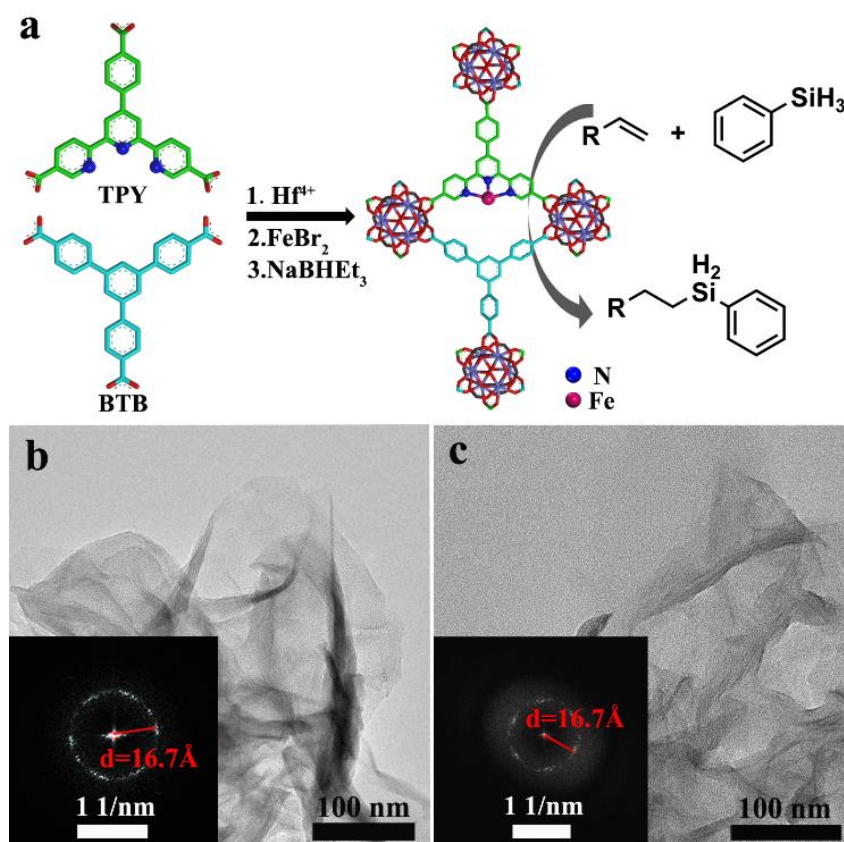
Figure 4-14. (a) Preparation of the MOL catalyst, **Fe-mTPY-MOL**; HRTEM and FFT images of **Fe-mTPY-MOL** before (b) and after catalysis (c). Copyright 2016 John Wiley and Sons.
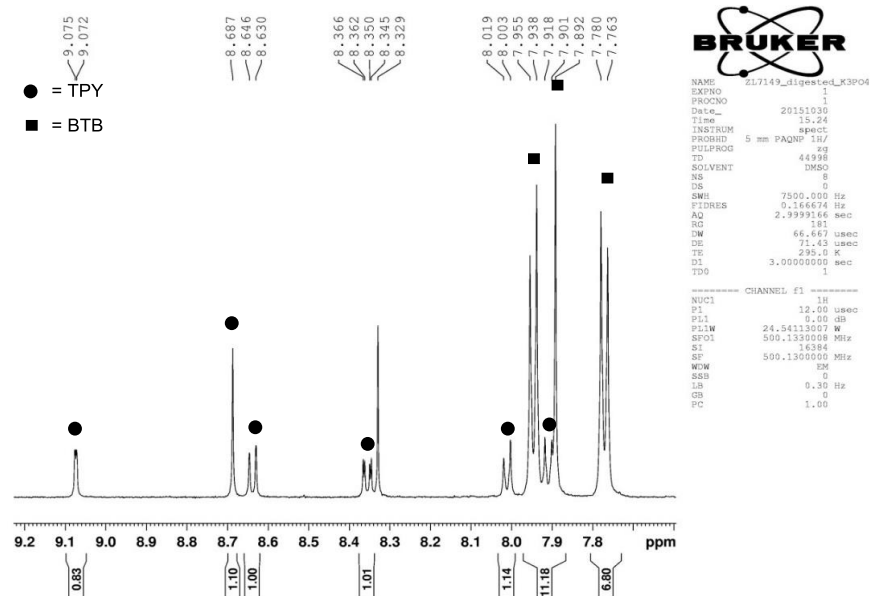
Figure 4-15. ^{1}H-NMR spectrum of digested **mTPY-MOL**. Copyright 2016 John Wiley and Sons.
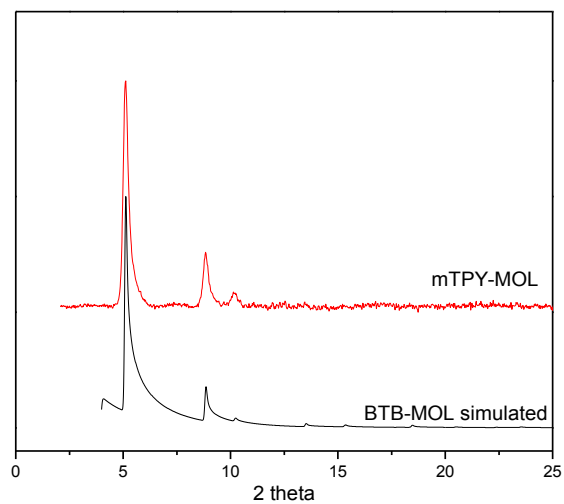
Figure 4-16. PXRD pattern of **mTPY-MOL**. Copyright 2016 John Wiley and Sons.
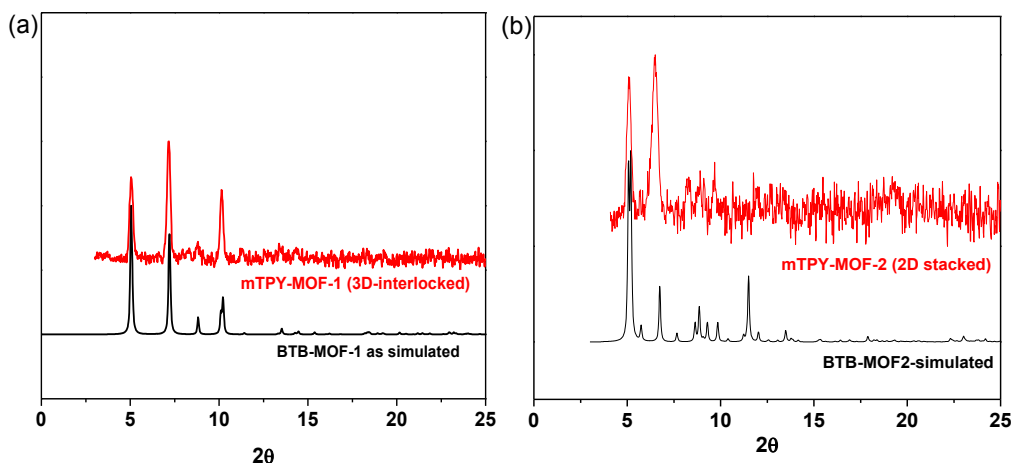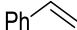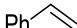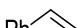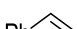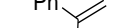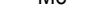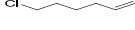
Figure 4-17. PXRD pattern of **mTPY-MOF-1** (a) and **mTPY-MOF-2** (b). Copyright 2016 John Wiley and Sons.

We rationalized that MOLs might provide a sterically protective environment to endow Fe-TPY catalytic activity for hydrosilylation of olefins.[36] At a 0.02% catalyst loading, **Fe-mTPY-MOL** catalyzed styrene hydrosilylation to afford pure anti-Markovnikov product in complete conversion in 48 hours (**Table 4-3**, entry1), corresponding to a turnover number (TON) of >5000. In contrast, no conversion was observed for the MOF with interlocked 3D structure, **Fe-mTPY-MOF-1** (**Table 4-3**, entry 2), and only 30% product was obtained for the **Fe-mTPY-MOF-2** with a stacked 3D structure (**Table 4-3**, entry 3). The zero or low activity of MOF catalysts can be attributed to the limited diffusion rates of the substrates and product in MOF channels, highlighting the advantage of MOLs vs. traditional MOFs as heterogeneous molecular catalysts owing to the relief from diffusional constraint. **Fe-mTPY-MOL** was separated from the reaction mixture by centrifugation, and reused 4 times without loss of activity (**Figure 4-18**). The heterogeneous nature of the catalysis was confirmed by the lack of activity for the reaction supernatant after removing MOLs by centrifugation. (**Figure 4-19**).

131

Table 4-3. MOLs loaded with Fe catalytic centers for hydrosilyation of terminal olefins
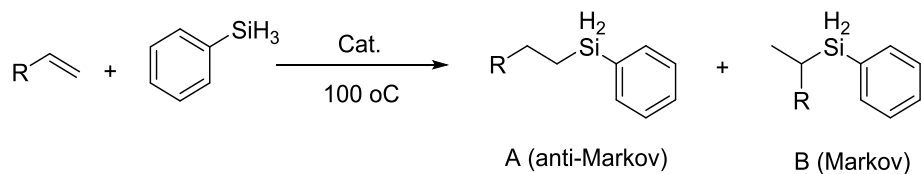
Entry	Olefin	Cat.	Cat. Loading (mol %)	Time	Yield (%)[a] A:B
1	Ph⟋	**Fe-mTPY-MOL**	0.02	2 d	100 : 0
2	Ph⟋	**Fe-mTPY-MOF-1**	0.02	6 d	0
3	Ph⟋	**Fe-mTPY-MOF-2**	0.02	2 d	30:0
4	Ph⟋	**Homo-Fe-tpy**	0.1	2 d	3:43
5	⟋⟋⟋⟋	**Fe-mTPY-MOL**	0.02	2 d	100 : 0
6	Ph / Me	**Fe-mTPY-MOL**	0.2	1 d	95 : 0
7	Cl⟋⟋⟋	**Fe-mTPY-MOL**	0.2	2 d	96 : 0
8	Ph⟋⟋	**Fe-mTPY-MOL**	0.2	2 d	90 : 0
9[b]	⟋⟋⟋⟋	**Fe-mTPY-MOL**	0.2	1 d	100 : 0
10[c]	⟋⟋⟋⟋	**Fe-mTPY-MOL**	0.2	4 d	85 : 0

[a] Entry 1-8 yields were determined by ^{1}H NMR with mesitylene as an internal standard; entry 9 and 10 yields were determined by GC-MS; [b] reaction was performed at 70°C, with Et_2SiH_2 as the silane; [c] reaction was performed at 100°C, with Ph_2SiH_2 as the silane.
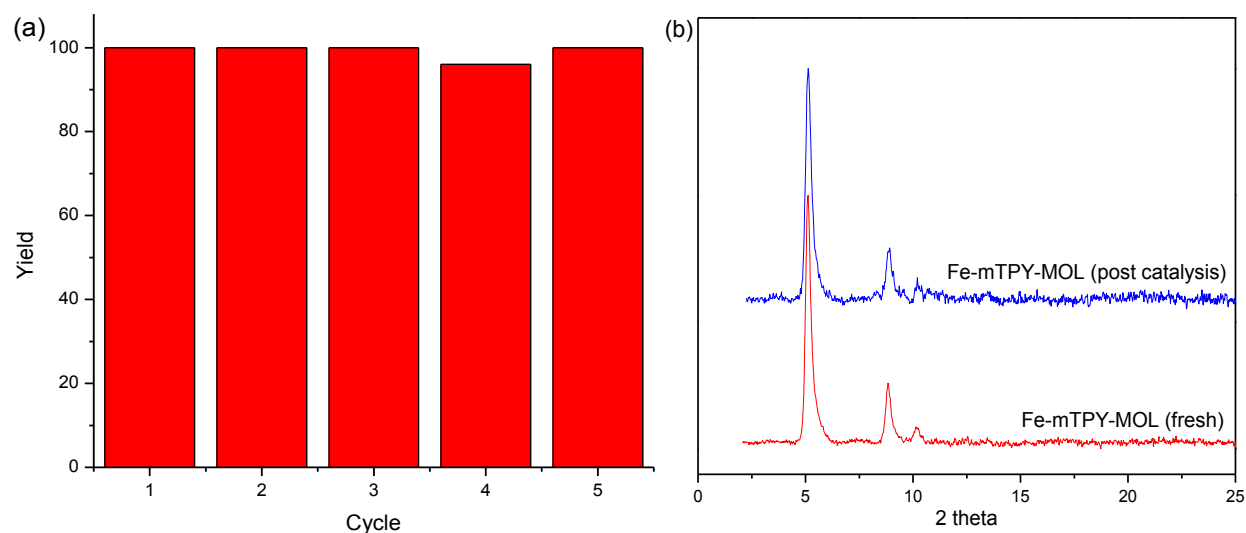
Figure 4-18. (a) Recycle and reuse of **Fe-mTPY-MOL** (0.1 mol % Fe): plot of yield (%) at various runs in the hydrosilylation of styrene with phenylsilane; (b) PXRD pattern of **Fe-mTPY-MOL** before and after hydrosilylation catalysis. Copyright 2016 John Wiley and Sons.
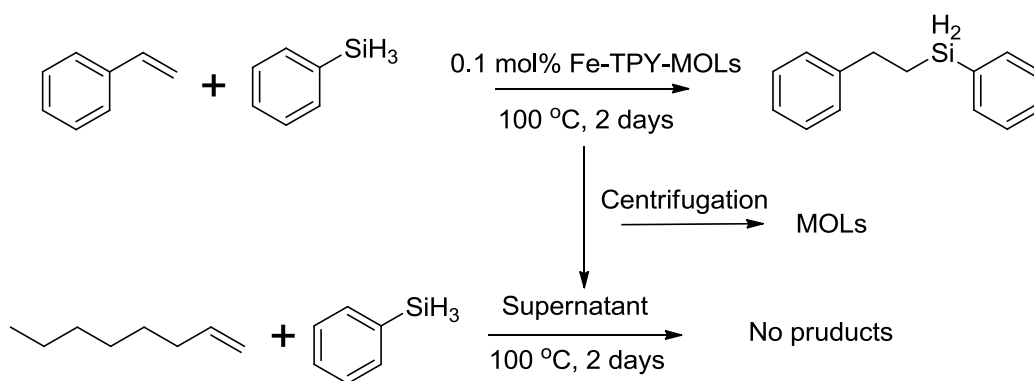
Figure 4-19. Experimental design to show the heterogeneous nature of MOL catalysis. Copyright 2016 John Wiley and Sons.

The substrate scope was also explored (**Table 4-3**, Entry 5 - 10). Interestingly, **Fe-mTPY-MOL** gave pure anti-Markov products for all the substrates while the "homogeneous" counterpart **Homo-Fe-tpy** had a selectivity towards the Markov product and exhibited ~10 times lower activity (**Table 4-3**, entry 4). It is likely that **Homo-Fe-tpy** decomposed under catalytic

133

conditions to afford Fe(0) nanoparticles that act as a less effective catalyst for hydrosilylation reactions with selectivity for the Markovnikov product. These results indicate that the MOL-immobilized Fe-TPY species can act as true molecular catalysts by preventing bimolecular disproportionation through site-isolation in MOLs.

4.3. Conclusion

We have developed a scalable bottom-up strategy for synthesizing stable MOLs with the thinness of a single monolayer in one-pot solvothermal reactions. We have shown that MOL catalysts significantly outperform traditional MOFs in activity by removing diffusional constraints of substrates and products. This work promises to open up a new class of 2D coordination materials with molecular functionalities for innovative applications.

4.4. Materials and Experimental Details

4.4.1. General Experimental

Reagents were commercially available and used without further purification unless otherwise indicated. 1-octene, styrene, and α-methylstyrene were distilled and then dried over freshly activated 4 Å molecular sieves prior to use. Thermogravimetric analysis (TGA) was performed in air using a Shimadzu TGA-50 equipped with an alumina pan and heated at a rate of 5°C per minute. The powder X-ray diffraction data were collected on Agilent SuperNova, Rigaku, and Bruker D8 Venture diffractometers using Cu Kα radiation sources (λ = 1.54178 Å). Nitrogen adsorption experiments were performed on a Micrometrics TriStar II 3020. Electron microscopy images were obtained on a Tecnai F20 and JEOL 2100 High Resolution Transmission Electron Microscopy. Three-dimensional electron diffractions were collected by using RED (rotation electron diffraction) data collection program on a JEOL JEM-2100 electron microscope. The collecting angle started from -29.8 ° till +40 °. The goniometer tilt step is 2 °,

and the beam tilt step is 0.2 °, with the beam tilt range of ± 1.0 °. In total, 385 frames were recorded for 3D reciprocal diffraction data reconstruction. AFM images were taken on a Bruker Multimode Ⅴ. Single crystal X-ray diffraction was collected with a Bruker APEX II CCD-based detector at ChemMatCARS (Sector 15), Advanced Photon Source (APS). ^{1}H NMR spectra were recorded on a Bruker NMR 500 DRX spectrometer at 500 MHz and a Bruker 400 MHz DRX spectrometer and referenced to the proton resonance resulting from incomplete deuteration of the CDCl$_3$ (δ 7.26) or DMSO-d^6 (δ 2.50). ICP-MS data were obtained with an Agilent 7700x ICP-MS and analyzed using ICP-MS MassHunter version B01.03. Samples were diluted in a 2% HNO$_3$ matrix and analyzed with a 159Tb internal standard against a 12-point standard curve over the range from 0.1 ppb to 500 ppb. The correlation coefficient was > 0.9997 for all analyses of interest. Data collection was performed in Spectrum Mode with five replicates per sample and 100 sweeps per replicate.

4.4.2. Synthesis and Characterization of Ligand.

4.4.2.1. Synthesis of 1-(5-methylpyridin-2-yl)ethanone.
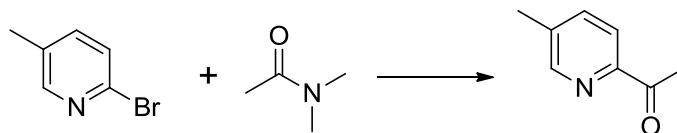
2-bromo-5-methylpyridine (8.60 g, 50.0 mmol) was dissolved in 100mL of dry Et$_2$O and cooled to -78 °C. n-BuLi (20 mL, 2,5M in hexene) was added dropwise over 30 mins. The mixture was stirred at -78 °C for 90 mins before dimethylacetamide (5 mL) was added dropwise and stirred for another 3 hours. Sat. NH$_4$Cl (aq.) was added to quench the reaction. The aqueous layer was washed with Et$_2$O a couple of times and all the organic parts were combined, dried over anhydrous Na$_2$SO$_4$, and filtered. After evaporation of the solvent, the residue was subjected

to flash column chromatography on silica gel (10:90 EtOAc/CH2Cl2 as eluent), affording 1-(5-methylpyridin-2-yl)ethanone (4.86 g, 36.0 mmol, 72.0% yield) as colorless oil. ^{1}H NMR (500 MHz, CDCl$_3$): δ 8.50 (s, 1 H), 7.95 (d, 1 H, J = 8.0 Hz), 6.21 (m, 1 H), 2.70 (s, 3 H), 2.42 (s, 3 H).

4.4.2.2. Synthesis of 4-(5,5''-dimethyl-[2,2':6',2''-terpyridin]-4'-yl)benzoic acid.
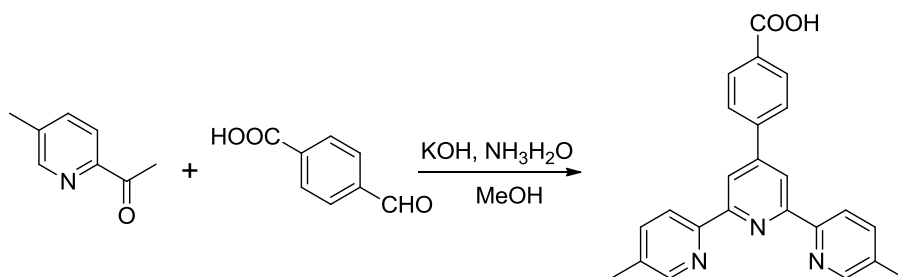
1-(5-methylpyridin-2-yl)ethanone (3.30 g, 24.4 mmol) and 4-Carboxybenzaldehyde (1.83 g, 12.2 mmol) were dissolved in MeOH (100 mL), followed by the addition of 15% KOH aqueous solution (110 mL) and NH$_3$·H2O (12.2 mL). The reaction mixture was stirred at room temperature for 3 days. The precipitate was separated via filtration, washed with CHCl$_3$ three times and dissolved in MeOH/H$_2$O (1:1). 1M HCl was added to adjust the pH to 3 to afford white precipitate, which was collected via filtration and washed with water. This procedure produced 4-(5,5''-dimethyl-[2,2':6',2''-terpyridin]-4'-yl)benzoic acid (3.26 g, 17.1 mmol, 70% yield). 1H NMR (500 MHz, DMSO-d^6) δ 8.75 (s, 2 H), 8.66 (m, 4 H), 8.16 (d, 2 H, J = 8.0 Hz), 8.09 (d, 2 H, J = 8.0 Hz), 7.95 (d, 2 H, J = 7.0 Hz), and 2.45 (s, 6 H).

4.4.2.3. Synthesis of 4'-(4-carboxyphenyl)-[2,2':6',2''-terpyridine]-5,5''-dicarboxylic acid (H₃TPY).
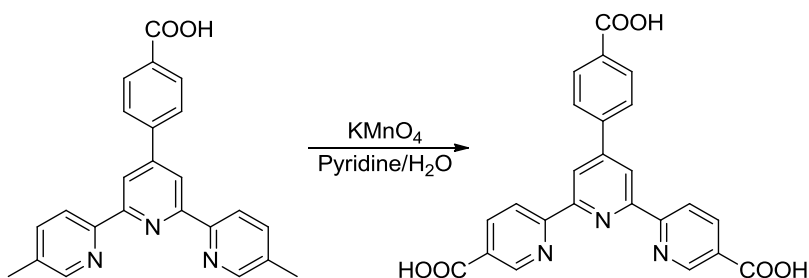
4-(5,5''-dimethyl-[2,2':6',2''-terpyridin]-4'-yl)benzoic acid (1.00 g, 2.62 mmol) was dissolved in pyridine/H_2O (3:1, 80 mL), followed by the addition of $KMnO_4$, (5.00 g, 31.6 mmol). The reaction mixture was heated at 100 ℃ overnight. More $KMnO_4$ (2.50 g, 15.8 mmol) was added into the reaction mixture to ensure complete oxidation. After refluxing for another day, the reaction mixture was cooled to room temperature, added with EtOH to react with residue $KMnO_4$, and filtered. The filtrate was put into a rotovap to remove most of the solvent. 1M HCl was added to the filtrate to adjust the pH to 3. White precipitates were collected via filtration, washed tremendously with water, and dried in vacuo to afford 4'-(4-carboxyphenyl)-[2,2':6',2''-terpyridine]-5,5''-dicarboxylic acid (1.04 g, 2.36 mmol, 90% yield). 1H NMR (500 MHz, DMSO-d⁶) δ 13.42 (br, 3 H), 9.25 (s, 2 H), 8.87 (s, 2 H), 8.82 (d, 2 H, J = 8.0 Hz), 8.52 (m, 2 H), 8.16 (d, 2 H, J = 8.0 Hz), and 8.10 (d, 2 H, J = 8.0 Hz).

4.4.3. Synthesis and Characterization of MOLs and MOFs

4.4.3.1. Synthesis of BTB-MOL

$HfCl_4$ (14mg) and H_3BTB (12.5mg) in a solvent mixture of DMF/HCOOH/H_2O (5mL/0.88mL/0.12mL) were sealed in a vial, stirred for a few minutes, and then placed in an oven at 120 ℃ for 3 days. The resulting solid was isolated by centrifugation, and washed with DMF and EtOH.

4.4.3.2. Synthesis of BTB-MOF-1

A mixture of $HfOCl_2 \cdot 8H_2O$ (61 mg) and H_3BTB (65 mg) was dissolved in a mixture of DMF (7.5 mL) and HCOOH (4.5mL) in a Teflon-lined autoclave, and kept at 120 °C for 3 days. Needle-like single crystals were obtained.

4.4.3.3. Synthesis of BTB-MOF-2

$HfOCl_2$ (81.8 mg), H_3BTB (22.0 mg) and benzoic acid (1.2 g) in 4 mL DEF were sealed in a vial, stirred for a few minutes, and then placed in an oven at 120 °C for 3 days. The resulting solid was isolated by centrifugation and washed with DMF and EtOH.

4.4.3.4. Synthesis of mTPY-MOL

$HfCl_4$ (14.0 mg), H_3TPY(6.0 mg), and H_3BTB (6.5mg) in a solvent mixture of DMF/HCOOH(distilled)/H_2O (5 mL/0.9 mL/0.1 mL) were sealed in a vial, sonicated for a few minutes, then placed in an oven at 120 °C for 3 days. The resulting solid was isolated by centrifugation, washed with DMF, DMSO, and acetone. **mTPY-MOL** were digested with sat. K_3PO_4/D_2O, extracted with DMSO-d_6 and analyzed by ^1H NMR to determine the percentage of TPY and BTB (TPY: 30 mol%, BTB: 70 mol%).

4.4.3.5. Synthesis of mTPY-MOF-1

$HfOCl_2$ (30.0 mg), H_3TPY(8.25 mg) and H_3BTB (24.0 mg) in a solvent mixture of DMF/HCOOH(distilled)/H_2O (3.75 mL/2.25 mL) were sealed in an autoclave, then placed in an oven at 120 °C for 3 days. The resulting solid was isolated by centrifugation, washed with DMF, DMSO and acetone. (TPY: 5%, BTB: 95%)

4.4.3.6. Synthesis of mTPY-MOF-2

HfOCl$_2$ (81.8 mg), H$_3$TPY(4.40 mg), H$_3$BTB (17.6mg), and benzoic acid (1.2 g) in 4 mL DEF were sealed in a vial, then placed in an oven at 120 °C for 3 days. The resulting solid was isolated by centrifugation, washed with DMF, DMSO, and acetone. (TPY: 16%, BTB: 84%)

4.4.4. Modelling Selected Area Electron Diffraction (SAED) parallel to a single layer

We modelled the SAED in a direction parallel to the monolayer.
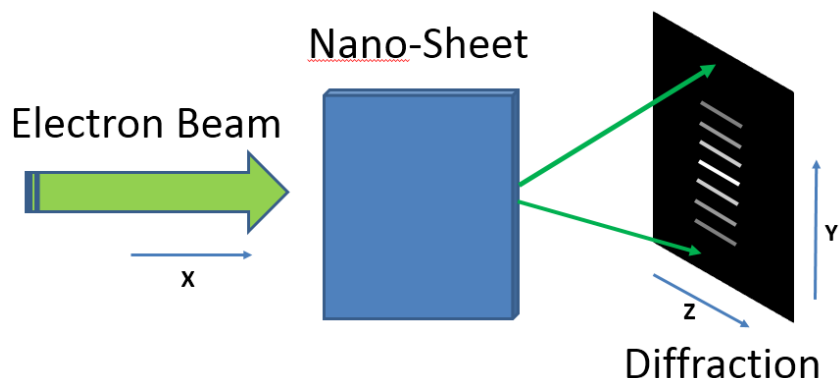
Figure 4-20. Scheme showing Selected Area Electron Diffraction parallel to the nano-sheet. Copyright 2016 John Wiley and Sons.

Considering the structural factor of a "crystal" with translation symmetry only in two dimensions, the diffracted electron beams contain contributions from a 2D net of atoms. We can write it in terms of structural factor

$$F = \sum_j f_j(\theta)e^{-i2\pi(\vec{K}\cdot\vec{r_j})} \qquad (1)$$

where $\vec{K} = \vec{k_0} - \vec{k'}$ is the scattering vector, $\vec{k_0}$ is the wave vector of the incoming electron beam, and $\vec{k'}$ is that of the diffracted beam.

$$|\vec{k_0}| = |\vec{k'}| = \frac{1}{\lambda} \text{,where } \lambda \text{ is the wavelength of the electron.} \qquad (2)$$

$f_j(\theta)$ is the atomic electron scattering factor, which is dependent on the scattering angle θ and atom type. $\vec{r_j}$ are the coordinates of the j th atom in the 2D net. The 2D net has translational symmetry in two directions, denoted as unit cell vectors $\vec{a}$ and $\vec{b}$. These two vectors define the plane of the 2D net. Perpendicular to this 2D net, no translational symmetry is present—only one layer of structure is present. For ease of description, we still denoted this direction by $\vec{c}$, the length of which corresponds to the thickness of the monolayer.

$$|\vec{a}| = a; \ |\vec{b}| = b; \ |\vec{c}| = c;$$

The coordinates of the atoms can then be expressed in fractional coordinates

$$\vec{r_j} = m\vec{a} + n\vec{b} + x_j\vec{a} + y_j\vec{b} + z_j\vec{c} \text{, where } m \text{ and } n \text{ are integers.} \qquad (3)$$

(1) can thus be converted to

$$\text{F} = \sum_{j,m,n} f_j(\theta) e^{-i2\pi(m\vec{K}\cdot\vec{a} + n\vec{K}\cdot\vec{b} + x_j\vec{K}\cdot\vec{a} + y_j\vec{K}\cdot\vec{b} + z_j\vec{K}\cdot\vec{c})} =$$

$$\sum_m e^{-i2\pi \, m\vec{K}\cdot\vec{a}} \sum_n e^{-i2\pi \, n\vec{K}\cdot\vec{b}} \sum_j f_j(\theta) e^{-i2\pi(x_j\vec{K}\cdot\vec{a} + y_j\vec{K}\cdot\vec{b} + z_j\vec{K}\cdot\vec{c})} = \frac{1}{1-e^{-i2\pi \, \overline{K}\cdot\overline{a}}} \cdot$$

$$\frac{1}{1-e^{-i2\pi \, \overline{K}\cdot\overline{b}}} \sum_j f_j(\theta) e^{-i2\pi(x_j\vec{K}\cdot\vec{a} + y_j\vec{K}\cdot\vec{b} + z_j\vec{K}\cdot\vec{c})} \qquad (4)$$

Diffraction can thus happen when $1 - e^{-i2\pi \, \vec{K}\cdot\vec{a}} = 0$ and $1 - e^{-i2\pi \, \vec{K}\cdot\vec{b}} = 0$ \qquad (5)

We thus reach the Laue equation $\vec{K} \cdot \vec{a} = h$ and $\vec{K} \cdot \vec{b} = \text{k}$ (h and k are integers). \qquad (6)

There are only two Laue equations because of the 2D nature of the crystal.

We can introduce the reciprocal lattice

$$\overrightarrow{a *} = \frac{\vec{b} \times \vec{c}}{\vec{a}\cdot(\vec{b}\times\vec{c})}, \overrightarrow{a *} \cdot \vec{a} = 1$$

$$\overrightarrow{b*} = \frac{\vec{c} \times \vec{a}}{\vec{b} \cdot (\vec{c} \times \vec{a})} \, , \quad \overrightarrow{b*} \cdot \vec{b} = 1$$

$$\overrightarrow{c*} = \frac{\vec{a} \times \vec{b}}{\vec{c} \cdot (\vec{a} \times \vec{b})} \, , \quad \overrightarrow{c*} \cdot \vec{c} = 1 \qquad\qquad (7)$$

(6) can be rewritten as

$$\vec{K} = h\overrightarrow{a*} + k\overrightarrow{b*} + \beta\overrightarrow{c*} \text{ (h and k are integers)} \qquad (8)$$
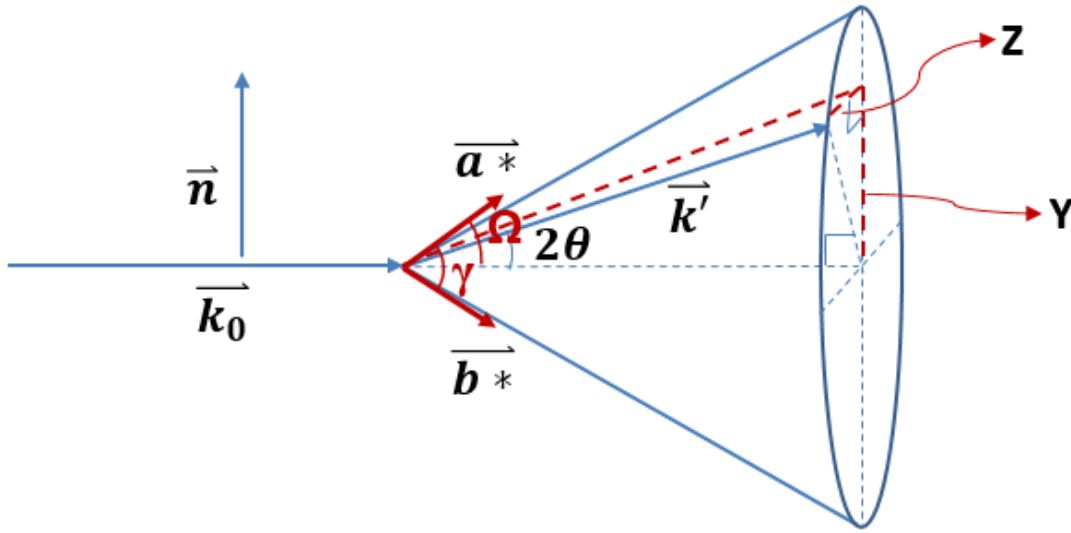
Figure 4-21. The relationship between different vectors. Copyright 2016 John Wiley and Sons.

We can rewrite the structure factor for specific h and k.

$$F(hk) = \sum_j f_j(\theta) e^{-i2\pi(hx_j + ky_j + \beta z_j)} = \sum_j f_j(\theta) e^{-i2\pi(hx_j + ky_j)} e^{-i2\pi(z_j \vec{K} \cdot \vec{c})}$$

$$= \sum_j f_j(\theta) e^{-i2\pi(hx_j + ky_j)} e^{-i2\pi z_j(\overrightarrow{k_0} - \overrightarrow{k'}) \cdot \vec{c}}$$

As shown in **Figure 4-20** and **4-21**, the $\vec{c}$ is along the Z axis and is perpendicular to the $\overrightarrow{k_0}$, so

$$\vec{k_0} \cdot \vec{c} = 0 \quad (9)$$

$$\vec{k'} \cdot \vec{c} = Zc \quad (10)$$

So

$$F(hk, Z, \theta) = \sum_j f_j(\theta) e^{-i2\pi(hx_j + ky_j)} e^{i2\pi z_j cZ} \quad (11)$$

From the geometric relationship in **Figure 4-21**,

$$\sqrt{Z^2 + Y^2} = \frac{\sin 2\theta}{\lambda} \quad (12)$$

We can obtain $\theta = \frac{1}{2}\arcsin(\lambda\sqrt{Z^2 + Y^2}) \quad (13)$

$F(hk)$ can thus be fully calculated from equation (11)

These hk diffractions can only appear at certain points on the Y axis on the detector, as determined by equation (8)

Assuming that the 2D crystal is oriented in a particular direction such that the angle between the $\vec{k_0}$ vector and the $\vec{a*}$ is Ω, from (8), using a normal vector $\vec{n}$ in the y direction, we can get

$$\vec{k_0} - \vec{k'} = h\vec{a*} + k\vec{b*} + \beta\vec{c*}$$

$$\Rightarrow \vec{n} \cdot (\vec{k_0} - \vec{k'}) = h\vec{n} \cdot \vec{a*} + k\vec{n} \cdot \vec{b*} + \beta\vec{n} \cdot \vec{c*}$$

$$\Rightarrow -Y = h|\vec{a*}|\sin\Omega + k|\vec{b*}|\sin(\Omega - \gamma)$$

$$\Rightarrow Y_{hk} = h\frac{\sin\Omega}{a \cdot \sin\gamma} - k\frac{\sin(\gamma - \Omega)}{b \cdot \sin\gamma} \quad (14)$$

Using this information, we can calculate the intensities on the detector

142

$$I(Z, Y_{hk}) = \left| F\left(hk, Z, \theta = \frac{1}{2}\arcsin\left(\lambda\sqrt{Z^2 + Y_{hk}{}^2} \right) \right) \right|^2$$

$$= \left| \sum_j f_j\left(\theta = \frac{1}{2}\arcsin\left(\lambda\sqrt{Z^2 + Y_{hk}{}^2} \right) \right) e^{-i2\pi(hx_j + ky_j)} e^{i2\pi z_j cZ} \right|^2$$

We can calculate the SAED parallel to the nano-sheets for bi-layer, tri-layer, and multi-layers in a similar fashion. We performed the simulation by Matlab and obtained the following images

4.4.5. Modelling PXRD pattern of MOLs

We modelled the PXRD pattern of the MOLs. Following the analysis in the previous section,

$$\vec{k_0} - \vec{k'} = h\vec{a*} + k\vec{b*} + \beta\vec{c*} \quad (15)$$

In the PXRD experiment, the crystals all had possible orientations to meet the requirement in equation (15).

For any given θ, a number of hk combinations can contribute to the intensity $I(\theta)$, since the parameter β can be freely adjusted to meet equation (15)

$$\vec{k_0} - \vec{k'} = h\vec{a*} + k\vec{b*} + \beta\vec{c*}$$

$$\Rightarrow \left(\vec{k_0} - \vec{k'} \right)^2 = \left(h\vec{a*} + k\vec{b*} + \beta\vec{c*} \right)^2$$

$$\Rightarrow \left(\vec{k_0} - \vec{k'} \right) \cdot \left(\vec{k_0} - \vec{k'} \right) = \left(h\vec{a*} + k\vec{b*} + \beta\vec{c*} \right) \cdot \left(h\vec{a*} + k\vec{b*} + \beta\vec{c*} \right)$$

$$\Rightarrow \frac{2(1 - \cos 2\theta)}{\lambda^2} = \frac{h^2 + k^2 + 2hk \cdot \cos\gamma}{(a \cdot \sin\gamma)^2} + \frac{\beta^2}{c^2}$$

143

$$\Rightarrow \beta_{hk,\theta} = c\sqrt{\frac{2(1-cos2\theta)}{\lambda^2} - \frac{h^2+k^2+2hk\cdot cos\gamma}{(a\cdot sin\gamma)^2}} \qquad (16)$$

So
$$F(hk,\theta) = \sum_j f_j(\theta)e^{-i2\pi(hx_j+ky_j+\beta z_j)} \qquad (17)$$

$I(\theta) = \frac{1+cos^2 2\theta}{2} \cdot \frac{1}{2sin^2\theta cos\theta} \cdot e^{-B\left(\frac{sin\theta}{\lambda}\right)^2} \sum_{h,k} \frac{sin2\theta}{\beta_{hk,\theta}}|F(hk,\theta)|^2$ where Lorentz and

polarization terms have been considered and the B is the temperature factor to account for thermal vibration.

4.4.6. X-ray Structure Determination

The diffraction data were collected with a Bruker APEX II CCD-based detector at ChemMatCARS (Sector 15), Advanced Photon Source (APS), Argonne National Laboratory and integrated with the Bruker SAINT© build in APEX II software package using a narrow-frame integration algorithm that also corrects for the Lorentz and polarization effects. Absorption corrections were applied using SADABS. The structure was solved by direct methods and refined to convergence by least squares method on F2 using the SHELXTL software suite. SQUEEZE subroutine of the PLATON software suite was applied to remove the scattering from the highly disordered guest molecules. The resulting new HKL4 file was used to further refine the structure. DFIX for bond lengths were applied, and all the phenyl rings were constrained to ideal six-membered rings. Non-hydrogen atoms were refined isotropically.

4.4.7. X-Ray Absorption Spectroscopic Analysis

4.4.7.1. Data collection.

X-ray absorption data was collected at Beamline 9-BM-C at the Advanced Photon Source (APS) at Argonne National Laboratory. Spectra were collected at the Hafnium LIII-edge in transmission mode. The X-ray beam was monochromatized by a Si(111) monochromater and

detuned by 25% to minimize harmonics. A metallic zinc foil standard was used as the reference for energy calibration and was measured simultaneously with experimental samples. The incident beam intensity (I_0) was measured by an ionization chamber with 70% N_2 and 30% He gas composition. Data was collected in three regions: a pre-edge region –150 to –20 eV (5 eV step size, dwell time 1.0 s), XANES region – 20 to 50 eV (0.5 eV step size, dwell time 1.0 s), and EXAFS region 3.62 Å -1 to 13.95 Å -1 (0.05 Å -1 step size, dwell time increased linearly from 1.0 to 3.9 seconds over the region to facilitate higher k-weighted data processing). All energies are listed relative to the elemental Zn K-edge (9659 eV). Multiple X-ray absorption spectra were collected at room temperature for each sample. Samples were ground and mixed with polyethyleneglycol (PEG) and packed in a 6-shooter sample holder to achieve adequate absorption length.

4.4.7.2. Data processing.

Data were processed using the Athena and Artemis programs of the IFEFFIT package based on FEFF 6. Prior to merging, spectra were calibrated against the reference spectra (metallic Zn) and aligned to the first peak in the smoothed first derivative of the absorption spectrum, background removed, and spectra processed to obtain a normalized unit edge step.

4.4.7.3. EXAFS fitting.

Fits of the EXAFS region were performed using the Artemis program of the IFEFFIT package. Fits were performed with a k-weight of 2 in R-space. Refinement was performed by optimizing an amplitude factor S_0^2 and energy shift ΔE_0 which are common to all paths, in addition to parameters for bond length (ΔR) and Debye-Waller factor (σ^2). The fitting models were based on the crystal structure of Zr-MOF1. Unique parameters for ΔR and σ^2 were provided for all scattering paths in all fits.

4.4.8. General Procedures for Catalytic Hydrosilylation

1.6 µL of NaEt$_3$BH (1.0 M in THF) was added to a THF suspension of **Fe-mTPY-MOL** (5 mg, 0.16 µmol based on Fe, suspended in 1.0 mL) or other catalyst. The mixture was stirred slowly for 1 h in the glovebox. The solid was centrifuged out and washed twice with THF and twice with heptane. Silane (1.2 mmol) was added to the vial and the resultant mixture was transferred to a Schlenk tube, followed by the addition of alkene (0.8 mmol). The tube was sealed with a glass stopper and then brought out of the glovebox and gently stirred at 100 °C for 2 d. After cooling to RT, MOL was separated by centrifugation, and the product was extracted away from the MOL with THF washes (4x). The combined organic extracts were concentrated on a rotary evaporator. The residue was added mesitylene as an internal standard and the yield was accessed via ^{1}H-NMR in CDCl$_3$.

4.4.9. Recycle and Reuse of Fe-mTPY-MOL

8.0 µL of NaEt$_3$BH (1.0 M in THF) was added to a THF suspension of **Fe-mTPY-MOL** (25 mg, 0.8 µmol based on Fe, suspended in 1.0 mL) or other catalyst. The mixture was stirred slowly for 1 h in a glovebox. The solid was centrifuged out and washed twice with THF and twice with heptane. Phenylsilane (1.2 mmol) was added to the vial and the resultant mixture was transferred to a Schlenk tube, followed by the addition of styrene (0.8 mmol). The tube was sealed with glass stopper and then brought out of the glovebox and gently stirred at 100 °C for 2 d. After cooling to RT, the reaction tube was transferred to a nitrogen filled glovebox. MOLs were separated by centrifugation, and the product was extracted away from the MOL with THF washes (4x). The combined organic extracts were concentrated on a rotary evaporator. Mesitylene was added to the residue as an internal standard and the yield was accessed via ^{1}H-NMR in CDCl$_3$. Recovered **Fe-mTPY-MOL** was transferred back into the reaction tube, and

phenylsilane (1.2 mmol) and styrene (0.8 mmol) were added. The reaction tube was sealed and conditions were repeated as described above.

4.4.10. Heterogeneity Test

To prove the heterogeneous nature of the catalysis, a "cross-over" experiment was performed. 8 µL of NaEt$_3$BH (1.0 M in THF) was added to a THF suspension of **Fe-mTPY-MOL** (25 mg, 0.8 µmol based on Fe, suspended in 1.0 mL). The mixture was stirred slowly for 1 h in a glovebox. The solid was centrifuged out and washed twice with THF and twice with heptane. Phenylsilane (1.2 mmol) was added to the vial and the resultant mixture was transferred to a Schlenk tube, followed by the addition of styrene (0.8 mmol). The tube was sealed with glass stopper and then brought out of the glovebox and gently stirred at 100 °C for 2 d. After the reaction, the Schlenk tube was quickly transferred to a nitrogen filled glovebox. MOL were removed by centrifugation. The remaining hot supernatant was transferred back into the reaction tube, and phenylsilane (1.2 mmol) and 1-octene (0.8 mmol) were added. The reaction tube was sealed and stirred at 100 °C for 2 days. Analysis of the final reaction mixture showed the formation of only hydrosilylation product of styrene but no product from 1-octene.

4.5. References

(1)   Manna, K.; Zhang, T.; Lin, W. *J. Am. Chem. Soc.* **2014**, *136*, 6566.
(2)   Cho, S. H.; Ma, B.; Nguyen, S. T.; Hupp, J. T.; Albrecht-Schmitt, T. E. *Chem. Commun.* **2006**, 2563.
(3)   Cohen, S. M. *Chem. Rev.* **2012**, *112*, 970.
(4)   Haneda, T.; Kawano, M.; Kawamichi, T.; Fujita, M. *J. Am. Chem. Soc.* **2008**, *130*, 1578.
(5)   Choi, K. M.; Na, K.; Somorjai, G. A.; Yaghi, O. M. *J. Am. Chem. Soc.* **2015**, *137*, 7810.
(6)   Feng, D.; Gu, Z.-Y.; Li, J.-R.; Jiang, H.-L.; Wei, Z.; Zhou, H.-C. *Angew. Chem. Int. Ed.* **2012**, *51*, 10307.
(7)   Zhao, M.; Ou, S.; Wu, C.-D. *Acc. Chem. Res.* **2014**, *47*, 1199.
(8)   Yee, K.-K.; Wong, Y.-L.; Zha, M.; Adhikari, R. Y.; Tuominen, M. T.; He, J.; Xu, Z. *Chem. Commun.* **2015**, *51*, 10941.

(9)   Xiao, D. J.; Bloch, E. D.; Mason, J. A.; Queen, W. L.; Hudson, M. R.; Planas, N.; Borycz, J.; Dzubak, A. L.; Verma, P.; Lee, K.; Bonino, F.; Crocellà, V.; Yano, J.; Bordiga, S.; Truhlar, D. G.; Gagliardi, L.; Brown, C. M.; Long, J. R. *Nat. Chem.* **2014**, *6*, 590.

(10)   Song, F.; Wang, C.; Falkowski, J. M.; Ma, L.; Lin, W. *J. Am. Chem. Soc.* **2010**, *132*, 15390.

(11)   Wang, C.; Zheng, M.; Lin, W. *J. Phys. Chem. Lett.* **2011**, *2*, 1701.

(12)   Zhang, T.; Manna, K.; Lin, W. *J. Amer. Chem. Soc.* **2016**, *138*, 3241.

(13)   Sawano, T.; Thacker, N. C.; Lin, Z.; McIsaac, A. R.; Lin, W. *J. Amer. Chem. Soc.* **2015**, *137*, 12241.

(14)   Betard, A.; Fischer, R. A. *Chem. Rev.* **2012**, *112*, 1055.

(15)   Novoselov, K. S.; Geim, A. K.; Morozov, S. V.; Jiang, D.; Zhang, Y.; Dubonos, S. V.; Grigorieva, I. V.; Firsov, A. A. *Science* **2004**, *306*, 666.

(16)   Mak, K. F.; Lee, C.; Hone, J.; Shan, J.; Heinz, T. F. *Phys. Rev. Lett.* **2010**, *105*.

(17)   Stepanow, S.; Lin, N.; Payer, D.; Schlickum, U.; Klappenberger, F.; Zoppellaro, G.; Ruben, M.; Brune, H.; Barth, J. V.; Kern, K. *Angew. Chem. Int. Ed.* **2007**, *46*, 710.

(18)   Lin, T.; Kuang, G.; Wang, W.; Lin, N. *ACS Nano* **2014**, *8*, 8310.

(19)   Dong, R.; Pfeffermann, M.; Liang, H.; Zheng, Z.; Zhu, X.; Zhang, J.; Feng, X. *Angew. Chem. Int. Ed.* **2015**, *54*, 12058.

(20)   Bauer, T.; Zheng, Z.; Renn, A.; Enning, R.; Stemmer, A.; Sakamoto, J.; Schlüter, A. D. *Angew. Chem. Int. Ed.* **2011**, *50*, 7879.

(21)   Sakamoto, R.; Hoshiko, K.; Liu, Q.; Yagi, T.; Nagayama, T.; Kusaka, S.; Tsuchiya, M.; Kitagawa, Y.; Wong, W. Y.; Nishihara, H. *Nat. Commun.* **2015**, *6*, 6713.

(22)   Peng, Y.; Li, Y.; Ban, Y.; Jin, H.; Jiao, W.; Liu, X.; Yang, W. *Science* **2014**, *346*, 1356.

(23)   Li, P. Z.; Maeda, Y.; Xu, Q. *Chem. Commun.* **2011**, *47*, 8436.

(24)   Amo-Ochoa, P.; Welte, L.; González-Prieto, R.; Sanz Miguel, P. J.; Gómez-García, C. J.; Mateo-Martí, E.; Delgado, S.; Gómez-Herrero, J.; Zamora, F. *Chem. Commun.* **2010**, *46*, 3262.

(25)   Zhao, M.; Wang, Y.; Ma, Q.; Huang, Y.; Zhang, X.; Ping, J.; Zhang, Z.; Lu, Q.; Yu, Y.; Xu, H.; Zhao, Y.; Zhang, H. *Adv. Mater.* **2015**, *27*, 7372.

(26)   Junggeburth, S. C.; Diehl, L.; Werner, S.; Duppel, V.; Sigle, W.; Lotsch, B. V. *J. Am. Chem. Soc.* **2013**, *135*, 6157.

(27)   Lin, H. X.; Lei, Z. C.; Jiang, Z. Y.; Hou, C. P.; Liu, D. Y.; Xu, M. M.; Tian, Z. Q.; Xie, Z. X. *J. Am. Chem. Soc.* **2013**, *135*, 9311.

(28)   Cavka, J. H.; Jakobsen, S.; Olsbye, U.; Guillou, N.; Lamberti, C.; Bordiga, S.; Lillerud, K. P. *J. Am. Chem. Soc.* **2008**, *130*, 13850.

(29)   Wang, R.; Wang, Z.; Xu, Y.; Dai, F.; Zhang, L.; Sun, D. *Inorg, Chem.* **2014**, *53*, 7086.

(30)   Vermoortele, F.; Bueken, B.; Le Bars, G.; Van de Voorde, B.; Vandichel, M.; Houthoofd, K.; Vimont, A.; Daturi, M.; Waroquier, M.; Van Speybroeck, V.; Kirschhock, C.; De Vos, D. E. *J. Am. Chem. Soc.* **2013**, *135*, 11465.

(31)   Stankovich, S.; Dikin, D. A.; Piner, R. D.; Kohlhaas, K. A.; Kleinhammes, A.; Jia, Y.; Wu,   Y.; Nguyen, S. T.; Ruoff, R. S. *Carbon* **2007**, *45*, 1558.

(32)   Zhu, L.; Zhang, D.; Xue, M.; Li, H.; Qiu, S. *CrystEngComm* **2013**, *15*, 9356.

(33)   Wiktor, C.; Turner, S.; Zacher, D.; Fischer, R. A.; Tendeloo, G. V. *Micropor. Mesopor. Mater.* **2012**, *162*, 131.

(34)   Díaz-García, M.; Mayoral, Á.; Díaz, I.; Sánchez-Sánchez, M. *Cryst. Grow. Design* **2014**, *14*, 2479.

(35)   CCDC 1444732-1444733 contain the supplementary crystallographic data for this paper. These data can be obtained free of charege from the Cambridge Crystallographic Data Centre via www.ccdc.cam.ac.uk/data_request/cif.

(36)   Tondreau, A. M.; Atienza, C. C. H.; Weller, K. J.; Nye, S. A.; Lewis, K. M.; Delis, J. G. P.; Chirik, P. J. *Science* **2012**, *335*, 567.

CHAPTER 5 Metal-Organic Layers Stabilize Earth-Abundant Metal-Terpyridine

Diradical Complexes for Catalytic C-H Activation

5.1. Introduction

Precious metals such as Rh, Ir, Pd, Pt and Ru have dominated the catalysis technology for the production of commodity and fine chemicals in the past few decades. Despite their high activities and selectivities, they have low abundance and pose significant challenges to the environment in their mining, as well as their removal from the products of catalytic reactions.[1] To address these challenges, much effort has been devoted to the development of earth-abundant-metal catalysts in the past decade. Earth-abundant-metal catalysts have high terrestrial abundance, low cost, and low toxicity. In addition, new catalysts based on earth-abundant-metals may have different reactivities and selectivities than precious metals, potentially providing access to novel transformations.[2] Although significant progress has been made in in the field of homogeneous earth-abundant-metal catalysis in the past decade, the design of homogenous base metal catalysts still requires bulky substituents proximal to the active sites to prevent intermolecular catalyst deactivation. These sterically encumbered protective ligands not only require multiple-step synthetic elaborations but can also attenuate the catalytic activity of base metal catalysts, both of which adversely impact the practicality of many earth-abundant metal catalysts.[3] Alternative strategies are needed to discover homogeneous base metal catalysts and to move them from the discoveries of novel molecular catalysis into practical applications.

Immobilizing homogeneous metal catalysts on solid supports, such as silicas, has been extensively explored with the goal of recycling and reusing these valuable catalysts.[4-6] However, such a strategy can lead to non-uniform distribution of catalysts and cannot completely prevent intermolecular interactions between catalytic sites or interactions of active sites with surface

functionalities. The difficulty of characterizing non-uniformly distributed heterogeneous catalysts presents another significant challenge. Over the past few years, our group has initiated research efforts to design earth-abundant-metal catalysts using metal-organic frameworks (MOFs), which have shown much enhanced catalytic activity over their homogeneous counterparts by taking advantage of active site isolation of MOF materials.[7-9] However, the diffusion of substrates and products through the framework can present a significant issue for MOF catalysts. [10,11] As discussed in Chapter 4, we have recently showed that this diffusion constraint can be lifted by reducing one dimension of the MOF crystals to afford a new category of 2D materials, MOL, that are only a few nanometers thick to minimize the diffusion distance.[12] In this chapter, I will discuss our recent efforts on using MOLs to uncover unprecedented M-terpyridine (M = Fe and Co) chemistry and to effect novel catalytic C-H activation reactions.

Owing to their distinct coordination, redox, and photophysical properties, terpyridines (tpy) and their metal complexes have been explored for potential applications in many fields, including polymer science,[13,14] optoelectronics,[15,16] medicinal chemistry,[17,18] nanotechnology,[19] and molecular catalysis.[15,20,21] Tpy derivatives provide a potentially interesting ligand platform for designing earth-abundant-metal catalysts due to their ability to function as electron reservoirs like other redox-active ligands, which allows multi-electron transformations without necessitating the metal to adopt an uncommon oxidation state. However, few examples of M-tpy catalysts have been reported in the literature,[21-24] in part due to their strong propensity to undergo disproportionation reactions to form catalytically inactive M(tpy)$_2$ complexes.[22,23] Installation of bulky groups on the 6,6''-positions of tpy could prevent such bimolecular deactivation processes in M-tpy catalysts, but often at the expense of their catalytic activities.[22]

By incorporating a tpy derivative into TPY-MOL, we effectively shut down the disproportionation decomposition pathway without relying on steric protection at the 6,6" positions, and obtained highly effective recyclable and reusable MOL catalysts based on M-tpy complexes (M = Co or Fe) for challenging benzylic C-H borylation and intramolecular sp^3 C-H amination reactions (**Figure 5-1**). Spectroscopic and computational studies identified unprecedented Co^{II}/Fe^{II}-terpyridine diradical complexes as catalytic active sites for the borylation and amination reactions.
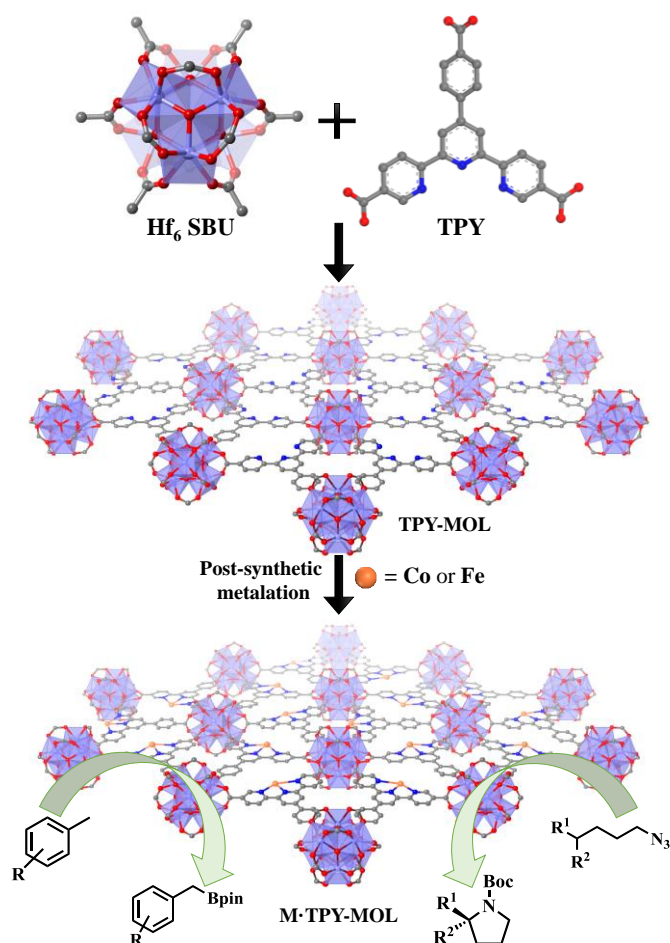
Figure 5-1. M•TPY-MOLs, constructed from Hf$_6$ SBUs and TPY and then metalated with Co and Fe, were used for benzylic C-H borylation and intramolecular sp^3 C-H Amination reactions, respectively.

5.2. Results and Discussion

5.2.1. Synthesis and Postsynthetic Metalation of TPY-MOL

TPY-MOL was synthesized in 76% yield by heating a mixture of $HfCl_4$, 4'-(4-carboxyphenyl)-[2,2':6',2"-terpyridine]-5,5"-dicarboxylic acid (H_3TPY), and formic acid in DMF and water at 120 °C for 24 h. The PXRD pattern of TPY-MOL matched the simulated pattern based on the (hk0) reflections only that are characteristic of 2D MOL structures and aligned well with that of isostructural BTB-MOL (BTB is 1,3,5-benzenetribenzoate, **Figure 5-2a**, **b**).[12] In contrast, $l \neq 0$ reflections were observed in the stacked BTB-MOF (**Figure 5-2c**).
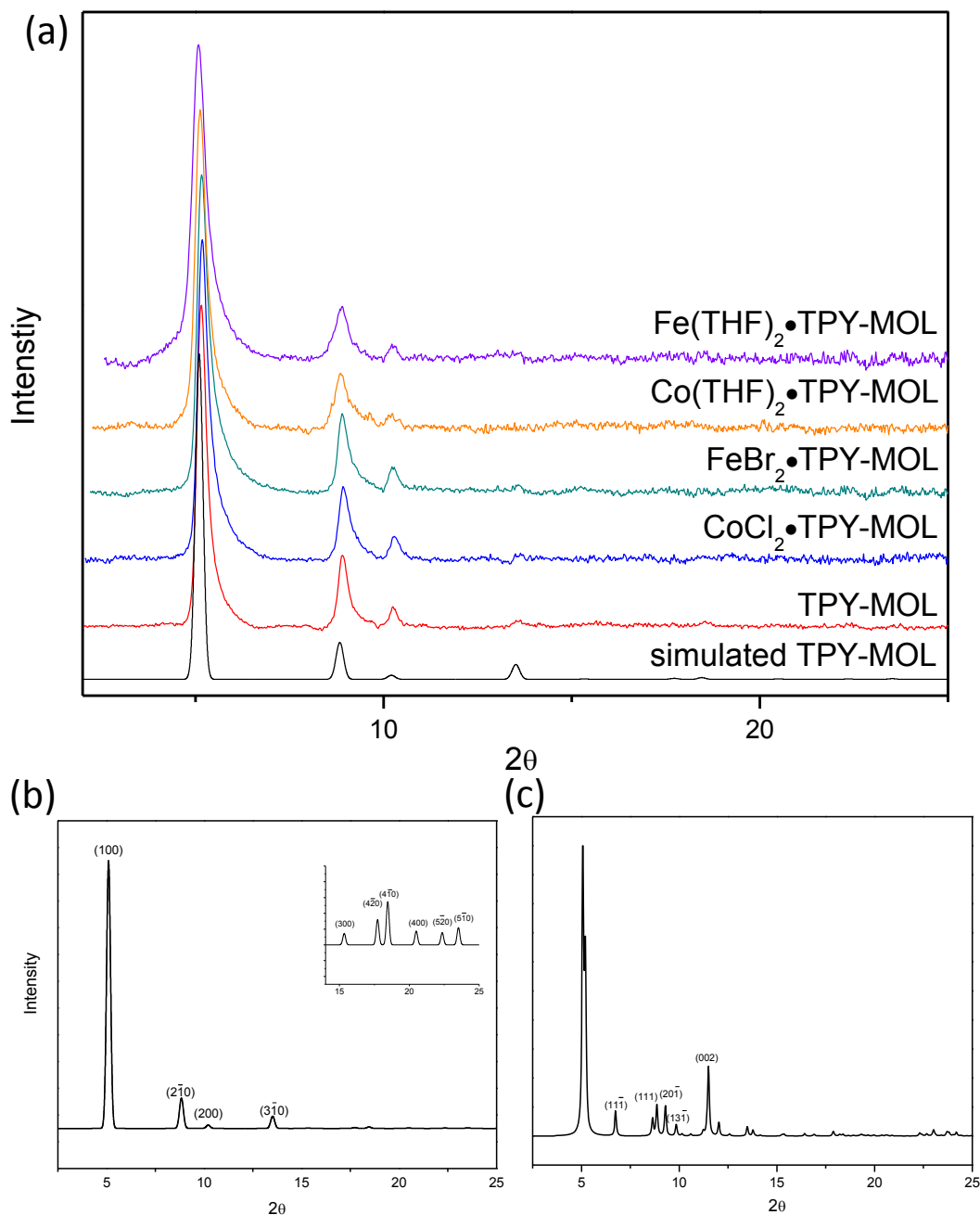
Figure 5-2. (a) PXRD patterns of TPY-MOL, CoCl₂•TPY-MOL, FeBr₂•TPY-MOL, Co(THF)₂•TPY-MOL, and Fe(THF)₂•TPY-MOL in comparison to the simulated PXRD pattern for TPY-MOL. (b) Simulated PXRD of TPY-MOL (inset shows the zoomed-in view of high angle diffractions); (c) Simulated PXRD of BTB-MOF.

154

Transmission Electron Microscopy (TEM) images showed ultra-thin films of TPY-MOL, whereas high resolution TEM (HR-TEM) images of TPY-MOL showed clear lattice with the dark spots corresponding to Hf_6 clusters (**Figure 5-3**). The distances between adjacent spots on the HRTEM image (20.1 Å) matched well with that between two adjacent Hf_6 SBUs (20.0 Å) in the MOL structural model. Atomic Force Microscopy (AFM) images of TPY-MOL indicated monolayer thickness for many nano-sheets with an average measured thickness of 1.2 nm, corresponding to the van der Waals size of Hf_6 SBUs (**Figure 5-4**).
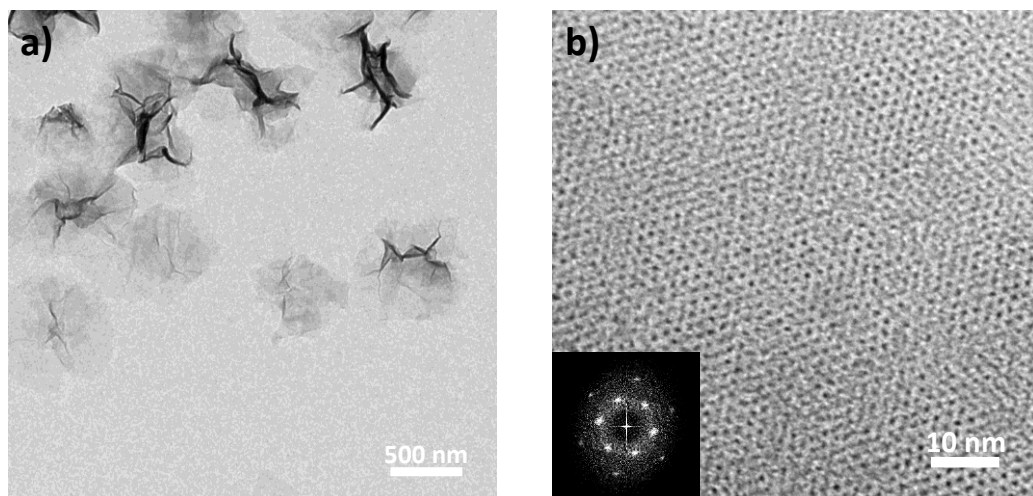
Figure 5-3. (a) TEM image of TPY-MOL; (b) HR-TEM image and fast Fourier transform (FFT) pattern of TPY-MOL.
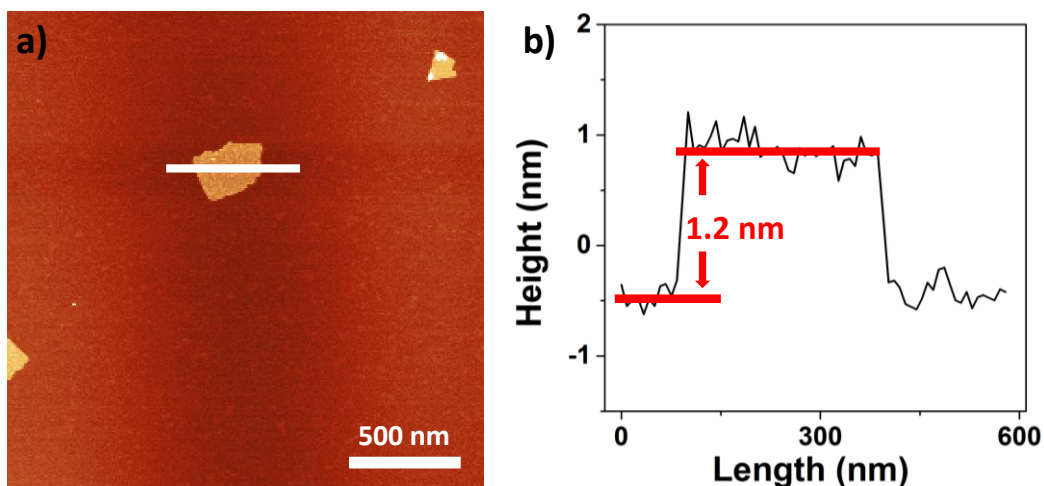
Figure 5-4. (a) Tapping-mode atomic-force microscope (AFM) topography; (b) Height profile along the white line of TPY-MOL.

TPY-MOL was readily metalated with $CoCl_2$ or $FeBr_2(THF)_2$ (1.05 eqv. w.r.t TPY) to afford $CoCl_2 \cdot$TPY-MOL or $FeBr_2 \cdot$TPY-MOL with 100% metal loading, as determined by inductively coupled plasma-mass spectrometry (ICP-MS). X-ray absorption near edge structure (XANES) analysis revealed +2 oxidation state for $CoCl_2 \cdot$TPY-MOL and $FeBr_2 \cdot$TPY-MOL by comparing the energy of pre-edges to standard compounds $CoCl_2$ and $FeBr_2(THF)_2$, respectively (**Figure 5-5**). The oxidation state assignments were further confirmed by X-ray photoelectron spectroscopy (XPS, **Figure 5-6**).
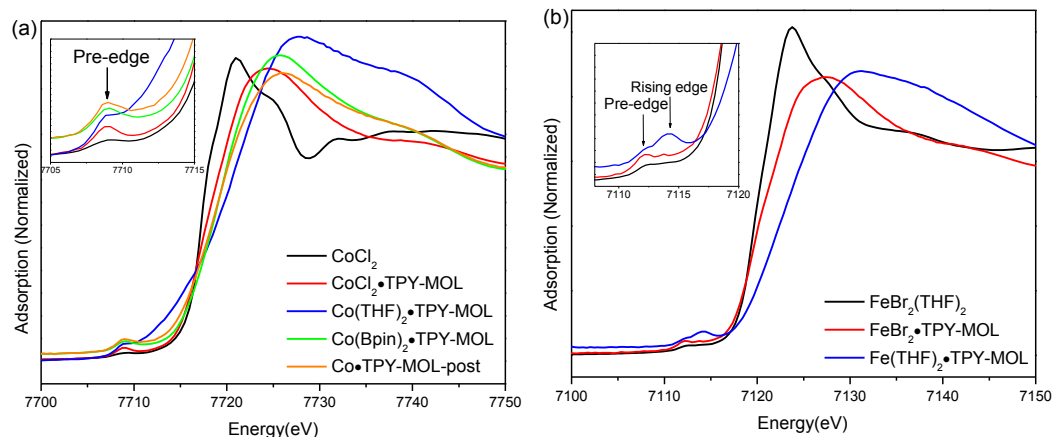
Figure 5-5. (a) XANES spectra of $CoCl_2$, $CoCl_2 \cdot TPY\text{-}MOL$, $Co(THF)_2 \cdot TPY\text{-}MOL$, $Co(Bpin)_2 \cdot TPY\text{-}MOL$, and $Co \cdot TPY\text{-}MOL\text{-}post$; (b) XANES spectra of $FeBr_2(THF)_2$, $FeBr_2 \cdot TPY\text{-}MOL$, and $Fe(THF)_2 \cdot TPY\text{-}MOL$.
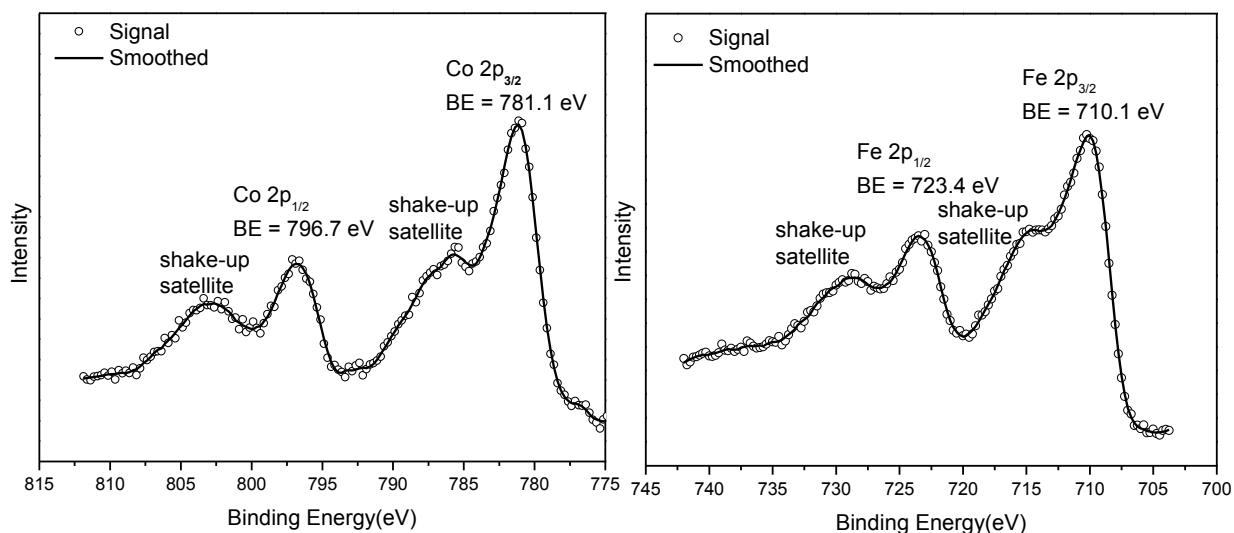
Figure 5-6. Co 2p and Fe 2p XPS spectra of $CoCl_2 \cdot TPY\text{-}MOL$ (left) and $FeBr_2 \cdot TPY\text{-}MOL$ (right).

Extended X-ray absorption fine structure (EXAFS) fitting indicated the coordination of Co^{II} to three N atoms of TPY and two chlorides in $CoCl_2 \cdot TPY\text{-}MOL$(**Figure 5-7a, Table 5-1**), and the coordination of Fe^{II} to three N atoms of TPY and two bromides in $FeBr_2 \cdot TPY\text{-}MOL$

(**Figure 5-7b, Table 5-2**). The similarity of EXAFS-derived bond distances in CoCl$_2$·TPY-MOL (Co-Nc = 2.09 ± 0.01Å, Co-Nt = 2.16 ± 0.01Å and Co-Cl = 2.28 ± 0.01Å) and crystallographically determined CoCl$_2$·tpy distances (Co-Nc = 2.071Å, Co-Nt = 2.139Å and Co-Cl = 2.298Å) validates the EXAFS fitting results.
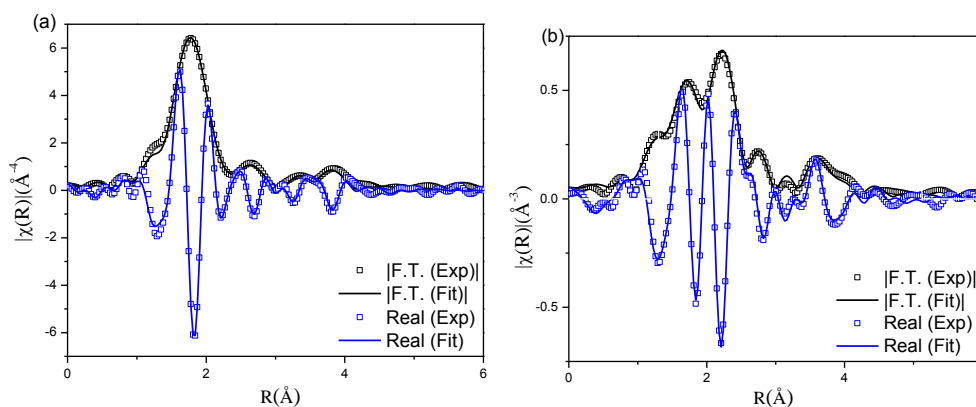
Figure 5-7. Experimental EXAFS spectra and fits of CoCl$_2$•TPY-MOL with R factor = 0.006 (a) and FeBr$_2$•TPY-MOL with R factor = 0.011 (b) in R space showing the magnitude of Fourier Transform (black hollow squares, black solid line) and real components (blue hollow squares, blue solid line).

Table 5-1. Summary of EXAFS fitting parameters for CoCl$_2$•TPY-MOL

Sample	CoCl$_2$•TPY-MOL
Fitting range	k 3.20 – 11.40 Å^{-1}
	R 1.3 – 5.4 Å
Independent points	21
Variables	11
Reduced chi-square	20.06
R-factor	0.006
S_0^2	1.000
ΔE_0(eV)	5.21±1.53

Table 5-1, continued

R (Co-N2) (1)	2.09±0.01 Å
R (Co-N1) (2)	2.16±0.01 Å
R (Co-Cl) (2)	2.28±0.01 Å
R (Co-C10) (2)	2.96±0.01 Å
R (Co-C11) (2)	3.06±0.03 Å
R (Co-C1) (2)	3.23±0.02 Å
R (Co-C7) (2)	4.40±0.04 Å
R (Co-C4) (2)	4.45±0.04 Å
R (Co-C2) (2)	4.54±0.04 Å
σ^2 (Co-N)	0.004±0.001 Å^2
σ^2 (Co-Cl)	0.010±0.001 Å^2
σ^2 (Co-C^{close})	0.004±0.002 Å^2
σ^2 (Co-C^{distal})	0.018±0.004 Å^2

Table 5-2. Summary of EXAFS fitting parameters for FeBr$_2$•TPY-MOL

Sample	FeBr$_2$•TPY-MOL
Fitting range	k 3.10 – 10.80 Å^{-1}
	R 1.3 – 5.1 Å
Independent points	18
Variables	12
Reduced chi-square	52.26
R-factor	0.011
S_0^2	1.000
ΔE_0(eV)	3.55±1.51
R (Fe-N2) (1)	2.06±0.04 Å
R (Fe-N1) (2)	2.22±0.01 Å

Table 5-2, continued

R (Fe-Br) (2)	2.44±0.01 Å
R (Fe-C16) (2)	3.09±0.02 Å
R (Fe-C17) (2)	3.14±0.02 Å
R (Fe-C1) (2)	3.39±0.06 Å
R (Fe-C15) (2)	4.08±0.06 Å
R (Fe-C18) (2)	4.21±0.06 Å
R (Fe-C8) (2)	4.31±0.08 Å
σ^2 (Fe-N)	0.004±0.005 Å^2
σ^2 (Fe-Br)	0.003±0.001 Å^2
σ^2 (Fe-C^{close})	0.006±0.003 Å^2
σ^2 (Fe-C^{distal})	0.001±0.001 Å^2

5.2.2. Co•TPY-MOL Catalyzed Benzylic C-H Borylation

We first investigated C-H borylation of *m*-xylene by Co•TPY-MOL. Organoboronic compounds are a useful class of intermediates for forming carbon-carbon and carbon-heteroatom bonds through coupling reactions. C-H borylation with boron reagents such as B_2pin_2 is one of the most direct and convenient methods for the synthesis of organoboronic compounds. Although C-H borylation with arenes has been developed in the past two decades, benzylic C-H borylation is still rare.[8,25-30] Upon activation with NaEt₃BH, CoCl₂•TPY-MOL (0.5 mol%) catalyzed *m*-xylene borylation with B_2pin_2 at 100 °C over 3 days to afford 42% yield of borylated products, with a 4.2:1 selectivity favoring the benzylic position (**Table 5-3**, entry 1). The borylated products were obtained in 95% yield with a slightly higher selectivity for benzylic borylation (4.6:1) when the catalyst loading increased to 1.0 mol% (**Table 5-3**, entry 2). The activation of CoCl₂•TPY-MOL with NaEt₃BH is necessary for the borylation reaction (**Table 5-3**,

entry 3). Under identical conditions, a TPY-MOF control, which is isostructural to the previously

reported BTB-MOF in which 2D layers stack in a staggered arrangement to result in a 3D

MOF,[12] gave no conversion, likely due to slow diffusion of the substrates and products (**Table 5-3**, entry 4).   The homogeneous analog gave 2% borylated products with a 5.7:1 selectivity

favoring the arene C-H bond (**Table 5-3**, entry 5). Such moderate arene borylation activity was

recently reported for homogenous tpy-Co derivatives.[23] Active site isolation in MOLs thus not

only increases the TON by more than 20 times (over the homogeneous analog) but also afforded

unusual selectivity of borylation for the benzylic C-H bond.

Table 5-3. Cobalt-catalyzed C-H borylation of *m*-xylene

Entry	Catalyst	Yield[a] (%) (*Bn : Ar*)
1	CoCl$_2$•TPY-MOL	42 (4.2 : 1)
2[b]	CoCl$_2$•TPY-MOL	95 (4.6:1)
3[c]	CoCl$_2$•TPY-MOL	0
4	CoCl$_2$•TPY MOF	0
5	"Homogeneous" CoCl$_2$(tpy)	2 (1 : 5.7)
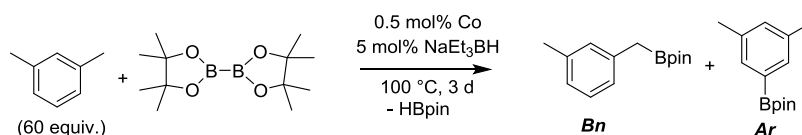
[a] NMR yield based on CH$_3$NO$_2$ as an internal standard; [b] 1.0 mol% Co; c without the addition of NaEt$_3$BH.

We further investigated the substrate scope for Co•TPY-MOL catalyzed C-H borylation

reactions. Benzylic borylated products were produced exclusively for *p*-xylene, 1-t-butyl-4-

methylbenzene, and mesitylene in >90% yields (**Table 5-4**, entries 2-4). For *p*-methoxytoluene, a

high selectivity of 59 : 6 : 1 was obtained for the benzylic borylated product (**Table 5-4**, entry 5).

For toluene, borylated products were obtained in 92% yield, but the selectivity for the benzylic

borylation product was moderate (**Table 5-4**, entry 6). These results indicate the influence of steric hindrance on the selectivity of benzylic vs. aromatic borylation by Co•TPY-MOL.

Table 5-4. Co•TPY-MOL catalyzed C-H borylation of arenes[a]

Entry	Substrate	Product	Yield (%) (*Bn : Ar*)
1			95 (4.6 : 1)
2			93
3[b]			91
4			91
5[b]			86 (59 : 6 : 1)
6			92 (0.91 : 1.4 : 1)

[a][Co] = CoCl$_2$•TPY-MOL + 10 equiv. NaEt$_3$BH, NMR yield with CH$_3$NO$_2$ as an internal standard; [b]4 mol% [Co].

Co•TPY-MOL was recovered and used for at least 10 times without any loss of activity in C-H borylation of p-xylene (**Figure 5-8a**). We conducted several tests to demonstrate the heterogeneity of Co•TPY-MOL. First, we showed that the PXRD of Co•TPY-MOL recovered from C-H borylation of p-xylene remained the same as that of freshly prepared Co•TPY-MOL (**Figure 5-8b**). Second, we used ICP-MS to show that the amounts of Co and Hf leaching into the supernatant during the C-H borylation of p-xylene were less 0.092% and 0.037%, respectively. Finally, we observed that the removal of Co•TPY-MOL from the reaction mixture after several hours stopped the C-H borylation of p-xylene (**Scheme 5-1**).
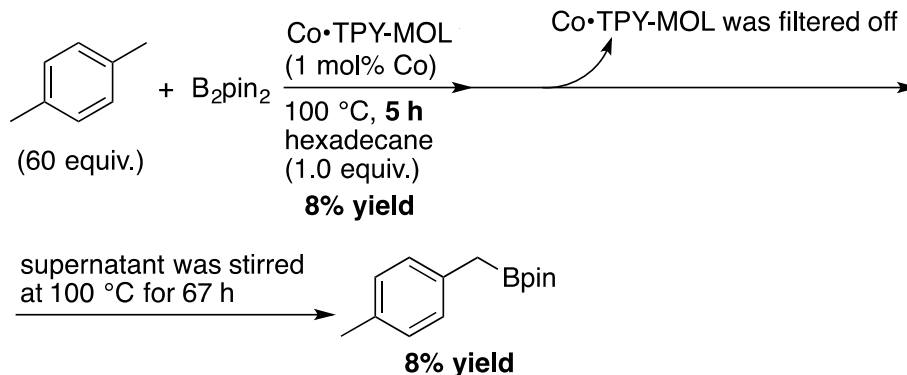
Scheme 5-1. Testing the heterogeneity of Co•TPY-MOL.
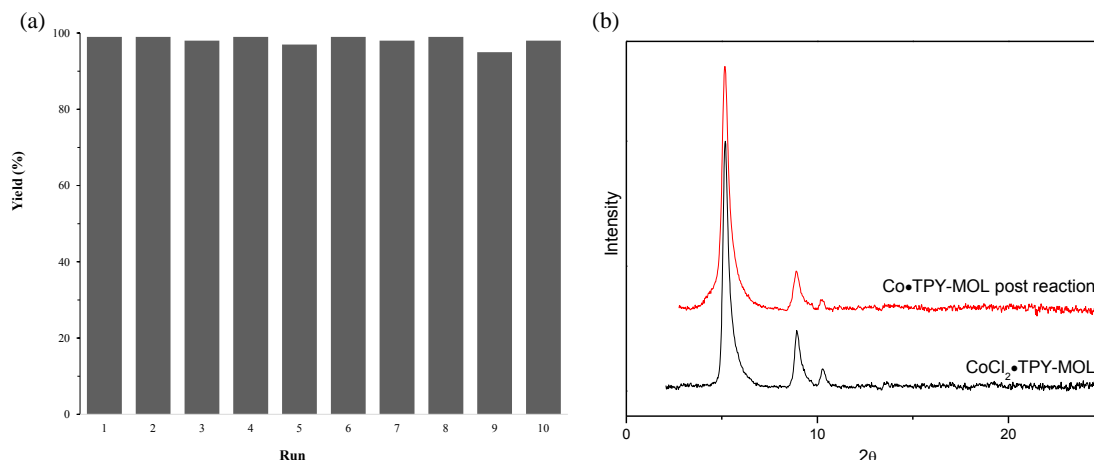
Figure 5-8. (a) Plots of yields (%) of 4,4,5,5-tetramethyl-2-(4-methylbenzyl)-1,3,2-dioxaborolane at different runs in the recycling experiments of Co•TPY-MOL for C-H borylation of *p*-xylene with B_2pin_2. The Co-loadings were 5 mol%; (b) PXRD of Co•TPY-MOL post reaction indicates the stability of MOL catalysts under reaction conditions.

5.2.3. Identification of the Co(THF)₂•TPY-MOL Catalyst

We studied the catalytically active species by hydrogen quantification, Infrared (IR), UV-Vis-NIR, XPS, and electron paramagnetic resonance (EPR) spectroscopy, XANES, EXAFS, and Density functional theory (DFT) calculations. One equiv. of H_2 was generated upon treatment of $CoCl_2$•TPY-MOL with $NaEt_3BH$, suggesting the formation of Co(THF)ₓ•TPY-MOL via

reductive elimination of H_2 from the putative $CoH_2\bullet$TPY-MOL intermediate. This 2-electron reduction process was also confirmed by titration of $Co(THF)_x\bullet$TPY-MOL with ferrocenium hexafluorophosphate which resulted in the generation of two equiv. of ferrocene w.r.t to Co•TPY-MOL. IR spectra showed no characteristic band of N≡N, ruling out the coordination of dinitrogen to Co. XANES analysis indicated +2 oxidation state for the Co centers (**Figure 5-5a**). This oxidation state assignment was further supported by XPS spectroscopy which gave a Co $2p_{3/2}$ binding energy of 781.2 eV with the expected shake-up peak for the Co^{II} centers (**Figure 5-9**).
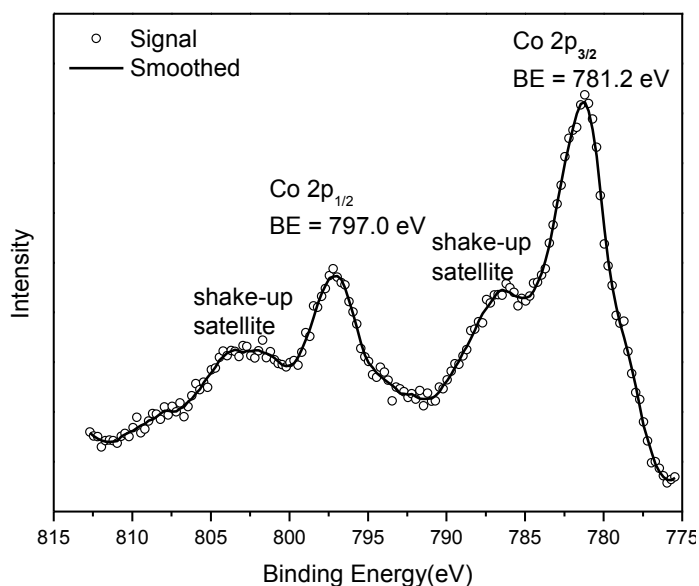
Figure 5-9. Co 2p and Fe 2p XPS spectra of $Co(THF)_2\bullet$TPY-MOL.

The EXAFS spectra at the Co K-edge were well fitted with a structural model in which Co coordinates with three N atoms of TPY and two THF molecules (**Figure 5-10**). Co-N bond distances (Co-N_c = 1.81 ± 0.02 Å, Co-N_t = 1.92 ± 0.02 Å) are shorter than those of the reported $[Co^I(tpy)_2]^{31}$ (Co-N_c = 2.003 Å, Co-N_t = 2.130Å), arguing against the +1 oxidation state for $Co(THF)_2\bullet$TPY-MOL. Furthermore, $Co(THF)_2\bullet$TPY-MOL has shorter Co-N bond distances than

those for $Co^{II}Cl_2 \cdot TPY\text{-}MOL$ ($Co\text{-}N_c = 1.90 \pm 0.01$ Å, $Co\text{-}N_t = 2.09 \pm 0.01$ Å), but similar Co-N

bond distances to a reported low-spin $Co^{II}(tpy)(BH_4)$ complex with the $(tpy^\bullet)^-$ ligand ($Co\text{-}N_c =$

1.810 Å, $Co\text{-}N_t = 1.925$ Å).[32] The Co-N bond distance analysis thus supports the formulation of

the $Co^{II}\text{-}(tpy^{\bullet\bullet})^{2-}$ electronic structure for $Co(THF)_2 \cdot TPY\text{-}MOL$.
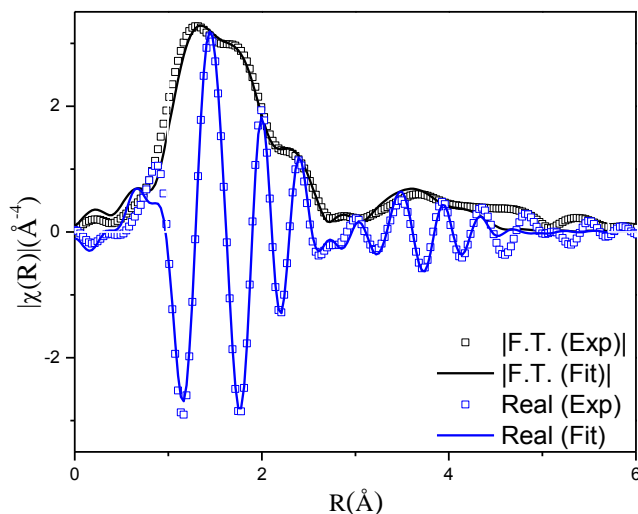
Figure 5-10. Experimental EXAFS spectra and fits of $Co(THF)_2 \cdot TPY\text{-}MOL$, R factor = 0.013 in

R space showing the magnitude of Fourier Transform (black hollow squares, black solid line)

and real components (blue hollow squares, blue solid line).

Table 5-5. Summary of EXAFS fitting parameters for Co(THF)$_2$•TPY-MOL

Sample	Co(THF)$_2$•TPY-MOL
Fitting range	k 3.00 – 10.00 Å^{-1}
	R 1.0 – 5.0 Å
Independent points	21
Variables	13
Reduced chi-square	29.81
R-factor	0.013
S_0^2	1.000
ΔE_0(eV)	1.34±2.81
R (Co-N2) (1)	1.81±0.02 Å
R (Co-N1) (2)	1.92±0.02 Å
R (Co-O) (2)	2.04±0.02 Å
R (Co-C11) (4)	2.88±0.04 Å
R (Co-C^{THF}) (4)	3.04±0.03 Å
R (Co-C1) (2)	3.13±0.09 Å
R (Co-C7) (2)	3.99±0.06 Å
R (Co-C4) (2)	4.04±0.09 Å
R (Co-C2) (2)	4.06±0.06 Å
R (Co-Co) (12)	2.51 Å
R (Co-Co) (6)	3.54 Å
σ^2 (Co-N)	0.001±0.001 Å^2
σ^2 (Co-O)	0.001±0.001 Å^2
σ^2 (Co-C^{close})	0.006±0.008 Å^2
σ^2 (Co-C^{distal})	0.010±0.006 Å^2
σ^2 (Co-Co)	0.002 Å^2
Fract	0.019±0.010

We used UV-Vis-NIR spectroscopy to discern the diradical nature of TPY ligands in CoTPY-MOLs (**Figure 5-11**). Co(THF)$_2$•TPY-MOL exhibited two intense, broad bands centered at 552 and 759 nm, and a weak but broad band at 1105 nm, indicative of π to π* and π* to π* transitions for the reduced tpy ligand.[33-37] In contrast, these bands are absent in CoCl$_2$•TPY-MOL with the neutral TPY ligand (**Figure 5-11**). The proposed (tpy$^{\bullet\bullet}$)$^{2-}$ species was previously observed in reduced M(tpy)$_2$ complexes, such as Cr^{III}(tpy)$_2$, V^{IV}(tpy)$_2$, and Ti^{IV}(tpy)$_2$, by Wieghardt and coworkers.[36,37] However, we are not aware of any example of M-tpy complexes featuring the (tpy$^{\bullet\bullet}$)$^{2-}$ species.
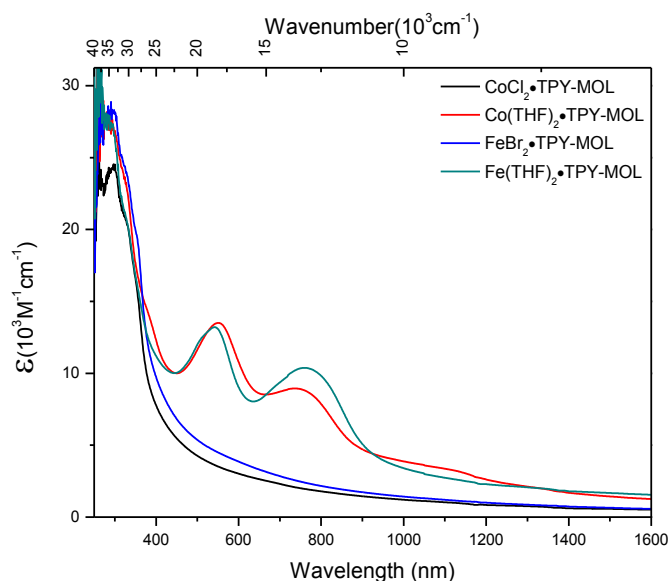
Figure 5-11. UV-Vis-NIR absorption spectra of CoCl$_2$•TPY-MOL, Co(THF)$_2$•TPY-MOL, FeBr$_2$•TPY-MOL, and Fe(THF)$_2$•TPY-MOL in THF at 25 °C.

Our XANES, EXAFS, and XPS results clearly indicate the Co^{II} oxidation state for Co(THF)$_2$•TPY-MOL whose electronic structure is best described as Co^{II}(THF)$_2$•(TPY$^{\bullet\bullet}$)$^{2-}$-MOL. The (tpy$^{\bullet\bullet}$)$^{2-}$ diradical dianion can have either a singlet (S=0) or a triplet (S=1) ground state, which can potentially be experimentally differentiated by EPR spectroscopy. EPR spectroscopy

of Co(THF)$_2$•TPY-MOL gave an isotropic signal with g$_{iso}$ = 2.003 at r.t. in a toluene suspension. The same MOL sample frozen at 20 K exhibited a stronger isotropic signal with g$_{iso}$ = 2.003, confirming that the same species was detected at r.t. and 20K (**Figure 5-12a**). More interestingly, the g value falls in the range of 2.003 – 2.005,[33,38,39] where radicals in extended organic π systems are often observed. The EPR signal intensity was temperature-dependent, which can be fitted with the Bleaney and Bowers equation[40] typically used for organic diradicals (**Figure 5-12a**). The fitting of temperature-dependent EPR signals indicates that the (TPY$^{••}$)$^{2-}$ diradical has a singlet ground state with a singlet-to-triplet energy gap of 0.04 kcal/mol. The observed EPR signal is thus attributed to the thermally populated TPY triplet excited state.[41] Moreover, a weak signal g$_{iso}$ ≈ 2.04 was observed at 20 K, consistent with low-spin Co^{II} centers. Therefore, our EPR data provide strong support to our proposed electronic structure Co^{II}(THF)$_2$•(TPY$^{••}$)$^{2-}$-MOL. We have ruled out the possibility of SBU-based free radicals because TPY-MOL treated with NaEt$_3$BH exhibited no signal at r.t. or 20K (**Figure 5-12b**).
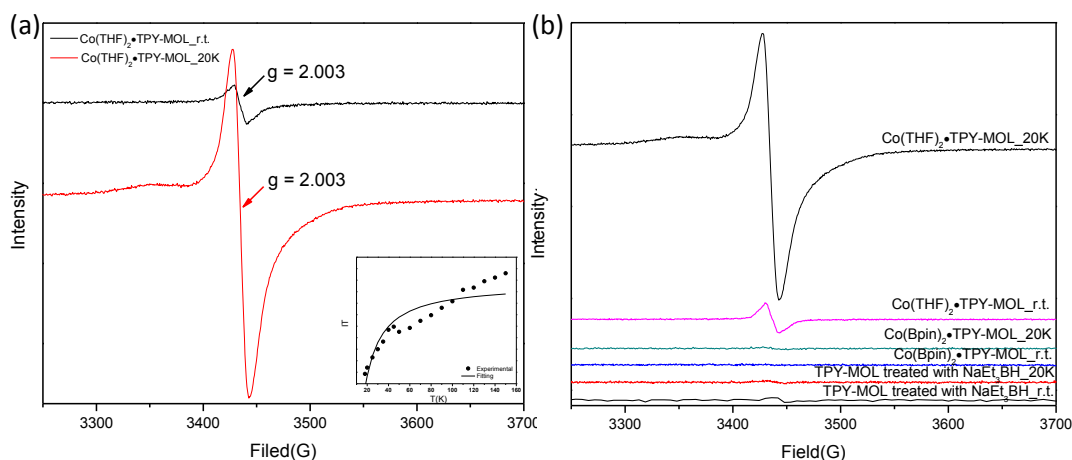
Figure 5-12. (a) X-band EPR spectra of Co(THF)$_2$•TPY-MOL suspended in toluene at r.t. and 20K. Microwave frequency: 9.629 GHz for Co(THF)$_2$•TPY-MOL at r.t.; 9.629 GHz for Co(THF)$_2$•TPY-MOL at 20K Insets are temperature-dependent EPR intensity plots and their fits

to the Bleaney and Bowers equation. The fitting results gave a singlet to triplet (TPY$^{\bullet\bullet}$)$^{2-}$ energy gap of 0.04 kcal/mol for Co(THF)$_2$•TPY-MOL; (b) X-band EPR spectra of TPY-MOL treated with NaEt$_3$BH, Co(Bpin)$_2$•TPY-MOL, and Co(THF)$_2$•TPY-MOL at r.t. and 20K.

Density functional theory (DFT) calculations and natural population analyses with the B3LYP/6-311G(d) basis set on Co(THF)$_2$•tpy gave a doublet ground state (GS) with high positive charge distribution (1.19) on the Co center and negative charge distribution (-1.29) on tpy (**Table 5-6**). A comparison charge distribution on CoCl$_2$•tpy revealed that the Co center in Co(THF)$_2$•tpy maintains +2 oxidation state. A Mulliken spin population analysis and spin density plot revealed that 0.939 unpaired spin resides on the Co center, affording a ground state with a low-spin Co^{II}, d^7 doublet (S$_{Co}$ = 1/2), and a tpy diradical dianion singlet (S$_{TPY}$ = 0) (**Figure 5-16b**). The singlet tpy diradical dianion is not expected to give any EPR signal. Interestingly, the energy of quartet state of Co(THF)$_2$•tpy is calculated to be only 0.40 kcal/mol higher than that of the doublet GS. This small energy gap is consistent to that deduced from temperature-dependent EPR signals of Co(THF)$_2$•tpy. The charge distribution of the quartet state is similar to that of the doublet GS with positive charge (1.29) on the Co center and negative charge (-1.40) on tpy (**Table 5-6**). The calculated bond distances are similar between the quartet state and the doublet GS (**Table 5-7**). A Mulliken spin density population and spin density plot of the quartet state revealed the residence of the 1.092 unpaired spin on Co center and 1.958 unpaired spins on tpy, affording a low-spin Co^{II}, d^7 doublet (S$_{Co}$ = 1/2), and a tpy triplet diradical dianion (S$_{tpy}$ = 1) (**Figure 5-16c**). The energetically accessible low-lying triplet excited state of (tpy$^{\bullet\bullet}$)$^{2-}$ was previously proposed for the hypothetical [Zn^{II}(tpy^{2-})(NH$_3$)$_2$]^0.[36] DFT calculations thus support the origin of the experimental tpy diradical dianion EPR signal as a thermally populated quartet state of Co^{II}(THF)$_2$•tpy$^{\bullet\bullet}$. Moreover, we believe that conjugation of Hf$_6$ SBU to

TPY can further stabilize TPY diradical dianion and lower energy difference between doublet and quartet states of $Co^{II}(THF)_2 \cdot TPY^{\bullet\bullet}$-MOL.

Table 5-6. NBO charge population analysis of $CoCl_2 \cdot tpy$ and $Co(THF)_2 \cdot tpy$

Fragment	$CoCl_2 \cdot tpy$	$Co(THF)_2 \cdot tpy$ _doublet	$Co(THF)_2 \cdot tpy$ _quartet
Co	1.45	1.20	1.29
tpy	0.200	-1.29	-1.40
X1	-0.824	0.025	0.080
X2	-0.822	0.067	0.030

Table 5-7. Selected DFT-calculated bond distances (Å) of complexes

X = Cl or THF
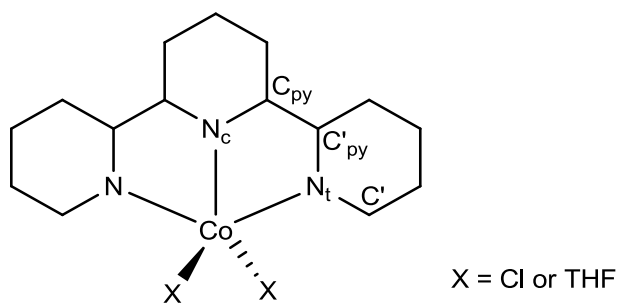
Complex	$M-N_c$	$M-N_t$	$C_{py}-C'_{py}$	N_c-C_{py}	$N_t-C'_{py}$	N_t-C'
$Co^{II}Cl_2 \cdot (tpy^0)$	2.046	2.172	1.489	1.342	1.351	1.334
$Co^{II}(THF)_2 \cdot (tpy^{2-})$	1.838[a]	1.940[a]	1.427[a]	1.383[a]	1.409[a]	1.355[a]
	1.856[b]	1.953[b]	1.423[b]	1.371[b]	1.411[b]	1.346[b]

[a]$(tpy^{\bullet\bullet})^{2-}$ ($S = 0$) ground state. [b]$(tpy^{\bullet\bullet})^{2-}$ ($S = 1$) excited state
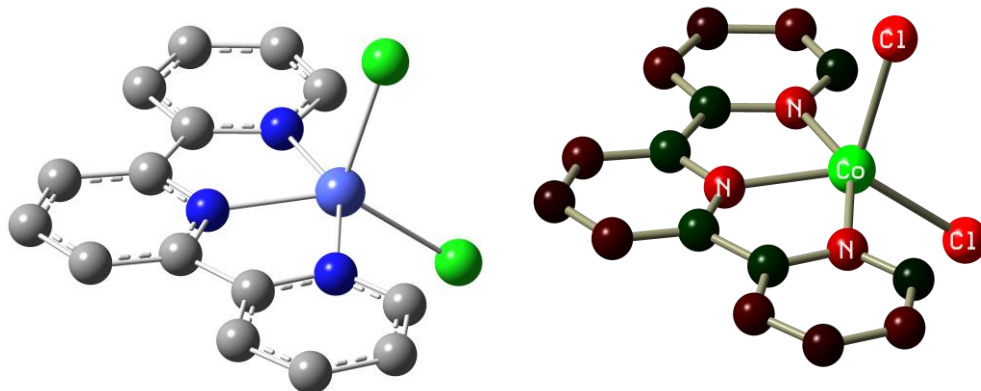
Figure 5-13. Optimized structure and calculated NBO charge distribution of CoCl$_2$•tpy. Positively charged and negatively charged atoms are denoted by green and red colors.

2.687
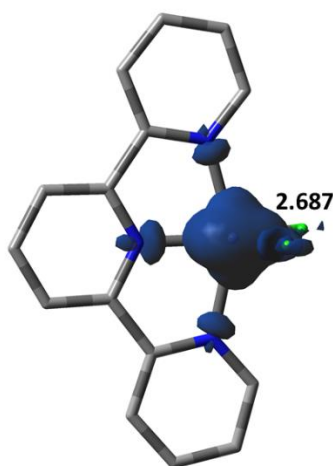
Figure 5-14. Spin density plot (blue: positive, green: negative) of CoCl$_2$•tpy.
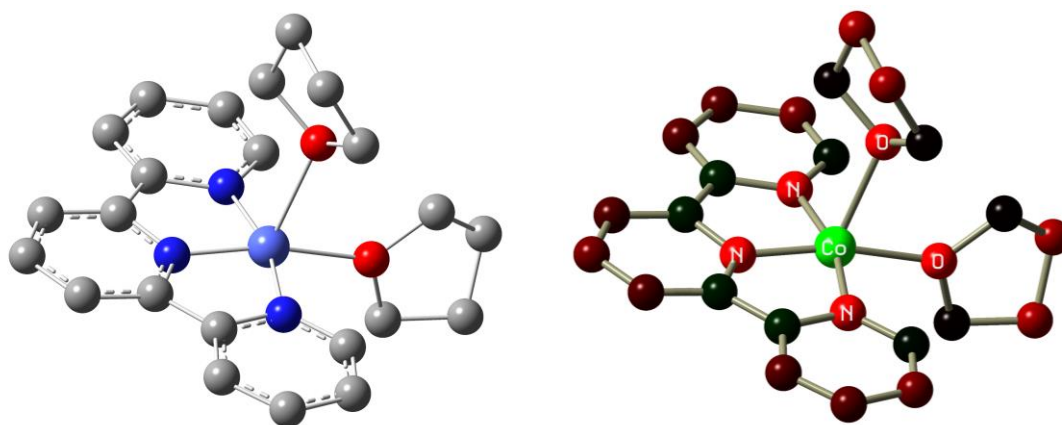
Figure 5-15. Optimized structure and calculated NBO charge distribution of Co(THF)₂•tpy. Positively charged and negatively charged atoms are denoted by green and red colors.
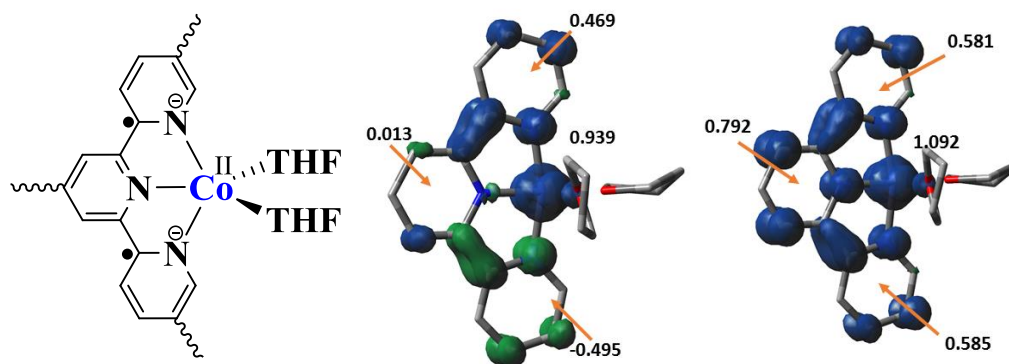
Figure 5-16. Proposed electronic structure of $Co^{II}(THF)_2 \cdot (TPY^{\cdot\cdot})^{2-}$-MOL (left); calculated Milliken spin density distribution and spin density plots (blue: positive; green: negative) of Co(THF)₂•tpy doublet state (middle) and Co(THF)₂•tpy quintet state (right)

We also investigated the activation of CoCl₂•tpy molecular complex with NaEt₃BH. Upon treating CoCl₂•tpy in THF with 10 equiv of NaEt₃BH, the mixture turned dark green immediately with concomitant formation of Co nanoparticles as black precipitate (**Figures 5-17** and **5-18**). The solution was filtered through Celite and evaporated to afford Co(tpy)₂ (HR-MS calculated for $C_{30}H_{22}N_6Co$ [M+]: 525.1238, found: 525.1257). EPR of Co(tpy)₂ at both r.t. and

20K gave a broad spectrum that exhibited a g value of 2.18 (**Figure 5-19**). This EPR spectrum is consistent with an S = 3/2 spin state assignment, similar to that reported for (^{Ar}tpy)$_2$Co.[23]
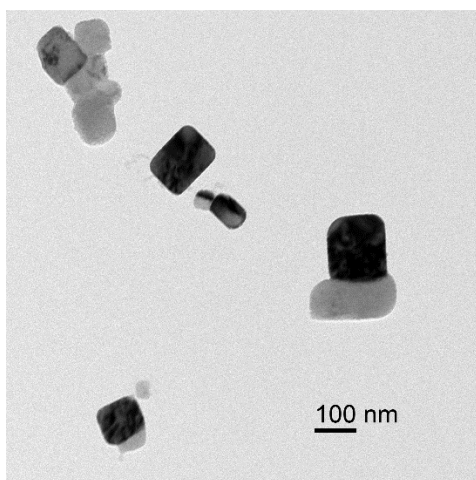
Figure 5-17. Transmission electron microscope (TEM) image of Co nanoparticles generated by treating CoCl$_2$•tpy with NaEt$_3$BH.
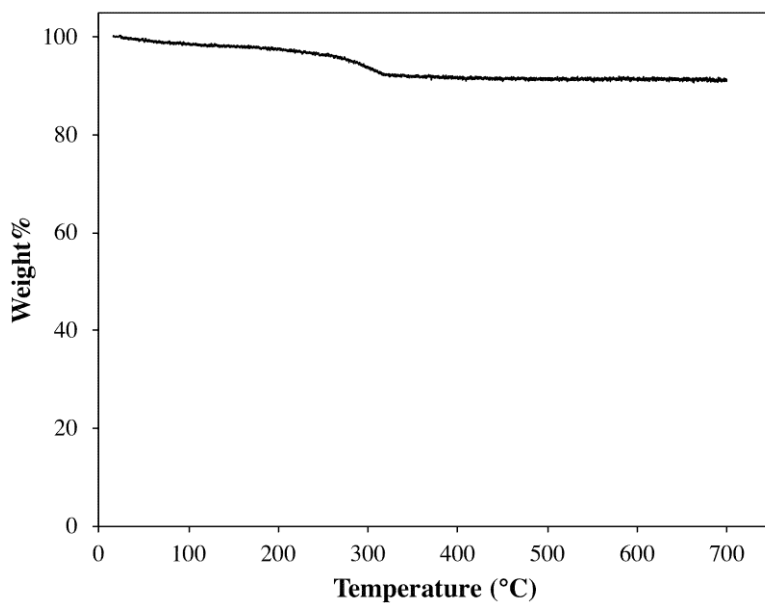
Figure 5-18. TGA curve of Co nanoparticles generated by treating CoCl$_2$•tpy with NaEt$_3$BH. 3.6% weight loss from 15 to 200° C is from the trapped solvent. 5.4% weight loss from 200 to

Figure 5-18, continued 700 °C should be from unreacted CoCl₂•tpy which has poor solubility in THF. Calculated weight percentage for CoCl₂•tpy is 16.2% for Co, 64.2% for tpy, and 19.5% for 2Cl. Therefore, the majority of the black precipitates are Co nanoparticles.
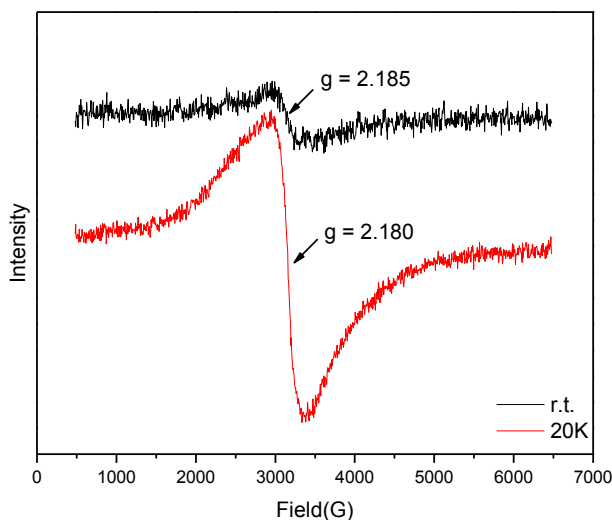
Figure 5-19. X-band EPR spectra of Co(tpy)₂ in toluene at r.t. and 20K. Microwave frequency: 9.634 GHz at r.t.; 9.632 GHz at 20K.

5.2.4. Mechanistic Studies of Co(THF)₂•TPY-MOL Catalyzed C-H Borylation

To gain insight into the mechanism of the C-H borylation reaction, we carried out several experiments. First, we performed kinetic isotope effect (KIE) studies in order to afford information on the rate-determining step of the C-H borylation reactions. The initial rates of C-H borylations with *p*-xylene and *p*-xylene-*d*₈ were determined by running parallel reactions in separate vessels, and the comparison of the initial rates gave a KIE value of 2.7 (**Scheme 5-2**). Such a primary KIE indicates the involvement of the C-H bond breaking in the rate-determining step.
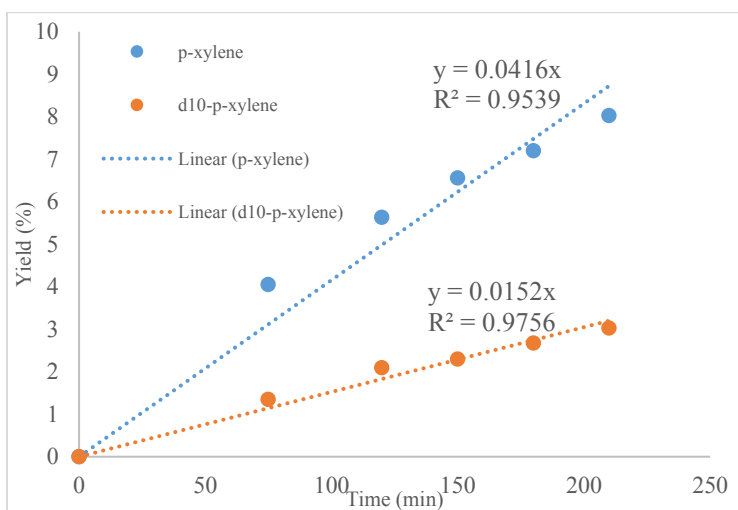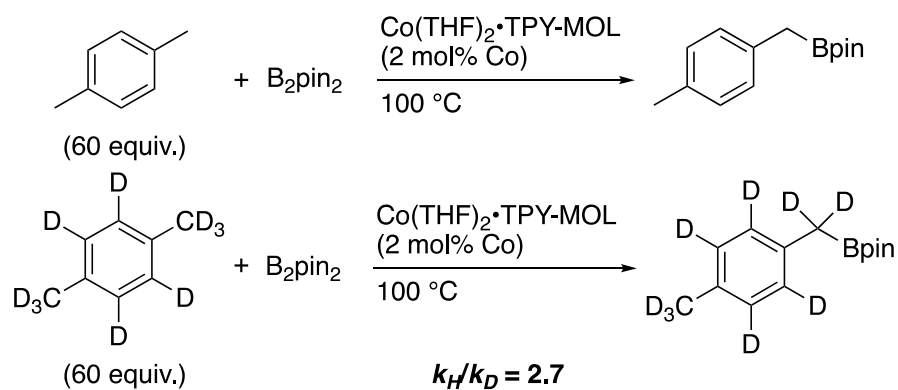
Scheme 5-2. Measurement of the kinetic isotope effect of C-H active borylation.

Second, we detected the presence of HBpin by gas chromatography-mass spectrometry (GC-MS) at the end of the C-H borylation reactions. Third, we determined the resting state of the catalyst by EXAFS studies. By treating Co(THF)$_2$•TPY-MOL with 20 equiv of B$_2$pin$_2$, we obtained the Co(Bpin)$_2$•TPY-MOL product in which Co coordinates to three N atoms of TPY and two Bpin groups according to EXAFS fitting. To determine the resting state of the catalyst, the C-H borylation reaction was stopped at 70% conversion, and the organic volatiles were evaporated. EXAFS studies indicated that the remaining residue (Co•TPY-MOL-post) had the same structure as Co(Bpin)$_2$•TPY-MOL. Finally, EPR spectra of Co(Bpin)$_2$•TPY-MOL did not

show any signals corresponding to a TPY-based radical EPR signal (**Figure 5-12b**), suggesting a typical Co^{II}•TPY complex with negative charge localized on the Bpin ligands.
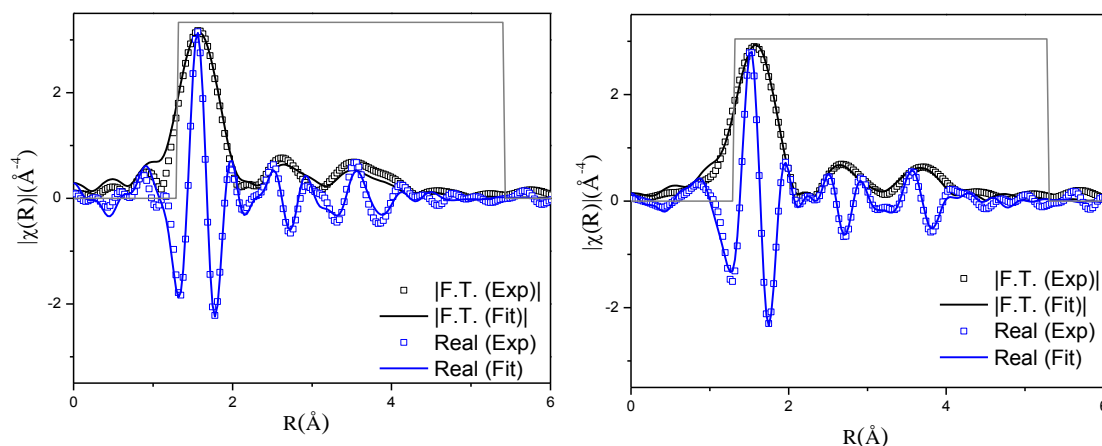
Figure 5-20. Experimental EXAFS spectra and fits of Co(Bpin)$_2$•TPY-MOL (left) and Co•TPY-MOL-post (right) in R space showing the magnitude of Fourier Transform (black hollow squares, black solid line) and real components (blue hollow squares, blue solid line). The fitting range was 1.0 – 5.7 Å in R space (within the dashed lines).

Table 5-8. Summary of EXAFS fitting parameters for Co(Bpin)$_2$•TPY-MOL and Co•TPY-MOL-post

Sample	Co(Bpin)$_2$•TPY-MOL	Co•TPY-MOL-post
Fitting range	k 3.10 – 10.30 Å^{-1}	k 3.20 – 10.60 Å^{-1}
	R 1.3 – 5.4 Å	R 1.3 – 5.3 Å
Independent points	18	18
Variables	12	12
Reduced chi-square	58.38	4.78
R-factor	0.023	0.010
S_0^2	1.000	1.000
ΔE_0(eV)	-3.20±1.84	1.23±1.88

Table 5-8, continued

R (Co-N2) (1)	1.99±0.01 Å	1.98±0.01 Å
R (Co-N1) (2)	2.07±0.01 Å	2.06±0.01 Å
R (Co-B) (2)	2.01±0.06 Å	2.00±0.03 Å
R (Co-C11) (4)	2.91±0.04 Å	2.89±0.03 Å
R (Co-O^{Bpin}) (4)	3.01±0.03 Å	3.00±0.02 Å
R (Co-C1) (2)	3.21±0.08 Å	3.23±0.01 Å
R (Co-C7) (4)	4.21±0.01 Å	4.21±0.05 Å
R (Co-C2) (2)	4.33±0.01 Å	4.43±0.05 Å
σ^2 (Co-N)	0.005±0.001 Å^2	0.007±0.001 Å^2
σ^2 (Co-B)	0.021±0.013 Å^2	0.022±0.011 Å^2
σ^2 (Co-O)	0.010±0.001 Å^2	0.009±0.004 Å^2
σ^2 (Co-C^{close})	0.010±0.003 Å^2	0.012±0.006 Å^2
σ^2 (Co-C^{distal})	0.018±0.015 Å^2	0.014±0.004 Å^2

On the basis of these experimental and calculation results, we propose a catalytic cycle for the C-H active borylation of methylarenes as shown in **Scheme 5-3**. The CoCl$_2$•(TPY)-MOL (I) is activated by NaEt$_3$BH in THF to give the CoH$_2$•(TPY)-MOL (II) intermediate, which quickly undergoes reductive elimination of H$_2$ to produce the Co^{II}(THF)$_2$•TPY$^{••}$-MOL (III) catalyst. Oxidative addition of B$_2$(pin)$_2$ to III results in Co(Bpin)$_2$•TPY-MOL (IV), which is the catalyst resting state for the C-H borylation reactions. σ-Bond metathesis between IV and methylarene proceeds as a rate-determining step to form Co(H)(Bpin)(TPY) (V) and the benzylic borylated product. The reaction of V with B$_2$pin$_2$ regenerates the intermediate IV and forms HBpin as a byproduct.
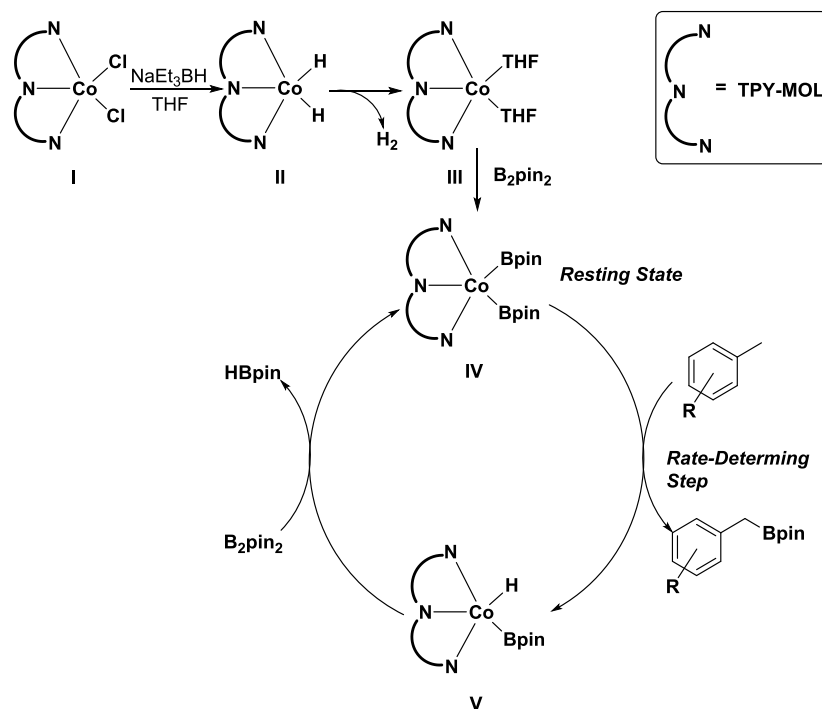
Scheme 5-3. Proposed Mechanism for the Co(THF)$_2$•TPY-MOL catalyzed C-H borylation of arenes with B$_2$pin$_2$.

5.2.5. Fe•TPY-MOL Catalyzed Intramolecular sp^3 C-H Amination

TPY-MOL was metalated with FeBr$_2$(THF)$_2$ to generate FeBr$_2$•TPY-MOL. Similar to the Co(THF)$_2$•TPY-MOL case, when FeBr$_2$•TPY-MOL was treated with 10 equiv of NaEt$_3$BH, Fe(THF)$_2$•TPY-MOL was generated along with one equiv. of H$_2$. This 2-electron reduction process was also confirmed by titration of Fe(THF)$_2$ • TPY-MOL with ferrcenium hexafluorophosphate which resulted in the generation of two equiv. of ferrocene. EXAFS fitting indicates Fe coordinates to three N from TPY and two THF molecules for Fe(THF)$_2$•TPY-MOL (**Figure 5-21**) while infrared spectroscopy indicates no coordination of dinitrogen to Fe centers. The oxidation state of Fe(THF)$_2$•TPY MOL was determined to be +2 by XANES analysis (**Figure 5-5**) since the pre-edge position for Fe(THF)$_2$•TPY-MOL (7111.6 eV) aligned well with FeBr$_2$(THF)$_2$ (7111.5 eV), FeBr$_2$•TPY-MOL (7111.5 eV), and two reported five-coordinate

species (^{iPr}PDI)FeCl$_2$ (7111.8eV) and (^{iPr}PDI)Fe(N$_2$)$_2$ (7111.9 eV).[42] Interestingly, a second feature was 7113.2 eV for Fe(THF)$_2$•TPY-MOL, assignable to the 1s to ligand π* transitions. This feature was also observed in a reported (^{iPr}PDI^{2-})Fe^{II}(N$_2$)$_2$ species (7114.0 eV). It is worth mentioning that [Fe(tpy)$_2$]$^{n+}$ (n = 0, 1, 2) were all determined to have Fe^{II} centers.[43] Furthermore, XPS spectroscopy clearly shows Fe^{II} oxidation state for Fe(THF)$_2$•TPY-MOL based on characteristic Fe 2P$_{3/2}$ binding energy of 709.2 eV and shake-up peaks (**Figure 5-22**).
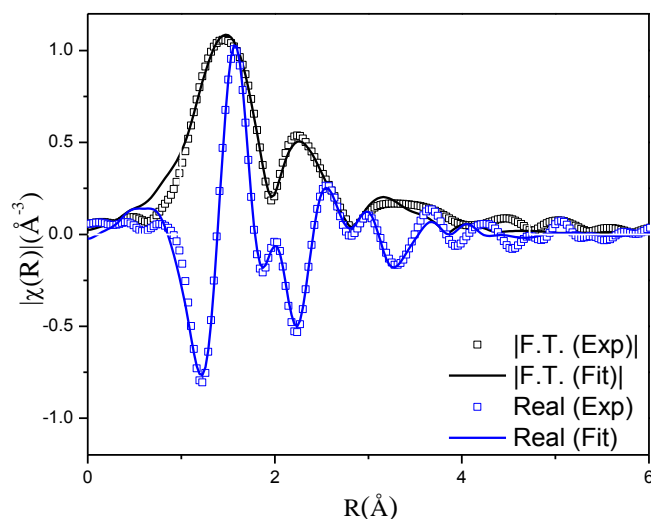
Figure 5-21. Experimental EXAFS spectra and fits of Fe(THF)$_2$•TPY-MOL, R factor = 0.015 in R space showing the magnitude of Fourier Transform (black hollow squares, black solid line) and real components (blue hollow squares, blue solid line).

Table 5-9. Summary of EXAFS fitting parameters for Fe(THF)$_2$•TPY-MOL

Sample	Fe(THF)$_2$•TPY-MOL
Fitting range	k 1.50 – 10.60 Å^{-1}
	R 1.0 – 4.7 Å
Independent points	21
Variables	14
Reduced chi-square	62.76
R-factor	0.015
$S_0{}^2$	1.000
ΔE_0(eV)	-1.94±1.05
R (Fe-N2) (1)	1.94±0.02 Å
R (Fe-N1) (2)	2.13±0.02 Å
R (Fe-O) (2)	2.00±0.02 Å
R (Fe-C16) (2)	3.12±0.04 Å
R (Fe-C17) (2)	3.17±0.04 Å
R (Fe-C1) (2)	3.47±0.05 Å
R (Fe-C^{THF}) (4)	2.95±0.04 Å
R (Fe-C15) (2)	4.34±0.09 Å
R (Fe-C18) (2)	4.47±0.09 Å
R (Fe-C8) (2)	4.37±0.07 Å
σ^2 (Fe-N)	0.001±0.001 Å^2
σ^2 (Fe-O)	0.010±0.003 Å^2
σ^2 (Fe-C^{close})	0.001±0.001 Å^2
σ^2 (Fe-C^{distal})	0.016±0.014 Å^2
σ^2 (Fe-C^{THF})	0.004±0.006 Å^2
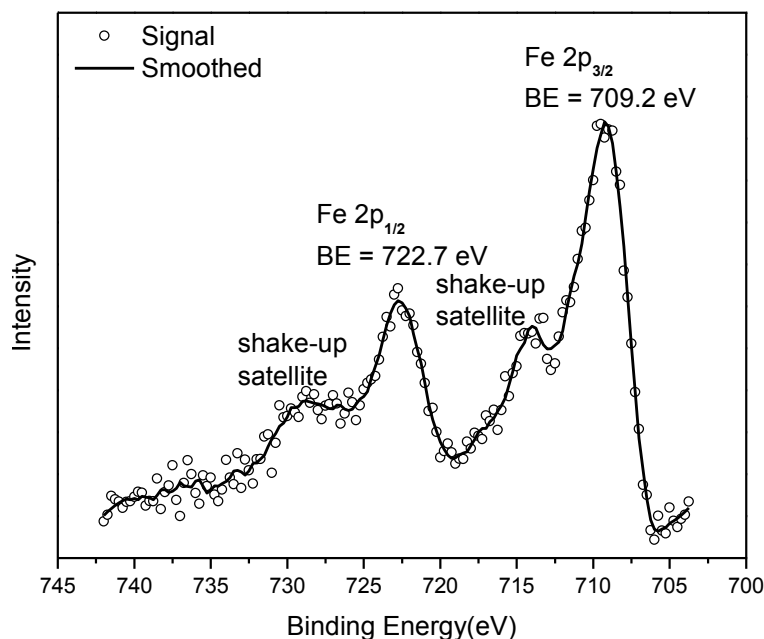
Figure 5-22. Fe 2p and Fe 2p XPS spectra of Fe(THF)$_2$•TPY-MOL.

The electronic spectrum of Fe(THF)$_2$•TPY-MOL is very similar to that of Co^{II}(THF)$_2$•(TPY$^{\bullet\bullet}$)$^{2-}$-MOL, indicating the presence of (TPY$^{\bullet\bullet}$)$^{2-}$ diradical dianion on Fe(THF)$_2$•TPY-MOL (**Figure 5-11**). Fe(THF)$_2$•TPY-MOL gave an EPR signal with g_{iso} = 2.003 at r.t. in a toluene suspension. The same MOL sample frozen at 20 K exhibited a stronger signal with g_{iso} = 2.003 (**Figure 5-23**). The fitting of temperature-dependent EPR signals indicates that the (TPY$^{\bullet\bullet}$)$^{2-}$ diradical has a singlet ground state with singlet-to-triplet energy gap of 0.10 kcal/mol. The observed EPR signal is thus attributed to the thermally populated TPY triplet excited (**Figure 5-23**).[41] Therefore, the EPR data provide strong evidence of our proposed electronic structure of the Fe^{II}(THF)$_2$•(TPY$^{\bullet\bullet}$)$^{2-}$-MOL catalyst.
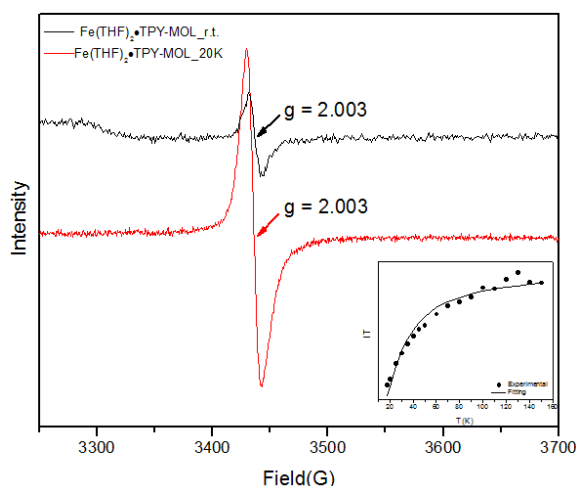
Figure 5-23. (a) X-band EPR spectra of Fe(THF)$_2$•TPY-MOL suspended in toluene at r.t. and 20K. Microwave frequency: 9.634 GHz for Fe(THF)$_2$•TPY-MOL at r.t.; 9.630 GHz for Fe(THF)$_2$•TPY-MOL at 20K Insets are temperature-dependent EPR intensity plots and their fits to the Bleaney and Bowers equation. The fitting results gave a singlet to triplet (TPY$^{••}$)$^{2-}$ energy gap of 0.10 kcal/mol for Fe(THF)$_2$•TPY-MOL.

DFT calculations and natural population analyses with the B3LYP/6-311G(d) basis set on Fe(THF)$_2$•tpy gave a triplet GS with high positive charge distribution (1.29) on the Fe center and negative charge distribution (-1.39) on tpy (**Table 5-10**). As compared to charge distribution on FeBr$_2$•tpy, Fe(THF)$_2$•tpy remains +2 oxidation state on Fe. A Mulliken spin population analysis and spin density plot of the GS revealed that 2.027 unpaired spins reside on the Fe center, affording an intermediate-spin Fe^{II}, d^6 center (S_{Fe} = 1), and a tpy singlet diradical dianion antiferromagnetically coupled to each other (S_{tpy} = 0) (**Figure 5-27**). The GS of Fe(THF)$_2$•tpy again is not expected to give any organic radical EPR signal. We believe that the experimental tpy EPR signal comes from thermal population of the quintet state of Fe(THF)$_2$•tpy which is calculated by DFT to be only 5.26 kcal/mol higher in energy than that of triplet GS, consistent to our variable-temperature EPR analysis. The charge distribution of the quintet state is similar to

that of triplet GS with positive charge (1.34) on the Fe center and negative charge (-1.44) on tpy

(**Table 5-10**). A Mulliken spin population analysis and spin density plot revealed that 2.093

unpaired spins reside on the Fe center and 1.961 unpaired spins on tpy, affording an

intermediate-spin Fe^{II}, d^6 compound ($S_{Fe} = 1$), and a tpy triplet diradical dianion ($S_{TPY} = 1$)

(**Figure 5-27**), which is consistent with our experimental EPR results. The coordination of Hf_6

SBUs to TPY is expected to further stabilize TPY diradical dianion and lower energy difference

between triplet and quintet states of $Fe^{II}(THF)_2$•TPY$^{\bullet\bullet}$-MOL.

Table 5-10. NBO charge population analysis of FeBr$_2$•tpy, and Fe(THF)$_2$•tpy.

Fragment	FeBr$_2$•tpy	Fe(THF)$_2$•tpy _triplet	Fe(THF)$_2$•tpy _quintet
Fe	1.50	1.29	1.34
tpy	-0.148	-1.39	-1.44
X1	-0.668	0.026	0.028
X2	-0.683	0.068	0.074

Table 5-11. Selected DFT-calculated bond distances (Å) of complexes
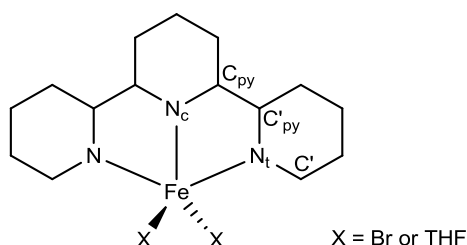
Complex	M-N$_c$	M-N$_t$	C$_{py}$-C'$_{py}$	N$_c$-C$_{py}$	N$_t$-C'$_{py}$	N$_t$-C'
Fe^{II}Br$_2$•(tpy^0)	2.149	2.202	1.487	1.340	1.352	1.336
Fe^{II}(THF)$_2$•(tpy^{2-})	1.856[a]	1.967[a]	1.429[a]	1.387[a]	1.410[a]	1.358[a]
	1.885[b]	1.992[b]	1.425[b]	1.373[b]	1.412[b]	1.348[b]

[a](tpy$^{\bullet\bullet}$)$^{2-}$ ($S = 0$) ground state. [b](tpy$^{\bullet\bullet}$)$^{2-}$ ($S = 1$) excited state
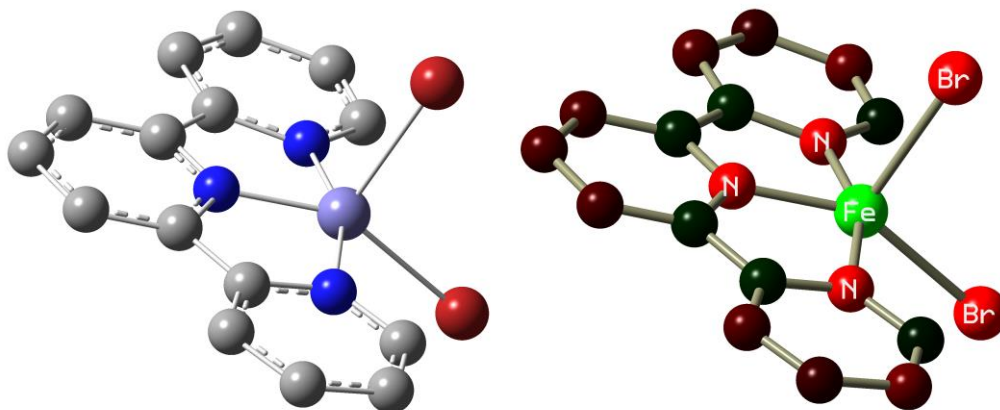
Figure 5-24. Optimized structure and calculated NBO charge distribution of $FeBr_2 \cdot$ tpy. Positively charged and negatively charged atoms are denoted by green and red colors.
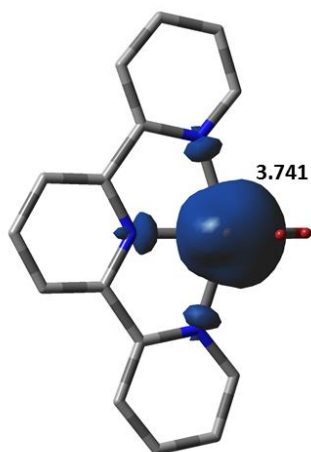
Figure 5-25. Spin density plot (blue: positive, green: negative) of $FeBr_2 \cdot$ tpy.
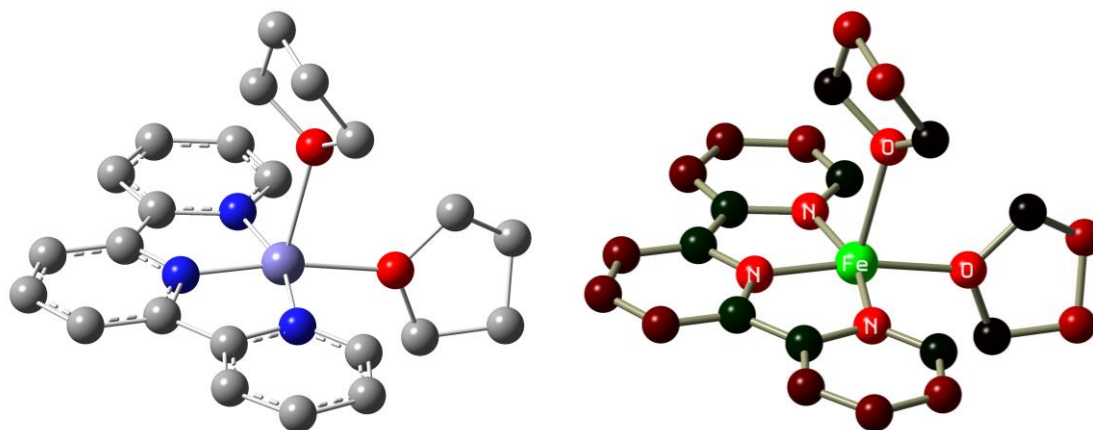
Figure 5-26. Optimized structure and calculated NBO charge distribution of Fe(THF)$_2$•tpy. Positively charged and negatively charged atoms are denoted by green and red colors.
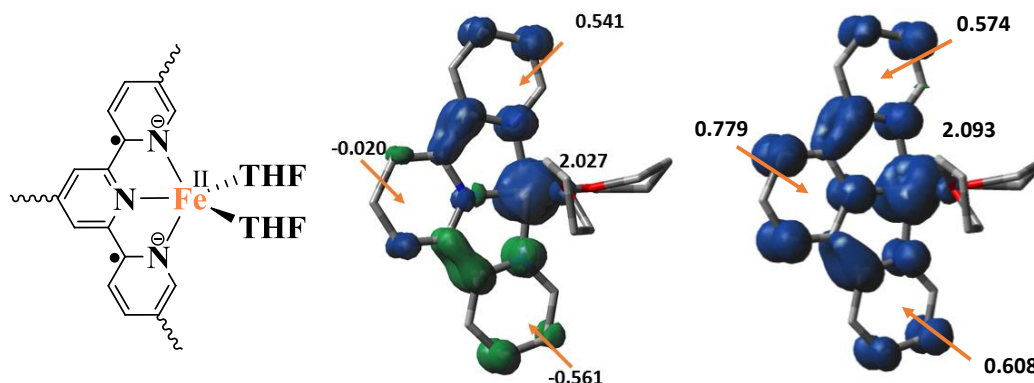
Figure 5-27. Proposed electronic structure of Fe^{II}(THF)$_2$•(TPY$^{··}$)$^{2-}$-MOL (left); calculated Milliken spin density distribution and spin density plots (blue: positive; green: negative) of Fe(THF)$_2$•tpy doublet state (middle) and Fe(THF)$_2$•tpy quintet state (right)

Upon activation with NaEt$_3$BH, 2 mol% of FeBr$_2$•TPY-MOL catalyzed intramolecular C$_{sp3}$-H amination of 1-azido-4-phenylbutane (**1a**) in the presence of two equivalents of di-tert-butyl dicarbonate (Boc$_2$O) at 90 °C to form Boc-protected α-phenyl pyrrolidine (**2a**) in 89% yield. This level of activity is 9 times as high as that of the MOF control (**Table 5-12**, entry 4). Under

identical conditions, the homogeneous tpy-Fe catalyst only afforded the product in 3% yield, probably due to the deactivation of tpy-Fe catalyst via bimolecular pathways (**Table 5-12**, entry 5). Indeed, Treatment of $FeBr_2 \cdot tpy$ with 10 equiv. of $NaEt_3BH$ produced a mixture $Fe(tpy)_2$ (ESI-MS calculated for $C_{30}H_{22}N_6Fe$ [M+]: 525.39, found: 522.5) and Fe nanoparticles (**Figure 5-28** to **5-30**); such a disproportionation reaction was previously observed for a series of $(PDI)FeBr_2$ complexes.[69-70]
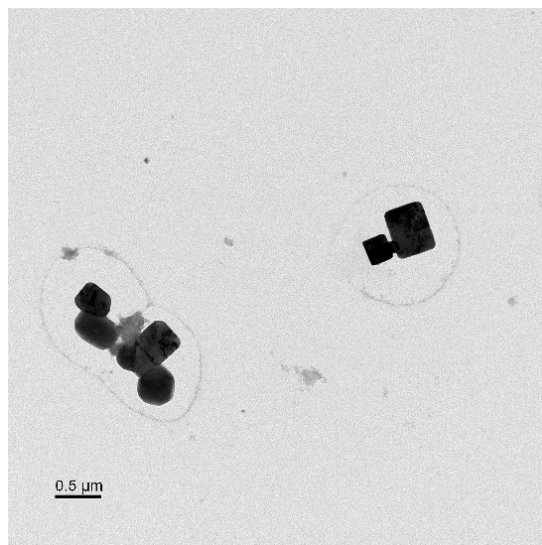
Figure 5-28. Transmission electron microscope (TEM) image of Fe nanoparticles generated by treating $FeBr_2 \cdot tpy$ with $NaEt_3BH$.
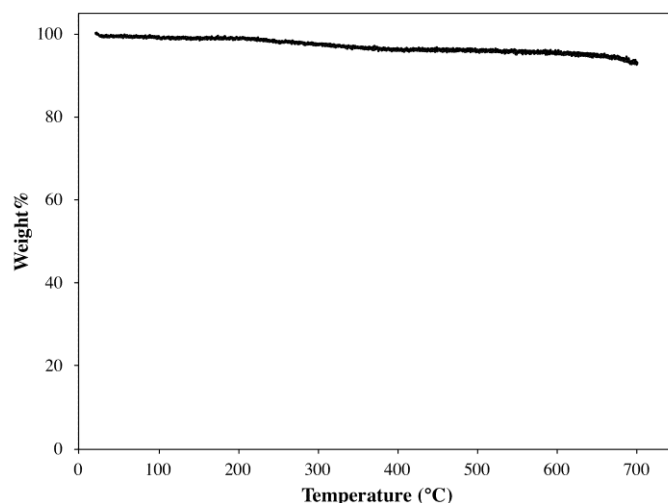
Figure 5-29. TGA curve of Fe nanoparticles generated by treating FeBr$_2$•tpy with NaEt$_3$BH. 1.0%

weight loss from 20 to 200°C is from the trapped solvent. 5.9% weight loss from 200 to 700°C

should be from unreacted Fe(tpy)Br$_2$ which has poor solubility in THF. Calculated weight

percentage for Fe(tpy)Br$_2$ is 12.4% for Fe, 52.0% for tpy, and 35.6% for 2Br. Therefore, the

majority of the black precipitates are Fe nanoparticles.
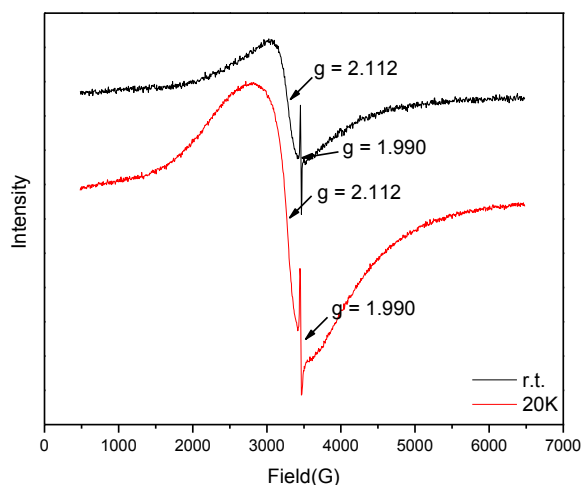
Figure 5-30. X-band EPR spectra of Fe(tpy)$_2$ in toluene at r.t. and 20K. Microwave frequency:

9.634 GHz at r.t.; 9.632 GHz at 20K. EPR spectra of Fe(tpy)$_2$ at r.t. and 20K gave a broad peak

with g = 2.112 and another sharp peak with g = 1.990, which contradicts a previous report for

187

Figure 5-30, continued Fe(tpy)$_2$.[34] We believe that the two EPR signals come from the monoanion [Fe(tpy)$_2$]$^-$ and the monocation [Fe(tpy)$_2$]$^+$ that results from the disproportionation reaction of Fe(tpy)$_2$.[43]

A higher TON of 76 was achieved when the Fe loading was decreased to 1 mol% (**Table 5-12**, entry 2). With a much simpler ligand, Fe-TPY-MOL outperformed Betley's Fe-dipyrrinato homogenous catalyst by 13 times,[44] and our recently reported NacNac-MOF catalysts by 4 times[9] in TONs. It is worth noting that FeBr$_2$•TPY-MOL without activation with NaEt$_3$BH showed low activity (**Table 5-12**, entry 3), suggesting that the formation of Fe-nitrene compound might be a key elementary step of the intramolecular C$_{sp3}$-H amination reaction.[44-50]

Table 5-12. Iron catalyzed intramolecular C-H amination
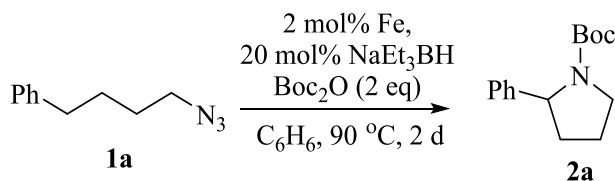
Entry	Catalyst	Yield (%)[a]	TON
1	FeBr$_2$•TPY MOL	89	44.5
2[b]	FeBr$_2$•TPY MOL	76	76
3[c]	FeBr$_2$•TPY MOL	16	8
4	FeBr$_2$•TPY MOF	10	5
5	"Homogeneous" Fe(tpy)Br$_2$	3	1.5

[a] NMR Yield with MeNO$_2$ as an internal standard; [b] 1 mol% Fe loading; c without addition of NaEt$_3$BH.

We further explored the substrate scope of intramolecular C$_{sp}$^{3}-H amination reactions. At 2 mol% catalyst loading, and in the presence of 2 equiv. of Boc$_2$O, the 2, 2-dimethylpyrrolidine (2b) was formed in 57% yield. Due to reactivity of the vinyl substituent in 2c, 5 eq of Boc$_2$O was required to give modest yield at 2 mol% Fe. Since the MOL catalysts are free from diffusion

constraints, substrates with a bulky substituent such as 3, 5-diphenylphenyl were also tolerated and gave 75% yield at 5 mol% Fe and 2 eq of Boc$_2$O.
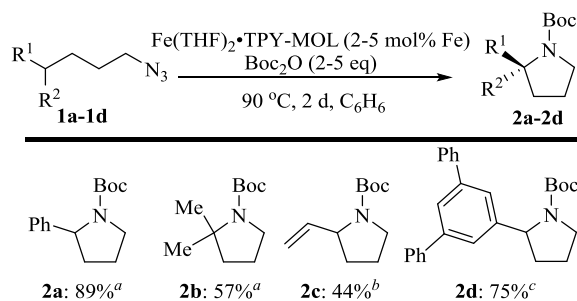
Figure 5-31. Substrate scope for α-substituted pyrrolidine synthesis. Reaction conditions: [a]Fe (2 mol%), Boc$_2$O (2 equiv.); [b]Fe (2 mol%), Boc$_2$O (5 equiv.); [c]Fe (5 mol%), Boc$_2$O (2 equiv.).

Piperidines can also be formed via C-H amination with the Fe•TPY-MOL catalyst. For example, 7-azidohept-1-ene was converted to the exclusively six-member ring product 1-Boc-2-vinylpiperidine in 37% yield. By comparison, Betley's Fe-dipyrrinato homogenous catalyst required a stoichiometric equivalent of catalyst to obtain 45% yield. Furthermore, the 1-Boc-2,2-dimethylpiperidine and 1-Boc-2-phenylpiperidine could also be formed from alkyl azides. In these examples, the pyrrolidine products were also observed.
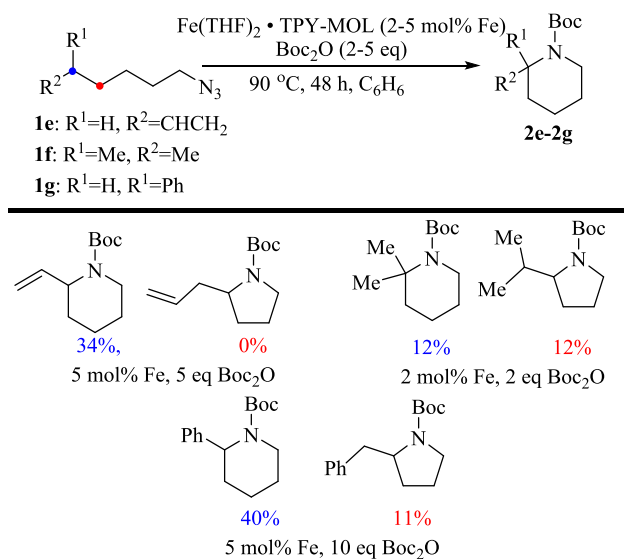
Figure 5-32. Substrate scope for α-substituted piperidine synthesis.

PXRD pattern of Fe•TPY-MOL catalysts recovered from C_{sp3}-H amination reactions suggested that the integrity of the MOL was maintained under reaction conditions (**Figure 5-33**). ICP-MS of the supernatant showed < 0.1% of Fe and < 0.1% of Hf had leached into the supernatant. The Fe•TPY MOL catalyst could be recovered and reused four times (**Scheme 5-4**). Furthermore, the heterogeneous nature of the Fe•TPY-MOL catalysts was confirmed by the lack of activity for the reaction supernatant after removing MOLs by centrifugation (**Scheme 5-5**).
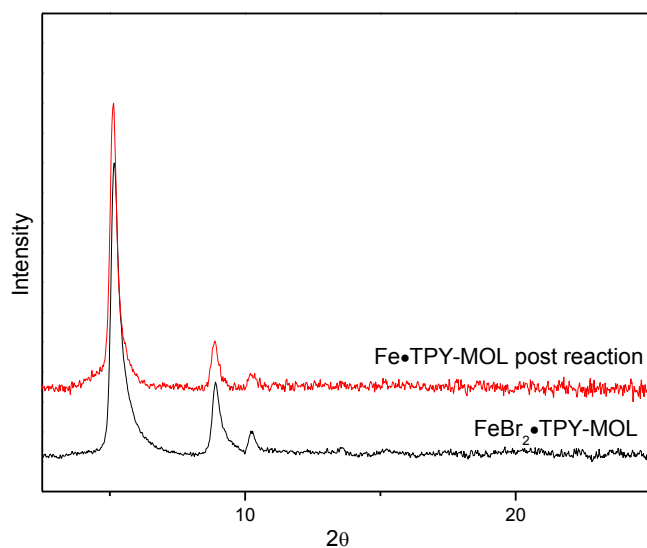
Figure 5-33. PXRD of Fe•TPY-MOL post reaction indicates the stability of MOL catalysts under reaction conditions.
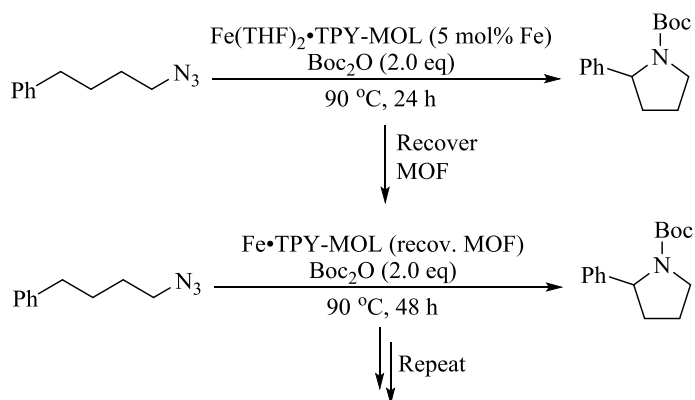
Run	Yield	Starting Material Remaining
1	100%	0%
2	60%	35%
3	59%	41%
4	53%	~50%
5	40%	~60%

Scheme 5-4. Recycling experiments for Fe(THF)$_2$•TPY-MOL catalyzed Csp^3 C-H Amination
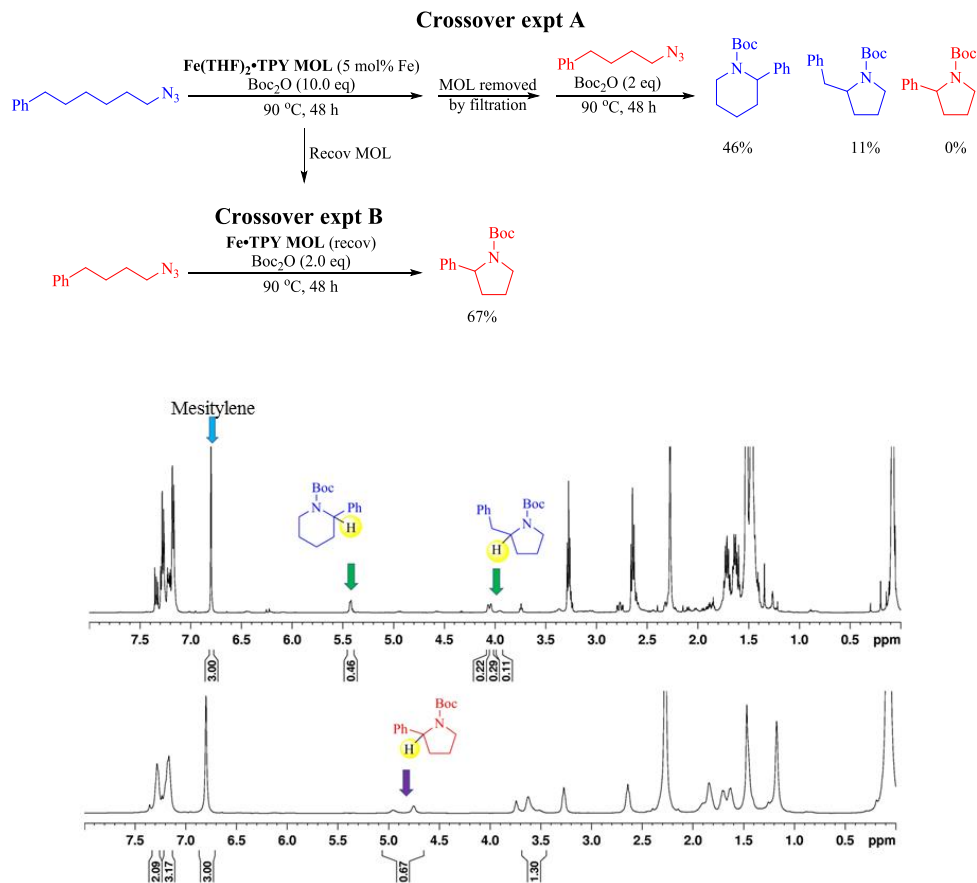
Scheme 5-5. Heterogeneity test and cross-over experiments of Fe(THF)$_2$•TPY-MOL catalyzed C$_{sp}^3$ C-H Amination

5.3. Conclusion

We have synthesized a terpyridine-based TPY-MOL and metalated TPY-MOL with CoCl$_2$ and FeBr$_2$ to generate M•TPY-MOL catalysts for benzylic C-H borylation and C$_{sp3}$-H amination reactions. Interestingly, M•TPY-MOL catalysts showed significantly higher activity and different chemo-selectivity than homogeneous and MOF controls. Spectroscopic studies and DFT calculations indicated the formation of unprecedented MOL-stabilized M^{II}-(TPY$^{••}$)$^{2-}$ species featuring divalent metals and TPY diradical dianions. We believe that the formation of novel M^{II}-TPY$^{••}$ (M = Co or Fe) species endows them with unique and enhanced catalytic activities in

C_{sp3}-H borylation and intramolecular C_{sp3}-H amination reactions. Our work demonstrates the ability to engineer MOLs as single-site solid catalysts without diffusional constraints and to elucidate intricate electronic structures of MOL-stabilized metal complexes.

5.4. Materials and Experimental Details

5.4.1. General Experimental

All of the reactions and manipulations were carried out under nitrogen with the use of standard inert atmosphere and Schlenk techniques. ^{1}H NMR spectra were recorded on a Bruker NMR 500 DRX spectrometer at 500 MHz and referenced to the proton resonance resulting from incomplete deuteration of $CDCl_3$ (δ 7.26). ^{13}C NMR spectra were recorded at 125 MHz, and all of the chemical shifts were reported downfield in ppm relative to the carbon resonance of $CDCl_3$ (δ 77.00). The following abbreviations are used here: s: singlet, d: doublet, t: triplet, q: quartet, m: multiplet, br: broad, app: apparent. Mass spectra were obtained with an Agilent 6224 Accurate Mass TOF LC/MS and an Agilent 1100 LC-MSD Mass Spectrometer. Thermogravimetric analysis (TGA) was performed in air using a Shimadzu TGA-50 equipped with a platinum pan. Powder X-ray diffraction (PXRD) patterns were collected on a Bruker D8 Venture, dual microsource (Cu and Mo) diffractometer with a CMOS detector. Cu Kα radiation was used for PXRD. The PXRD patterns were processed with the APEX 2 package using PILOT plug-in. Gas chromatography (GC) data was obtained with a SHIMADZU GC-2010 Plus gas chromatograph. ICP-MS data was obtained with an Agilent 7700x ICP-MS and analyzed using ICP-MS MassHunter version B01.03. Samples were diluted in a 2% HNO_3 matrix and analyzed with a 159Tb internal standard against a nine-point standard curve over the range from 1 ppb to 500 ppb. The correlation coefficient was > 0.9997 for all analyses of interest. Data collection was performed in Spectrum Mode with five replicates per sample and 100 sweeps per replicate.

Electron microscopy images were obtained on a Tecnai F20 transmission electron microscopy. Atomic force microscopy (AFM) images were taken on a Bruker Ⅴ/Multimode 8 instrument. Electron paramagnetic resonance (EPR) spectra were collected with a Bruker Elexsys 500 X-band EPR spectrometer. Tetrahydrofuran (THF) was purified by passing through a neutral alumina column under N_2. Co(tpy)Cl_2 and Fe(tpy)Br_2 were prepared according to literature procedures. [22,51]

5.4.2. Synthesis and Characterization of TPY-MOL and TPY-MOF

5.4.2.1. Synthesis of TPY-MOL

HfCl$_4$ (14.0 mg, 0.044 mmol) and 4'-(4-carboxyphenyl)-[2,2':6',2''-terpyridine]-5,5''-dicarboxylic acid (H$_3$TPY)[33] (12.5 mg, 0.028 mmol) were added to DMF (5 mL), freshly distilled formic acid (0.75 mL), and water (0.3 mL). The mixture was sonicated for 2-3 minutes and placed in an oven at 120 °C for 24 hours. The resulting solid was isolated by centrifugation and washed with DMF and THF. Yield: 13.1 mg (76%).

5.4.2.2. Synthesis of TPY-MOF

0.2 mL of DEF was added to a mixture of ZrOCl$_2$·8H$_2$O (3.2 mg, 9.9 µmol), H$_3$TPY (1.1 mg, 2.5 µmol), and benzoic acid (60 mg, 0.49 mmol). The suspension was sonicated for 2-3 minutes and placed in an oven at 120 °C for 24 hours. The resulting solid was isolated by centrifugation and washed with DMF and THF. Yield: 1.7 mg (58%).

5.4.2.3. Synthesis of CoCl$_2$•TPY-MOL

In a N_2 glovebox, TPY-MOL (4.0 µmol based on TPY) was dispersed in THF (1 mL) and followed by the addition of CoCl$_2$ (4.2 µmol, 1.05 eqv., 0.02 M in THF solution). The resulting mixture was kept at r.t. overnight and then washed with THF for at least three times to obtain

CoCl$_2$•TPY-MOL. The extent of Co metalation was determined to be 100% based on TPY equivalents by ICP-MS. Co: 22.23 ± 0.36 ppb; Hf: 194.24 ± 1.28 ppb.

5.4.2.4. Synthesis of FeBr$_2$•TPY-MOL

In a N$_2$ glovebox, TPY-MOL (4.0 µmol based on TPY) was dispersed in THF (1 mL) and followed by the addition of FeBr$_2$(THF)$_2$ (4.2 µmol, 1.05 eqv., 0.02 M in THF solution). The resulting mixture was kept at r.t. overnight and then washed with THF for at least three times to obtain FeBr$_2$•TPY-MOL. Fe metalation was determined to be 100% based on TPY equivalents by ICP-MS. Fe: 34.91 ± 0.37 ppb; Hf: 327.21 ± 4.84 ppb.

5.4.2.5. Synthesis of Co(THF)$_2$•TPY-MOL

In a N$_2$ glovebox, CoCl$_2$•TPY-MOL (4.0 µmol based on Co) was dispersed in THF (1 mL) and followed by the addition of NaEt$_3$BH (40 µL, 1M THF solution, 10 eqv.). The resulting mixture was kept at r.t. for 1 h and then washed with THF for at least three times to obtain Co(THF)$_2$•TPY-MOL in quantitative yield.

5.4.2.6. Synthesis of Fe(THF)$_2$•TPY-MOL

In a N$_2$ glovebox, FeBr$_2$•TPY-MOL (4.0 µmol based on Fe) was dispersed in THF (1 mL) and followed by the addition of NaEt$_3$BH (40 µL, 1M THF solution, 10 eqv.). The resulting mixture was kept at r.t. for 1 h and then washed with THF for at least three times to obtain Fe(THF)$_2$•TPY-MOL in quantitative yield.

5.4.3. Quantification of H$_2$

Hydrogen detection experiments were performed with Agilent 7890B GC with a TCD detector. All GC results were quantified according to the calibration curve. The calibration curve was prepared by injecting known volumes of Scotty Gas 1% hydrogen in nitrogen standard into

the GC to obtain a linear curve comparing peak area verses hydrogen injection volume with a correlation constant of 0.999.

M = Co, X = Cl
M = Fe, X = Br
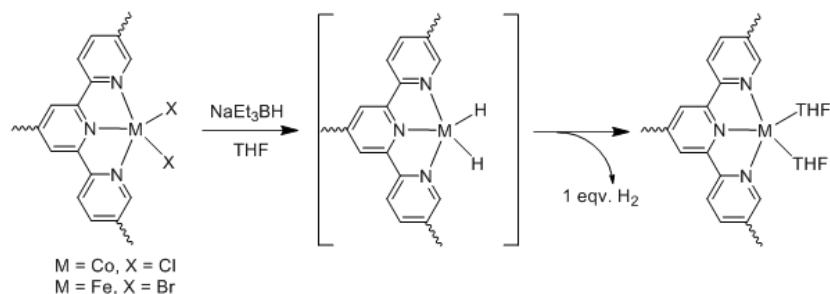
In a N_2 glovebox, $CoCl_2$•TPY-MOL (4 μmol based on Co•TPY) in 1.5 mL benzene was charged into a glass vial. $NaEt_3BH$ (100 μL, 1M toluene solution, 25 eqv.) was added into the vial and the mixture was kept at r.t. for 20 mins. The headspace gas (total volume 2.8 mL) was analyzed by gas chromatography. A parallel experiment with the same amount of TPY-MOL (based on TPY) was also conducted for background removal of H_2 generated from protons at SBUs. Consistent results were obtained in three runs. The amount of H_2 was calculated to be 4.17 ± 0.32 μmole (expected 4 μmole).

$$\frac{(7.20 \pm 0.55) \, \mu L}{200 \, \mu L} \times 2.8 \, mL \times 101 \, kPa \div 8.314 \, J \cdot mol^{-1} \cdot K^{-1} \div 295 = 4.17 \pm 0.32 \, \mu mol$$

In a N_2 glovebox, $FeBr_2$•TPY-MOL (4 μmol based on Fe•TPY) in 1.5 mL benzene was charged into a glass vial. $NaEt_3BH$ (100 μL, 1M toluene solution, 25 eqv.) was added into the vial and the mixture was kept at r.t. for 20 mins. The headspace gas (total volume 2.8 mL) was analyzed by gas chromatography. A parallel experiment with the same amount of TPY-MOL (based on TPY) was also conducted for background removal of H_2 generated from protons at

SBUs. Consistent results were obtained in three runs. The amount of H_2 was calculated to be $3.97 \pm 0.18\ \mu mole$ (expected $4\ \mu mole$).

$$\frac{(6.85\ \pm\ 0.30)\ \mu L}{200\ \mu L}\ \times 2.8\ mL\ \times 101\ kPa\ \div 8.314\ J \cdot mol^{-1} \cdot K^{-1}\ \div 295\ = 3.97\ \pm 0.18\ \mu mol$$

5.4.4. Quantification of Ferrocenium Reduction

Standard solutions with various amount of ferrocene were added with $20\ \mu mol$ of mesitylene as internal standard and analyzed by GC-MS to obtain a calibration curve for ferrocene.

In a N_2 glovebox, Co(THF)$_2$•TPY-MOL ($5\ \mu mol$ based on Co•TPY) was titrated with ferrocenium hexaflorophosphate ($2\ mM$ in DCM). The blue ferrocenium hexaflorophosphate solution reacted with Co(THF)$_2$•TPY-MOL quickly to turn yellow, indicating the generation of ferrocene. The supernatant was separated from MOL via centrifugation. The titration stopped when the supernatant became green to light blue. All yellow supernatant were combined and added with $20\ \mu mol$ of mesitylene as internal standard and analyzed by GC-MS to determine the amount of ferrocene generated. 2 equiv. of ferrocene ($10.6 \pm 2.07\ \mu mol$) w.r.t to CoTPY was detected.

In a N_2 glovebox, Fe(THF)$_2$•TPY-MOL ($5\ \mu mol$ based on Co•TPY) was titrated with ferrocenium hexaflorophosphate ($2\ mM$ in DCM). The blue ferrocenium hexaflorophosphate solution reacted with Co(THF)$_2$•TPY-MOL quickly to turn yellow, indicating the generation of ferrocene. The supernatant was separated from MOL via centrifugation. The titration stopped when the supernatant became green to light blue. All yellow supernatant were combined and added with $20\ \mu mol$ of mesitylene as internal standard and analyzed by GC-MS to determine the

amount of ferrocene generated. 2 equiv. of ferrocene (11.6 ± 0.86 µmol) w.r.t to CoTPY was detected.

5.4.5. Synthesis and Characterization of CoCl₂•tpy, Co(tpy)₂, FeBr₂•tpy, and Fe(tpy)₂

CoCl₂•tpy [CAS: 14854-50-3]: In a N₂–filled glovebox, a solution of terpyridine (200 mg, 0.857 mmol) in THF (20 mL) was slowly added to CoCl₂ (0.857 mmol, 0.02 M in THF solution). The resulting mixture was stirred at r.t. for 12 h and then filtered. After washing the resulting solid with THF, the green solid was dried under vacuum to give Co(tpy)Cl₂ (248 mg, 80% yield). HR-MS (ESI) calcd for $C_{15}H_{11}Cl_2CoN_3$ $[M]^+$ 361.9662, found 361.9646.

FeBr₂•tpy [CAS: 17203-81-5]: In a N₂–filled glovebox, a solution of terpyridine (200 mg, 0.857 mmol) in THF (20 mL) was slowly added to FeBr₂ (0.857 mmol, 0.02 M in THF solution). The resulting mixture was stirred at r.t. for 12 h and then filtered. After washing the resulting solid with THF, the purple solid was dried under vacuum to give Fe(tpy)Br₂ (258 mg, 67% yield). ESI-MS: calcd for $C_{15}H_{11}BrFeN_6$ $[M-Br]^+$ 368.0, found 368.0.

Co(tpy)₂: A mixture of Co(tpy)Cl₂ (50 mg, 0.1377 mmol) and NaBEt₃H (1.377 mmol, 1.0 M in THF) in THF (3.0 mL) was stirred at r.t. for 12 h. After removing of Co NPs by centrifugation, the supernatant was filtered with Celite and dried in vacuo to give Co(tpy)₂. HR-MS (ESI) calcd for $C_{30}H_{22}CoN_6$ $[M]^+$ 525.1238, found 525.1257.

Fe(tpy)₂ [CAS: 20515-11-1]: A mixture of Fe(tpy)Br₂ (50 mg, 0.111 mmol) and NaBEt₃H (1.11 mmol, 1.0 M in THF) in THF (3.0 mL) was stirred at r.t. for 12 h. After the removal of FeNPs by centrifugation, the supernatant was filtered with Celite and then dried in vacuo to give Fe(tpy)₂ . ESI-MS: calcd for $C_{30}H_{22}FeN_6$ $[M]^+$ 522.1, found 522.5.

5.4.6.X-ray Absorption Spectroscopy

5.4.6.1. Data Collection.

X-ray absorption data were collected at Beamline 10-BM-A, B at the Advanced Photon Source (APS) at Argonne National Laboratory. Spectra were collected at the cobalt K-edge (7709 eV) or iron K-edge (7112 eV) in transmission mode. The X-ray beam was monochromatized by a Si(111) monochromater and detuned by 50% to reduce the contribution of higher-order harmonics below the level of noise. A metallic cobalt or iron foil standard was used as a reference for energy calibration and was measured simultaneously with experimental samples. For cobalt samples, the incident beam intensity (I_0), transmitted beam intensity (I_t), and reference (I_r) were measured by 20 cm ionization chambers with gas compositions of 63% N_2 and 37% He, 73% N_2 and 27% Ar, and 100% N_2, respectively. For iron samples, the incident beam intensity (I_0), transmitted beam intensity (I_t), and reference (I_r) were measured by 20 cm ionization chambers with gas compositions of 51% N_2 and 49% He, 79% N_2 and 21% Ar, and 100% N_2, respectively. Data were collected over six regions: -250 to -30 eV (10 eV step size, dwell time of 0.25 s), -30 to -12 eV (5 eV step size, dwell time of 0.5 s), -12 to 30 eV (0.4 eV step size, dwell time of 1 s), 30 eV to 6 $Å^{-1}$, (0.05 $Å^{-1}$ step size, dwell time of 2 s), 6 $Å^{-1}$ to 12 $Å^{-1}$, (0.05 $Å^{-1}$ step size, dwell time of 4 s), and 12 $Å^{-1}$ to 15 $Å^{-1}$, (0.05 $Å^{-1}$ step size, dwell time of 8 s). Multiple X-ray absorption spectra were collected at room temperature for each sample. Samples were ground and mixed with polyethylene glycol (PEG) and packed in a 6-shooter sample holder to achieve adequate absorption length.

5.4.6.2. Data Processing.

Data were processed using the Athena and Artemis programs of the IFEFFIT package based on FEFF 6.[52,53] Prior to merging, spectra were calibrated against the reference spectra and

aligned to the first peak in the smoothed first derivative of the absorption spectrum, the background noise was removed, and the spectra were processed to obtain a normalized unit edge step.

5.4.6.3. EXAFS Fitting.

Fits of the EXAFS regions were performed using the Artemis program of the IFEFFIT package. Fits were performed in *R*-space with a *k*-weight of 3 for cobalt samples and a *k*-weight of 2 for iron samples. Refinement was performed by optimizing an amplitude factor S_0^2 and energy shift ΔE_0, which are common to all paths, in addition to parameters for bond length (ΔR) and Debye-Waller factor (σ^2).

5.4.7. Electron Paramagnetic Resonance Spectroscopy

EPR Measurements were performed using a Bruker Elexsys 500 X-band EPR spectrometer. For low temperature measurements, the samples were held at 20 K using an Oxford Systems continuous-flow He Cryostat coupled with a 10 K He stinger from Bruker. Spectra were acquired with the Bruker Win-EPR software suite. The spectrometer was equipped with a dual mode cavity, operating in the perpendicular mode.

5.4.8. X-ray Photoelectron Spectroscopy (XPS)

XPS data were collected using the AXIS Nova spectrometer (Kratos Analytical) with monochromatic Al Kα X-ray source. The Al anode was powered at 10 mA and 15 kV. The instrument work function was calibrated to give an Au $4f_{7/2}$ metallic gold binding energy (BE) of 83.95 eV. Instrument base pressure was *ca.* 1×10^{-9} Torr. The analysis area size was 0.3×0.7 mm^2. For calibration purposes, the binding energies were referenced to the C 1s peak at 284.8 eV. Survey spectra were collected with a step size of 1 eV and 160 eV pass energy. The Co 2p and Fe 2p spectra of Co(THF)$_2$•TPY-MOL and Fe(THF)$_2$•TPY-MOL were collected with a pass

energy of 160 eV and 0.25 eV step size using 10 and 15 sweeps of 300 and 600 seconds for each sweep, respectively. The MOL samples were introduced into the XPS analysis chamber without exposure to air.

5.4.9. Synthesis of Substrates

5.4.9.1. Synthesis of 5'-(4-bromobutyl)-1,1':3',1''-terphenyl

3,5-diphenyl-1-bromobenzene (909 mg, 2.9 mmol) was charged into a dry 1-neck round-bottom flask with a stir bar. The flask was degassed and placed under N_2 atmosphere. THF (20 mL) was added. The resulting solution was cooled to -78°C, and ^{n}BuLi (1.2 mL, 2.5M in hexene) was added dropwise. The solution was kept at -78°C for 40 min and added into 1,4-dibromobutane (846 mg, 3.9 mmol, dissolved in 5 mL THF) dropwise. The solution was kept at -78°C for 2 h, and then warmed to r.t. overnight. Et$_2$O (40 mL) was added, and the organic layer was washed with H$_2$O (20 mL×2), dried over MgSO$_4$, and the solvent removed in vacuo. The resulting solid was purified by column chromatography on silica gel with 10% EtOAc/88% Hexane/2% DCM as eluent to obtain the desired product as a colorless solid (410 mg, 38% yield).
^{1}H NMR (500 MHz, CDCl$_3$): δ 7.64 (d, J = 8.0 Hz, 4H), 7.63 (s, 1H), 7.46 (t, J = 8.0 Hz, 4H), 7.39 (s, 2H), 7.37 (t, J = 8.0 Hz, 2H), 3.46 (t, J = 7.0 Hz, 2H), 2.78 (t, J = 7.5 Hz, 2H), 1.97 (m, 2H), 1.88 (m, 2H).

5.4.9.2. Synthesis of 5'-(4-azidobutyl)-1,1':3',1''-terphenyl
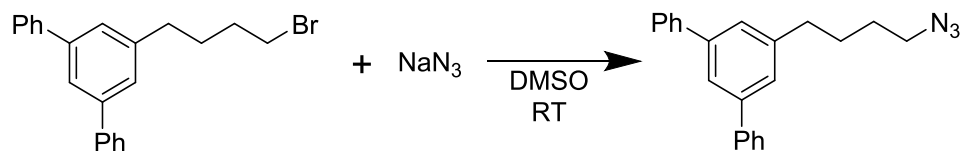
NaN$_3$ (107 mg, 1.65 mmol) was charged into a dry 50 mL round-bottom flask with a stir bar. The flask was evacuated and flushed with N$_2$. Dry DMSO (6 mL) was added, and the solution was stirred for 2 h until the NaN$_3$ was completely dissolved. 5'-(4-bromobutyl)-1,1':3',1''-terphenyl (401 mg, 1.1 mmol) was dissolved in dry DMSO (2 mL) and added to the stirring solution. The solution as allowed to stir at r.t. for 2 d. The solution was added water (10 mL) dropwise followed by Et$_2$O (10 mL) in one portion. The organic layer was separated from the aqueous layer in a separatory funnel. The aqueous layer was further extracted with Et$_2$O (20 mL×3). All organics were combined, dried over Na$_2$SO$_4$, and concentrated in vacuo. The crude residue was purified with column chromatography on silica gel using 5% EtOAc/92% Hexane/3% DCM as eluent to obtain the desired product as a colorless oil (278 mg, 77% yield). ^{1}H NMR (500 MHz, CDCl$_3$): δ 7.68 (m ,5H), 7.49 (t, J = 8.0 Hz, 4H), 7.42 (s, 2H), 7.40 (t, J = 8.0 Hz, 2H), 3.34 (t, J = 7.0 Hz, 2H), 2.81 (t, J = 7.5 Hz, 2H), 1.84 (m, 2H), 1.73 (m, 2H).). ^{13}C NMR (125 MHz, CDCl$_3$): δ 142.89, 141.99, 141.29, 128.84, 127.45, 127.34, 126.36, 124.01, 51.41, 35.62, 28.62, 28.60.

5.4.10. Benzylic C-H Borylation of Arenes with Co(THF)$_2$•TPY-MOL

5.4.10.1. A typical Procedure for Co(THF)$_2$•TPY-MOL Catalyzed Benzylic C-H Borylation of Arenes.

Co(THF)$_2$•TPY-MOL (1.5 μmol Co) was prepared as described above. After washing the MOL with *m*-xylene twice, B$_2$pin$_2$ (38.1 mg, 0.15 mmol) and *m*-xylene (1.11 mL, 9.0 mmol) were added to Co(THF)$_2$•TPY-MOL (1.5 μmol Co). The reaction mixture was stirred under nitrogen at 100 °C for 3 d. The MOL was removed from the solution by centrifugation. The supernatant was transferred to a round-bottom flask, and the MOL was washed with THF twice. The combined organic extracts were concentrated in vacuo to afford 4,4,5,5-tetramethyl-2-(3-methylbenzyl)-1,3,2-dioxaborolane (78% NMR yield based on MeNO$_2$) and 2-(3,5-dimethylphenyl)-4,4,5,5-tetramethyl-1,3,2-dioxaborolane (17% NMR yield based on MeNO$_2$).

5.4.10.2. Recycling Wxperiments for Co•TPY-MOL Catalyzed Benzylic C-H Borylation of p-xylene.

Co(THF)$_2$•TPY-MOL (12.3 μmol Co) was prepared as described above. After washing the MOL with *p*-xylene twice, B$_2$pin$_2$ (62.5 mg, 0.246 mmol) and *p*-xylene (1.82 mL, 14.8 mmol) were added to Co(THF)$_2$•TPY-MOL (12.3 μmol Co). The reaction mixture was stirred under nitrogen at 100 °C for 2 d. Co•TPY-MOL was recovered from the solution by centrifugation. The yield of 4,4,5,5-tetramethyl-2-(4-methylbenzyl)-1,3,2-dioxaborolane was determined by gas chromatography (99% yield). The recovered solid catalyst was used for subsequent reactions, and the reaction mixture was stirred for 2 d in each run.

5.4.10.3. Testing the Heterogeneity of Co(THF)$_2$•TPY-MOL

Co(THF)$_2$•TPY-MOL (0.96 μmol Co) was prepared as described above. After washing the MOL with *p*-xylene twice, B$_2$pin$_2$ (24.4 mg, 0.096 mmol), *p*-xylene (0.711 mL, 5.76 mmol),

and hexadecane (28 μL, 0.096 mmol) were added to Co(THF)$_2$•TPY-MOL (0.96 μmol Co). The reaction mixture was stirred under nitrogen at 100 °C for 5 h. The MOL was removed by centrifugation, and the supernatant was filtered through Celite. Gas chromatography (GC) of the filtrate gave a yield of 8% for 4,4,5,5-tetramethyl-2-(4-methylbenzyl)-1,3,2-dioxaborolane with hexadecane as an internal standard. The filtrate was allowed to react for an additional 67 h, but the reaction did not proceed further (8% of 4,4,5,5-tetramethyl-2-(4-methylbenzyl)-1,3,2-dioxaborolane based on hexadecane internal standard).

5.4.10.4. Measurement of the Kinetic Isotope Effect of C-H Borylation

Co(THF)$_2$•TPY-MOL (4.14 μmol Co) was prepared as described above. After washing the MOL with *p*-xylene or *p*-xylene-d_{10} twice, B$_2$pin$_2$ (52.6 mg, 0.207 mmol), *p*-xylene or *p*-xylene-d_{10} (1.52 mL, 12.4 mmol) and hexadecane (61 μL, 0.207 mmol) were added to Co(THF)$_2$•TPY-MOL (4.14 μmol Co). The reaction mixture was stirred under nitrogen at 100 °C. At various time points, aliquots were taken from the mixture and analyzed by gas chromatography. From the initial rates for the borylation of *p*-xylene and *p*-xylene-d_{10}, the kinetic isotope effect was determined.

5.4.11. Fe-catalyzed Amination

5.4.11.1. A Typical Procedure of Fe(THF)$_2$•TPY-MOL Catalyzed C$_{sp}^3$ C-H Amination
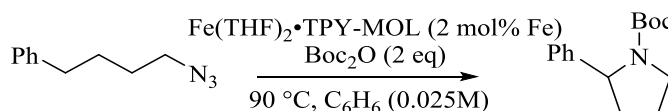
Inside a nitrogen filled glovebox, Fe(THF)$_2$•TPY-MOL (2.3 μmol, suspended in 1.0 mL benzene), was added 1-azido-4-phenylbutane (**1a**) (20.15 mg, 115 μmol) dissolved in 1.3 mL benzene. Boc$_2$O (52.8 μL, 231 μmol) was added, and the flask was sealed with a glass stopper.

After removing the reaction flask from the glovebox, the sidearm was connected to a Schlenk line and subjected to vacuum then backfilled with N_2 five times. The sidearm was then opened to positive N_2 flow [IMPORTANT as CO_2 is released throughout the reaction], and the reaction flask was heated at 90 °C with gentle stirring for 48 h. After cooling to r.t., MOL was separated by centrifugation, and the product was extracted from the MOL with THF washes (4 x 1 mL). The combined organic extracts were concentrated on a rotary evaporator. The residue was added nitromethane (6.17 μL) as an internal standard and the yield was determined by ^{1}H NMR in CDCl$_3$. Crude reaction mixture was then subjected to flash chromatography on silica gel to give **2a** as a colorless oil. The ^{1}H NMR data matched those of the literature report.[16]

5.4.11.2. Recycling Experiments for Fe(THF)$_2$•TPY-MOL Catalyzed C$_{sp}^3$ C-H Amination

Inside a nitrogen filled glovebox, Fe(THF)$_2$•TPY-MOL (0.68 μmol, suspended in 0.47 mL benzene) was added 1-azido-4-phenylbutane (**1a**) (2.38 mg, 13.6 μmol) dissolved in 0.1 mL of benzene. Boc$_2$O (6.2 μL, 27.2 μmol) was added, and the flask was sealed with a glass stopper. After removing the reaction flask from the glovebox, the sidearm was connected to a Schlenk line and subjected to vacuum then backfilled with N_2 (5x). The sidearm was then opened to positive N_2 flow [IMPORTANT as CO_2 is released throughout reaction], and the reaction flask was heated at 90 °C with gentle stirring for 48 h. After cooling to r.t., the flask was transferred back to the N_2-glovebox, where the MOL was separated by centrifugation, and the product was extracted away from the MOL with THF washes (4x). The combined organic extracts were concentrated on a rotary evaporator. The residue was added mesitylene (1.89 μL) as an internal standard and the yield was determined by ^{1}H NMR in CDCl$_3$. Recovered Fe•TPY-MOL was transferred back into the reaction tube, and **1a** (2.38 mg, 14.2 μmol), benzene (0.57 mL), and

Boc$_2$O (6.5 μL, 28.4 μmol) were added. The reaction vessel was sealed and reactions repeated under the conditions as described above.

5.4.11.3. Heterogeneity Test and Cross-over Experiments of Fe(THF)$_2$•TPY-MOL Catalyzed C$_{sp}^3$ C-H Amination

Inside a nitrogen filled glovebox, Fe(THF)$_2$•TPY-MOL (0.68 μmol, suspended in 0.47 mL benzene) was added to 1-azido-5-phenylpentane (**1g**) (2.57 mg, 13.6 μmol) dissolved in 0.1 mL benzene. Boc$_2$O (31.2 μL, 136 μmol) was added, and the flask was sealed with a glass stopper. After removing the reaction flask from the glovebox, the sidearm was connected to a Schlenk line and subjected to vacuum then backfilled with N$_2$ (5x). The sidearm was then opened to positive N$_2$ flow [IMPORTANT as CO$_2$ is released throughout reaction], and the reaction flask was heated at 90 °C with gentle stirring for 48 h. After cooling to r.t., the MOL was separated by centrifugation, and the supernatant was filtered through a short plug of Celite which was subsequently washed with 0.5 mL benzene. 1-azido-4-phenylbutane (**1a**) (2.38 mg, 13.6 μmol) and Boc$_2$O (6.2 μL, 27.2 μmol) were added to the supernatant, and the resulting solution was heated at 90 °C under N$_2$ protection for 48 h. The reaction mixture was concentrated in vacuo. The resulting residue was added mesitylene as internal standard, and the yields of possible amination products were determined from ^{1}H NMR spectra taken in CDCl$_3$. After removal of the MOL, no product is formed from 1-azido-4-phenylbutane. Recovered Fe•TPY-MOL was transferred back into the reaction tube, and **1a** (2.38 mg, 13.6 μmol), benzene (0.57 mL), and Boc$_2$O (6.5 μL, 27.2 μmol) were added. The reaction vessel was sealed and reaction repeated under the conditions as described above. A yield of 67% was observed for 1-azido-4-phenylbutane, confirming the heterogeneous nature of the MOL catalyst.

5.4.12. Density Functional Theory Calculation

Density functional theory (DFT) calculations were performed for $Fe(tpy)X_2$ and $Co(tpy)X_2$ systems with X=Cl, Br, or THF, using the Gaussian 09 software suite, version E01.[54] These complexes were optimized at the level of open-shell B3LYP/6-311G(d) theory. Tetrahydrofuran solvation was incorporated with the implicit solvent model, the conductor-like polarizable continuum model (CPCM).

5.5. References

(1)   Baker, R. T.; Tumas, W. *Science* **1999**, *284*, 1477.
(2)   Bauer, I.; Knölker, H.-J. *Chem. Rev.* **2015**, *115*, 3170.
(3)   Gladysz, J. A.; Bedford, R. B.; Fujita, M.; Gabbai, F. P.; Goldberg, K. I.; Holland, P. L.; Kiplinger, J. L.; Krische, M. J.; Louie, J.; Lu, C. C.; Norton, J. R.; Petrukhina, M. A.; Ren, T.; Stahl, S. S.; Tilley, T. D.; Webster, C. E.; White, M. C.; Whiteker, G. T. *Organometallics* **2014**, *33*, 1505.
(4)   De Vos, D. E.; Dams, M.; Sels, B. F.; Jacobs, P. A. *Chem. Rev.* **2002**, *102*, 3615.
(5)   Song, C. E.; Lee, S.-g. *Chem. Rev.* **2002**, *102*, 3495.
(6)   Westerhaus, F. A.; Jagadeesh, R. V.; Wienhofer, G.; Pohl, M. M.; Radnik, J.; Surkus, A. E.; Rabeah, J.; Junge, K.; Junge, H.; Nielsen, M.; Bruckner, A.; Beller, M. *Nat. Chem.* **2013**, *5*, 537.
(7)   Zhang, T.; Manna, K.; Lin, W. *J. Amer. Chem. Soc.* **2016**, *138*, 3241.
(8)   Manna, K.; Ji, P.; Lin, Z.; Greene, F. X.; Urban, A.; Thacker, N. C.; Lin, W. *Nat. Comm.* **2016**, *7*, 12610.
(9)   Thacker, N. C.; Lin, Z.; Zhang, T.; Gilhula, J. C.; Abney, C. W.; Lin, W. *J. Amer. Chem. Soc.* **2016**, *138*, 3501.
(10)   Song, F.; Wang, C.; Falkowski, J. M.; Ma, L.; Lin, W. *J. Am. Chem. Soc.* **2010**, *132*, 15390.
(11)   Wang, C.; Zheng, M.; Lin, W. *J. Phys. Chem. Lett.* **2011**, *2*, 1701.
(12)   Cao, L.; Lin, Z.; Peng, F.; Wang, W.; Huang, R.; Wang, C.; Yan, J.; Liang, J.; Zhang, Z.; Zhang, T.; Long, L.; Sun, J.; Lin, W. *Angew. Chem. Int. Edi.* **2016**, *55*, 4962.
(13)   Wild, A.; Winter, A.; Schlutter, F.; Schubert, U. S. *Chem. Soc. Rev.* **2011**, *40*, 1459.
(14)   Whittell, G. R.; Hager, M. D.; Schubert, U. S.; Manners, I. *Nat. Mater.* **2011**, *10*, 176.
(15)   Schubert, U. S.; Winter, A.; Newkome, G. R. *Terpyridine-based Materials: For Catalytic, Optoelecttronic and Life Science Applications*; WILEY-VCH, 2011.
(16)   Yam, V. W.-W.; Au, V. K.-M.; Leung, S. Y.-L. *Chem. Rev.* **2015**, *115*, 7589.
(17)   Eryazici, I.; Moorefield, C. N.; Newkome, G. R. *Chem. Rev.* **2008**, *108*, 1834.
(18)   Andreas, W.; Michael, G.; George, R. N. a. U. S. S. *Curr. Top. Med. Chem.* **2012**, *12*, 158.
(19)   Winter, A.; Hager, M. D.; Newkome, G. R.; Schubert, U. S. *Adv. Mater.* **2011**, *23*, 5728.
(20)   Winter, A.; Newkome, G. R.; Schubert, U. S. *ChemCatChem* **2011**, *3*, 1384.
(21)   Liu, P.; Zhou, C.-Y.; Xiang, S.; Che, C.-M. *Chem. Commun.* **2010**, *46*, 2739.

(22) Kamata, K.; Suzuki, A.; Nakai, Y.; Nakazawa, H. *Organometallics* **2012**, *31*, 3825.
(23) Léonard, N. G.; Bezdek, M. J.; Chirik, P. J. *Organometallics* **2016**.
(24) Zhang, C.; Srivastava, P.; Ellis-Guardiola, K.; Lewis, J. C. *Tetrahedron* **2014**, *70*, 4245.
(25) Furukawa, T.; Tobisu, M.; Chatani, N. *Chemical Communications* **2015**, *51*, 6508.
(26) Palmer, W. N.; Obligacion, J. V.; Pappas, I.; Chirik, P. J. *J. Amer. Chem. Soc.* **2016**, *138*, 766.
(27) Larsen, M. A.; Wilson, C. V.; Hartwig, J. F. *J. Amer. Chem. Soc.* **2015**, *137*, 8633.
(28) Ishiyama, T.; Ishida, K.; Takagi, J.; Miyaura, N. *Chem. Lett.* **2002**, 1082.
(29) Shimada, S.; Batsanov, A. S.; Howard, J. A. K.; Marder, T. B. *Angew. Chem. Int. Ed.* **2001**, *40*, 2168.
(30) Palmer, W. N.; Zarate, C.; Chirik, P. J. *J. Amer. Chem. Soc.* **2017**, *139*, 2589.
(31) England, J.; Bill, E.; Weyhermuller, T.; Neese, F.; Atanasov, M.; Wieghardt, K. *Inorg. Chem.* **2015**, *54*, 12002.
(32) Corey, E. J.; Cooper, N. J.; Canning, W. M.; Lipscomb, W. N.; Koetzle, T. F. *Inorg. Chem.* **1982**, *21*, 192.
(33) Hamacher, C.; Hurkes, N.; Kaiser, A.; Klein, A.; Schuren, A. *Inorg. Chem.* **2009**, *48*, 9947.
(34) Braterman, P. S.; Song, J. I.; Peacock, R. D. *Inorg. Chem.* **1992**, *31*, 555.
(35) Berger, R. M.; Mcmillin, D. R. *Inorg. Chem.* **1988**, *27*, 4245.
(36) Scarborough, C. C.; Lancaster, K. M.; DeBeer, S.; Weyhermueller, T.; Sproules, S.; Wieghardt, K. *Inorg. Chem.* **2012**, *51*, 3718.
(37) Wang, M.; Weyhermuller, T.; England, J.; Wieghardt, K. *Inorg. Chem.* **2013**, *52*, 12763.
(38) Jones, G. D.; Martin, J. L.; McFarland, C.; Allen, O. R.; Hall, R. E.; Haley, A. D.; Brandon, R. J.; Konovalova, T.; Desrochers, P. J.; Pulay, P.; Vicic, D. A. *J. Amer. Chem. Soc.* **2006**, *128*, 13175.
(39) Leffler, J. E. *An introduction to Free Radicals*; Wiley-Interscience: New York, 1993.
(40) Bleaney, B.; Bowers, K. D. *Proc. R. Soc. Lon. Ser-A* **1952**, *214*, 451.
(41) Abe, M. *Chem. Rev.* **2013**, *113*, 7011.
(42) Stieber, S. C. E.; Milsmann, C.; Hoyt, J. M.; Turner, Z. R.; Finkelstein, K. D.; Wieghardt, K.; DeBeer, S.; Chirik, P. J. *Inorg. Chem.* **2012**, *51*, 3770.
(43) England, J.; Scarborough, C. C.; Weyhermüller, T.; Sproules, S.; Wieghardt, K. *Eur. J. Inorg. Chem.* **2012**, *2012*, 4605.
(44) Hennessy, E. T.; Betley, T. A. *Science* **2013**, *340*, 591.
(45) King, E. R.; Hennessy, E. T.; Betley, T. A. *J. Amer. Chem. Soc.* **2011**, *133*, 4917.
(46) Cowley, R. E.; Eckert, N. A.; Vaddadi, S.; Figg, T. M.; Cundari, T. R.; Holland, P. L. *J. Amer. Chem. Soc.* **2011**, *133*, 9796.
(47) Cowley, R. E.; Holland, P. L. *Inorg .Chem.* **2012**, *51*, 8352.
(48) Wiese, S.; McAfee, J. L.; Pahls, D. R.; McMullin, C. L.; Cundari, T. R.; Warren, T. H. *J. Amer. Chem. Soc.* **2012**, *134*, 10114.
(49) Badiei, Y. M.; Dinescu, A.; Dai, X.; Palomino, R. M.; Heinemann, F. W.; Cundari, T. R.; Warren, T. H. *Angew. Chem. Int. Ed.* **2008**, *47*, 9961.
(50) Bagh, B.; Broere, D. L.; Sinha, V.; Kuijpers, P. F.; van Leest, N. P.; de Bruin, B.; Demeshko, S.; Siegler, M. A.; van der Vlugt, J. I. *J. Am. Chem. Soc.* **2017**.
(51) Sato, Y.; Nakayama, Y.; Yasuda, H. *J. of Organomet. Chem.* **2004**, *689*, 744.
(52) Rehr, J. J.; Albers, R. C. *Rev. Mod. Phys.* **2000**, *72*, 621.
(53) Ravel, B.; Newville, M.; *J. Synchrotron Rad.*: **2005**; *12*, 537.

(54)   Frisch, M. J.; Trucks, G. W.; Schlegel, H. B.; Scuseria, G. E.; Robb, M. A.; Cheeseman, J. R.; Scalmani, G.; Barone, V.; Mennucci, B.; Petersson, G. A.; Nakatsuji, H.; Caricato, M.; Li, X.; Hratchian, H. P.; Izmaylov, A. F.; Bloino, J.; Zheng, G.; Sonnenberg, J. L.; Hada, M.; Ehara, M.; Toyota, K.; Fukuda, R.; Hasegawa, J.; Ishida, M.; Nakajima, T.; Honda, Y.; Kitao, O.; Nakai, H.; Vreven, T.; Montgomery, Jr., J. A.; Peralta, J. E.; Ogliaro, F.; Bearpark, M.; Heyd, J. J.; Brothers, E.; Kudin, K. N.; Staroverov, V. N.; Keith, T.; Kobayashi, R.; Normand, J.; Raghavachari, K.; Rendell, A.; Burant, J. C.; Iyengar, S. S.; Tomasi, J.; Cossi, M.; Rega, N.; Millam, J. M.; Klene, M.; Knox, J. E.; Cross, J. B.; Bakken, V.; Adamo, C.; Jaramillo, J.; Gomperts, R.; Stratmann, R. E.; Yazyev, O.; Austin, A. J.; Cammi, R.; Pomelli, C.; Ochterski, J. W.; Martin, R. L.; Morokuma, K.; Zakrzewski, V. G.; Voth, G. A.; Salvador, P.; Dannenberg, J. J.; Dapprich, S.; Daniels, A. D.; Farkas, O.; Foresman, J. B.; Ortiz, J. V.; Cioslowski, J. and Fox, D. J. Gaussian, Inc., Wallingford CT, 2013